2016-12-14

High Fidelity Aeroelasticity Simulations of Aircraft and Turbomachinery with Fully-Coupled Fluid-Structure Interaction

Jiaye Gan
University of Miami, j.gan@umiami.edu

UNIVERSITY OF MIAMI

HIGH FIDELITY AEROELASTICITY SIMULATIONS OF AIRCRAFT AND TURBOMACHINERY WITH FULLY-COUPLED FLUID-STRUCTURE INTERACTION

By

Jiaye Gan

A DISSERTATION

Submitted to the Faculty
of the University of Miami
in partial fulfillment of the requirements for
the degree of Doctor of Philosophy

Coral Gables, Florida

December 2016

UNIVERSITY OF MIAMI

A dissertation submitted in partial fulfillment of
the requirements for the degree of
Doctor of Philosophy

HIGH FIDELITY AEROELASTICITY SIMULATIONS OF AIRCRAFT AND TURBOMACHINERY WITH FULLY-COUPLED FLUID-STRUCTURE INTERACTION

Jiaye Gan

Approved:

Ge-Cheng Zha, Ph.D.
Professor of
Mechanical and Aerospace Engineering

Hongtan Liu, Ph.D.
Professor of
Mechanical and Aerospace Engineering

Qingda Yang, Ph.D.
Associate Professor of
Mechanical and Aerospace Engineering

Guillermo Prado, Ph.D.
Dean of the Graduate School

Wangda Zuo, Ph.D.
Assistant Professor of
Civil, Architectural, and Environmental Engineering

GAN, JIAYE (Ph.D., Mechanical and Aerospace Engineering)
High Fidelity Aeroelasticity Simulations of Aircraft and Turbomachinery with Fully-Coupled Fluid-Structure Interaction (December 2016)

Abstract of a dissertation at the University of Miami.

Dissertation supervised by Professor Ge-Cheng Zha.
No. of pages in text. (234)

The purpose of this research is to develop high fidelity numerical methods to investigate the complex aeroelasticity fluid-structural problems of aircraft and aircraft engine turbomachinery.

Unsteady 3D compressible Navier-Stokes equations in generalized coordinates are solved to simulate the complex fluid dynamic problems in aeroelasticity. An efficient and low diffusion E-CUSP (LDE) scheme designed to minimize numerical dissipation is used as a Riemann solver to capture shock waves in transonic and supersonic flows. An improved hybrid turbulence modeling, delayed detached eddy simulation (DDES), is implemented to simulate shock induced separation and rotating stall flows. High order accuracy (3rd and 5th order) weighted essentially non-oscillatory (WENO) schemes for inviscid flux and a conservative 2nd and 4th order viscous flux differencing are employed. To resolve the nonlinear interaction between flow and vibrating blade structures, a fully coupled fluid-structure interaction (FSI) procedure that solves the structural modal equations and time accurate Navier-Stokes equations simultaneously is adopted. A rotor/stator sliding interpo-

lation technique is developed to accurately capture the blade rows interaction at the interface with general grid distribution. Phase lag boundary conditions (BC) based on the time shift (direct store) method and the Fourier series phase lag BC are applied to consider the effect of phase difference for a sector of annulus simulation.

Extensive validations are conducted to demonstrate high accuracy and robustness of the high fidelity FSI methodology. The accuracy and robustness of RANS, URANS and DDES turbulence models with high order schemes for predicting the lift and drag of the DLR-F6 configuration are verified. The DDES predicts the drag very well whereas the URANS model significantly over predicts the drag. DDES of a finned projectile base flows is conducted to further validate the high fidelity methods with vortical flow. The DDES is demonstrated to be superior to the URANS for the projectile flow prediction due to more accurate base vortex structures and pressure prediction.

DDES of a 3D transonic wing flutter is validated with AGARD Wing 445.6 aeroelasticity experiment at free stream Mach number varied from subsonic to supersonic. The predicted flutter boundary at different free stream Mach number including the sonic dip achieves very good agreement with the experiment. In particular, the predicted flutter boundaries at the supersonic conditions match the experiment accurately. The mechanism of sonic dip is investigated. It is observed that the amplitude ratio of first bending mode to the second torsion mode is increased dramatically when the sonic dip occurs with a reversed trend to the flutter speed index boundary. The reduced torsional amplitude is attributed to the decreased pitching moment, which appears to be caused by the lift generation shifted toward mid-chord location.

Simulation of supersonic fluid-structural interaction of a flat panel is performed by

using DDES with high order shock capturing scheme. The panel vibration induced by the shock boundary layer interaction is well resolved by the high fidelity method. The dominant panel response agrees well with the experiment in terms of the mean panel displacement and frequency.

The DDES methodology is used to investigate the stall inception of NASA Stage 35 compressor. The process of rotating stall is compared between the results using both URANS and DDES with full annulus. The stall process begins with spike inception and develops to full stall. The numbers of stall cell, and the size and propagating speed of the stall cells are well captured by both URANS and DDES. Two stall cells with 42% rotor rotating speed are resolved by DDES and one stall cell with 90% rotor rotating speed by URANS. It is still not conclusive which method is more accurate since there is no experimental data to compare, but the DDES does show more realistic vortical turbulence with more small scale structures.

The non-synchronous vibration (NSV) of a high speed 1-1/2 stage axial compressor is investigated by using rigid blade and vibrating blade with fluid-structural interaction. An interpolation sliding boundary condition is used for the rotor-stator interaction. The URANS simulation with rigid blades shows that the leading edge(LE) circumferentially traveling vortices, roughly above 80% rotor span, travel backwards relative to the rotor rotation and cause an excitation with the frequency agreeing with the measured NSV frequency. The predicted excitation frequency of the traveling vortices in the rigid blade simulation is a non-engine order frequency of 2603 Hz, which agrees very well with the rig measured frequency of 2600 Hz. For the FSI simulation, the results show that there exist two dominant frequencies in the spectrum of the blade vibration. The lower dominant

frequency is close to the first bending mode. The higher dominant frequency close to the first torsional mode agrees very well with the measured NSV frequency. To investigate whether the NSV is caused by flow excitation or by flow-structure locked-in phenomenon, the rotating speed is varied within a small RPM range, in which the rig test detected the NSV. The unsteady flows with rigid blades are simulated first at several RPMs. A dominant excitation NSV frequency caused by the circumferentially traveling tip vortices are captured. The simulation then switches to fluid structure interaction that allows the blades to vibrate freely. The simulation indicates that the structure response follows the frequency of the flow excitations that exist with the rigid blades. At least under the present simulated conditions, the NSV does not appear to be a lock-in phenomenon, which has the flow frequency locks in with the structure frequency.

Overall, the high fidelity FSI methodology developed in this thesis for aircraft and engine fan/compressor aeroelasticity simulation is demonstrated to be accurate and robust. It has advanced the forefront of the state of the art.

Dedicated to my wife and to my parents
for their love, support, encouragement and inspiration.

Acknowledgment

I give my gratitude and respect to my academic advisor, Professor Ge-Cheng Zha for suggesting this topic and providing continued technical and personal guidance, valuable comments, suggestions, patience, and time throughout the course of my study at the University of Miami. He has given me considerable freedom and shown patience as I pursued the idea development in this thesis.

I thank my fellow students for useful discussions and various help including computer technique support and giving me high priority in using computer resources. I would like to thank Dr. Hongsik IM, who is like my second advisor, for his valuable guidance and discussion.

Finally, I would like to thank my family, especially my wife and my parents. Your patience and understanding are greatly appreciated.

The computing resource support from the Center for Computational Sciences at University of Miami is greatly appreciated. The High Performance Computing Challenge Project of DoD Supercomputing Resource Centers provided the resource to investigate the AGARD wing flutter and supersonic panel flutter simulation. The DoD DSRC supercomputing facilities under the US Army ARDEC program is used for the projectile simulation.

Contents

List of Figures

List of Tables

List of Symbols

a, c	speed of sound, $\sqrt{\gamma p/\rho}$
A, B, C	Jacobian matrix of inviscid flux $\mathbf{E}, \mathbf{F}, \mathbf{G}$ in ξ, η, ζ direction
C	speed of sound in generalized coordinates, $c\sqrt{l_\xi^2 + l_\eta^2 + l_\zeta^2}$
$\mathbf{C}$	absolute velocity vector
C_{DES}	DES coefficient, 0.65
C_m	meridional absolute velocity, $\sqrt{C_x^2 + C_r^2}$
C_p	specific heat capacity at constant pressure
C_x, C_θ, C_r	absolute velocities in x, θ, r direction
C_t	tip chord of the compressor rotor
d	distance from the closest wall
$\tilde{d}$	length scale of DES, $min(d, C_{DES}\Delta)$
dQ	head added to system
dW	total work done of the system
dE	change in total energy of system
D	source term of Navier-Stokes equations in generalized coordinates
$\mathbf{E}, \mathbf{F}, \mathbf{G}$	inviscid flux vectors in ξ, η, ζ direction
e	total energy per unit mass
$\mathbf{e}_x, \mathbf{e}_y, \mathbf{e}_z$	unit normal vector in reference xyz
$\mathbf{F}$	sum of fluid force acting on the structure or on a finite control volmue
$\mathbf{F}_b$	body force acting on a finite control volmue
$\mathbf{F}_s$	surface force acting on a finite control volmue
H	blade active length or wing span

I	identity matrix
I_o	rothalpy
J	Jacobian of the coordinate transformation, $\frac{\partial(\xi,\eta,\zeta)}{\partial(x,y,z)}$
L	reference or characteristic length
$\mathbf{l},\mathbf{m},\mathbf{n}$	normal vector on ξ,η,ζ surface with its magnitude equal to the elemental surface area and pointing to the direction of increasing ξ,η,ζ
l_t	grid moving velocity
L,M,N	Jacobian matrix of viscous flux $\mathbf{R},\mathbf{S},\mathbf{T}$ in ξ,η,ζ
$\mathbf{M},\mathbf{C},\mathbf{K}$	vibration mass, damping, stiffness matrices
m	pseudo time marching step
M_∞	reference Mach number, $\frac{V_\infty}{a_\infty}$
M_ξ	contravariant Mach number in ξ direction, $M_\xi = \frac{U}{C}$
n	physical time marching step
N_B	number of blade
N_D	number of nodal diameter
p,P	static pressure
p_o,P_o	total pressure
$\overline{p_o},\overline{P_o}$	pitchwise mass averaged total pressure
Pr	Prandtl number
Pr_t	turbulent Prandtl number
$\mathbf{Q}$	conservative variable vector
q_k	total heat flux in Cartesian coordinates
R	gas constant

$\mathbf{R}, \mathbf{S}, \mathbf{T}$	viscous flux vectors in ξ, η, ζ direction
r	radius of computational domain with rotating axis of x, $\sqrt{y^2+z^2}$
$\mathbf{r}$	position vector in reference XYZ
R_e	Reynolds number, $\frac{\rho_\infty V_\infty L_\infty}{\mu_\infty}$
R_o	Rossby number, $\frac{\Omega L_\infty}{V_\infty}$
S_v	S-A turbulence model source term
T	static temperature, or period
$\mathbf{T}$	surface stress vector, $\sigma \cdot \mathbf{n}$
T_o	total temperature
t	time
U, V, W	contravariant velocities in ξ, η, ζ direction
$V_\infty (= C_\infty)$	inlet absolute total velocity as reference velocity, $\sqrt{C_m^2 + C_\theta^2}$
u, v, w	relative velocities in x, y, z direction
u^+	dimensionless velocity, u/u_τ
u_τ	friction velocity, $\sqrt{\tau_w/\rho}$
$\mathbf{V}$	relative velocity vector
V	cell volume
V_x, V_θ, V_r	relative velocities in x, θ, r direction
x, y, z	cartesian coordinates in moving frame of reference
X, Y, Z	cartesian coordinates in fixed frame of reference
y^+	dimensionless wall normal distance, $\frac{u_\tau y}{\nu}$

- Greek Symbols -

θ, r, x	Cylindrical coordinates

α swirl angle, $tan^{-1}(C_\theta/C_m)$

β pitch angle, $tan^{-1}(C_r/C_x)$

ΔS Change of entropy, $C_p ln\frac{To}{To_\infty} - Rln\frac{Po}{Po_\infty}$

Δt physical time step

δ_{ik} Kronecker delta function

ε convergence criterion taken by FSI solver

γ specific heat ratio

λ_j structure eigenvalue of the jth mode

μ viscosity

μ_{DES} turbulent eddy viscosity determined by DES

ν kinematic viscosity

ϕ structure mode shape

$\tilde{\phi}$ structure mass normalized mode shape

$\tilde{\nu}$ working variable of the S-A model related to turbulent eddy viscosity

Ω rotor angular velocity in rad/s

ρ fluid density

τ_{ik} shear stress in Cartesian coordinates

τ_w fluid shear stress at the wall surface

φ position vector in reference xyz

ξ, η, ζ generalized coordinates

- Flutter parameters -

b_s bade (or wing) root semi-chord

$\bar{m}$ blade (or wing panel) mass

$\bar{V}$ frustum volume

V^* reduced velocity, $\frac{U_\infty}{b_s \omega_\alpha}$

V_f flutter speed index, $\frac{V^*}{\mu}$

ω_α 1st torsional mode natural frequency (=ω_2)

ω_{ij} fluid particle angular velocity tensor, $\frac{1}{2}(\frac{\partial u_i}{\partial x_j} - \frac{\partial u_j}{\partial x_i})$

ω_j blade (or wing) angular eigenfrequency

$\bar{\mu}$ mass ratio, $\frac{\bar{m}}{\bar{V}\rho_\infty}$

- Subscripts -

b computational domain outer boundary

i computational domain inner boundary

i, j, k indices

∞ reference point

- Abbreviations -

AOA Angle of Attack

BC Boundary Condition

BPF Blade Passing Frequency

BTW Backward Travelling Wave

CFD Computational Fluid Dynamics

CFL Courant-Friedrichs-Lewy number

CSD Computational Structural Dynamics

CUSP Convective Upwind and Split Pressure

DDES Delayed Detached Eddy Simulation

DES Detached Eddy Simulation

DNS	Direct Numerical Simulation
DOF	Degree of Freedom
FSI	Fluid-Structural Interaction
FSPL	Fourier Series Phase Lag
FTW	Forward Travelling Wave
FVS	Flux Vector Splitting
GCF	Greatest Common Factor
HCF	High Cycle Fatigue
IGV	Inlet Guide Vane
LCO	Limit Cycle Oscillation
LDE	Low Diffusion E-CUSP scheme
LES	Large Eddy Simulation
LHS	Left Hand Side
MSD	Modeled-Stress Depletion
MUSCL	Monotone Upstream-centered Schemes for Conservation Laws
NSV	Non-Synchronous Vibration
RANS	Reynolds Averaged Navier-Stokes equations
RHS	Right Hand Side
$S-A$	Spalart-Allmaras (S-A) one equation turbulence model
TSPL	Time Shifted Phase Lag
URANS	Unsteady Reynolds Averaged Navier-Stokes equations
WENO	Weighted Essentially Non-Oscillatory scheme

Chapter 1

Introduction

1.1 Background

Fluid-structure interaction (FSI) studies the multiphysics involving the interactions between flexible and moving structures and a external or internal flows. FSI exists in many engineering fields. For example, the interaction of wind and tall buildings and bridges, fluid flowing through flexible pipes, flow induced vibration on aircraft wing and turbomachinery blades, and so on. The focus of this thesis will be on the aeroelastic problems that occur in aircraft and aircraft engine turbomachinery.

Aeroelasticity involves interactions among the inertial, elastic, and aerodynamic forces. There are static and dynamic aeroelastic problems. Static aeroelasticity covers the interaction between aerodynamic force and elastic force. And dynamic aeroelasticity studies the interaction among the aerodynamic, elastic, and inertial forces. Examples of dynamic aeroelastic phenomena are forced response, flutter and buffet.

1.1.1 Aircraft Dynamic Aeroelasticity

Aircraft dynamic aeroelasticity is concerned with the oscillatory effects of the interactions between air flow and aircraft wing, control surfaces and the skin of fuselage. Flutter and buffeting are the common dynamic aeroelastic phenomena. This thesis is focused on the former. Buffeting is a high-frequency instability, occurring because of the interaction of airflow separation or shock wave oscillation.

Flutter is a self-excited aeroelastic instability of an elastic structure in a fluid flow. Flutter occurs when the structural damping is insufficient to damped the energy absorbed from air flow and can lead to structural failure. Flutter may happen at subsonic and supersonic flows.

Flutter in transonic flow regime is of significant interest in aircraft wing and control surface design since modern transport aircraft mostly cruise in transonic Mach number regime. However, the presence of shock waves on the wing surface introduces strong aerodynamic non-linearity, which posts great challenge on the aeroelastic analysis and prediction of flutter boundary. The transonic dip phenomena in transonic flutter boundary with the flutter speed index suddenly dropping at sonic speed are not fully understood. It may be attributed to the shift in dynamic center of pressure associated with the shock motion in transonic flow regime [3]. Efforts of both experiment and numerical simulation are still needed to understand better the sonic dip mechanism.

Flutter may also occur in modern high performance compressor and turbine stages due to the load with increased high pressure ratio. The flow fields in transonic rotors are dominated by shock waves that manifests itself in the blade passage. For turbomachinery blade rows, flutter are observed primarily in a single natural mode, with oscillating shock waves

on the blade surfaces being one of the primary sources for instability. The shock waves could have a stabilizing or destabilizing effect on blade stability.

Supersonic flutter is one of the major structural issues for high speed airplanes, aerospace vehicles and rockets. The surface skin of a flight vehicle in supersonic flow may experience a sudden structural fatigue failure resulting in the loss of the vehicle. The determination of flutter stability boundaries is essential to avoid such losses.

Accurate prediction of dynamic aeroelasticity remains very challenging since it involves both aerodynamics and structural dynamics. The interaction between flow and elastic structure is inherently unsteady and nonlinear. For most dynamic aeroelastic problems, it is impossible to obtain analytical solutions. On the other hand, wind tunnel test or flight flutter testing is very expensive and time consuming. Thus, the development of efficient and accurate prediction methods are needed to save the cost of flight test.

Computational fluid dynamics (CFD) has been extensively developed and used for predicting aeroelasticity in the past several decades. However, high fidelity numerical simulation (HFNS) of dynamic aeroelastic problem is arduous since they involve both aerodynamics and structural dynamics. There are complex unsteady flow phenomena such as flow separation and shock wave/turbulent boundary layer interaction(STBLI). For the structure at high speed such as supersonic or hypersonic flow, the skin temperature could be sufficiently high to cause large nonlinear deflection. The numerical difficulties maybe the reason that currently there are no benchmarking "standards" for validating computational aeroelasticity codes at high speed.

Methods in HFNS must include models that are capable of predicting strong nonlinear and viscous flow phenomena encountered at various flight speeds with minimal errors in

fluid structure coupling.

1.1.2 Turbomachinery Dynamic Aeroelasticity

Modern aircraft engines also have serious aeroelastic (aeromechanic) problems. The demands of high performance and low weight have pushed the turbomachinery towards higher aerodynamic loading, lower blade stiffness, closer blade row spacing and higher rotational speeds. These factors increase the susceptibility of flow-induced blade vibrations which have negative impacts on engine readiness and operating costs [4–6].

According to U.S. Air Force, 55% of USAF fighter jet engine parts are mishaped by high cyle fatigue (HCF) [7], which is a serious problem in aircraft engine design and development. HCF of turbomachinery blades may be caused by such as flutter, forced response vibration, non-synchronous vibration(NSV), separation flow vibration, and acoustic resonance.

Classical blade vibrations are flutter and forced response. Among those vibration phenomena, flutter is the most dangerous aeroelastic problems. Turbomachinery flutter is similar to wing flutter in that both are self-excited aeroelastic instability. It occurs when the blade structure damping is insufficient to damp out the energy absorbed from the unsteady flow in the turbomachinery. Blade flutter is observed primarily in the first natural mode with several traveling waves [8].

The shock instabilities, rotating stall and even choking are know as main sources that trigger flutter in a transonic fan/compressor of aircraft engines [8–14]. The type of flutter in a compressor depends on the point of operation on the characteristic compressor map. Various types of turbomachinery flutter have been observed, such as unstall supersonic flutter,

subsonic/transonic stall flutter, supersonic stall flutter, and choke flutter. The transonic stall flutter will be studied in this thesis.

Transonic stall flutter occurs at near stall condition where the flow incidence angles are high. Stall flutter is one of the most difficult aeroelastic problems to predict in turbomachinery. There are complex flow phenomena, such as flow separation at the suction surface and shock oscillation during stall flutter in transonic turbomachinery. Currently, the prediction of stall flutter of turbomachinery blades are mostly based on low fidelity methods [8, 9]. The flow mechanism leading to stall flutter in transonic flutter is not fully understood yet.

Forced response are induced by blade row interaction or inlet distortion. The aerodynamic excitation frequencies are integer multiples of the wheel speed. When the blade passing frequency is synchronous to system natural frequency, resonance may occur, which would causes blades HCF failure. The Campbell diagram is used for aeroelastic preliminary design of turbomachinery blades to the potential resonance. The Campbell diagram is a plot of blade natural frequencies and the various engine order lines with respect to the rotor rotating speed. It is a good tool to clarify blade vibration terms used in aircraft engines. If a vibration with a frequency with an integer multiple of the rotational speed, it is called engine order vibration or synchronous vibration to the engine. Hence, the forced response is engine order vibration. Flutter is usually low frequency close to the 1st eigen frequency of the blade structure and non-synchronous to the engine order [15].

Recently, a less known aeroelastic vibration, non-synchronous vibration (NSV), was studied by many people [16–22]. NSV is a non-engine order vibration and is usually locked-on between two engine order lines with high frequency and amplitude enough to cause high cycle fatigue (HCF), in which the stress level is over the material endurance

limit due to unsteady aerodynamic excitation forces acting on the blades. NSV is usually observed on the first stage rotor of a multistage high pressure compressor [16, 20]. Since lack of understanding on NSV will increase cost and development time, many efforts have been made by major engine manufacturers to investigate the mechanism behind NSV. Investigation of the NSV mechanism is thus one of the purposes of this thesis.

Numerical simulations of FSI phenomena flutter, forced vibration, and NSV are very challenging, because FSI problems involve both fluid dynamic, structure dynamic and their coupling. The flows in the turbomachinery are three dimensional (3D), unsteady, highly non-linear. Currently, there are few high fidelity methods to adequately resolve turbulence, shock/turbulent boundary layer and fluid-structure interaction.

The highly non-linear nature of the transonic and supersonic flow results in a strong couple of the structural and flow equations. Hence, those equations need to be solved simultaneously so that the non-linear effects can be captured accurately, such as large variations of the aerodynamic forces due to the small blade vibration. However, most of FSI simulation methods use a loosely coupled procedure [23–27], in which the equations for fluid, structure and mesh deformation are solved sequentially, in an uncoupled mode. The loosely coupled method is lack of convergence and incapable of predicting the non-linear effects. Therefore, a tool that can capture the simultaneous fluid/structure interaction is crucial in the design and analysis of aircraft engine fans/compressors. In this thesis, the fully coupled FSI strategy [21, 28–31] is developed for turbomachinery.

1.2 Turbulence Modeling

Turbulence modeling is critical for the prediction of aerodynamic forces in FSI simulation, such as the viscous force. The commonly used models today are still the Reynolds averaged Navier-Stokes(RANS) models, which is in general considered as inaccurate for predicting the flow with large separations. RANS model treat large eddy structures as isotropic and are not consistent with the physics. However, RANS models have their advantage of CPU efficiency and can handle many engineering problems with calibrated models. However, for high Reynolds number flows such as those of transonic wings and turbomachinery blades, to resolve wall boundary layer, LES needs the CPU resource not much less than the Direct Numerical Simulation(DNS). This makes the LES too expensive for fluid-structural interaction unsteady calculations.

Hence, hybrid turbulence modeling methods, such as the Detached Eddy Simulation (DES) suggested by suggested by Spalart et al. [32] is a very good balance between the accuracy and CPU. In DES, RANS method is used within the wall boundary layer and LES is used away from the wall surface boundary layer. By using the RANS model near walls, the mesh size as well as the CPU time can be tremendously reduced. However, a defect of the first generation DES model [32], DES97, has been also exposed. DES97 may behave incorrectly and cause modeled stress depletion (MSD) in the regions of thick boundary layers and shallow separation regions due to the grid spacing dependence [33]. Delayed detached-eddy simulation (DDES) by Spalart [33] is an improved version of the DES97 model. With DDES, a blending function similar to the one used by Menter and Kuntz [34] for the SST model is introduced to limit the length scale of DES97 to ensure the transition of RANS to LES be independent of grid spacing. DDES is employed to simulate the FSI

problems in this thesis.

1.3 Objective

The objective of this research are to develop and adopt high fidelity numerical methods for predicting and investigating complex aeroelastic problems in aircraft and multistage fan/compressor. In order to fulfill the goal, the following tasks are achieved in this thesis:

- Investigate the physics of the unsteadiness caused by the shock, the shock/boundary layer interaction.
- Study the shock wave effect on stall inception in a transonic compressor
- Simulate the flutter boundary transonic compressor stage
- Investigate the mechanism of sonic dip phenomenon for a transonic wing
- Develop tools for predicting supersonic panel flutter
- Further investigate the mechanism of non-synchronous vibration in turbomachinery

1.4 Strategy

The high fidelity numerical strategy for turbomachinery aeroelasticity is adopted and developed based on the following novel numerical methods.

1) Unsteady 3D compressible Navier-Stokes equations are solved with a system of 5 decoupled structure modal equations in a fully coupled manner. The low diffusion E-CUSP scheme with a 5th order WENO reconstruction for the inviscid flux and a set of 2nd

order central differencing for the viscous terms are used to accurately capture the shock wave/turbulent boundary layer interaction of the vibrating wing and blades.

2) The fully coupled fluid/structure interaction approach and an efficient mesh deforming technique are used in aeroelasticity simulations of aircraft and turbomachinery.

3) An advanced LES/RANS hybrid turbulence model, DDES suggested by Spalart et al. [33] is employed for high fidelity aeroelasticity simulation.

4) A rotor/stator sliding interpolation BC is developed for multistage turbomachinery simulation in order to resolve the wake propagation between blade rows.

5) A time shifted phase lag boundary condition instead of periodic boundary condition is used in the turbomachinery simulations with a sector of geometry.

1.5 Outline of The Thesis

The overview of the numerical algorithms employed for aircraft and turbomachinery FSI simulation are given in Chapter 2.

Non-inertial reference frame is adopted for both flow and structure governing equations. The time accurate Navier-Stokes equations are derived in a rotating frame as the flow governing equations in Chapter 3. For the structure governing equations, the decoupled modal equations are derived in the same rotating frame in Chapter 3.2.

In Chapter 4, the numerical methods are described including the implicit discretization of the Navier-Stokes equations, the low diffusion E-cusp scheme as an accurate approximate Riemann solver, and the high order inviscid and viscous flux reconstruction schemes.

Validation studies on the DDES turbulence modeling method are given in Chapter 5 by

the prediction of force and moment coefficients of wing body configuration and projectile. The high fidelity FSI methodology is validated with of AGARD Wing flutter boundary simulation in Chapter 6 and panel aeroelasticity in Chapter 7.

In Chapter 8, high fidelity simulations of stall inception for NASA Stage 35 are conducted by using both DDES and URANS. The full annulus of the Stage 35 is simulated. The detail process of rotating stall is captured. The stall flutter of NASA Stage 35 is also simulated with both DDES and URANS with fully coupled FSI in Chapter 9.

In Chapter 10, investigation of non-synchronous vibration mechanism of a GE aircraft engine axial compressor is conducted using the high fidelity FSI methodology developed in this thesis.

Chapter 2

Literature Review

There are in general three methods to study aeroelasticity, including theoretical, numerical simulation and measurement. The focus of this research is on the high fidelity methods for aeroelasticity simulation. The state of the art with respect to the numerical simulations in aircraft and turbomachinery aeroelasticity is reviewed in this chapter.

2.1 Wing Flutter and Panel Flutter

Among aeroelastic problems, flutter is the most dangerous vibration and should be considered in the early phase of aircraft aeroelasticity design. Experimental testing of aircraft aeroelasticity is very expensive in the design phase. Therefore, tools for flutter prediction are very important in aircraft design.

2.1.1 Transonic Wing Flutter

Wing flutter may occur at any Mach number from subsonic to supersonic. There may be complex flow phenomena such as flow separation and shock wave/turbulent boundary layer interaction(STBLI) during flutter. Various flow models have been developed to predict the flutter boundary of aircraft. The classical linear models [35] including piston theory and full potential flow models are widely used in aeroelastic design for their advantage of computational efficiency. The disadvantage of linear flow models is that they fail to accurately capture the location and strength of local shock motion in transonic and supersonic regime.

To predict the transonic or supersonic flutter boundary with better accuracy, tools based on nonlinear Euler equations have been developed. Bendiksen et al. [36] study the transonic flutter of typical section wing models by solving the Euler equation coupled with a two degrees of freedom of structural dynamic equations. Reasonable flutter results are obtained in the regions with no strong shock. Rausch et al. [37] predict flutter boundary of a set of configurations by solving unsteady Euler aerodynamic equations on unstructured grid. Good agreement with experiment is obtained in the predicted flutter boundary for subsonic flow. However the predicted flutter characteristics in transonic regime are not satisfactory. Since the viscous effect on these flutter boundary prediction is neglected, neither potential flow model nor Euler equations are suitable for understanding the STBLI and the mechanism that causes flutter.

Prananta et al. [38] report the results of aeroelastic simulations using the Euler and Navier-Stokes solvers. Their calculations show that the viscous effect plays a very important role in determining the transonic dip and flutter boundary for a NACA64A010 airfoil. Lee-Rausch et al. [39] also study the effect of viscosity on the flutter boundary

of AGARD wing 445.6 by comparing the Euler and Navier-Stokes results over a range of Mach numbers from 0.499 to 1.14. Their calculation shows a significant viscous effect on the supersonic flutter boundary. Viscous effects and the STBLI may induce flow separation and shock wave oscillation that affect flutter speed. Isogai [40] considers that the drop of transonic flutter boundary is due to the presence of part chord shock and its oscillation that is not in phase with the airfoil motion. Bendiksen [3] attributes the sonic dip to the shock motion transition from Tijdeman type A to type B [41] that throttles the aerodynamic work done on the wing and forms single degree of freedom flutter occurred at transonic.

To understand the mechanism of the non-linear aeroelasticity behavior, high fidelity solver based on Navier-Stokes equations coupled with the structural dynamic governing equations is required. Computational methods using Reynolds Averaged Navier Stokes (RANS) [42, 43], large eddy simulation (LES) [44], and direct numerical simulation (DNS) [42, 45] have been utilized to study the STBLI. DNS and LES provide better comparison with experimental results than RANS. Priebe et al [45] employed DNS to study the STBLI on a ramp configuration. They demonstrate that the shock impingement amplifies the pressure fluctuation and there are high-level, low-frequency (< 1000 Hz) vortex structures in the turbulent boundary layer. However, DNS and LES will not be feasible for high Reynolds number aeroelastic problems for a long time due to the excessive computational cost. On the other hand, RANS cannot accurately capture the shock oscillation due to the interaction with the turbulent layer without shock unsteadiness correction [44].

The hybrid RANS/LES approach, Detached eddy simulation (DES) suggested by Spalart [33], is developed for complex turbulence problems as a compromise between prediction accuracy and CPU efficiency. In DES, a RANS model is used in the near wall regions

to reduce the grid density, and the LES is used outside the near wall regions to deal with massively separated flows. Spalart et al [33] suggested delayed DES(DDES) in 2006 to overcome the modeled stress depletion(MSD) problem of the original DES when the mesh is thin compared with boundary layer thickness. In DDES, a blending function similar to the one used by Mentor and Kuntz [34] for the SST model is introduced to limit the length scale of DES97 to ensure the transition of RANS to LES to be independent of grid spacing.

The other very important issue of FSI simulation is the artificial dissipation from the CFD schemes, which affects the prediction of aerodynamic damping to the structure. It includes the resolution of acoustic waves and high order mode of structure vibration with high reduced frequency, which is a small scale wave phenomenon. Most of the current CFD simulations for FSI use 2nd order schemes for the convective fluxes, which have high numerical dissipation due to the upwinding requirement to capture shock waves. 120In this thesis, the high order shock capturing schemes for FSI with 5th order weighted essentially non-oscillatory (WENO) scheme for inviscid fluxes [29, 30, 46, 47] are employed.

The advantage of high order low diffusion schemes is demonstrated in the simulation of the transonic NLR 7301 airfoil limited cycle oscillation (LCO). Since the LCO has bifurcation, some other research groups using 2nd order schemes only capture the amplitude about 10 times higher than the measured one in wind tunnel. Their schemes tend to be too diffusive to capture the LCO with the amplitude as small as 2/1000 of the airfoil chord. The simulation of Wang et al [29, 30] of the present author's group is the only one, and the first one, that accurately captures the small LCO amplitude measured in the experiment.

Recently, Chen et al. [48] predict the transonic flutter boundary of AGARD wing 445.6 using delayed-detached-eddy simulation(DDES) [33]. In their study, time accurate Navier-

Stokes equations are solved with a system of 5-decoupled structure modal equations in a fully coupled manner [49, 50]. The computed transonic flutter boundary agrees very well with the experiment. The same method was utilized by Im et al. in the author's group [51] to improve the prediction of the supersonic flutter boundary of the AGARD wing 445.6 model. Their results appear to be the first time that a numerical prediction of supersonic flutter boundary matches with experiment accurately. However, the flutter mechanisms in transonic and supersonic condition are not investigated in [48, 51]. Furthermore, the complete AGARD wing 445.6 flutter boundary at different Mach numbers from subsonic to supersonic is not simulated in their work.

2.1.2 Supersonic Panel Flutter

Supersonic panel flutter is a self-excited aeroelastic instability which typically have high amplitude and may cause fatigue damage. Study of the supersonic panel flutter is very important for supersonic/hypersonic vehicle design. However, high fidelity numerical simulation of supersonic panel flutter is very challenging due to the complex shock-turbulent boundary layer interaction(STBLI). For the structure, the skin panel temperature could reach several hundreds degree due to aerodynamic heating, which may lead to large deflection and the panel motion become non-linear.

The previous research on the prediction of panel flutter are mainly based on analytical and experimental methods. The analytical methods include the governing partial differential equations (PDE) in conjunction with the Galerkin method [52] and the finite element methods [53] for nonlinear supersonic panel flutter. The aerodynamic models used in those methods are mainly linearized, such as linear piston and linearized potential flow model.

However, linear aerodynamic models are difficult to capture the STBLI since this flow phenomenon is non-linear and unsteady. The STBLI would result in an amplification of the heating, the aeroacoustic loading, and flow separation. Priebe et al [45] employed direct numerical simulation (DNS) to study the STBLI on a ramp configuration. They demonstrate that the shock impingement amplifies the pressure fluctuation and there are high-level, low-frequency (< 1000 Hz) vortex structures in the turbulent boundary layer. Although computational method using Reynolds Averaged Navier Stokes (RANS) [42, 43], large eddy simulation (LES) [44], and direct numerical simulation (DNS) [42, 45] have been utilized to study the STBLI, few researches are focused specifically on the analysis of STBLIs on panel aeroelasticity.

Crowell et al [54] developed a CFD-FEM based partitioned aerothermal solver, for investigating the thermal response of surface panels subject to shock turbulent boundary layer interactions (STBLIs). Their results show that a static approximation, in which the flow is simulated a priori without consideration of the surface motion, significantly under predicts the peak temperature rise and affects the length of the panel. Dechaumphai et al [55] used 2D finite element fluid-thermal-structural solver to study hypersonic flow over metallic thin panels in both aligned and inclined configurations with respect to the free stream. Their results show that even very modest deformations alter flow features and introduced shocks, expansions, and recirculation regions that significantly influenced the heat load. However, their CFD-FEM solver are only implemented for two dimensional problems in loosely coupled way. Gogulapati et al [56] studied the flow-structural response of thin-gauge panels subject to shock impingement with steady CFD and reduced order of FEM method. The unsteady pressure fluctuation on the panel surface are the surrogate of

the steady CFD and empirical correlation. The computed dynamic panel displacements are largely deviated from experiment up to a few orders of magnitude.

2.2 Turbomachinery Aeroelasticity

The focus of this research work on turbomachinery aeroelasticity is to develop and adopt high fidelity CFD methodology for complex turbomachinery aeromechanical problems, such as stall flutter and turbomachinery NSV. Hence, the achievements of turbomachinery aeroelasticity using numerical simulation are reviewed in this section.

The numerical predictions of turbomachinery aeroelastic problems have been performed for more than 5 decades. Excellent review of this field can be seen in a number of publications, such as the AGARD Manual on aeroelasticity in axial flow turbomachines [57], Unsteady Aerodynamics and Aeroelasticity of Turbomachines [58, 59], and an IGTI Scholar Paper by Srinivasan [15]. The early works [60] mostly adopted the analysis techniques that are based on 2D, incompressible, and inviscid assumptions. One of the advantage of the analysis methods is the computational cost is very low. Hence, the main parametric variables that control the aeroelastic phenomena can be found efficiently and they are very suitable for preliminary aeroelastic design of the blades.

However, transonic flutter near stall conditions in turbomachinery are highly unsteady, non-linear and three dimensional, which include flow induced vibration, flow separation, shock unsteadiness, shock wave/turbulent boundary interactions. Numerical methods without considering the viscous effect are impossible to predict those complex flow phenomena accurately. The driving mechanism of the stall flutter in transonic turbomachinery may var-

ied between the large separation and shock wave oscillation. Lepicovsky et al. [61] shows that the transonic stall flutter is triggered by the high frequency stall cell propagation in separated area on the airfoil suction side. There are no shock waves at high subsonic inlet Mach numbers (about 0.95) when transonic stall flutter occurred in their study [61]. Shwa et al. [62] demonstrates that the energy from shock wave oscillations is not strong enough to induce the transonic stall flutter based on a shock wave motion model. On the other hand, unsteady shock oscillation rather than blade stall was found to be the driving mechanism for flutter instability in a transonic fan [63]. The shock location and movement and its relation to the inter blade phase angle contributes significantly to the variation in the aerodynamic damping [64]. The comparison with measured data for the onset of a transonic fan flutter by Chew et al. [14] shows that the shock movement of the blade passage appears to be an important parameter causing the fan flutter due to the interaction of the passage shocks with the suction surface boundary layer. Vahdati et al. [8] shows that the flow separation behind the shock on the suction surface is the key driver of a wide-chord transonic fan flutter. Another study shows that shock has both stabilizing and destabilizing effect with the inter-blade phase angle and location of shock having a significant impact on stability [11, 65]. All these studies indicate the complexity of the stall flutter that can be induced by different flow phenomena. Accurate simulation of compressor/fan flutter is crucial for industrial design and diagnosis.

Turbomachinery flutter is an classical aeromechanical problem and has been studied for decades. Recently, a new turbomachinery aeromechanical problem, namely non-synchronous vibration(NSV), whose blade vibration frequency is away from harmonics of rotor shaft frequency, has attracted a lot of attention [16–20, 22, 66–68]. The high speed

axial compressor investigated in this study exhibits such an non-engine order vibration on the 1st stage rotor blades during the engine acceleration in the rig testing [17, 21, 22], i.e. non-synchronous vibration (NSV). The NSV frequency collapses between 2600 Hz and 2661 Hz with a large amplitude close to the blade 1T (1st torsional) mode. Im and Zha [69] simulated the GE 1-1/2 stage compressor with rigid blade and discovered that the tangential traveling vortex matches the NSV excitation frequency. No rotating stall is observed when the NSV occurs.

The main flow mechanism leading to NSV is strongly related to the tip clearance flow instability and leading edge vortex shedding near the tip span. A propagating vortex structure near the blade tip in a low speed axial compressor is reported in [19] as a rotating instability (RI) that causes the axial compressor NSV. Their measurements show that the RI is limited to the blade tip region with the peak amplitude at 92% of the blade height around 20% to 30% of the chord and it travels in the opposite direction to rotor rotation. Similarly, the experiment for a 10 stage high pressure axial compressor [16] shows a NSV of the 1st stage rotor blades due to a RI. The measured frequencies indicate radial dependency of the NSV with high coherence above 74% rotor span, which decays away from the RI and is eventually no more detectable below 65% blade span.

Thomassin, et al. [20, 66] suggested a theory different from the rotating instability to explain the NSV based on the resonance of a impinging jet vortex structure and the acoustic feedback of a vibrating plate. The jet core feedback theory has been proved by an experiment conducted in [20, 66]. It shows that when the acoustic reflection wave length equals to the jet-to-plate distance, the jet vortical structures lock-on to the acoustic wave frequency and significant amplification of the pressure fluctuation and vibration of the flexible plate

are observed. They suggest a simple model to predict the critical tip velocity based on their impinging jet experiment. Vo's [68] simulation shows a tip clearance flow instability for an isolated subsonic axial compressor rotor. In the blade tip region the trailing edge back flow causes flow impingement on the pressure side that leads to the flow unsteadiness associated with the NSV.

Camp et al. [70] reports that there were step changes in response frequency as the wheel speed changed in a low speed compressor. A helical acoustic structure was detected by using casing dynamic pressure transducer, which was taken as acoustic resonance. This phenomenon may be understood by using a model involved vortex induced vibration (VIV) [17]. Spiker et al. [71] and Clark et al. [72, 73] consider the NSV as a lock-in phenomenon, which is observed in flow past an oscillating blunt body configuration, such as cylinder and airfoil, in which the vortex shedding frequency is locked in the natural frequency of the structure vibration. Once lock-in phenomenon occurs, the vortex shedding frequency is independent of in coming flow velocity and can be far way from Strouhal frequency [74]. The vortex shedding model has been introduced to predict the NSV behavior in turbomachinery by researchers.

Spiker et al. [71] developed a reduced order computation fluid dynamic(CFD) method to study to lock in effect of 2-D cascade. The results indicate the largest LCO amplitude is away from the natural shedding frequency. Clark et al. [72] use a multidegree-of-freedom, traditional van der Pol oscillator to model NSV in turbomachinery. The lock-in phenomenon typical of NSV is captured for various fluid-structure frequency ratios. The results also show the maximum amplitude of the LCO occurs at an off-resonant condition, i.e., when the natural shedding frequency of the aerodynamic instability is not coincident

with the natural modal. Besem et al. [75] study the frequency lock-in effect of a vortex induced vibrating airfoil at high angle of attack by using harmonic balance(HB) CFD method. The predicted vortex shedding frequency and lock-in region have a good agreement with experiment. Most people used reduced-order model to analogize the non-engine order vibration due to high computational cost in solving viscous, nonlinear, 3D unsteady flow and structural vibration equations.

Gan et al. [76] simulated the NSV in a high speed multistage axial compressor using rigid blade and vibrating blade with fluid-structural interaction(FSI). The numerical results show that the predicted the dominant excited frequencies of both rigid blade and vibrating blade are close to the first torsional mode and agrees very well with the measured NSV frequency, which indicates that the NSV is excited by the traveling vortex near the rotor leading edge. However, the simulation in [76] is only for one operating point, which is not conclusive whether the blade vibration is induced by the flow instability or it is lock-in phenomenon.

The compressor may experience rotating stall during the blade flutter. Rotating stall is one of the rotating instability in turbomachinery, which may augment the blade flutter if the frequency of stall cells is close to the blade natural frequency. Hence, the prediction of rotating stall is the first step of stall flutter simulation and a good demonstration of the capability of the high fidelity methods.

Rotating stall usually starts from blade tip. The roles of tip clearance vortex, passage shock and their interactions on stall inception are important to study. Tip clearance vortex breakdown is considered as one of the causes for stall inception of conventional rotors [77]. For the high-speed compressors, the pattern of flow breakdown through stall or surge is not

well understood due to the effects of compressibility, difficulties in detailed measurement, shaft speed, and geometry. Hah et al. [78] numerically studied stall inception in a forward-swept transonic compressor rotor. There is no tip clearance vortex breakdown during the operation of rotor, even in the stall condition. The passage shock oscillation is considered as one of the courses that drive the stall inception. Recently, Reuss et al. [79] tested a jet engine high pressure compressor to investigate the effect of inlet total pressure distortions on rotating stall. Their experiment shows that the spike type stall cell moves at approximately 60% of the compressor speed. After two to three more revolutions, rotating stall has been established. The speed of the cell is reduced to about 45% of the compressor speed and its length scale is roughly 50% of the annulus.

The stall inception of NASA Stage 35 is investigated by several research groups. Bright et al. [80] performed rig test to investigate the stall inception of Stage 35 by considering 5 different conditions. Their results show that the stall inception is a modal type at clean-inlet condition. Mina et al. [81] carried out numerical simulation of rotating stall inception for NASA Stage 35 using a single blade passage. It is observed that at near stall, the tip vortex grows larger in size and its trajectory becomes perpendicular to the main axial flow. A low-momentum area near rotor tip leading edge causes the flow spillage and leads to stall inception. Davis and Yao [82] also used NASA stage 35 single blade passage to investigate stall inception. Their finding agrees with Hoying et al. [83] who show that the circulation of tip clearance vortex plays an important role in stall inception development. Vo [84] conducted rotating stall simulation for a low speed rotor with relative tip Mach number of 0.2 and the transonic NASA stage 35 rotor using 6 blade passages. Their results indicate that leading edge tip clearance flow has spillage below blade tip and back flow

at the trailing-edge at the onset of spike. Chen et al. [85, 86] conducted a full annulus simulation of NASA Stage 35 at the full speed using an URANS model. In their simulation, a simplified "roof top" type tip clearance mesh is used to model the tip clearance flow. Their results show that a disturbance first travels at the rotor speed, and then changes to a spike disturbance propagating at 84% rotor speed consisting with multiple stall cells. The disturbance eventually forms a single rotating stall cell of 43% rotor speed [85]. Gan et al. [87] conducted full annulus simulation of the stall inception of Stage 35 by using URANS method. A spike type of stall cell which covers about 6 blade passages and propagates with about 90% of rotor speed was captured.

To achieve high fidelity simulation of nonlinear fluid/structural instabilities during the fan/compressor flutter, the governing equations of structural and fluid motion should be simultaneously solved in order to capture the flow and structure responses at the same time as happening in reality. However, many of fluid-structural interaction (FSI) simulations are implemented by a loosely coupled procedure, i.e the structural response lags behind the flow solver by one or several time steps [23]. For example, Gnesin et al. [25] solved the unsteady Euler equations with the modal approach for the structure analysis in an loosely coupled manner. Doi et al. [24] loosely coupled an explicit Runge-Kutta multigrid flow solver with a FEM structure solver to predict the aeroelastic forced responses of NASA Rotor 67 blade. In the work of Carstens et al. [26] and Sayma et al. [27], the structural part of the governing equations is time-integrated using Newmark scheme, while the unsteady air loads are computed at every time step by a Navier-Stokes code in an loosely coupled manner. Chew et al. [14] used inviscid linearized model, to capture stall flutter (or referred to as part-speed flutter) of a civil wide chord fan and a low aspect ratio military fan engine.

Due to neglecting viscous terms, end wall boundary layers and tip clearance, their computation fails to show any signs of flutter instability, which was observed in the testing. It is also shown that the conventional energy method, in which the blade vibration and aerodynamic forces may be treated independently, could not accurately capture the modern fan flutter boundary whereas the coupled mode flutter analysis methods do [88].

In the work of Im et al. [65], a fully coupled FSI developed by Chen et al. [28] is extended for turbomachinery by implementing an advanced blade tip deforming mesh technique to capture the transonic rotor flutter. In the fully coupled FSI [28], the governing equations of structural and fluid motion are simultaneously solved by exchanging the unsteady aerodynamic force and structural displacement within each physical time step via a successive iteration on the pseudo-time step. The fully coupled FSI methodology adopted in this study is shown to accurately predict the flutter boundary of a transonic single rotor [65] and AGARD wing with the shock/boundary layer interaction [31, 89].

Chapter 3

Governing Equations

Aeroelasticity involves both aerodynamics and structural dynamics. The governing equations of aerodynamics is different from those of structural dynamics because of the different basic principles. They also have different frames of reference. This chapter describes the governing equations for both aerodynamics and structural dynamics in detail.

3.1 The Flow Governing Equations

The governing equations for flow are time accurate compressible Navier-Stokes equations, which are a system of unsteady and non-linear partial differential equations for the conservation of mass, momentum, and energy. For turobmachinery flow simulation, the Navier-Stokes equations are transformed in a relative moving frame of reference in order to take into account the effects of Coriolis force $(2\Omega \times \mathbf{W})$ and the centrifugal force$(\Omega \times \Omega \times \mathbf{r})$. To treat complex arbitrary geometries with high accuracy, the Navier-Stokes equations are transformed from the physical space to the computational space.

3.1.1 Motion in Moving Frame [1]

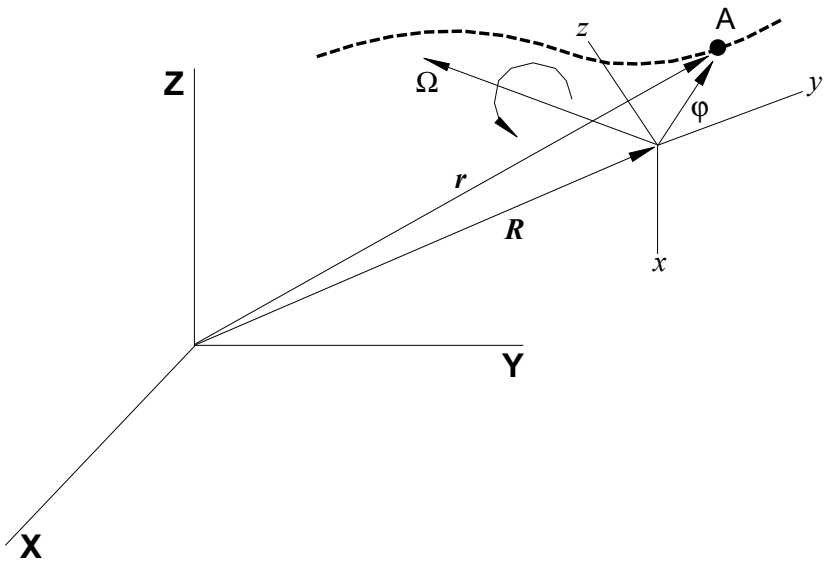

Figure 3.1: Motion of a moving frame of *xyz* relative to the fixed frame of *XYZ*

The motion of a particle A in a relative frame *xyz* to the fixed frame *XYZ* can be depicted in Fig. 3.1. The vector **r** is defined in the *XYZ* reference as

$$\mathbf{r} = \mathbf{R} + \varphi \tag{3.1}$$

where **R** is the vector of the reference *xyz* relative to the fixed coordinates *XYZ* and φ a position vector in reference *xyz*.

Applying the material(or Lagrangian) derivative of the vector **r** with respect to time for

the XYZ reference, then we have

$$\mathbf{V}_{XYZ} = \mathbf{W}_{xyz} + \dot{\mathbf{R}} + \Omega \times \varphi \tag{3.2}$$

where Ω is the angular velocity vector with unit normal vector $\mathbf{e}$ in a moving frame of xyz. $\mathbf{V}$ is the absolute velocity vector in the XYZ reference and $\mathbf{W}$ is the relative velocity vector in the xyz reference.

$$\Omega = \Omega_x \mathbf{e}_x + \Omega_y \mathbf{e}_y + \Omega_z \mathbf{e}_z \tag{3.3}$$

The acceleration of a particle A for different references can be obtained [90] by carrying out the derivative of the velocity vector $\mathbf{V}_{XYZ}$ with respect to time for the XYZ reference as

$$\begin{aligned} \mathbf{a}_{XYZ} = \tfrac{D\mathbf{V}}{Dt})_{XYZ} = \tfrac{D\mathbf{W}}{Dt})_{xyz} + \Omega \times \mathbf{W} + \ddot{\mathbf{R}} + \Omega \times \tfrac{D\varphi}{Dt})_{xyz} + \Omega \times \Omega \times \varphi \\ + \tfrac{D\Omega}{Dt})_{XYZ} \times \varphi \end{aligned} \tag{3.4}$$

The superscript $\dot{}$ and $\ddot{}$ stand for first and second order derivative with respect to time. Since the rotating axis of turbomachinery with the constant angular velocity of Ω used in this study has no translational motion($\dot{R} = 0$) to the fixed or absolute frame(X, Y, Z), in above equation $\ddot{R} = 0$, $D\Omega/Dt = 0$, $\varphi = \mathbf{r}$ and $D\varphi/Dt_{xyz} = \mathbf{W}$. Eq. (3.4) is then rewritten in a rotating Cartesian coordinate(x, y, z) as presented in Fig. 3.2.

$$\tfrac{D\mathbf{V}}{Dt})_{XYZ} = \tfrac{D\mathbf{W}}{Dt}_{xyz} + 2\Omega \times \mathbf{W} + \Omega \times \Omega \times \mathbf{r} \tag{3.5}$$

The relationship given by Eq. (3.5) can be used to derive both the aerodynamic and

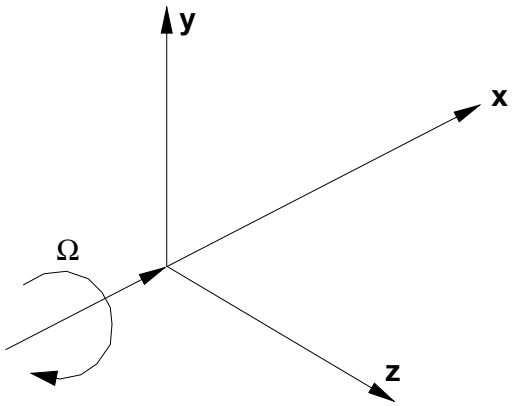

Figure 3.2: The rotating frame in Cartesian coordinates for turbomachinery

structure model equations. In the Eq. (3.5), $2\Omega \times \mathbf{W}$ is called the Coriolis acceleration vector and $\Omega \times \Omega \times \mathbf{r}$ is the Centrifugal acceleration vector.

3.1.2 Spatially Filtered NS Equations in Rotating Frame

The Navier-Stokes equations are considered to be able to directly solve engineering turbulent flows. However, such a direct numerical simulation has largely been limited to simple geometries at low Reynolds number since in general it requires a tremendous mesh and very small temporal scale, for example grid points $\simeq Re^{9/4}$ and times steps $\simeq Re^{3/4}$ to resolve all scales of turbulence [91].

Since turbulence consists of random fluctuations of the various flow properties, the statistical approach such as time, spatial or ensemble averaging is usually more meaningful in engineering practice. The spatial filtering eliminates the small scale high frequency components of the fluid motion, while keeping the unsteadiness associated with the large scale turbulent motion [92]. For an arbitrary function $u(x_i,t)$, the filtered variable $\overline{u}(x_i,t)$ is

defined as:

$$\bar{u}(x_i,t) = \int_D G(x_i - \xi_i, \Delta) u(\xi_i, t) d\xi_i \tag{3.6}$$

where G is the filter function and Δ is the filter width and is associated with the mesh size. Similar to the case of RANS, for compressible flows, it is convenient to introduce the Favre-filtered variable $\tilde{u}(x_i,t)$ as:

$$\tilde{u}(x_i,t) = \frac{\overline{\rho u}}{\bar{\rho}} \tag{3.7}$$

A variable can be thus decomposed into its Favre-filtered component and fluctuating component as:

$$u(x_i,t) = \tilde{u}(x_i,t) + u''(x_i,t) \tag{3.8}$$

The molecular viscous stress tensor, $\bar{\tau}$ is estimated as:

$$\bar{\tau}_{ij} = \frac{2}{3}\tilde{\mu}\frac{\partial \tilde{u}_k}{\partial x}_k \delta_{ij} + \mu\left(\frac{\partial \tilde{u}_i}{\partial x_j} + \frac{\partial \tilde{u}_j}{\partial x_i}\right), \qquad i,j = 1,2,3 \tag{3.9}$$

The above equation is in the tensor form, where the subscript 1, 2, 3 represent the coordinates, x, y, z and the Einstein summation convention is used. The molecular viscosity $\tilde{\mu} = \tilde{\mu}(\tilde{T})$ is determined by Sutherland law.

The σ is the subgrid scale stress tensor due to the filtering process and is expressed as:

$$\sigma_{ij} = -\bar{\rho}(\widetilde{u_i u_j} - \tilde{u}_i \tilde{u}_j) \tag{3.10}$$

The energy flux Q is expressed as:

$$Q_i = \tilde{u}_j(\bar{\tau}_{ij} + \sigma_{ij}) - \bar{q}_i + \Phi_i \tag{3.11}$$

where Φ is the subscale heat flux:

$$\Phi_i = -C_p\bar{\rho}(\widetilde{u_i T} - \tilde{u}_i\tilde{T}) \tag{3.12}$$

The $\bar{q}_i$ is the molecular heat flux:

$$\bar{q}_i = -\frac{C_p\tilde{\mu}}{Pr}\frac{\partial\tilde{T}}{\partial x_i} \tag{3.13}$$

$$\bar{\rho}\tilde{e} = \frac{\bar{p}}{(\gamma-1)} + \frac{1}{2}\bar{\rho}(\tilde{u}^2 + \tilde{v}^2 + \tilde{w}^2 - \Omega^2 r^2) + \rho k \tag{3.14}$$

where γ is the ratio of specific heats, ρk is the subscale kinetic energy per unit volume.

$$\rho k = \frac{1}{2}\bar{\rho}(\widetilde{u_i u_i} - \tilde{u}_i\tilde{u}_i) = -\frac{1}{2}\sigma_{ii} \tag{3.15}$$

In the current simulations, the ρk in Eq.(3.14) is omitted based on the assumption that the effect is small.

Applying above definitions for the Navier-Stokes equations and using the eddy viscosity concept, then the shear stress $\bar{\tau}_{ik}$ and total heat flux $\bar{q}_k$ can be expressed in Cartesian coordinates as follows:

$$\bar{\tau}_{ik} = (\mu + \mu_{DES})\left[\left(\frac{\partial\tilde{u}_i}{\partial x_k} + \frac{\partial\tilde{u}_k}{\partial x_i}\right) - \frac{2}{3}\delta_{ik}\frac{\partial\tilde{u}_j}{\partial x_j}\right] \tag{3.16}$$

$$\bar{q}_k = -\left(\frac{\mu}{Pr} + \frac{\mu_{DES}}{Pr_t}\right)\frac{\partial \tilde{T}}{\partial x_k} \tag{3.17}$$

Note that μ_{DES} is obtained by high fidelity delayed detached eddy simulation (DDES) of turbulence [32,33] in this study. For simplicity, all the bar and tilde in above equations will be dropped for the rest of the thesis.

3.1.3 Nondimensionalization of the Governing Equations

The flow governing equations are normalized by a characteristic dimension L and freestream conditions.

$$\begin{gathered} t^* = \frac{tV_\infty}{L}, \quad x^* = \frac{x}{L}, \quad y^* = \frac{y}{L}, \quad z^* = \frac{z}{L} \\ \mu^* = \frac{\mu}{\mu_\infty}, \quad u^* = \frac{u}{V_\infty}, \quad v^* = \frac{v}{V_\infty}, \quad w^* = \frac{w}{V_\infty} \\ \rho^* = \frac{\rho}{\rho_\infty}, \quad T^* = \frac{T}{T_\infty}, \quad p^* = \frac{p}{\rho_\infty V_\infty^2}, \quad e^* = \frac{e}{V_\infty^2} \end{gathered} \tag{3.18}$$

As the nondimensional numbers introduced in this study, Reynolds number Re, Mach number M, and Rossby number R_o are defined as

$$Re = \frac{\rho_\infty L V_\infty}{\mu_\infty} \tag{3.19}$$

$$M_\infty = \frac{V_\infty}{\sqrt{\gamma R T_\infty}} \tag{3.20}$$

$$R_o = \frac{\Omega L}{V_\infty} \tag{3.21}$$

Above normalization results in

$$\mu^* = \frac{\mu}{\mu_\infty} = \frac{\mu Re}{\rho_\infty L V_\infty} \tag{3.22}$$

$$\mu^* = (T^*)^{1.5} \frac{T^* + 110/T_\infty}{T^* + 1} \tag{3.23}$$

$$p^* = \frac{\rho^* T^*}{\gamma M_\infty^2} \tag{3.24}$$

$$\rho^* e^* = \frac{P^*}{\gamma - 1} + \frac{1}{2}\rho^*(u^{*2} + v^{*2} + w^{*2} - {R_o}^2 r^{*2}) \tag{3.25}$$

For simplicity, the superscript asterisk will be dropped for the rest of the thesis. The normalized filtered compressible Navier-Stokes(NS) equations in Cartesian coordinates in a rotating frame can be expressed in a conservative flux vector form as

$$\frac{\partial \mathbf{Q}}{\partial t} + \frac{\partial \mathbf{E}}{\partial x} + \frac{\partial \mathbf{F}}{\partial y} + \frac{\partial \mathbf{G}}{\partial z} = \frac{1}{Re}\left(\frac{\partial \mathbf{E_v}}{\partial x} + \frac{\partial \mathbf{F_v}}{\partial y} + \frac{\partial \mathbf{G_v}}{\partial z}\right) + S_R \tag{3.26}$$

where S_R is the source term appeared due to the rotor rotation. The variable vector $\mathbf{Q}$, inviscid flux vectors $\mathbf{E}$, $\mathbf{F}$, $\mathbf{G}$, and the viscous fluxes $\mathbf{E_v}$, $\mathbf{F_v}$, $\mathbf{G_v}$ are given as the following.

$$\mathbf{Q} = \begin{pmatrix} \rho \\ \rho u \\ \rho v \\ \rho w \\ \rho e \end{pmatrix} \tag{3.27}$$

$$\mathbf{E} = \begin{pmatrix} \rho u \\ \rho u^2 + p \\ \rho uv \\ \rho uw \\ (\rho e + p)u \end{pmatrix}, \mathbf{F} = \begin{pmatrix} \rho v \\ \rho vu \\ \rho v^2 + p \\ \rho vw \\ (\rho e + p)v \end{pmatrix}, \mathbf{G} = \begin{pmatrix} \rho w \\ \rho wu \\ \rho wv \\ \rho w^2 + p \\ (\rho e + p)w \end{pmatrix} \tag{3.28}$$

$$\mathbf{E_v} = \begin{pmatrix} 0 \\ \tau_{xx} \\ \tau_{xy} \\ \tau_{xz} \\ u_k \tau_{xk} - q_x \end{pmatrix}, \mathbf{F_v} = \begin{pmatrix} 0 \\ \tau_{yx} \\ \tau_{yy} \\ \tau_{yz} \\ u_k \tau_{yk} - q_y \end{pmatrix}, \mathbf{G_v} = \begin{pmatrix} 0 \\ \tau_{zx} \\ \tau_{zy} \\ \tau_{zz} \\ u_k \tau_{zk} - q_z \end{pmatrix} \tag{3.29}$$

$$S_R = \begin{pmatrix} 0 \\ 0 \\ \rho R_o^2 y + 2\rho R_o w \\ \rho R_o^2 z - 2\rho R_o v \\ 0 \end{pmatrix} \tag{3.30}$$

where

$$\tau_{ik} = (\mu + \mu_{DES} Re)[\frac{\partial u_i}{\partial x_k} + \frac{\partial u_k}{\partial x_i} - \frac{2}{3}\delta_{ik}\frac{\partial u_j}{\partial x_j}] \tag{3.31}$$

$$q_j = -\frac{1}{(\gamma - 1)M_\infty^2}(\frac{\mu}{Pr} + \frac{\mu_{DES} Re}{Pr_t})\frac{\partial T}{\partial x_j} \tag{3.32}$$

3.1.4 Delayed Detached Eddy Simulation

In 1997 Spalart et al. [32] suggested a hybrid RANS/LES turbulence, the detached eddy simulation (DES), based on the Spalart-Allmaras (S-A) one equation model [93] which solves a transport equation for the working variable $\tilde{\nu}$ related to the turbulent eddy ν and LES subgrid-scale (SGS) viscosity. Using the normalization given in Eq. (3.18), the nondimensionalized S-A model including closure coefficients and damping functions is written in terms of eddy viscosity ν_t as follows.

Turbulent Eddy Viscosity:

$$\mu_{DES} = \rho \nu_t = \rho \tilde{\nu} f_{v1} \tag{3.33}$$

Eddy Viscosity Equation:

$$\begin{aligned} \frac{\partial \bar{\rho}\bar{\tilde{\nu}}}{\partial t} + \bar{\nabla} \cdot \left(\bar{\rho}\bar{\tilde{\nu}}\bar{\vec{V}} \right) \quad &= \frac{1}{Re}\bar{\nabla} \cdot \left[\frac{\bar{\rho}}{\sigma}(\bar{\nu} + \bar{\tilde{\nu}})\bar{\nabla}\bar{\tilde{\nu}} \right] + \bar{\rho} c_{b1} (1 - f_{t2}) \left(\bar{S} + \frac{1}{Re}\frac{\bar{\tilde{\nu}}}{\kappa^2 \bar{d}^2} f_{v2} \right) \bar{\tilde{\nu}} - \\ &\frac{1}{Re}\bar{\rho} \left(c_{w1} f_w - \frac{c_{b1}}{\kappa^2} f_{t2} \right) \left(\frac{\bar{\tilde{\nu}}}{\bar{d}} \right)^2 - \frac{1}{Re}\frac{1}{\sigma} \left(\bar{\nu} + \bar{\tilde{\nu}} \right) \bar{\nabla}\bar{\tilde{\nu}} \cdot \bar{\nabla}\bar{\rho} + \\ &\frac{1}{Re}\frac{\bar{\rho}}{\sigma} c_{b2} \left(\bar{\nabla}\bar{\tilde{\nu}} \right)^2 + Re\bar{\rho} f_{t1} \left(\Delta \bar{q} \right)^2 \end{aligned} \tag{3.34}$$

Closure Coefficients:

$$\begin{gathered} c_{b1} = 0.1355, c_{b2} = 0.622, \sigma = \tfrac{2}{3}, c_{w1} = \tfrac{c_{b1}}{k^2} + \tfrac{1 + c_{b2}}{\sigma} \\ c_{w2} = 0.3, c_{w3} = 2, k = 0.41, c_{v1} = 7.1, c_{t1} = 1.0, c_{t2} = 2.0, c_{t3} = 1.1, c_{t4} = 2.0 \end{gathered} \tag{3.35}$$

Auxiliary Relations:

$$\chi = \frac{\tilde{\nu}}{\nu}, \quad g = r + c_{w2}(r^6 - r), \quad r = \frac{\tilde{\nu}}{Re\tilde{S}k^2 d^2} \tag{3.36}$$

$$f_{v1} = \frac{\chi^3}{\chi^3 + c_{v1}^3}, \quad f_{v2} = 1 - \frac{\chi}{1 + \chi f_{v1}}, \quad f_w = g(\frac{1 + c_{w3}^6}{g^6 + c_{w3}^6})^{1/6} \tag{3.37}$$

$$\tilde{S} = S + \frac{\tilde{\nu}}{Rek^2 d^2} f_{v2}, \quad S = \sqrt{2\omega_{ij}\omega_{ij}}, \quad g_t = min\left(0.1, \frac{\Delta q}{\omega_t \Delta x_t}\right) \tag{3.38}$$

$$f_{t2} = c_{t3} exp\left(-c_{t4}\chi^2\right), \quad f_{t1} = c_{t1} g_t exp\left[-c_{t2}\frac{\omega_t^2}{\Delta U^2}\left(d^2 + g_t^2 d_t^2\right)\right] \tag{3.39}$$

Where $\omega_{ij} = \frac{1}{2}\left(\frac{\partial u_i}{\partial x_j} - \frac{\partial u_j}{\partial x_i}\right)$ is the fluid particle angular velocity tensor. ω_t is the wall vorticity at the wall boundary layer trip location, d is the distance to the closest wall, d_t is the distance of the field point to the trip location, Δq is the difference of the velocities between the field point and the trip location, Δx_t is the grid spacing along the wall at the trip location.

In DES, the coefficients c_{t1} and c_{t3} in the S-A model are set to zero and the distance to the nearest wall, d, is replaced by $\tilde{d}$ as

$$\tilde{d} = min(d, C_{DES}\Delta) \tag{3.40}$$

where Δ is the largest spacing of the grid cell in all the directions. Within the boundary layer close to the wall, $\tilde{d} = d$, hence the turbulence is simulated by RANS mode of Spalart-Allmaras [93]. Outside of a wall the boundary layer, $\tilde{d} = C_{DES}\Delta$ is most of the cases. When the production and destruction terms of the model are balanced, the length scale $\tilde{d}$ will yield a Smagorinsky-like eddy viscosity and the turbulence is simulated by the LES model. The coefficient $C_{DES} = 0.65$ is used as set in the homogeneous turbulence [94]. The Pr_t may

take the value of 0.9 within the boundary layer for RANS mode and 0.5 for LES mode away from the wall surface.

To overcome the modeled stress depletion problem and make the DES limiter independent of grid spacing, the DDES model suggested by Spalart et al. [33] switches the subgrid scale formulation in the S-A model by redefining the distance to the nearest wall $\tilde{d}$ as

$$\tilde{d} = d - f_d max(0, d - C_{DES}\Delta) \tag{3.41}$$

where

$$f_d = 1 - tanh([8r_d]^3) \tag{3.42}$$

$$r_d = \frac{\nu_t + \nu}{(U_{i,j}U_{i,j})^{0.5}k^2d^2R_e} \tag{3.43}$$

$$U_{i,j} = \frac{\partial u_i}{\partial x_j} \tag{3.44}$$

where Δ is the largest spacing of the grid cell in all the directions, $U_{i,j}$ represents the velocity gradient, and k denotes the Karmann constant. Within the boundary layer close to walls, $\tilde{d} = d$, and away from the boundary layer, $\tilde{d} = d - f_d(d - C_{DES}\Delta)$ is most of the case. This mechanism enables DDES to behave as a RANS model in the near-wall region, and LES away from walls. This modification in $\tilde{d}$ reduces the grey transition area between RANS and LES.

To couple the SA based DES/DDES with Navier-Stokes equations, the eddy viscosity

equation (3.34) is also transformed to the computational space and can be expressed in the generalized coordinate system as

$$\frac{\partial \frac{1}{J}\rho\tilde{\nu}}{\partial t}+\frac{\partial \rho\tilde{\nu}U}{\partial \xi}+\frac{\partial \rho\tilde{\nu}V}{\partial \eta}+\frac{\partial \rho\tilde{\nu}W}{\partial \zeta}=\frac{1}{Re}\left(\frac{\partial \frac{\rho}{\sigma}(\nu+\tilde{\nu})(\mathbf{l}\bullet\nabla\tilde{\nu})}{\partial \xi}\right.$$
$$\left.+\frac{\partial \frac{\rho}{\sigma}(\nu+\tilde{\nu})(\mathbf{m}\bullet\nabla\tilde{\nu})}{\partial \eta}+\frac{\partial \frac{\rho}{\sigma}(\nu+\tilde{\nu})(\mathbf{n}\bullet\nabla\tilde{\nu})}{\partial \zeta}+\frac{1}{J}S_{\nu}\right) \tag{3.45}$$

where

$$\begin{aligned} S_{\nu}=&\rho c_{b1}(1-f_{t2})\tilde{S}\tilde{\nu}+\tfrac{1}{Re}\left[-\rho\left(c_{w1}f_{w}-\tfrac{c_{b1}}{\kappa^{2}}f_{t2}\right)\left(\tfrac{\tilde{\nu}}{d}\right)^{2}\right.\\ &\left.+\tfrac{\rho}{\sigma}c_{b2}(\nabla\tilde{\nu})^{2}-\tfrac{1}{\sigma}(\nu+\tilde{\nu})\nabla\tilde{\nu}\bullet\nabla\rho\right]+Re\left[\rho f_{t1}(\Delta q)^{2}\right] \end{aligned} \tag{3.46}$$

In summary, the spatially filtered Navier-Stokes equations with the improved DES turbulence closure in a rotating frame of reference in the generalized coordinates(ξ,η,ζ) can be written in a conservative form as the following:

$$\frac{\partial \mathbf{Q}}{\partial t}+\frac{\partial \mathbf{E}}{\partial \xi}+\frac{\partial \mathbf{F}}{\partial \eta}+\frac{\partial \mathbf{G}}{\partial \zeta}=\frac{1}{Re}\left(\frac{\partial \mathbf{R}}{\partial \xi}+\frac{\partial \mathbf{S}}{\partial \eta}+\frac{\partial \mathbf{T}}{\partial \zeta}\right)+\mathbf{D} \tag{3.47}$$

where

$$\mathbf{Q}=\frac{1}{J}\begin{bmatrix}\rho\\ \rho u\\ \rho v\\ \rho w\\ \rho e\\ \rho\tilde{\nu}\end{bmatrix} \tag{3.48}$$

$$\mathbf{E}=\begin{bmatrix}\rho U\\ \rho uU+l_x p\\ \rho vU+l_y p\\ \rho wU+l_z p\\ (\rho e+p)U-l_t p\\ \rho\tilde{\nu}U\end{bmatrix},\mathbf{F}=\begin{bmatrix}\rho V\\ \rho uV+m_x p\\ \rho vV+m_y p\\ \rho wV+m_z p\\ (\rho e+p)V-m_t p\\ \rho\tilde{\nu}V\end{bmatrix},\mathbf{G}=\begin{bmatrix}\rho W\\ \rho uW+n_x p\\ \rho vW+n_y p\\ \rho wW+n_z p\\ (\rho e+p)W-n_t p\\ \rho\tilde{\nu}W\end{bmatrix} \tag{3.49}$$

$$\mathbf{R}=\begin{bmatrix}0\\ l_k\tau_{xk}\\ l_k\tau_{yk}\\ l_k\tau_{zk}\\ l_k(u_i\tau_{ik}-q_k)\\ \frac{\rho}{\sigma}(\nu+\tilde{\nu})(\mathbf{l}\bullet\nabla\tilde{\nu})\end{bmatrix},\mathbf{S}=\begin{bmatrix}0\\ m_k\tau_{xk}\\ m_k\tau_{yk}\\ m_k\tau_{zk}\\ m_k(u_i\tau_{ik}-q_k)\\ \frac{\rho}{\sigma}(\nu+\tilde{\nu})(\mathbf{m}\bullet\nabla\tilde{\nu})\end{bmatrix},\mathbf{T}=\begin{bmatrix}0\\ n_k\tau_{xk}\\ n_k\tau_{yk}\\ n_k\tau_{zk}\\ n_k(u_i\tau_{ik}-q_k)\\ \frac{\rho}{\sigma}(\nu+\tilde{\nu})(\mathbf{n}\bullet\nabla\tilde{\nu})\end{bmatrix} \tag{3.50}$$

$$\mathbf{D}=\frac{1}{J}\begin{bmatrix}0\\ 0\\ \rho R_o^2 y+2\rho R_o w\\ \rho R_o^2 z-2\rho R_o v\\ 0\\ \frac{S_\nu}{Re}\end{bmatrix} \tag{3.51}$$

where

$$\tau_{ik} = (\mu + \mu_{DES} Re)[\frac{\partial u_i}{\partial x_k} + \frac{\partial u_k}{\partial x_i} - \frac{2}{3}\delta_{ik}\frac{\partial u_j}{\partial x_j}] \tag{3.52}$$

$$q_k = -\frac{1}{(\gamma - 1)M_\infty^2}(\frac{\mu}{Pr} + \frac{\mu_{DES} Re}{Pr_t})\frac{\partial T}{\partial x_k} \tag{3.53}$$

3.2 The Structure Governing Equations

The structural equation of motion of an N-DOF (degree of freedom) system with the mechanical damping and the aerodynamic loading as the excitation force, and which can be expressed as the following:

$$[\mathbf{M}]\{\ddot{\mathbf{X}}\} + [\mathbf{C}]\{\dot{\mathbf{X}}\} + [\mathbf{K}]\{\mathbf{X}\} = \{\mathbf{F}\} \tag{3.54}$$

where, **M**, **C**, **K** are the global mass, structural damping and stiffness matrices. **F** is total aerodynamic force acting on the blade surface.

Total aerodynamic force can be defined as follows:

$$\mathbf{F} = -\oint P \cdot \hat{n} dA + \oint \tau_{\mathbf{w}} \cdot \hat{t} dA \tag{3.55}$$

where, $\hat{n}$ is the unit normal vector to the blade surface and $\hat{t}$ is the unit tangent vector to the blade surface. P is the fluid static pressure and $\tau_{\mathbf{w}}$ is the fluid wall shear stress acting on the blade surface. The effects of viscosity can not be neglected for the highly loaded transonic rotor because rotating stall with large structure of flow separation may occur in/near stall conditions.

To obtain the solution of forced vibration in terms of the normal coordinates of the system, first a finite number of mode shapes(ϕ_j) are obtained by solving the characteristic equation of motion.

$$\mathbf{K}\phi_j = \lambda_j \mathbf{M}\phi_j \tag{3.56}$$

where $\lambda_j (= \omega_j^2)$ is the eigenvalue of the j-th mode and ω_j is the corresponding natural frequency. Note that **K** is the global stiffness matrix of Eq. (3.54), in which the centrifugal force term is added in the perpendicular directions of rotating axis. It is desirable to use the mass normalized mode shape($\tilde{\phi}$) defined as the normal modes divided by square root of the the generalized mass($\sqrt{\phi^T m \phi}$) since the orthogonality in terms of the orthogonal modes becomes

$$\tilde{\phi}_j^T M \tilde{\phi}_j = 1 \tag{3.57}$$

To decouple Eq. (3.54), let the displacement vector as

$$\{\mathbf{X}\} = [\tilde{\Phi}]\{\mathbf{q}\} \tag{3.58}$$

and premultiply Eq. (3.54) by the transpose $[\tilde{\Phi}]^T$

$$\begin{aligned} [\tilde{\Phi}]^T[\mathbf{M}][\tilde{\Phi}]\{\ddot{\mathbf{q}}\} + [\tilde{\Phi}]^T[\mathbf{C}][\tilde{\Phi}]\{\dot{\mathbf{q}}\} + [\tilde{\Phi}]^T[\mathbf{K}][\tilde{\Phi}]\{\mathbf{q}\} \\ = [\tilde{\Phi}]^T\{\mathbf{F}\} \end{aligned} \tag{3.59}$$

where **q** is the vector of the principal coordinates. Apply the orthogonality of eigenvectors of the system defined as

$$\phi_j^T M \phi_i = 0; i \neq j \tag{3.60}$$

$$\phi_j^T K \phi_i = 0; i \neq j \tag{3.61}$$

$$\phi_i^T M \phi_i = M_{ii} \tag{3.62}$$

$$\phi_i^T K \phi_i = K_{ii} \tag{3.63}$$

where M_{ii} and K_{ii} are called the generalized mass and the generalized stiffness. Assume damping matrix to be a linear combination of the mass and stiffness matrices as

$$\mathbf{C} = \alpha \mathbf{M} + \beta \mathbf{K} \tag{3.64}$$

and define the modal damping ratio by

$$2\varsigma_j \omega_j = \alpha + \beta \omega_j^2 \tag{3.65}$$

Eq. (3.59) is then completely decoupled and the *j*th equation will have the form as

$$\ddot{q}_j + 2\zeta_j \omega_j \dot{q}_j + \omega_j^2 q_j = \frac{\tilde{\phi}_j^T}{m_j} \mathbf{F} \tag{3.66}$$

where $[\tilde{\Phi}]^T = [\tilde{\phi}_1, \cdots, \tilde{\phi}, \cdots, \tilde{\phi}_N]^T$. N is the number of modal coordinates. ω_j and ζ_j are natural frequency and modal damping ratio for mode j. m_j denotes the jth diagonal element of the generalized mass matrix and is unity, resulting in

$$\ddot{q}_j + 2\zeta_j \omega_j \dot{q}_j + \omega_j^2 q_j = \tilde{\phi}_j^T \mathbf{F} \tag{3.67}$$

In the current study, the structural system may be reduced to only five mode shapes,

since a few bending and torsional frequencies are usually sufficient to determine aeromechanical phenomena of turbomachinery such as flutter and non-synchronous vibration.

3.2.1 Normalization of Modal Equation

The modal equation (3.67) is further normalized to be consistent with the aerodynamic model for the fully coupled fluid/structure interaction procedure. The following dimensionless parameters are introduced.

$$x^* = \frac{x}{L} \tag{3.68}$$

$$q^* = \frac{q}{L} \tag{3.69}$$

$$t^* = t\omega_\alpha \tag{3.70}$$

$$\mathbf{F}^* = \frac{\mathbf{F}}{\rho_\infty U_\infty^2 L^2} \tag{3.71}$$

where t is structural time, ω_α is the characteristic frequency of the system (or in general the first torsional mode natural frequency), and L is the characteristic length used in the normalization of the aerodynamic model. ρ_∞ and U_∞ are the fluid density and velocity at a point of reference. Apply above normalization to Eq. (3.67), then we have

$$\frac{d^2 q_j^*}{dt^{*2}} + 2\zeta_j \left(\frac{\omega_j}{\omega_\alpha}\right) \frac{dq_j^*}{dt^*} + \left(\frac{\omega_j}{\omega_\alpha}\right)^2 q_j^* = \tilde{\phi}_j^T \cdot \mathbf{F}^* \cdot \frac{\rho_\infty U_\infty^2 L}{\omega_\alpha{}^2} \tag{3.72}$$

To reflect the effects of three wing flutter control parameters: mass ratio $\bar{\mu} = \frac{\bar{m}}{V\rho_\infty}$, reduced velocity $V^* = \frac{U_\infty}{b_s\omega_\alpha}$ and flutter speed index $V_f = \frac{V^*}{\mu}$, the modal force term on the right hand side of the normalized modal equation (3.72) can be expressed as [28].

$$\ddot{q}_j + 2\zeta_j(\frac{\omega_j}{\omega_\alpha})\dot{q}_j + (\frac{\omega_j}{\omega_\alpha})^2 q_j = \frac{\tilde{\phi}_j^T}{m_j^*} \cdot \mathbf{F}^* \cdot {V_f}^2 \cdot \frac{b_s^2 L}{V} \cdot \bar{m} \tag{3.73}$$

where the dimensionless quantities are denoted by an asterisk. $\bar{m}$ is the measured blade mass (or wing panel mass), $\bar{V}$ represents the conical frustum volume as illustrated in Fig. 3.3.

$$\bar{V} = \frac{\pi H}{3}(b_s^2 + b_s b_t + b_t^2) \tag{3.74}$$

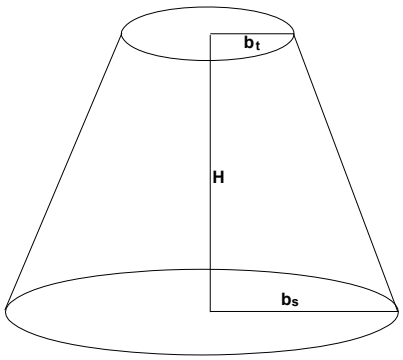

Figure 3.3: Frustrum volume

where b_s is the streamwise root semi chord (or blade semi root chord), b_t is the streamwise tip semi chord(or blade semi tip chord), and H is the blade active length or the wing span. L is the reference length and ω_α is the angular frequency of the first torsional mode in units $radians/sec$. $\bar{\mu}$ stands for the mass ratio, i.e. the ratio between the structural mass and the mass of the equivalent volume of fluid at reference density. It is noticed that m_j^* should be equal to one when the mass normalized mode shapes are used. Note that the structural

dimensionless time t^* may be calculated based on the dimensionless time(t^*_{fluid}) used in the normalized flow governing equation Eq. (3.47) as follows.

$$t^* = t^*_{fluid} \cdot \frac{L}{V^* b_s} \tag{3.75}$$

In order to use the time accurate FSI solver developed for the fluid flow [95], the equations are then transformed to a state form as follows:

$$[\mathbf{M}]\frac{\partial \mathbf{S}}{\partial t} + [\mathbf{K}]\{\mathbf{S}\} = \mathbf{q} \tag{3.76}$$

where

$$\mathbf{S} = \begin{pmatrix} q_j \\ \dot{q}_j \end{pmatrix}, \mathbf{M} = [I], \mathbf{K} = \begin{pmatrix} 0 & -1 \\ (\frac{\omega_j}{\omega_\alpha})^2 & 2\zeta_j(\frac{\omega_j}{\omega_\alpha}) \end{pmatrix}$$

$$\mathbf{q} = \begin{pmatrix} 0 \\ \phi_j^T \cdot \mathbf{F}^* \cdot V_f \cdot \frac{b_s^2 L}{\bar{V}} \cdot \bar{m} \end{pmatrix}$$

3.2.2 Parameters for Flutter Control

There are in general three wing flutter control(or input) parameters: mass ratio $\bar{\mu} = \frac{\bar{m}}{V\rho_\infty}$, reduced velocity $V^* = \frac{U_\infty}{b_s \omega_\alpha}$, and flutter speed index $V_f = \frac{V^*}{\mu}$. The mass ratio $\bar{\mu}$ takes into account the effect of stiffness in flutter. It represents the ratio between the structural mass and the mass of the equivalent volume of fluid at reference density. Typically flutter speed index V_f is selected as the main parameter in flutter boundary prediction because V_f reflects the effects of both dynamic pressure of the surrounding flow and stiffness of the structure.

The effect of aircraft altitude in wind tunnel tests [2, 96] is obtained based on variation of dynamic pressure(varying the density) at constant Mach number. Liu [97] and Chen [28] used V_f, whereas Bakhle [98] used V^* to find the flutter boundary at a given Mach number. In this study, either V_f or V^* can be used explicitly as shown in Eq. (3.73). The V_f is selected for the wing flutter simulation.

Several iterations are usually needed for a given freestream Mach number to search the neutrally stable point, which is treated as the flutter boundary. Most of the computations only need to calculate a few periods to see whether the responses are divergent or damped with time. The flutter velocity index V_f is iterated to find the flutter boundary, all other variables such as inlet total pressure, inlet total temperature, and the static pressure at outlet are not varied. The Reynolds number, $R_e = \frac{\rho_\infty V_\infty L}{\mu_\infty}$ varies with the freestream velocity. In the wing flutter experiment [96], dynamic pressure $q = \frac{1}{2}\rho_\infty V_\infty^2$ is the main fluid quantity to adjust flutter level. The way to control the dynamic pressure is either by varying the free stream density using the real gas such as freon-12 or by changing the velocity instead of density. In this paper, we vary the freestream velocity, V_∞, which has direct relation with the reduced velocity V^*, and hence the flutter velocity index V_f.

For turbomachinery, the flutter boundary is typically determined along the speedline at a given rotor speed instead of varying the freestream Mach number unlike wing flutter because the change in the back pressure of fan/compressor controls the flow at inlet, resulting in the change in the mass flow and total pressure ratio.

Chapter 4

Numerical Methodology

In this chapter, an implicit finite difference discretization for the flow governing equations is described. The inviscid fluxes are discretized using a low diffusion E-CUSP scheme [99]. The fifth-order WENO scheme [100, 101] is used to reconstruct the conservative variables at volume interfaces. A set of fully conservative fourth-order accurate finite central differencing schemes for the viscous terms is employed in this research [46, 102]. The structure governing equations are discretized and solved implicitly in the same manner to be consistent with the flow governing equations.

4.1 Implicit Discretization

Let $J = \frac{1}{\Delta V}$, then 3D Navier-Stokes equations (3.47) is rewritten in a conservative flux vector form as

$$\frac{\partial \Delta V \mathbf{Q}}{\partial t} + \frac{\partial (\mathbf{E} - \mathbf{R}')}{\partial \xi} + \frac{\partial (\mathbf{F} - \mathbf{S}')}{\partial \eta} + \frac{\partial (\mathbf{G} - \mathbf{T}')}{\partial \zeta} = \Delta V \mathbf{D} \tag{4.1}$$

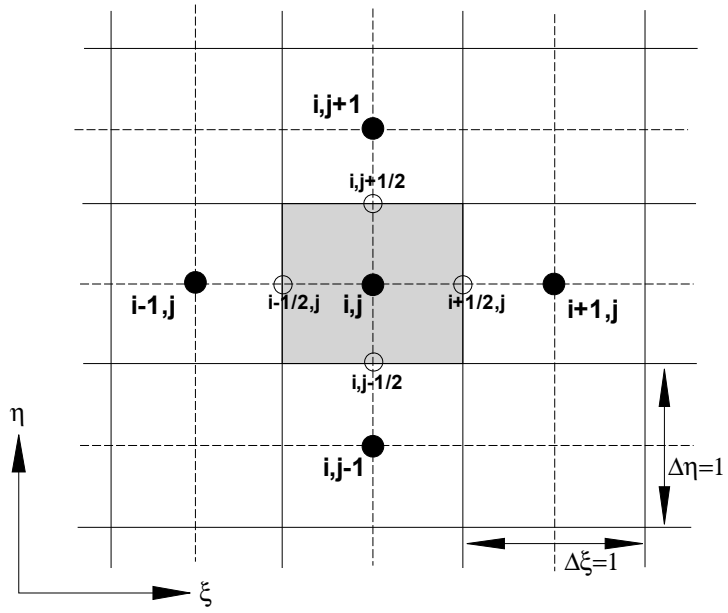

Figure 4.1: Discretization domain indicating the cell center(i,j)

where ΔV denotes the volume of the cell and $\mathbf{R}' = \mathbf{R}/Re$, $\mathbf{S}' = \mathbf{S}/Re$, $\mathbf{T}' = \mathbf{T}/Re$. For steady state solutions, the governing equation will be elliptic type at subsonic and hyperbolic at supersonic. This will make it difficult to discretize the Navier-Stokes equations using a consistent scheme. The temporal term is thus included for steady state solutions to keep the governing equations to have the same hyperbolic type across Mach number 1. For steady state solution, the accuracy of the temporal term is irrelevant since it must be zero when it is converged. Hence, the temporal term is discretized using first order Euler method for its simplicity. The discretized temporal term becomes

$$\frac{\Delta V(\mathbf{Q}^{n+1}-\mathbf{Q}^{n})}{\Delta t}+[\frac{\partial(\mathbf{E}-\mathbf{R}')}{\partial\xi}]^{n+1}+[\frac{\partial(\mathbf{F}-\mathbf{S}')}{\partial\eta}]^{n+1}+[\frac{\partial(\mathbf{G}-\mathbf{T}')}{\partial\zeta}]^{n+1}=\Delta V\mathbf{D}^{n+1} \quad (4.2)$$

where n and $n+1$ are two sequential time levels, which have a time interval of Δt. Eq. (4.2) can be further discretized in space using a conservative differencing as the following:

$$\begin{aligned}
&\frac{\Delta V_{ijk}(\mathbf{Q}_{ijk}^{n+1}-\mathbf{Q}_{ijk}^{n})}{\Delta t} \\
&+(\mathbf{E}_{i+\frac{1}{2}}-\mathbf{E}_{i-\frac{1}{2}})^{n+1}-(\mathbf{R}'_{i+\frac{1}{2}}-\mathbf{R}'_{i-\frac{1}{2}})^{n+1} \\
&+(\mathbf{F}_{j+\frac{1}{2}}-\mathbf{F}_{j-\frac{1}{2}})^{n+1}-(\mathbf{S}'_{j+\frac{1}{2}}-\mathbf{S}'_{j-\frac{1}{2}})^{n+1} \\
&+(\mathbf{G}_{k+\frac{1}{2}}-\mathbf{G}_{k-\frac{1}{2}})^{n+1}-(\mathbf{T}'_{k+\frac{1}{2}}-\mathbf{T}'_{k-\frac{1}{2}})^{n+1} \\
&=\Delta V_{ijk}\mathbf{D}_{ijk}^{n+1}
\end{aligned} \tag{4.3}$$

To evaluate the inviscid fluxes at the cell interface $\mathbf{E},\mathbf{F},\mathbf{G}$, the characteristic based upwind schemes are usually employed due to importance of capturing strong shocks and careful treatment of discontinuity, while the central differencing is used for the viscous fluxes $\mathbf{R},\mathbf{S},\mathbf{T}$. For implicit methods, a Jacobian must be introduced at time level $n+1$ for linearization. This Jacobian is formed by the derivatives of the flux values with respect to each conservative variables at a cell center point.

The implicit matrices will result in 9 elements around the diagonal element for 3D with first order upwind for inviscid fluxes and second order central differencing scheme. The first order upwind scheme for the implicit matrix will have the diagonal dominance required by Gauss-Seidel iteration [103]. Using Gauss-Seidel line relaxation, a block tri-diagonal matrix is inversed along each mesh line.

With an upwind scheme, the numerical flux is split into its left(L) and right(R) side fluxes. For example, the inviscid flux $\mathbf{E}$ at $i+\frac{1}{2}$ can be expressed as

$$\mathbf{E}_{i+\frac{1}{2}}=\mathbf{E}_L+\mathbf{E}_R=\mathbf{E}^{+}_{i+\frac{1}{2}}+\mathbf{E}^{-}_{i+\frac{1}{2}} \tag{4.4}$$

Since Eq. (4.1) is nonlinear, a linearization procedure is necessary. Let us apply a Taylor series expansion to the flux vectors at time level $n+1$ as

$$\mathbf{E}^{n+1} \cong \mathbf{E}^n + \frac{\partial \mathbf{E}}{\partial t}\Delta t + O[(\Delta t)^2] \tag{4.5}$$

$$\frac{\partial \mathbf{E}}{\partial t} = \frac{\partial \mathbf{E}}{\partial \mathbf{Q}}\frac{\partial \mathbf{Q}}{\partial t} \cong \frac{\partial \mathbf{E}}{\partial \mathbf{Q}}\frac{\Delta \mathbf{Q}}{\Delta t} \tag{4.6}$$

$$\mathbf{E}^{n+1} \cong \mathbf{E}^n + A \bullet \Delta \mathbf{Q} \tag{4.7}$$

where $A(=\frac{\partial \mathbf{E}}{\partial \mathbf{Q}})$ is the inviscid flux Jacobian matrix and the change in the conservative variable vector, $\Delta\mathbf{Q}$, is defined by

$$\Delta \mathbf{Q} = \mathbf{Q}^{n+1} - \mathbf{Q}^n \tag{4.8}$$

The inviscid flux $\mathbf{E}$ at the cell interface $i+\frac{1}{2}$ can be given as

$$\mathbf{E}^{n+1}_{i+\frac{1}{2}} = \mathbf{E}^n_{i+\frac{1}{2}} + (\frac{\partial \mathbf{E}^+}{\partial \mathbf{Q}})_L \bullet \Delta \mathbf{Q}_L + (\frac{\partial \mathbf{E}^-}{\partial \mathbf{Q}})_R \bullet \Delta \mathbf{Q}_R \tag{4.9}$$

where $\Delta\mathbf{Q}$ approaches zero when it is converged. Hence the accuracy order for $\Delta\mathbf{Q}$ is not important. The first order accuracy is used to evaluate $\Delta\mathbf{Q}$.

$$\Delta \mathbf{Q}_L = \Delta \mathbf{Q}_i, \quad \Delta \mathbf{Q}_R = \Delta \mathbf{Q}_{i+1} \tag{4.10}$$

Let

$$A^L_{i+\frac{1}{2}} = (\frac{\partial \mathbf{E}^+}{\partial \mathbf{Q}})_L, \quad A^R_{i+\frac{1}{2}} = (\frac{\partial \mathbf{E}^-}{\partial \mathbf{Q}})_R \tag{4.11}$$

Then,

$$\mathbf{E}^{n+1}_{i+\frac{1}{2}} = \mathbf{E}^{n}_{i+\frac{1}{2}} + A^{L}_{i+\frac{1}{2}}\Delta\mathbf{Q}_{i} + A^{R}_{i+\frac{1}{2}}\Delta\mathbf{Q}_{i+1} \tag{4.12}$$

Thus,

$$\begin{gathered}\mathbf{E}^{n+1}_{i+\frac{1}{2}} - \mathbf{E}^{n+1}_{i-\frac{1}{2}} = \\ (\mathbf{E}^{n}_{i+\frac{1}{2}} - \mathbf{E}^{n}_{i-\frac{1}{2}}) + A^{R}_{i+\frac{1}{2}}\Delta\mathbf{Q}_{i+1} + (A^{L}_{i+\frac{1}{2}} - A^{R}_{i-\frac{1}{2}})\Delta\mathbf{Q}_{i} - A^{L}_{i-\frac{1}{2}}\Delta\mathbf{Q}_{i-1}\end{gathered} \tag{4.13}$$

The viscous fluxes are linearized using central differencing.

$$\begin{aligned}(\mathbf{R}'_{i+\frac{1}{2}})^{n+1} &= (\mathbf{R}'_{i+\frac{1}{2}})^{n} + \frac{\partial \mathbf{R}'_{i+\frac{1}{2}}}{\partial \mathbf{Q}_{i+1}}\Delta\mathbf{Q}_{i+1} + \frac{\partial \mathbf{R}'_{i+\frac{1}{2}}}{\partial \mathbf{Q}_{i}}\Delta\mathbf{Q}_{i} \\ &= (\mathbf{R}'_{i+\frac{1}{2}})^{n} + L^{R}_{i+\frac{1}{2}}\Delta\mathbf{Q}_{i+1} + L^{L}_{i+\frac{1}{2}}\Delta\mathbf{Q}_{i}\end{aligned} \tag{4.14}$$

Thus,

$$\begin{gathered}(\mathbf{R}'_{i+\frac{1}{2}})^{n+1} - (\mathbf{R}'_{i-\frac{1}{2}})^{n+1} = \\ (\mathbf{R}'_{i+\frac{1}{2}})^{n} - (\mathbf{R}'_{i-\frac{1}{2}})^{n} + L^{R}_{i+\frac{1}{2}}\Delta\mathbf{Q}_{i+1} + (L^{L}_{i+\frac{1}{2}} - L^{R}_{i-\frac{1}{2}})\Delta\mathbf{Q}_{i} - L^{L}_{i-\frac{1}{2}}\Delta\mathbf{Q}_{i-1}\end{gathered} \tag{4.15}$$

The source term can be linearized by

$$\mathbf{D}^{n+1}_{i,j,k} \cong \mathbf{D}^{n}_{i,j,k} + (\frac{\partial \mathbf{D}}{\partial \mathbf{Q}})_{i,j,k} \bullet \Delta\mathbf{Q}_{i,j,k} \tag{4.16}$$

To apply above linearization to the fluxes in η and ζ direction, then the integrated governing equations are written as

$$
\begin{aligned}
&(I-\Theta)\Delta\mathbf{Q}_{i,j,k}+\hat{A}^{+}\Delta\mathbf{Q}_{i+1,j,k}+\hat{A}\Delta\mathbf{Q}_{i,j,k}+\hat{A}^{-}\Delta\mathbf{Q}_{i-1,j,k}\\
&+\hat{B}^{+}\Delta\mathbf{Q}_{i,j+1,k}+\hat{B}\Delta\mathbf{Q}_{i,j,k}+\hat{B}^{-}\Delta\mathbf{Q}_{i,j-1,k}\\
&+\hat{C}^{+}\Delta\mathbf{Q}_{i,j,k+1}+\hat{C}\Delta\mathbf{Q}_{i,j,k}+\hat{C}^{-}\Delta\mathbf{Q}_{i,j,k-1}=\mathbf{RHS}^{n}
\end{aligned}
\tag{4.17}
$$

where $\Theta=\Delta t\bullet(\frac{\partial\mathbf{D}}{\partial\mathbf{Q}})^{n}_{i,j,k}$. The coefficients A,A^{+},A^{-}, B,B^{+},B^{-}, and C,C^{+},C^{-} are called the left hand side (LHS) coefficient matrices and given as

$$
\begin{aligned}
\hat{A}^{+} &= \tfrac{\Delta t}{\Delta V}(A^{R}_{i+\frac{1}{2}}-L^{R}_{i+\frac{1}{2}})\\
\hat{A} &= \tfrac{\Delta t}{\Delta V}(A^{L}_{i+\frac{1}{2}}-L^{L}_{i+\frac{1}{2}}-A^{R}_{i-\frac{1}{2}}+L^{R}_{i-\frac{1}{2}})\\
\hat{A}^{-} &= -\tfrac{\Delta t}{\Delta V}(A^{L}_{i-\frac{1}{2}}-L^{L}_{i-\frac{1}{2}})\\
\hat{B}^{+} &= \tfrac{\Delta t}{\Delta V}(B^{R}_{j+\frac{1}{2}}-M^{R}_{j+\frac{1}{2}})\\
\hat{B} &= \tfrac{\Delta t}{\Delta V}(B^{L}_{j+\frac{1}{2}}-M^{L}_{j+\frac{1}{2}}-B^{R}_{j-\frac{1}{2}}+M^{R}_{j-\frac{1}{2}})\\
\hat{B}^{-} &= -\tfrac{\Delta t}{\Delta V}(B^{L}_{j-\frac{1}{2}}-M^{L}_{j-\frac{1}{2}})\\
\hat{C}^{+} &= \tfrac{\Delta t}{\Delta V}(C^{R}_{k+\frac{1}{2}}-N^{R}_{k+\frac{1}{2}})\\
\hat{C} &= \tfrac{\Delta t}{\Delta V}(C^{L}_{k+\frac{1}{2}}-N^{L}_{k+\frac{1}{2}}-C^{R}_{k-\frac{1}{2}}+N^{R}_{k-\frac{1}{2}})\\
\hat{C}^{-} &= -\tfrac{\Delta t}{\Delta V}(C^{L}_{k-\frac{1}{2}}-N^{L}_{k-\frac{1}{2}})
\end{aligned}
\tag{4.18}
$$

In Eq. (4.17), $\mathbf{RHS}^{n}$ is the summation of all terms on the right hand side (RHS) of the discretized equation and written as

$$
\begin{aligned}
&\mathbf{RHS}^{n}=-\tfrac{\Delta t}{\Delta V}[(\mathbf{E}_{i+\frac{1}{2}}-\mathbf{E}_{i-\frac{1}{2}})^{n}+(\mathbf{F}_{i+\frac{1}{2}}-\mathbf{F}_{i-\frac{1}{2}})^{n}+(\mathbf{G}_{i+\frac{1}{2}}-\mathbf{G}_{i-\frac{1}{2}})^{n}\\
&-(\mathbf{R}'_{i+\frac{1}{2}}-\mathbf{R}'_{i-\frac{1}{2}})^{n}-(\mathbf{S}'_{i+\frac{1}{2}}-\mathbf{S}'_{i-\frac{1}{2}})^{n}-(\mathbf{T}'_{i+\frac{1}{2}}-\mathbf{T}'_{i-\frac{1}{2}})^{n}]+\Delta t\bullet\mathbf{D}^{n}
\end{aligned}
\tag{4.19}
$$

Since the delta formulation($\Delta\mathbf{Q}$), the left hand side (LHS) in Eq. (4.17) constructed by employing 1st order scheme, does not affect the final solution, the accuracy of the converged solution relies on the accuracy of $\mathbf{RHS}^n$. The 5th order WENO scheme with an efficient upwind Riemann solver, so called the low diffusion E-CUSP (LDE) scheme [99], is used to evaluate the interface inviscid fluxes in $\mathbf{RHS}^n$. A fully conservative 4th order central differencing scheme [46] is used to evaluate the viscous fluxes. The unfactored Gauss-Seidel line iteration method is adopted to solve the Eq. (4.17) because the diagonal dominance is achieved through the 1st order implicit discretization and it is shown to be the most efficient relaxation method for transonic flow simulation [104].

4.2 Upwind Characteristics

Upwind schemes are designed to resolve the flow physics reasonably by accounting for the wave propagation, in which the flux vector is decomposed into a negative and a positive contributions according to the signs of the eigenvalues of the Jacobian matrices. Forward difference is then applied for the negative flux and backward difference for the positive flux. In the present study the Van Leer scheme [105] as a family of CUSP scheme is used for the LHS side in Eq. (4.17) and the LDE scheme [99] is applied for the RHS side in Eq. (4.17), which is described in detail in the following sections.

Before the upwind schemes are proposed to solve the LHS coefficients and RHS fluxes shown in Eq. (4.17), the characteristics of hyperbolic system as basis of the upwind schemes are explored. For example, the inviscid Jacobian matrix in ξ-direction can be computed as

$$\begin{aligned}\frac{\partial \mathbf{E}}{\partial \mathbf{Q}} &= \frac{\partial(E_1,E_2,E_3,E_4,E_5)}{\partial(Q_1,Q_2,Q_3,Q_4,Q_5)} \\ &= \begin{bmatrix} \frac{\partial E_1}{\partial Q_1} & \frac{\partial E_1}{\partial Q_2} & \frac{\partial E_1}{\partial Q_3} & \frac{\partial E_1}{\partial Q_4} & \frac{\partial E_1}{\partial Q_5} \\ \frac{\partial E_2}{\partial Q_1} & \frac{\partial E_2}{\partial Q_2} & \frac{\partial E_2}{\partial Q_3} & \frac{\partial E_2}{\partial Q_4} & \frac{\partial E_2}{\partial Q_5} \\ \frac{\partial E_3}{\partial Q_1} & \frac{\partial E_3}{\partial Q_2} & \frac{\partial E_3}{\partial Q_3} & \frac{\partial E_3}{\partial Q_4} & \frac{\partial E_3}{\partial Q_5} \\ \frac{\partial E_4}{\partial Q_1} & \frac{\partial E_4}{\partial Q_2} & \frac{\partial E_4}{\partial Q_3} & \frac{\partial E_4}{\partial Q_4} & \frac{\partial E_4}{\partial Q_5} \\ \frac{\partial E_5}{\partial Q_1} & \frac{\partial E_5}{\partial Q_2} & \frac{\partial E_5}{\partial Q_3} & \frac{\partial E_5}{\partial Q_4} & \frac{\partial E_5}{\partial Q_5} \end{bmatrix} \end{aligned} \tag{4.20}$$

$$\mathbf{Q} = \frac{1}{J}\begin{bmatrix} \rho & \rho u & \rho v & \rho w & \rho e \end{bmatrix} = \begin{bmatrix} Q_1 & Q_2 & Q_3 & Q_4 & Q_5 \end{bmatrix} \tag{4.21}$$

$$\mathbf{E} = \begin{bmatrix} \rho\bar{U} \\ \rho u\bar{U} + l_x P \\ \rho v\bar{U} + l_y P \\ \rho w\bar{U} + l_z P \\ (\rho e + P)\bar{U} \end{bmatrix} = \begin{bmatrix} \rho(l_x u + l_y v + l_z w) \\ \rho u(l_x u + l_y v + l_z w) + l_x P \\ \rho v(l_x u + l_y v + l_z w) + l_y P \\ \rho w(l_x u + l_y v + l_z w) + l_z P \\ (\rho e + P)(l_x u + l_y v + l_z w) \end{bmatrix} = \begin{bmatrix} E_1 \\ E_2 \\ E_3 \\ E_4 \\ E_5 \end{bmatrix} \tag{4.22}$$

where $\bar{U} = U - l_t$ and the static pressure for a perfect gas can be stated as

$$P = (\gamma - 1)[\rho e - \rho\frac{1}{2}(u^2 + v^2 + w^2 - \Omega^2 r^2)] \tag{4.23}$$

then, Eq. (4.22) and Eq. (4.23) can be reconstructed using the conservative variable vector **Q** as

$$E_1 = l_x Q_2 + l_y Q_3 + l_z Q_4 \tag{4.24}$$

$$E_2 = \frac{Q_2}{Q_1}(l_x Q_2 + l_y Q_3 + l_z Q_4) + l_x(\gamma - 1)(Q_5 - q) \tag{4.25}$$

$$E_3 = \frac{Q_3}{Q_1}(l_x Q_2 + l_y Q_3 + l_z Q_4) + l_y(\gamma - 1)(Q_5 - q) \tag{4.26}$$

$$E_4 = \frac{Q_4}{Q_1}(l_x Q_2 + l_y Q_3 + l_z Q_4) + l_z(\gamma - 1)(Q_5 - q) \tag{4.27}$$

$$E_5 = [\gamma Q_5 - (\gamma - 1)q](l_x \frac{Q_2}{Q_1} + l_y \frac{Q_3}{Q_1} + l_z \frac{Q_4}{Q_1}) \tag{4.28}$$

where

$$q = \frac{1}{2}(\frac{Q_2^2}{Q_1} + \frac{Q_3^2}{Q_1} + \frac{Q_4^2}{Q_1} - Q_1 \Omega^2 r^2) \tag{4.29}$$

The resulting Jacobian matrix A is

$$A = \frac{\partial \mathbf{E}}{\partial \mathbf{Q}} = J \begin{pmatrix} 0 & l_x & l_y & l_z & 0 \\ -u\bar{U} + (\gamma-1)l_x e_k & \bar{U} + (2-\gamma)l_x u & l_y u + (1-\gamma)l_x v & l_z u + (1-\gamma)l_x w & (\gamma-1)l_x \\ -v\bar{U} + (\gamma-1)l_y e_k & l_x v + (1-\gamma)l_y u & \bar{U} + (2-\gamma)l_y v & l_z v + (1-\gamma)l_y w & (\gamma-1)l_y \\ -w\bar{U} + (\gamma-1)l_z e_k & l_x w + (1-\gamma)l_z u & l_y w + (1-\gamma)l_z v & \bar{U} + (2-\gamma)l_z w & (\gamma-1)l_z \\ a_{51} & (1-\gamma)\bar{U}u + I_o l_x & (1-\gamma)\bar{U}v + I_o l_y & (1-\gamma)\bar{U}w + I_o l_z & \gamma\bar{U} \end{pmatrix} \tag{4.30}$$

$$a_{51} = \bar{U}[(\gamma - 1) * (e_k + \Omega^2 r^2) - I_o] \tag{4.31}$$

where rothalpy I_o is defined as

$$I_o = \frac{\gamma}{\gamma-1}\frac{P}{\rho} + e_k = \frac{a^2}{\gamma-1} + e_k \tag{4.32}$$

$$e_k = \frac{1}{2}(u^2 + v^2 + w^2 - \Omega^2 r^2) \tag{4.33}$$

The eigenvalues($\lambda_{1,2,3,4,5}$) of the Jacobian matrix A that represent the characteristic direction of propagation are determined by

$$A = X_A \Lambda_A X_A^{-1} \tag{4.34}$$

$$\Lambda_A = \begin{bmatrix} \lambda_1 & 0 & 0 & 0 & 0 \\ 0 & \lambda_2 & 0 & 0 & 0 \\ 0 & 0 & \lambda_3 & 0 & 0 \\ 0 & 0 & 0 & \lambda_4 & 0 \\ 0 & 0 & 0 & 0 & \lambda_5 \end{bmatrix} = \begin{bmatrix} \bar{U} & 0 & 0 & 0 & 0 \\ 0 & \bar{U} & 0 & 0 & 0 \\ 0 & 0 & \bar{U} & 0 & 0 \\ 0 & 0 & 0 & \bar{U}+C & 0 \\ 0 & 0 & 0 & 0 & \bar{U}-C \end{bmatrix} \tag{4.35}$$

where Λ_A is a diagonal matrix with its element being the eigenvalues of A, X_A is the eigenvector matrix. C is the contravariant speed of sound given as

$$C = c\sqrt{l_x^2 + l_y^2 + l_z^2} \tag{4.36}$$

The eigenvector X_A is

$$X_A = [\vec{X}_1 \quad \vec{X}_2 \quad \vec{X}_3 \quad \vec{X}_4 \quad \vec{X}_5]$$

$$= \begin{pmatrix} 0 & 1 & 0 & 1 & 1 \\ -\frac{l_y}{l_x} & \frac{\bar{U}}{l_x} & -\frac{l_z}{l_x} & u + c\hat{l}_x & u - c\hat{l}_x \\ 1 & 0 & 0 & v + c\hat{l}_y & v - c\hat{l}_y \\ 0 & 0 & 1 & w + c\hat{l}_z & w - c\hat{l}_z \\ \frac{l_y u - lxv}{lx} & \frac{2u(l_y v + l_z w) - (v^2 + w^2 - u^2)l_x}{2l_x} & \frac{l_x w - l_z u}{l_x} & I_o + \frac{c\bar{U}}{\sqrt{l_x^2 + l_y^2 + l_z^2}} & I_o - \frac{c\bar{U}}{\sqrt{l_x^2 + l_y^2 + l_z^2}} \end{pmatrix} \tag{4.37}$$

where

$$\hat{l}_x = \frac{l_x}{\sqrt{l_x^2 + l_y^2 + l_z^2}}$$

$$\hat{l}_y = \frac{l_y}{\sqrt{l_x^2 + l_y^2 + l_z^2}} \tag{4.38}$$

$$\hat{l}_z = \frac{l_z}{\sqrt{l_x^2 + l_y^2 + l_z^2}}$$

X_A^{-1} is the inverse eigenvector matrix of X_A such that

$$X_A^{-1} X_A = I \tag{4.39}$$

Note that the flux vector **E** equals $A\mathbf{Q}$ and is homogeneous function of degree one. The eigenvalues are real and consist of positive and negative eigenvalues. The signs of the eigenvalues indicate the direction of wave propagation, hence the flux vector can be split into positive or negative characteristics.

For example, for the subsonic flow where $M_\xi (= \frac{U}{C}) < 1$, the eigenvalues U, U, U and

$U+C$ are positive, and $U-C$ is negative. If the Steger-Warming flux vector splitting (FVS) scheme [106] is taken into account, then the Jacobian matrix A can be split as the following.

$$A = A^+ + A^- \tag{4.40}$$

where

$$A^+ = X_A \Lambda_A^+ X_A^{-1} \tag{4.41}$$

$$A^- = X_A \Lambda_A^- X_A^{-1} \tag{4.42}$$

Λ_A^+ is a diagonal matrix whose elements are the positive eigenvalues of A and Λ_A^- is a diagonal matrix whose elements are the negative eigenvalues of A. For example, if $\lambda_1 (= U)$ is positive, then

$$\Lambda_A^+ = \begin{bmatrix} \bar{U} & 0 & 0 & 0 & 0 \\ 0 & \bar{U} & 0 & 0 & 0 \\ 0 & 0 & \bar{U} & 0 & 0 \\ 0 & 0 & 0 & \bar{U}+C & 0 \\ 0 & 0 & 0 & 0 & 0 \end{bmatrix} \tag{4.43}$$

where $\Lambda_A^- = \Lambda_A - \Lambda_A^+$. Then, the flux vector $\mathbf{E}$ can be split as

$$\mathbf{E}^+ = A^+ \mathbf{Q} \tag{4.44}$$

$$\mathbf{E}^- = A^- \mathbf{Q} \tag{4.45}$$

The other inviscid coefficients matrices, B and C are determined in the same manner as the matrix A. For the supersonic flow ($M_\xi > 1$), all five eigenvalues are positive and which results in

$$A^+ = A \tag{4.46}$$

$$A^- = 0 \tag{4.47}$$

4.3 The Low Diffusion E-CUSP (LDE) Scheme

The Low Diffusion E-CUSP (LDE) Scheme [99] is used to evaluate the inviscid fluxes. The basic idea of the LDE scheme is to split the inviscid flux into the convective flux E^c and the pressure flux E^p based on the upwind characteristics. In generalized coordinate system, the flux **E** can be split as the following:

$$\mathbf{E}' = E^c + E^p = \begin{pmatrix} \rho U \\ \rho u U \\ \rho v U \\ \rho w U \\ \rho e U \\ \rho \tilde{\nu} U \end{pmatrix} + \begin{pmatrix} 0 \\ l_x p \\ l_y p \\ l_z p \\ p\overline{U} \\ 0 \end{pmatrix} \tag{4.48}$$

where, U is the contravariant velocity in ξ direction and is defined as the following:

$$U = l_t + l_x u + l_y v + l_z w \tag{4.49}$$

$\overline{U}$ is defined as:

$$\overline{U} = l_x u + l_y v + l_z w \tag{4.50}$$

The convective term, E^c is evaluated by

$$E^c = \rho U \begin{pmatrix} 1 \\ u \\ v \\ w \\ e \\ \tilde{\nu} \end{pmatrix} = \rho U f^c,\ f^c = \begin{pmatrix} 1 \\ u \\ v \\ w \\ e \\ \tilde{\nu} \end{pmatrix} \tag{4.51}$$

let

$$C = c\left(l_x^2 + l_y^2 + l_z^2\right)^{\frac{1}{2}} \tag{4.52}$$

where $c = \sqrt{\gamma RT}$ is the speed of sound.

Then the convective flux at interface $i + \frac{1}{2}$ is evaluated as:

$$E^c_{i+\frac{1}{2}} = C_{\frac{1}{2}}\left[\rho_L C^+ f^c_L + \rho_R C^- f^c_R\right] \tag{4.53}$$

where, the subscripts L and R represent the left and right hand sides of the interface. The Mach number splitting of Edwards [107] is borrowed to determine C^+ and C^- as the fol-

lowing:

$$C_{\frac{1}{2}} = \frac{1}{2}\left(C_L + C_R\right) \tag{4.54}$$

$$C^{+} = \alpha_L^{+}\left(1+\beta_L\right)M_L - \beta_L M_L^{+} - M_{\frac{1}{2}}^{+} \tag{4.55}$$

$$C^{-} = \alpha_R^{-}\left(1+\beta_R\right)M_R - \beta_R M_R^{-} + M_{\frac{1}{2}}^{-} \tag{4.56}$$

$$M_L = \frac{U_L}{C_{\frac{1}{2}}},\ M_R = \frac{U_R}{C_{\frac{1}{2}}} \tag{4.57}$$

$$\alpha_{L,R} = \frac{1}{2}\left[1 \pm sign\left(M_{L,R}\right)\right] \tag{4.58}$$

$$\beta_{L,R} = -max\left[0, 1 - int\left(\left|M_{L,R}\right|\right)\right] \tag{4.59}$$

$$M_{\frac{1}{2}}^{+} = M_{\frac{1}{2}}\frac{C_R + C_L\Phi}{C_R + C_L},\ M_{\frac{1}{2}}^{-} = M_{\frac{1}{2}}\frac{C_L + C_R\Phi^{-1}}{C_R + C_L} \tag{4.60}$$

$$\Phi = \frac{\left(\rho C^2\right)_R}{\left(\rho C^2\right)_L} \tag{4.61}$$

$$M_{\frac{1}{2}} = \beta_L\delta^{+}M_L^{-} - \beta_R\delta^{-}M_R^{+} \tag{4.62}$$

$$M_{L,R}^{\pm} = \pm\tfrac{1}{4}\left(M_{L,R} \pm 1\right)^2 \tag{4.63}$$

$$\delta^{\pm} = \tfrac{1}{2}\left\{1 \pm sign\left[\tfrac{1}{2}\left(M_L + M_R\right)\right]\right\} \tag{4.64}$$

The pressure flux, E^p is evaluated as the following

$$E^p_{i+\frac{1}{2}} = \begin{pmatrix} 0 \\ \mathscr{P}^+ p l_x \\ \mathscr{P}^+ p l_y \\ \mathscr{P}^+ p l_z \\ \frac{1}{2} p\left[\overline{U} + \overline{C}_{\frac{1}{2}}\right] \\ 0 \end{pmatrix}_L + \begin{pmatrix} 0 \\ \mathscr{P}^- p l_x \\ \mathscr{P}^- p l_y \\ \mathscr{P}^- p l_z \\ \frac{1}{2} p\left[\overline{U} - \overline{C}_{\frac{1}{2}}\right] \\ 0 \end{pmatrix}_R \tag{4.65}$$

The contravariant speed of sound $\overline{C}$ in the pressure vector is consistent with $\overline{U}$. It is computed based on C as the following,

$$\overline{C} = C - l_t \tag{4.66}$$

The use of $\overline{U}$ and $\overline{C}$ instead of U and C in the pressure vector is to take into account of the grid speed so that the flux will transit from subsonic to supersonic smoothly. When the grid is stationary, $l_t = 0, \overline{C} = C, \overline{U} = U$.

The pressure splitting coefficient is:

$$\mathscr{P}_{L,R}^{\pm} = \frac{1}{4}\left(M_{L,R} \pm 1\right)^2 \left(2 \mp M_L\right) \tag{4.67}$$

The LDE scheme can capture crisp shock profile and exact contact surface discontinuities as accurately as the Roe scheme [108]. With an extra equation from the DES, the splitting is basically the same as the original scheme for the Euler equation. This is an advantage over the Roe scheme [109], for which the eigenvectors need to be derived when any extra equation is added to the governing equations. In addition, it is simpler and more CPU efficient than the Roe scheme due to no matrix operation.

4.4 The 5th Order WENO Scheme

The interface flux, $E_{i+\frac{1}{2}} = E(Q_L, Q_R)$, is evaluated by determining the conservative variables Q_L and Q_R using fifth-order WENO scheme [100, 101]. For example,

$$(Q_L)_{i+\frac{1}{2}} = \omega_0 q_0 + \omega_1 q_1 + \omega_2 q_2 \tag{4.68}$$

where

$$\begin{aligned} q_0 &= \tfrac{1}{3}Q_{i-2} - \tfrac{7}{6}Q_{i-1} + \tfrac{11}{6}Q_i \\ q_1 &= -\tfrac{1}{6}Q_{i-1} + \tfrac{5}{6}Q_i + \tfrac{1}{3}Q_{i+1} \\ q_2 &= \tfrac{1}{3}Q_i + \tfrac{5}{6}Q_{i+1} - \tfrac{1}{6}Q_{i+2} \end{aligned} \tag{4.69}$$

$$\omega_k = \frac{\alpha_k}{\alpha_0 + \ldots + \alpha_{r-1}} \tag{4.70}$$

$$
\begin{aligned}
&\alpha_k = \tfrac{C_k}{\varepsilon + IS_k},\ k = 0, \ldots, r-1 \\
&C_0 = 0.1,\ C_1 = 0.6,\ C_2 = 0.3 \\
&IS_0 = \tfrac{13}{12}\left(Q_{i-2} - 2Q_{i-1} + Q_i\right)^2 + \tfrac{1}{4}\left(Q_{i-2} - 4Q_{i-1} + 3Q_i\right)^2 \\
&IS_1 = \tfrac{13}{12}\left(Q_{i-1} - 2Q_i + Q_{i+1}\right)^2 + \tfrac{1}{4}\left(Q_{i-1} - Q_{i+1}\right)^2 \\
&IS_2 = \tfrac{13}{12}\left(Q_i - 2Q_{i+1} + Q_{i+2}\right)^2 + \tfrac{1}{4}\left(3Q_i - 4Q_{i+1} + Q_{i+2}\right)^2
\end{aligned}
\tag{4.71}
$$

where, ε is originally introduced to avoid the denominator becoming zero and is supposed to be a very small number. In [101], it is observed that IS_k will oscillate if ε is small and also shift the weights away from the optimum values in the smooth region. The higher the ε values, the closer the weights approach the optimum weights, C_k, which will give the symmetric evaluation of the interface flux with minimum numerical dissipation. When there are shocks in the flow field, ε can not be too large to maintain the sensitivity to shocks. In [101], the optimized value of $\varepsilon = 10^{-2}$ is recommended for the transonic flow with shock waves.

4.5 The 4th Order Central Differencing for Viscous Terms

A set of conservative fourth-order accurate finite central differencing schemes for the viscous terms is suggested [46]. These central differencing schemes are constructed so that the stencil widths are within the WENO scheme stencil. This requires that the central differencing achieves their maximum order accuracy in the WENO stencil.

We take the viscous flux derivative in ξ-direction as the example to explain how the schemes are constructed. To conservatively discretize the viscous derivative term in Navier-Stokes equations Eq. (3.47), we have

$$\frac{\partial R}{\partial \xi}|_i = \frac{\tilde{R}_{i+1/2} - \tilde{R}_{i-1/2}}{\Delta\xi} \tag{4.72}$$

To obtain 4th order accuracy, $\tilde{R}$ needs to be reconstructed as

$$\tilde{R}_{i-1/2} = \sum_{I=i-3/2}^{i+1/2} \alpha_I R_I \tag{4.73}$$

where

$$\alpha_{i-3/2} = -\frac{1}{24},\ \alpha_{i-1/2} = \frac{26}{24},\ \alpha_{i+1/2} = -\frac{1}{24}$$

$$R_{i-1/2} = [(\xi_x \tau_{xx}) + (\eta_y \tau_{xy}) + (\zeta_z \tau_{xz})]_{i-1/2}$$

$$\begin{aligned}(\tau_{xx}) = \quad & \mu\{\tfrac{4}{3}\left[(\xi_x \tfrac{\partial u}{\partial \xi}) + (\eta_x \tfrac{\partial u}{\partial \eta}) + (\zeta_x \tfrac{\partial u}{\partial \zeta})\right] \\ & -\tfrac{2}{3}[(\xi_y \tfrac{\partial v}{\partial \xi}) + (\eta_y \tfrac{\partial v}{\partial \eta}) + (\zeta_y \tfrac{\partial v}{\partial \zeta}) \\ & (\xi_z \tfrac{\partial w}{\partial \xi}) + (\eta_z \tfrac{\partial w}{\partial \eta}) + (\zeta_z \tfrac{\partial w}{\partial \zeta})]\}\end{aligned} \tag{4.74}$$

If R in Eq. (4.73) can be approximated with the accuracy order not lower than 4th order, the Taylor series expansion analysis of (4.72) and (4.73) will give

$$\frac{1}{\Delta\xi}(\tilde{R}_{i+1/2} - \tilde{R}_{i-1/2}) = R^{'}(\xi_i) + O(\Delta\xi^4) \tag{4.75}$$

and the 4th order accuracy is achieved (to be proved later). It needs to point out that in Eq. (4.72), $\tilde{R}_{i-1/2}$ can not be replaced by $R_{i-1/2}$. Otherwise, the 4th order accuracy can not be achieved even though the high order approximation of $R_{i-1/2}$ is used. The 4th order accuracy from Eq. (4.72)-(4.75) is also based on the uniform spacing $\Delta\xi = C$.

In order to achieve the highest order accuracy of R_I with $I = i-3/2, i-1/2, i+1/2$,

the approximation of each term in Eq. (4.73) using the same points is given below:

$$\mu_I = \sum_{l=m}^{n} C_l^I \mu_{i+l}, \tag{4.76}$$

$$\frac{\partial u}{\partial \xi}|_I = \frac{1}{\Delta\xi} \sum_{l=r}^{s} D_l^I u_{i+l}, \tag{4.77}$$

$$\frac{\partial u}{\partial \eta}|_I = \sum_{l=m}^{n} C_l^I \frac{\partial u}{\partial \eta}|_{i+l,j} \tag{4.78}$$

where

$$\frac{\partial u}{\partial \eta}|_{i,j} = \frac{1}{\Delta\eta} \sum_{l=p}^{q} C_l^c u_{i,j+l}, \tag{4.79}$$

By choosing different ranges for $(m,n),(r,s),(p,q)$ and different coefficients C_l^I, D_l^I, C_l^c, one can obtain different order accuracy approximation to the viscous terms. The principle of choosing $(m,n),(r,s),(p,q)$ is to ensure that the approximation of $\frac{\partial R}{\partial \xi}|_i$ in Eq. (4.72) is a central differencing. For example, let $(m,n) = (-2,1),(r,s) = (-3,2), and\ (p,q) = (-2,2)$, and they give

$$\mu_I = \sum_{l=m}^{n} C_l^I \mu_{i+l} + O(\Delta\xi^4), \tag{4.80}$$

$$\frac{\partial u}{\partial \xi}|_I = \frac{1}{\Delta\xi} \sum_{l=r}^{s} D_l^I u_{i+l} + O(\Delta\xi^5), \tag{4.81}$$

$$\frac{\partial u}{\partial \eta}|_I = \sum_{l=m}^{n} C_l^I \frac{\partial u}{\partial \eta}|_{i+l,j} + O(\Delta\xi^4, \Delta\eta^4), \tag{4.82}$$

where

$$\frac{\partial u}{\partial \eta}|_{i,j} = \frac{1}{\Delta\eta} \sum_{l=p}^{q} C_l^c u_{i,j+l} + O(\Delta\eta^4) \tag{4.83}$$

the coefficients C_l^I, D_l^I, C_l^c can be obtained by Taylor's series expansion and are given in Tables 4.1-4.3. For example,

$$\begin{cases} \mu_{i-3/2} = \frac{1}{16}(5\mu_{i-2} + 15\mu_{i-1} - 5\mu_i + \mu_{i+1}) + O(\Delta\xi^4) \\ \mu_{i-1/2} = \frac{1}{16}(-\mu_{i-2} + 9\mu_{i-1} + 9\mu_i - \mu_{i+1}) + O(\Delta\xi^4) \\ \mu_{i+1/2} = \frac{1}{16}(\mu_{i-2} - 5\mu_{i-1} + 15\mu_i + 5\mu_{i+1}) + O(\Delta\xi^4) \end{cases} \tag{4.84}$$

$$\begin{cases} \frac{\partial u}{\partial \xi}|_{i-3/2} = \frac{1}{\Delta\xi}(\frac{71}{1920}u_{i-3} - \frac{141}{128}u_{i-2} + \frac{69}{64}u_{i-1} + \frac{1}{192}u_i - \frac{3}{128}u_{i+1} + \frac{3}{640}u_{i+2}) + O(\Delta\xi^5) \\ \frac{\partial u}{\partial \xi}|_{i-1/2} = \frac{1}{\Delta\xi}(-\frac{3}{640}u_{i-3} + \frac{25}{384}u_{i-2} - \frac{75}{64}u_{i-1} + \frac{75}{64}u_i - \frac{25}{384}u_{i+1} + \frac{3}{640}u_{i+2}) + O(\Delta\xi^5) \\ \frac{\partial u}{\partial \xi}|_{i+1/2} = \frac{1}{\Delta\xi}(-\frac{3}{640}u_{i-3} + \frac{3}{128}u_{i-2} - \frac{1}{192}u_{i-1} - \frac{69}{64}u_i + \frac{141}{128}u_{i+1} - \frac{71}{1920}u_{i+2}) + O(\Delta\xi^5) \end{cases} \tag{4.85}$$

The other terms are determined similarly. For comparison, the terms used in Ref. [110, 111] by De Rango and Zingg et al. are given as the following,

$$\begin{cases} \mu_{i-3/2} = \frac{1}{16}(-\mu_{i-3} + 9\mu_{i-2} + 9\mu_{i-1} - \mu_i) + O(\Delta\xi^4) \\ \mu_{i-1/2} = \frac{1}{16}(\mu_{i-2} + 9\mu_{i-1} + 9\mu_i - \mu_{i+1}) + O(\Delta\xi^4) \\ \mu_{i+1/2} = \frac{1}{16}(\mu_{i-1} + 9\mu_i + 9\mu_{i+1} - \mu_{i+2}) + O(\Delta\xi^4) \end{cases} \tag{4.86}$$

$$\begin{cases} \frac{\partial u}{\partial \xi}|_{i-3/2} = \frac{1}{24\Delta\xi}(-u_{i-3} - 27u_{i-2} + 27u_{i-1} - u_i) + O(\Delta\xi^4) \\ \frac{\partial u}{\partial \xi}|_{i-1/2} = \frac{1}{24\Delta\xi}(-u_{i-2} - 27u_{i-1} + 27u_i - u_{i+1}) + O(\Delta\xi^4) \\ \frac{\partial u}{\partial \xi}|_{i+1/2} = \frac{1}{24\Delta\xi}(-u_{i-1} - 27u_i + 27u_{i+1} - u_{i+2}) + O(\Delta\xi^4) \end{cases} \tag{4.87}$$

Compare Eqs. (4.84),(4.85) and Eqs. (4.86),(4.87), it can be seen that μ_I in present paper has the same accuracy order, as that of De Rango and Zingg et al., but has small stencil width $(i-2,\cdots,i+1)$, $\frac{\partial u}{\partial \xi}|_I$ has the same stencil width, but obtains one accuracy order higher than that in Ref. [110, 111].

Table 4.1: The coefficients of C_l^I

I	C_{-2}^I	C_{-1}^I	C_0^I	C_1^I
$i-3/2$	5/16	15/16	-5/16	1/16
$i-1/2$	-1/16	9/16	9/16	-1/16
$i+1/2$	1/16	-5/16	15/16	5/16

Table 4.2: The coefficients of D_l^I

I	D_{-3}^I	D_{-2}^I	D_{-1}^I	D_0^I	D_1^I	D_2^I
$i-3/2$	71/1920	-141/128	69/64	1/192	-3/128	3/640
$i-1/2$	-3/640	25/384	-75/64	75/64	-25/384	3/640
$i+1/2$	-3/640	3/128	-1/192	-69/64	141/128	-71/1920

Table 4.3: The coefficients of C_l^c

C_{-2}^c	C_{-1}^c	C_0^c	C_1^c	C_2^c
1/12	-8/12	0	8/12	-1/12

It can be proved that the scheme Eq. (4.72) is symmetric with respect to cell i. For example, the coefficients of $\mu_{i-2}u_{i-3}$, $\mu_{i+2}u_{i+3}$, $\mu_{i-1}u_{i-2}$, and $\mu_{i+1}u_{i+2}$ can be found as (in the following formula, $\tilde{C}_l^I$ and $\tilde{D}_l^I$ are the coefficients of μ_{i+l}, u_{i+l} in R_I for $\tilde{R}_{i+1/2}$, respectively. It's clear that there are $\tilde{C}_l^I = C_{l-1}^{I-1}$ and $\tilde{D}_l^I = D_{l-1}^{I-1}$, $\tilde{\alpha}_I = \alpha_{I-1}$, $I = i-1/2, i+$

$1/2, i+3/2$):

$$
\begin{aligned}
C_{i-2,i-3} &= -\sum_{I=i-3/2}^{i+1/2} \alpha_I C_{-2}^I D_{-3}^I \\
&= -\left[(\tfrac{-1}{24}) \cdot \tfrac{5}{16} \cdot \tfrac{71}{1920} + \tfrac{26}{24} \cdot (\tfrac{-1}{16}) \cdot (\tfrac{-3}{640}) + (\tfrac{-1}{24}) \cdot \tfrac{1}{16} \cdot (\tfrac{-3}{640})\right] \\
&= \tfrac{7}{46080}
\end{aligned}
$$

$$
\begin{aligned}
C_{i+2,i+3} &= \sum_{I=i-1/2}^{i+3/2} \tilde{\alpha}_I \tilde{C}_2^I \tilde{D}_3^I \\
&= (\tfrac{-1}{24}) \cdot \tfrac{1}{16} \cdot \tfrac{3}{640} + \tfrac{26}{24} \cdot (\tfrac{-1}{16}) \cdot \tfrac{3}{640} + (\tfrac{-1}{24}) \cdot \tfrac{5}{16} \cdot (\tfrac{-71}{1920}) \\
&= \tfrac{7}{46080}
\end{aligned}
$$

$$
\begin{aligned}
C_{i-1,i-2} &= \sum_{I=i-1/2}^{i+3/2} \tilde{\alpha}_I \tilde{C}_{-1}^I \tilde{D}_{-2}^I - \sum_{I=i-3/2}^{i+1/2} \alpha_I C_{-1}^I D_{-2}^I \\
&= (\tfrac{-1}{24}) \cdot \tfrac{5}{16} \cdot \tfrac{71}{1920} + \tfrac{26}{24} \cdot (\tfrac{-1}{16}) \cdot (\tfrac{-3}{640}) + (\tfrac{-1}{24}) \cdot \tfrac{1}{16} \cdot (\tfrac{-3}{640}) \\
&\quad - \left[(\tfrac{-1}{24}) \cdot \tfrac{15}{16} \cdot (\tfrac{-141}{128}) + \tfrac{26}{24} \cdot \tfrac{9}{16} \cdot \tfrac{25}{384} + (\tfrac{-1}{24}) \cdot (\tfrac{-5}{16}) \cdot \tfrac{3}{128}\right] \\
&= -\tfrac{479}{5760}
\end{aligned}
$$

$$
\begin{aligned}
C_{i+1,i+2} &= \sum_{I=i-1/2}^{i+3/2} \tilde{\alpha}_I \tilde{C}_1^I \tilde{D}_2^I - \sum_{I=i-3/2}^{i+1/2} \alpha_I C_1^I D_2^I \\
&= (\tfrac{-1}{24}) \cdot (\tfrac{-5}{16}) \cdot (\tfrac{-3}{128}) + \tfrac{26}{24} \cdot \tfrac{9}{16} \cdot (\tfrac{-25}{384}) + (\tfrac{-1}{24}) \cdot \tfrac{15}{16} \cdot \tfrac{141}{128} \\
&\quad - \left[(\tfrac{-1}{24}) \cdot \tfrac{1}{16} \cdot \tfrac{3}{640} + \tfrac{26}{24} \cdot (\tfrac{-1}{16}) \cdot \tfrac{3}{640} + (\tfrac{-1}{24}) \cdot \tfrac{5}{16} \cdot (\tfrac{-71}{1920})\right] \\
&= -\tfrac{479}{5760}
\end{aligned}
$$

So we have $C_{i-2,i-3} = C_{i+2,i+3}$, $C_{i-1,i-2} = C_{i+1,i+2}$, and so on. Hence the scheme Eq. (4.72) is symmetric with respect to grid node i. The symmetry of central differencing for

Eq. (4.72) satisfies the diffusion property of the viscous flux.

Next, we prove that the order of accuracy given by Eq.(4.75) is satisfied. Take the term $T^- = \mu \partial u/\partial \xi$ in Eq.(4.75) as the example,

In $\tilde{R}_{i-1/2}$, at $I = i-3/2$, based on Taylor's series expansion

$$\begin{aligned} T^-_{i-3/2} &= \Sigma^n_{l=m} C^I_l \mu_{i+l} (\tfrac{1}{\Delta\xi} \Sigma^s_{l=r} D^I_l u_{i+l}) \\ &= \left[\mu_{i-3/2} + A_I \mu^{(4)}_{i-3/2} \Delta\xi^4 + O(\Delta\xi^5)\right] \left[\tfrac{\partial u}{\partial \xi}|_{i-3/2} + O(\Delta\xi^5)\right] \\ &= \mu_{i-3/2} \tfrac{\partial u}{\partial \xi}|_{i-3/2} + A_I \mu^{(4)}_{i-3/2} \tfrac{\partial u}{\partial \xi}|_{i-3/2} \Delta\xi^4 + O(\Delta\xi^5) \end{aligned}$$

A_I is the coefficient of Taylor's series expansion.

The corresponding term T^+ in $\tilde{R}_{i+1/2}$ is at $I = i-1/2$, and

$$\begin{aligned} T^+_{i-1/2} &= \Sigma^n_{l=m} \tilde{C}^I_l \mu_{i+1+l} (\tfrac{1}{\Delta\xi} \Sigma^s_{l=r} \tilde{D}^I_l u_{i+1+l}) \\ &= \left[\mu_{i-1/2} + \tilde{A}_I \mu^{(4)}_{i-1/2} \Delta\xi^4 + O(\Delta\xi^5)\right] \left[\tfrac{\partial u}{\partial \xi}|_{i-1/2} + O(\Delta\xi^5)\right] \\ &= \mu_{i-1/2} \tfrac{\partial u}{\partial \xi}|_{i-1/2} + \tilde{A}_I \mu^{(4)}_{i-1/2} \tfrac{\partial u}{\partial \xi}|_{i-1/2} \Delta\xi^4 + O(\Delta\xi^5) \end{aligned}$$

Note that $A_I = \tilde{A}_I$, hence

$$T^+_{i-1/2} - T^-_{i-3/2} = \mu_{i-1/2} \frac{\partial u}{\partial \xi}|_{i-1/2} - \mu_{i-3/2} \frac{\partial u}{\partial \xi}|_{i-3/2} + O(\Delta\xi^5)$$

The other two terms can be analyzed similarly as above, then Eq.(4.75)

$$\frac{1}{\Delta\xi}(\tilde{R}_{i+1/2} - \tilde{R}_{i-1/2}) = R'(\xi_i) + O(\Delta\xi^4)$$

is proved, i.e. the constructed schemes are formally 4th order accuracy.

4.6 Implicit Time Integration

When a unsteady solution is considered, higher order approximation for the time derivative is desirable. For unsteady flow, Jameson formulated so called the 2nd order dual time stepping scheme [112]. By introducing a pseudo time term, the unsteady problem at each physical time step is treated as a steady state problem for pseudo time. Without losing time accuracy, the dual time stepping scheme can greatly improve the computation efficiency by enhancing diagonal dominance [113].

4.6.1 Implicit Time Accurate Flow Solver

The time accurate governing equations are solved using dual time stepping method suggested by Jameson [112]. To achieve high convergence rate, the implicit pseudo time marching scheme is used with the unfactored Gauss-Seidel line relaxation [95]. The physical temporal term is discretized implicitly using a three point, backward differencing as the following:

$$\frac{\partial Q}{\partial t} = \frac{3Q^{n+1} - 4Q^{n} + Q^{n-1}}{2\Delta t} \tag{4.88}$$

where $n-1$, n and $n+1$ are three sequential time levels, which have a time interval of Δt. The first-order Euler scheme is used to discretize the pseudo temporal term to enhance diagonal dominance. The semi-discretized equations of the governing equations are finally given as the following:

$$\begin{aligned}\left[\left(\frac{1}{\Delta\tau}+\frac{1.5}{\Delta t}\right)I-\left(\frac{\partial R}{\partial Q}\right)^{n+1,m}\right]\delta Q^{n+1,m+1}\\ =R^{n+1,m}-\frac{3Q^{n+1,m}-4Q^{n}+Q^{n-1}}{2\Delta t}\end{aligned} \tag{4.89}$$

where the $\Delta\tau$ is the pseudo time step, R is the net flux evaluated on a grid point using the fifth-order WENO scheme.

4.6.2 Implicit Structural Solver

To solve the structural equations with the present CFD solver [99] in a fully coupled manner [28], the decoupled structural equations are integrated using the same method as the flow governing equations(4.89) within each physical time step:

$$\begin{aligned}\left(\frac{1}{\Delta\tau}I+\frac{1.5}{\Delta t}M+K\right)\delta S^{n+1,m+1}\\ =q^{n+1,m+1}-M\frac{3S^{n+1,m}-4S^{n}+S^{n-1}}{2\Delta t}-KS^{n+1,m}\end{aligned} \tag{4.90}$$

4.6.3 Flow-Structure Coupling

The fully coupled procedure for fluid-structure interaction (FSI) simulation is achieved by removing time lag between the fluid flow and the structure as sketched in Fig. 4.2. Within each physical time step(m), the flow and structural governing equations are solved without time lag via every successive pseudo time step until the net flux residual R given by Eq. (4.89) satisfies the prescribed convergence criteria(ε). Note the residual q for the structure equation (3.76) gets converged quickly within a few steps. Therefore, the convergence of FSI is determined according to R. After the convergence criteria is reached, the fluid-structural interaction goes to next physical time step, $n+1$.

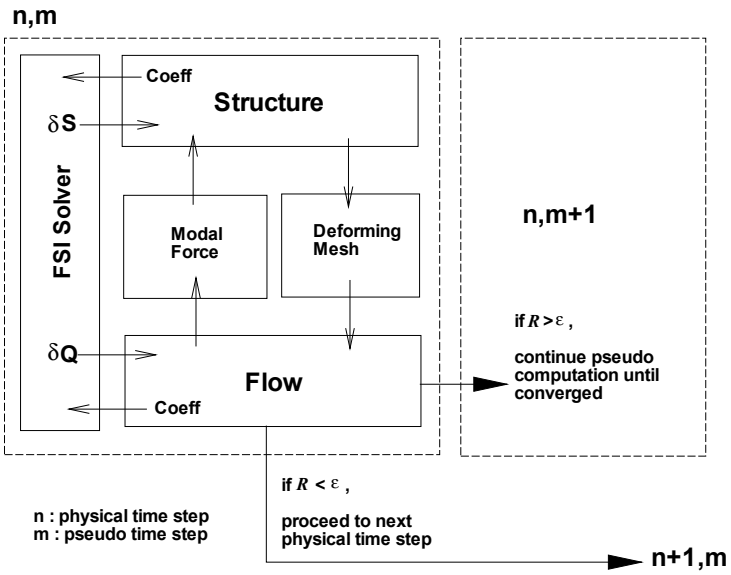

Figure 4.2: Procedure of fully coupled fluid-structure interaction

Chapter 5

Validation of DDES

Turbulence modeling is critical for drag prediction, in particular for surface friction drag. The commonly used turbulence models today are still the Reynolds averaged Navier-Stokes(RANS) models, which can not accurately predict the flows with large separations. RANS models treat large eddy as isotropic structures and are not consistent with the physics. However, RANS models have their advantage of CPU efficiency and can handle many engineering problems with calibrated parameters. The recent Detached Eddy Simulation (DES) of Spalart and Delayed DES are more widely used for their better capability to treat separated flows.

In addition to turbulence modeling, accurate resolving shock waves and viscous terms with minimal numerical dissipation is also crucial for skin friction prediction. The high order numerical schemes, in general higher than 2nd order, are preferred for this purpose. For numerical simulation of complicated transonic flow fields, it is required that the numerical schemes have the ability of shock capturing and fine-scale feature resolution. Due to the capability of capturing shock waves and high order accuracy in smooth regions, the

WENO (weighted essentially non-oscillatory) schemes are a desirable option for transonic flows with shock waves.

The purpose of this chapter is to compare the accuracy and robustness of RANS, URANS and DDES turbulence models with high order schemes for predicting the lift and drag of a projectile and a DLR-F6 configuration.

5.1 Projectile

5.1.1 Mesh and Boundary Condition

The projectile simulated in this thesis is a cone-cylinder-finned configuration as shown in Fig. 5.1. The length of the projectile model is 12.5in and the diameter is 1.25in. The cone nose is 3.5 in long and the after-body length is 9 in. Four fins are located at the end of the projectile. Each fin has the dimension of 1.25in in long, 1.25in in height and 1in in thickness. The Mach number is 0.752 and Reynolds number is 400000.

The computational mesh for the projectile model is in a O-type shape as shown in Fig. 5.2. Two different domain sizes of computational model are tested for considering the effect of the far-field boundary on the results. One model is 3 times body length away from the model in all the three directions. The other mesh has a bigger domain, which uses a large domain mesh surrounding a smaller mesh domain. The final size of the computational domain is about 40 times of the body length of the projectile in all the directions. To avoid singular point at the tip of the nose, a small tip 'O-type' block is created. Fig. 5.2 shows a 3-D view of the full projectile mesh. The total number of grid points of the small computational domain is about 7 million with 184 blocks. The mesh size of the large

domain is about 14 million with 328 blocks. Fig. 5.3 shows an expanded view of the grid in the small mesh. The first wall grid point spacing is at Y^+ value of about 1.0 for both the meshes. The growth rate of the grids away from the solid wall is 1.25.

The total pressure, total temperature and flow angle are specified at computational domain inlet as the boundary conditions. The static pressure at the outlet is specified to determine the freestream Mach number. In the computation, the free stream flow is kept horizontal. For a flow with an angle of attack(AoA), the mesh is rotated to create the AoA as demonstrated in Fig. 5.3.

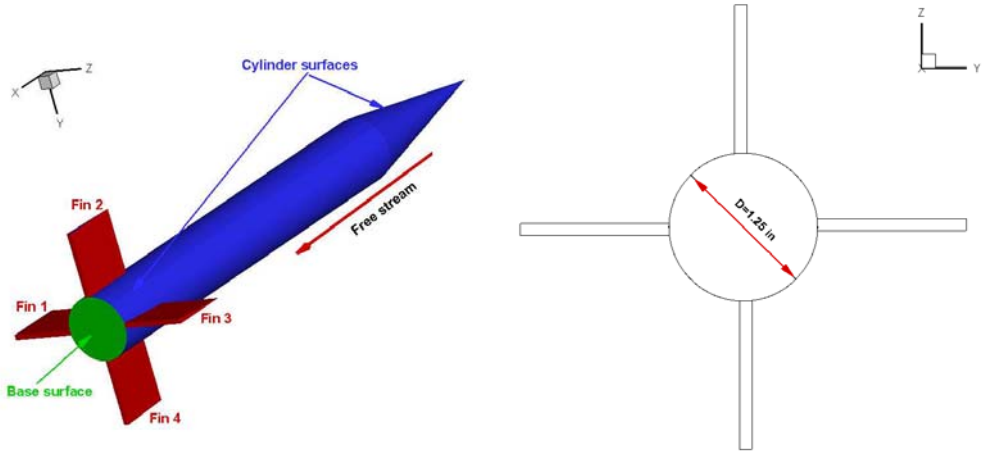

Figure 5.1: Geometry of projectile

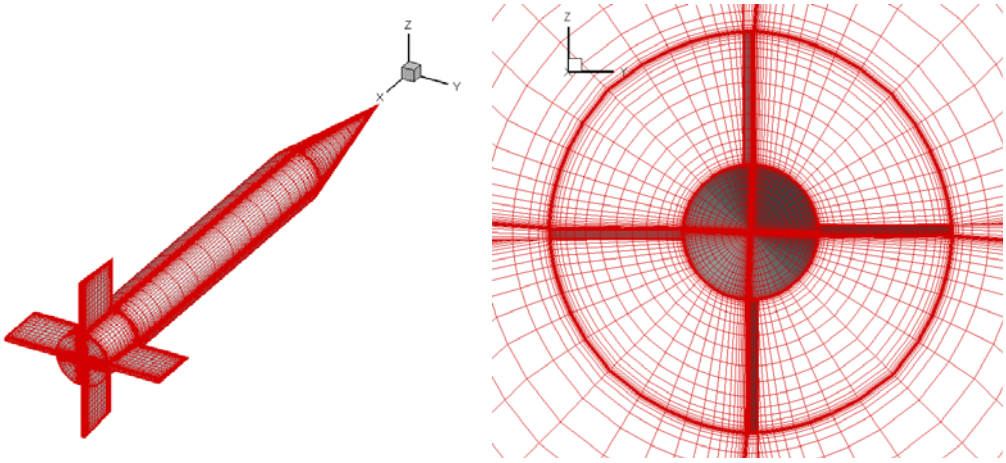

Figure 5.2: Surface mesh of the projectile model

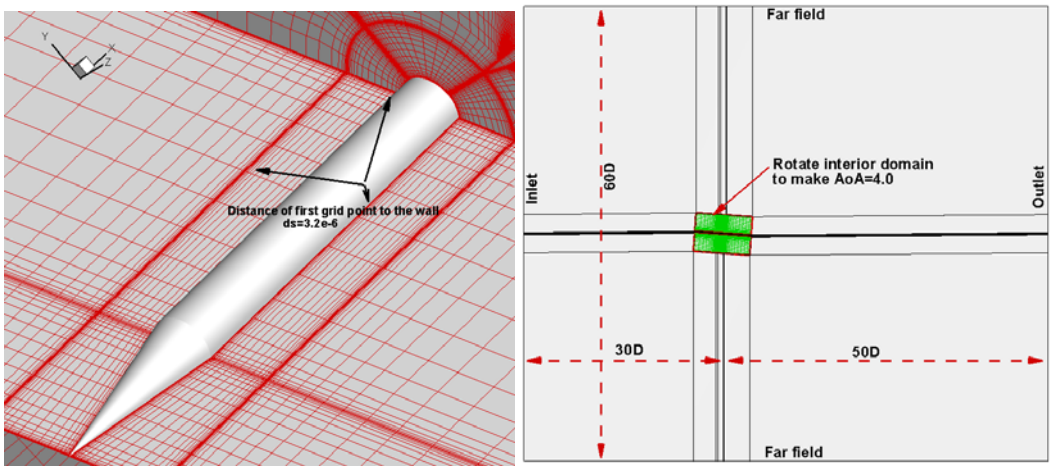

Figure 5.3: Iso view of the mesh

5.1.2 Results Of The Projectile Simulation

The simulations are performed with parallel computing with about 40,000-50,000 cells in each mesh block. The calculations took about 10 hours to converge for steady simulation and 168 hours for the unsteady DDES calculation. The unsteady calculation reaches the stable solution at about 250 characteristic time. The solution residuals are reduced at least 2 orders of magnitude within each physical time step and the aerodynamic coefficients vary less than 0.1% over the last 100 time steps. The aerodynamic force coefficients are the determining factor in convergence.

To accurately predict wall friction, the mesh near the solid surface is refined. However, the quality of the mesh may decrease due to the high aspect ratio as the number of grid points is increased in the boundary layer. To have a suitable mesh density with acceptable CPU time and numerical accuracy, three different grid distributions are tested for grid convergence. The first mesh(Mesh1) is to make sure y^+=1 on every solid wall surface, including the leading edge, the tip surfaces of the fins and solid surface at the leading edge of the nose. The second one(Mesh2) is to keep the same grid distribution as mesh1, ex-

cept neglecting the effect of small walls, including the surfaces at the leading edge and the tips of the fins, and the surface at the leading edge of the nose. Coarse grid distribution are used on those small wall surfaces and wall function boundary conditions are employed for Mesh2. To study the effect of y^+ on the forces calculation, a third computational mesh (Mesh3) with y^+ value equal to 6 is tested. All cases are run at AoA=0° with RANS model. The Mach number using in the grid convergence test is 0.677. The computed axial forces with different meshes are presented in Table 5.1. We can see that the predicted force and moment from Mesh1 and Mesh2 are almost the same and closer to experiment data than that of Mesh3. The computed y^+ of Mesh2 and Mesh3 at wall surface are shown in Fig. 5.4. It can be seen that y^+=1.0 around the cylinder body are achieved in Mesh2. Therefore, Mesh2 is used in the unsteady DDES simulation.

To reduce the uncertainty in the drag prediction, two different ways of wall shear stress calculation are developed. Method 1 is based on the velocity gradient near the wall, in which the tangential velocity and the distance of the first cell center away from the wall are calculated. The other method (Method 2) extracts the shear stress directly from the viscous term of the Navier-Stokes equations. The results are shown in 5.5. It is shown that both results are in excellent agreement.

Table 5.1: Force and Moment at AoA=0°, M=0.677

Item	CA	CN	CM_pitch	CM_roll
Exp	0.521	0.000	0.000	0.331
Mesh1	0.615	0.000	0.000	0.334
Mesh2	0.618	0.000	0.000	0.334
Mesh3	0.632	0.000	0.000	0.347

The time history of CA, CN, CM_pitching and CM_roll at AoA=0° and M=0.752 are shown in Fig. 5.6. The results of DDES method are compared with those of URANS.

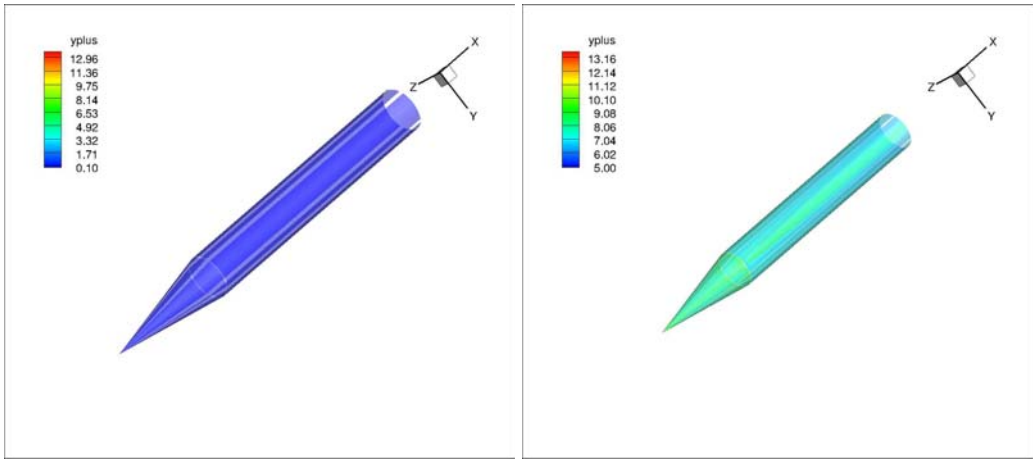

Figure 5.4: Boundary layer resolving mesh comparison. Left: mesh2, Right: mesh3

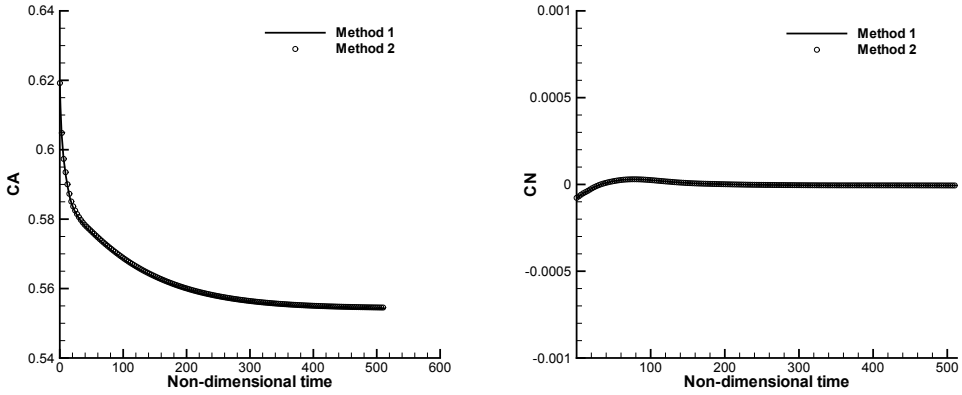

Figure 5.5: Force results of different calculation methods

Both simulations are started from the same RANS results. The predicted drag of DDES agree better with the experiment than the URANS. The difference of the drag prediction by DDES and URANS in the subsonic regime indicates that the unsteady wake flow impacts the upstream side forces. The roll moment from the URANS follows the same trends as that of DDES.

The DDES force and moment convergence history of CA, CN, CM_pitching and CM_roll at AoA=4° and M=0.752 are shown in Fig. 5.7 and Fig. 5.8. The URANS is used for the first 2000 time steps and the calculation is switched to DDES. Fig. 5.8 shows that there are

discontinuities in the convergence histories when the calculation is switched from URANS to DDES.

The results of RANS, URANS and DDES at AoA=0° and M=0.752 are summarized in Table 5.2. From the table, DDES significantly reduce the axial force prediction error to about 4.5%, URANS has an error of 12.3%, and RANS has an error of 16.6%. DDES is demonstrated to have the best accuracy among the three methods. The URANS gives more accurate results than the steady state RANS because the vortex vortex shedding in the wake region is unsteady. All three methods have excellent agreement in predicting the rolling moment. The predicted normal force and pitching moment are close to zero at AoA=0° as the experiment since the geometry is mostly axi-symmetric except the fins that generate circumferential force.

The comparisons of different methods at AoA=4° and M=0.752 are shown in Table 5.3. The axial force predicted by DDES has an error of 3.9% compared with the experiment, significantly more accurate than that predicted by URANS with an error of 12%. For the nomal forces, the URANS and DDES have the deviation about 10.0% and 8.7% respectively. The DDES is again more accurate than the URANS even though the deviation is greater than the axial force.

Table 5.2: Force and Moment at AoA=0° and M=0.752

Item	CA	error	CN	error	CM_pitch	error	CM_roll	error
Exp	0.530		0.0		0.0		0.333	
RANS	0.618	16.6%	0.0	0.0	0.0	0.0	0.336	1.0%
URANS	0.595	12.3%	0.0	0.0	0.0	0.0	0.336	1.0%
DDES	0.554	4.5%	0.0	0.0	0.0	0.0	0.334	0.3%

Table 5.4 and Table 5.5 present the the breakdowns of the normal and axial forces of each component including the projectile main body, the base surface, and the fins. In

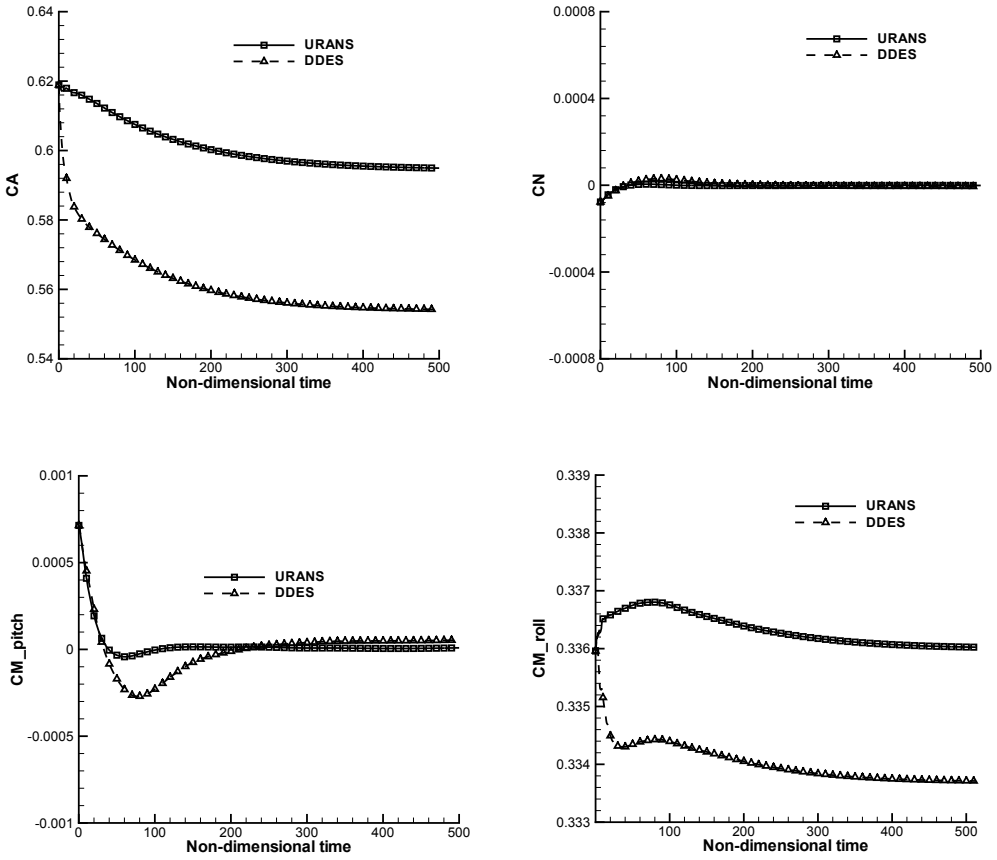

Figure 5.6: Coefficient of axial force(CA), normal force(CN), pitching moment(CM_pitch) and rolling moment(CM_roll) at AoA=0° and M=0.752, predicted by URANS and DDES

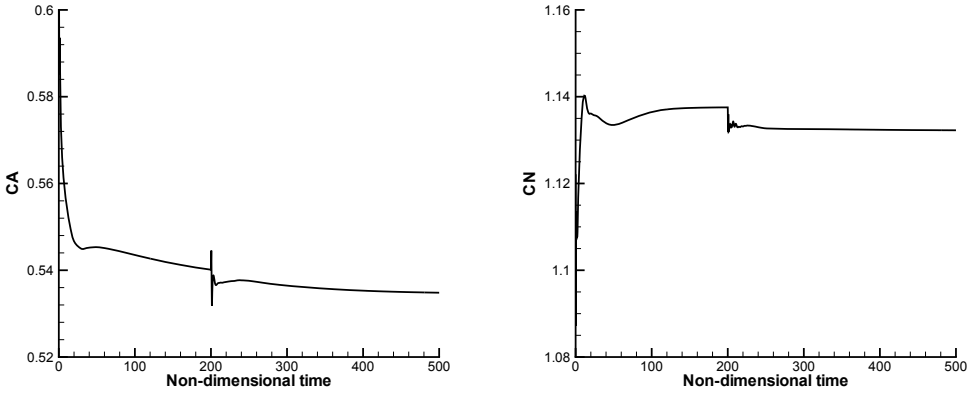

Figure 5.7: Force coefficient at AoA=4° and M=0.752 with DDES

the table, C_{Lp} is the lift contributed by pressure, C_{Lv} is the lift contributed by viscous shear stress lift, C_{Dp} is the drag contributed by pressure and C_{Dv} is the drag contributed by

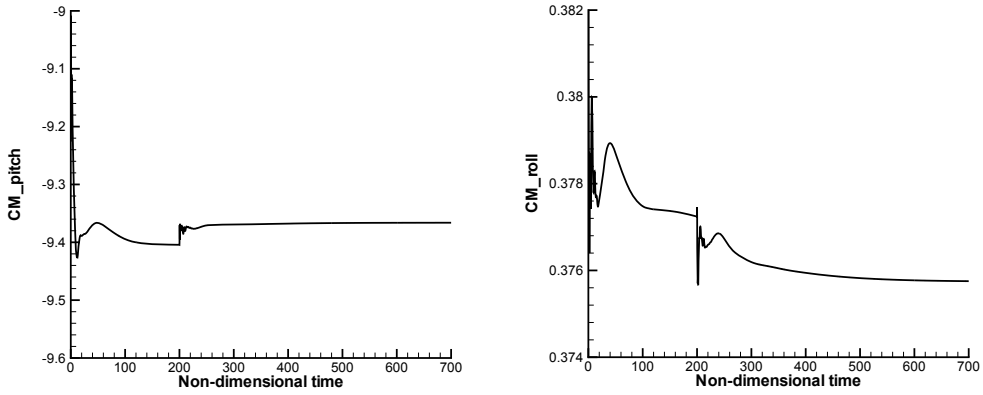

Figure 5.8: Moment coefficient at AoA=4° and M=0.752 with DDES

Table 5.3: Force and Moment at AoA=4.0° and M=0.752

Item	CA	error	CN	error	CM_pitch	error	CM_roll	error
Exp	0.516		1.040		-8.48		0.362	
RANS	0.635	23.1%	1.122	7.3%	-9.226	8.8%	0.384	6.1%
URANS	0.578	12.0%	1.144	10.0%	-9.464	11.6%	0.378	4.4%
DDES	0.535	3.9%	1.132	8.7%	-9.366	10.5%	0.376	3.9%

the viscous shear stresses. The predicted friction drags are almost the same between the URANS and DDES for both the case of at AoA=0° or AoA=4°. The reason is that within the wall boundary layer, URANS is also used by DDES. For the predicted pressure drag, URANS and DDES are quite different. At AoA=0°, C_{Dp} predicted by URANS is about 10% greater than that of DDES. At AoA=4°, it is about 9.5% larger. The pressure value at the base redicted by DDES is about 4% greater than that of URANS, which results in a smaller overall drag since the predicted drag of the main body are about the same. Drag contribution of the fin is about 36% of the total drag at AoA=0° and is increased to 41% at AoA=4°. The pressure drag predicted by DDES is smaller than that of URANS.

Fig. 5.9 shows the Mach contours obtained by URANS and DDES at AoA=0° and M=0.752 at the mid-plane. Both plots show similar flow structures over the projectile. The vortex shedding at the trailing edge of the projectile is captured as shown in Fig. 5.10. The

flow field at AoA=4° has similar flow structure as the case at AoA=0°. Fig. 5.11 shows the velocity vector field behind the fins. It shows the fin tip vortices due to the lift that creates the the roll moment and cause the body to spin with Magus effect. Fig.5.12 illustrates instantaneous entropy contours, which indicates that the wake region suffers high loss due to the base flow. Fig 5.13 is the Mach number contour in the wake region for both the AoA=0° and 4°. The wakes of the fins merge with the wake of the base surface.

Fig.5.14 shows the instantaneous static pressure contour predicted by DDES at M=0.752. The base area has very low pressure that contributes to the base drag. Fig. 5.15 shows the surface pressure contours and the surface pressure distributions of the mid plane on the lower and upper side. At AoA=0°, the pressure is symmetric with no lift. The pressure decreases rapidly from leading edge to the cone-cylinder transition point due to the converging area, and then increase rapidly after that due to fast area expansion. At AoA= 4°, the pressure variation trend along the body is similar to that at AoA= 0°, but the pressures on the upper and lower side is largely different due to generating the lift. The fin surface pressure coefficients predicted by DDES at AoA=0° and 4° are shown in Fig.5.16 and Fig.5.17, respectively. At AoA=0°, the fins do not generate lift and the pressure distributions on the 4 fins are the same. At AoA=4°, the fin surface pressure are not symmetric due to the lift generation.

Table 5.4: Force contributions of different parts at AoA=0° and M=0.752

Item	Method	C_{Lp}	C_{Lv}	C_{Dp}	C_{Dv}
Cylinder	URANS	0.000	0.000	2.558	0.100
	DDES	0.000	0.000	2.558	0.100
Base	URANS	0.000	0.000	-2.268	0.000
	DDES	0.000	0.000	-2.303	0.000
Fins	URANS	0.000	0.000	0.150	0.056
	DDES	0.000	0.000	0.145	0.055

Table 5.5: Force contributions of different parts at AoA=4° and M=0.752

Item	Method	C_{Lp}	C_{Lv}	C_{Dp}	C_{Dv}
Cylinder	URANS	0.061	0.001	2.563	0.101
	DDES	0.058	0.001	2.562	0.101
Base	URANS	0.158	0.000	-2.264	0.000
	DDES	0.161	0.000	-2.300	0.000
Fins	URANS	0.884	-0.004	0.204	0.052
	DDES	0.876	-0.004	0.198	0.052

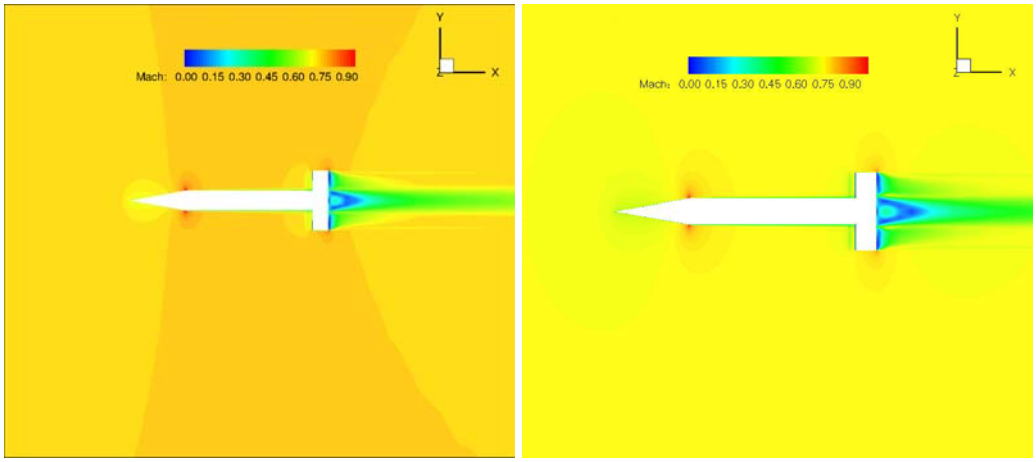

Figure 5.9: Instantaneous Mach number contour at AoA=0° and M=0.752, left for URANS, right for DDES

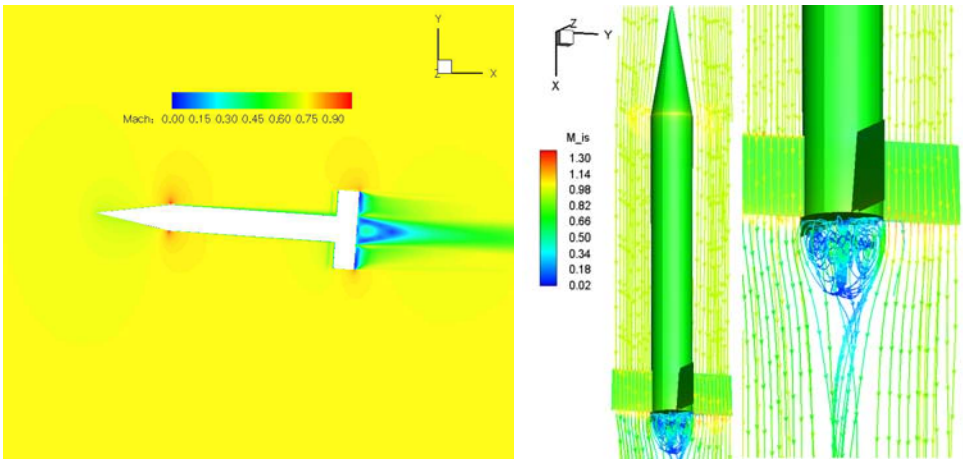

Figure 5.10: Flow field around the body and near the tail at AoA=4° and M=0.752, left for mach contour, right for streamline

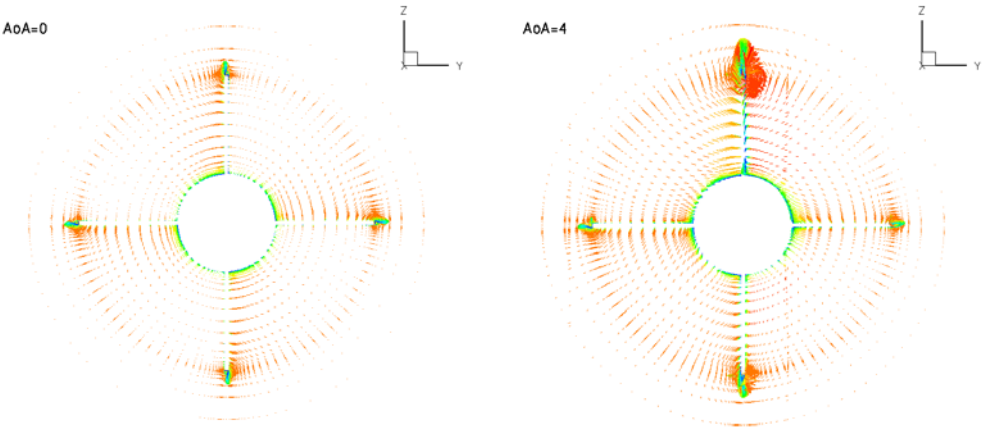

Figure 5.11: Vortex structure around the fin

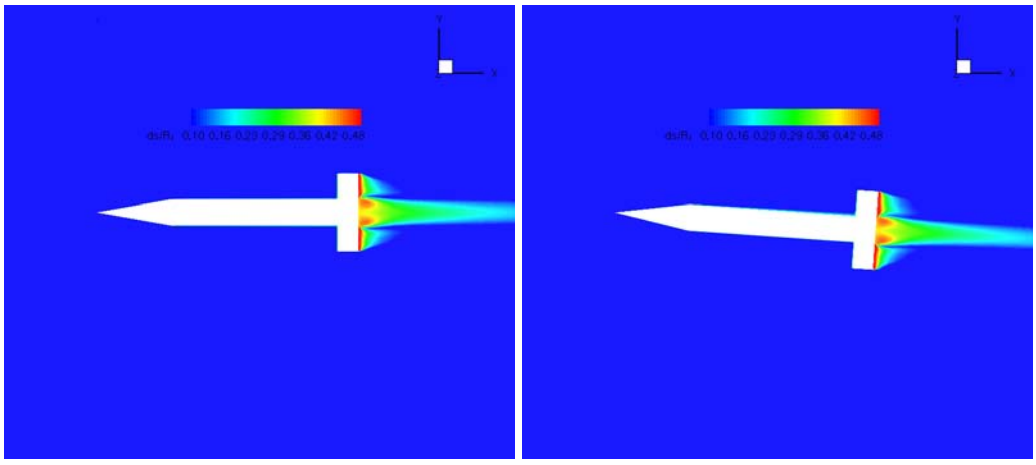

Figure 5.12: Entropy contour: left for AoA=0°, right for AoA=4°

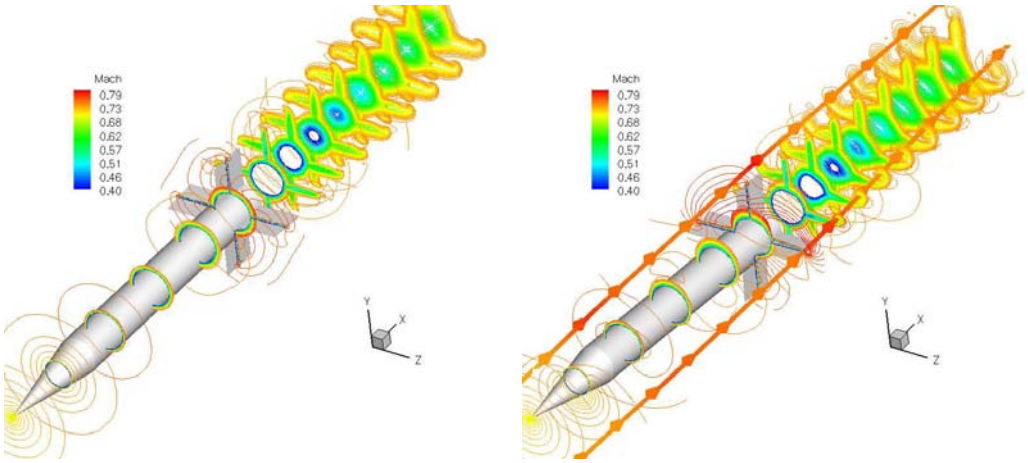

Figure 5.13: Mach line contours: left for AoA=0°, right for AoA=4°

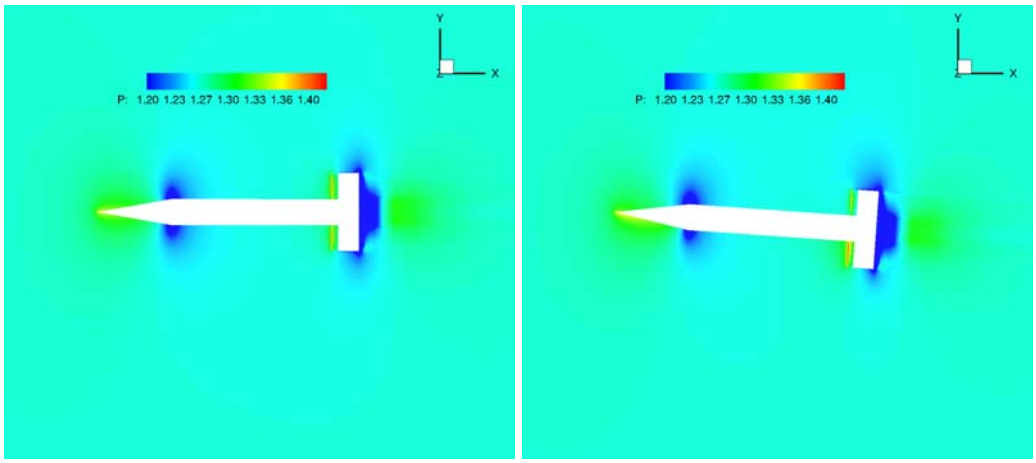

Figure 5.14: Static pressure contour: left for AoA=0°, right for AoA=4°

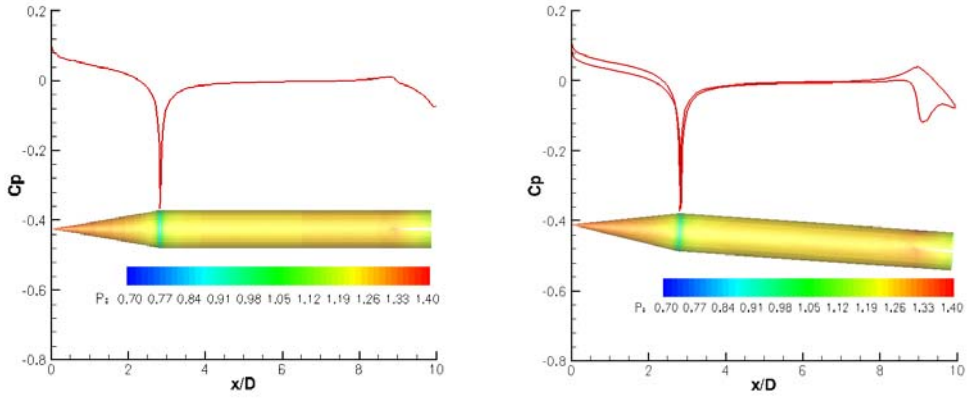

Figure 5.15: Computed Surface Pressure: left for AoA=0°, right for AoA=4°

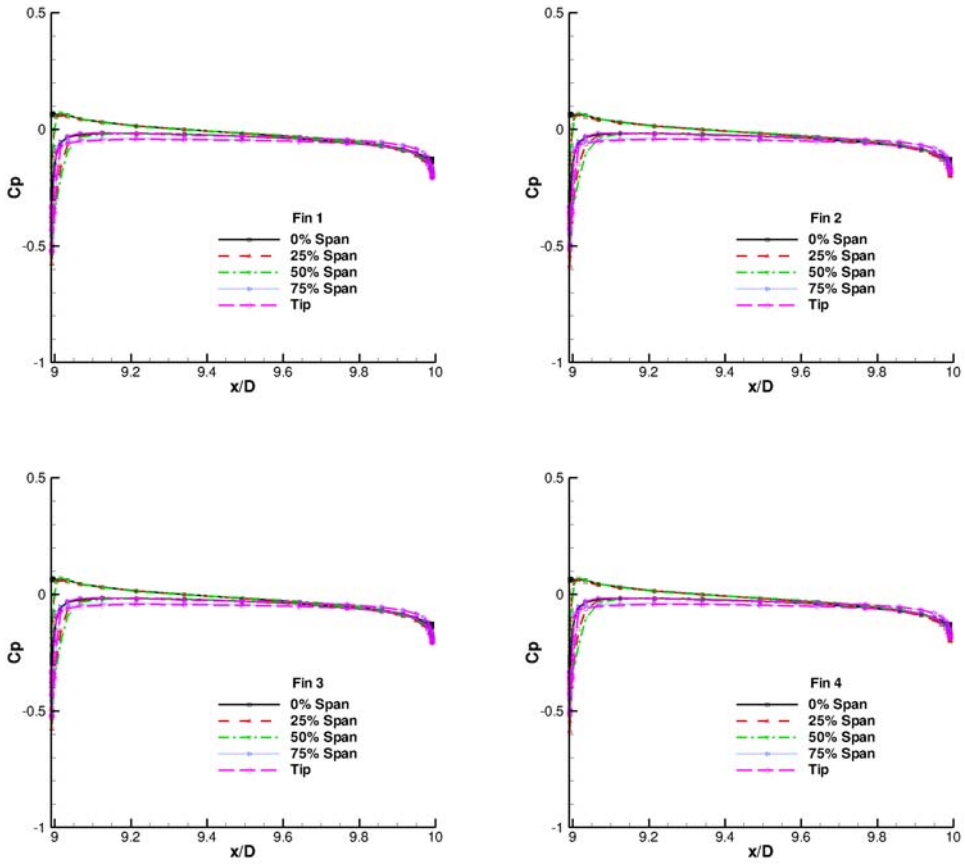

Figure 5.16: Computed pressure coefficient for AoA=0°

5.2 Wing body configuration

5.2.1 Results and Discussion

In this section, the DLR-F6 wing-body configuration as shown in Fig. 5.18, used by the second AIAA Drag Prediction Workshop is calculated. The Mach number is 0.75, Reynolds number based on the mean aerodynamic chord is 3.0×10^6. The total pressure and total temperature are given at computational domain inlet as the boundary conditions. The static pressure at the outlet of computational domain is to make the inlet Mach number matching the experimental value. In the far field, zero gradient boundary condition is used. The unsteady DDES calculation reaches the stable solution at about 250 characteristic time. The solution residuals are reduced at least 2 orders of magnitude within each physical time step and the aerodynamic coefficients vary less than 0.1% over the last 100 time steps. The aerodynamic coefficients were the determining factor in convergence in all cases.

5.2.2 Grid Convergence Study

The community of the drag prediction workshop had provided a series of grids that include 1-to-1 connected multiblock grid, structural overlap grid, and unstructured grid. The 1-to-1 point matched grid from ICEM is used as a baseline mesh for computation in this section. Because the mesh topologies near the wing tip from ICEM software are very complex and the mesh size of each block is varied distinctly, computational grids are regenerated to have simpler mesh-topologies and better load balance for parallel computation. The overall topology of the new mesh employs a O-type topology as shown in Fig. 5.19. The computational domain models only half of the configuration and symmetry boundary conditions

are applied to the symmetrical plane. In the new mesh, the first layer of blocks used for the viscous boundary layer computation, is kept the same as the supplied mesh. The mesh topologies at the nose, wing tip and tail of the fuselage are changed to the O-type topology, as shown in Fig. 5.20. The length of the first grid cell in surface normal direction is 0.001 mm. This value was found to be sufficient to guarantee a value of y^+=1. In order to conduct a grid convergence study, three levels of mesh sizes have been generated. The coarse mesh model has a total of 2184140 grid cells, in which the number of grid points in the boundary layer is 29. The medium mesh has a total of 6364462 grid cells with 41 points in the boundary layer blocks. And there are 49 grid points in first layer of blocks of in the third level of mesh, resulting a total number of 8410092 grid cells.

All the grid models were run with DDES method at AoA=0.49°. The computed results are shown in Table. 5.6. For comparison, the experimental data is also listed in the same table. In the table, C_L is lift coefficient and C_D is drag coefficient. The C_L comparison between DDES and experiment is given by relative errors. And the C_D comparison is given by relative drag counts, in which 1 count is 0.0001. It can be seen that there is a linear variation in C_L with the mesh refinement, which indicates that the three cases achieve grid convergence for DDES method. However, the grid convergence test of DDES is not achieved in C_D prediction. The C_D from medium mesh shows about 28 drag counts(0.0028) deviated from experiment and has the maximum relative error of 9.559%. Whereas the coarse level grid has the lowest relative errors of 3.347% with about 10 drag counts. Compared with the coarse and medium mesh model, the fine mesh model provides the lowest relative error in C_L prediction and about 15 drag counts in C_D prediction.

The convergence histories of C_L and C_D are shown in Fig. 5.21 and Fig. 5.22 re-

Table 5.6: Lift, drag coefficients from DDES at AoA=0.49

Item	C_L	error, %	C_D	ΔC_D
Exp	0.498400	0.000	0.029396	0
Coarse	0.479830	3.726	0.030380	10
Medium	0.482161	3.258	0.032206	28
Fine	0.485735	2.541	0.030941	15

spectively. Results of the three different mesh size are plot. It is seen that the calculation converged after about 100 non-dimensional time. The C_L curve predicted by the DDES method is about the same as URANS. And the C_D value predicted by DDES tend to lower than that of URANS.

Fig. 5.23 to Fig. 5.30 are time averaged the coefficient of pressure at different wing sections at AoA=0.49°. Each figure shows the DDES results of the coarse, medium and fine grid models. Overall, the numerical results predicted by using DDES agree very well with the experiments, including the shock wave strength and location along the span. All mesh models show large errors at 0.15 span, where there is a separation at wing-body conjunction. This predicted separation location is consistent with the conclusion of the second drag prediction workshop, which concluded that it was the separated flow regions at wing/body junctures cause large error of predicted results and make it difficult to draw meaningful conclusions. It appears that the separation bubble still affect the present results of DDES. Compared to the coarse mesh model, the medium and fine mesh model provide slightly better Cp results at lower span in the 50% chordwise location. The shock location is well resolved in Fig. 5.25 and Fig. 5.26, in particular with the medium and fine mesh. Shock location moves more upstream in the mid-span.

Table. 5.7 lists the two components of total force coefficients, the pressure force coefficient and the friction force coefficient, predicted by using DDES on the sequence of grids.

In the table, px, py and pz are the force coefficients contributed by pressure in x, y, and z direction respectively. And vx, vy, vz are the force coefficients contributed by the viscous shear stresses in x, y, and z direction respectively. The force in x direction contributes to the drag. The force in z direction is lift. The force in y direction is the lateral force, which should be zero approximately when the whole configuration is considered. The forces are integrated at time step of 6000, which is different from the time averaged results in Table. 5.6. The breakdown of the force may help to identify the main source of the errors in lift and drag prediction. It can be seen that the general trends of pressure and viscous drag data are consistent with the total drag in mesh refinement study. The pressure drag is converged based on mesh size. It is the friction drag still varies with the mesh size. The table also shows that the viscous drag contribution is about 82% of the pressure drag, a little smaller but in the same order of magnitude. This also indicates that there is a large room to reduce the total drag by reducing the pressure drag. While the viscous lift contribution to the total lift is negligible compared with the lift generated by pressure.

Table 5.7: Force components of different mesh at AoA=0.49°

Item	px	py	pz	vx	vy	vz
Coarse	0.016301	4.769143	0.479410	0.014063	-0.000113	-0.000139
Medium	0.017135	4.767384	0.478435	0.015037	-0.000008	-0.000077
Fine	0.017158	4.766717	0.481208	0.013719	-0.000072	-0.000108

The surface pressure contours and streamlines of three level of mesh sizes are shown in Fig. 5.31. The plots compares the wing/body juncture flow at upper-surface wing trailing edge at AoA=0.49° by using DDES method. The separation bubbles are clearly seen in all three mesh simulations and the predicted separation bubbles are about the same. But the fine mesh resolves more detailed flow structures.

5.2.3 Effect of Turbulence Modeling

Although this thesis focus on DDES method for aerodynamic drag prediction, it is useful to compare the results with the commonly used steady RANS model and unsteady RANS(URANS) model. Both RANS and URANS employ the one-equation Spalart-Allmaras (SA) model. Table. 5.8 and Table. 5.9 summarized the results of RANS and URANS at AoA=0.49° respectively. The predicted C_L results of both RANS and URANS show good agreement with experiment. The maximum relative errors are less than 3% in all test cases. Still, the coarse mesh provide better results than medium and fine mesh. It is noted that drag counts predicted by DDES shown in Table. 5.6 are less than the drag counts of both RANS and URANS, in particular for the coarse and medium mesh.

Table 5.8: Lift, drag coefficients from RANS at AoA=0.49°

Item	C_L	errors, %	C_D	ΔC_D
Exp	0.498400	0.000	0.029396	0
Coarse	0.489087	1.869	0.030937	15
Medium	0.484887	2.711	0.032552	32
Fine	0.486100	2.468	0.030993	16

Table 5.9: Lift, drag coefficients from URANS at AoA=0.49°

Item	C_L	errors, %	C_D	ΔC_D
Exp	0.498400	0.000	0.029396	0
Coarse	0.488338	2.019	0.030830	14
Medium	0.482526	3.185	0.032527	31
Fine	0.485611	2.566	0.031167	18

Table. 5.10 lists the total drag coefficients as well its two components, the pressure drag coefficient and the friction drag coefficient for fine mesh model, for all the three different turbulence modeling methods. The predicted friction drag counts among the three turbulence models are less than one count for the case at AoA=0.49°. The reason appears to be that they all employ the same turbulence modes within the wall boundary layer. For the

predicted pressure drag that is more affected by the flow structures outside of the boundary layer, DDES provides about 2 drag counts less than RANS and URANS. The RANS methods has almost the same px value as that of the URANS method, which indicates that unsteady flow effect is not important for the wing body configuration model.

Table 5.10: Force components of different turbulence modeling method at AoA=0.49°

Item	px	py	pz	vx	vy	vz
RANS	0.017395	4.766450	0.492607	0.013808	-0.000085	-0.000169
URANS	0.017394	4.766713	0.482234	0.013736	-0.000091	-0.000131
DDES	0.017158	4.766717	0.481208	0.013719	-0.000072	-0.000108

The MUSCL and WENO schemes are implemented in current codes for comparison. The comparisons of different reconstruction schemes are listed in Table. 5.11. MUSCL3 has 3rd order accuracy for the inviscid flux without using any limiters. WENO3 and WENO5 are the 3rd and 5th order of WENO schemes respectively. The results are from steady state RANS simulation at AoA=0.49°. It can be seen from the table that the prediction by using the WENO5 scheme has larger errors in C_L than that with the 3rd order schemes. And the WENO5 scheme predicts about 2 drag counts lower than those 3rd order schemes and is closer to the experiment.

Table 5.11: Lift, drag coefficient comparisons at AoA=0.49° by using RANS method

Item	C_L	errors, %	C_D	ΔC_D
Exp	0.498400	0.000	0.029396	0
MUSCL3	0.492437	1.196	0.031203	18
WENO3	0.491657	1.353	0.031180	18
WENO5	0.486100	2.468	0.030993	16

Fig. 5.32 are the coefficient of pressure at three typical wing spans at AoA=0.49°. At 0.15 span, all the turbulence modeling methods captured the separation bubble. The DDES gives the best prediction at the tailing edge separation region, which indicates the advantage

as it is designed to have. The pressure predicted by the three methods are almost the same at outer span where there is no flow separation.

Fig. 5.33 shows the lift and the drag versus different angle of attacks. The C_L predicted by all the methods agree very well with the experiment. The C_L errors of URANS and DDES method become larger at higher positive angle of attack. Regarding the C_D curve, numerical results match the experiment at positive angle of attack and show large errors at negative AoA with the maximum error less than 25 counts. The DDES model again shows a better agreement between the predicted and measured drag than RANS and URANS model at low AoA about 15 counts.

5.3 Conclusions

This chapter compares the accuracy and robustness of DDES, RANS, and URANS turbulence modeling using high order schemes for predicting the lift and drag of the projectile and DLR-F6 configuration. The implicit time marching method with unfactored Gauss-Seidel line relaxation is used with a 5th order WENO finite difference scheme for Navier-Stokes equations The viscous terms are discretized using a 4th order conservative central differencing. The effect of grid density, spatial difference schemes and turbulence modeling methods are studied.

For a projectile at M=0.752, AoA=0° and 4°, the DDES significantly reduces the axial force prediction error to about 4%, whereas the URANS has an error of 12%, and the RANS has an error of 16% to 23%. The primary difference of the drag prediction between the DDES and URANS is the pressure drag prediction in the base region. The DDES is

demonstrated to be superior to the URANS for the projectile flow prediction due to more accurate base large vortex structures and pressure simulation.

In the simulation of wing body configuration, grid convergence in the prediction of lift coefficients is achieved by using DDES method, but the C_D still has variation of over 10 counts. The C_D from medium mesh shows about 28 drag counts(0.0028) deviated from experiment and has the maximum relative error of 9.559%. Compared to the coarse and medium mesh, the fine mesh model provides the lowest error in C_L prediction and about 15 drag counts in C_D prediction. All meshes show large surface pressure deviation at 0.15 span, which is located at separation region of the wing-body conjunction.

The predicted C_L results of both RANS and URANS show good agreement with experiment. The maximum errors are less than 3% in all test cases. The coarse mesh provide better results than medium and fine mesh. The drag counts predicted by the DDES are less than the drag counts of both RANS and URANS, which indicates the advantage of DDES in turbulence modeling.

The predicted friction drag counts difference between the URANS and DDES is less than one count for the case at AoA=0.49°. The reason may be that DDES method employ the same turbulence modes as URANS within the wall boundary layer. For the predicted pressure drag, DDES provides about 2 drag counts less than RANS and URANS. The prediction by using the 5th WENO scheme provides lower C_L and drag counts than the 3rd order schemes.

Since the same mesh provided by the workshop are used for the RANS model and DDES model, even though the mesh is generated for RANS models only. In other words, the DDES conducted in this thesis should be treated as a rough reference instead of being

conclusive. A more rigorous mesh refinement study for DDES drag prediction will be conducted as the next step.

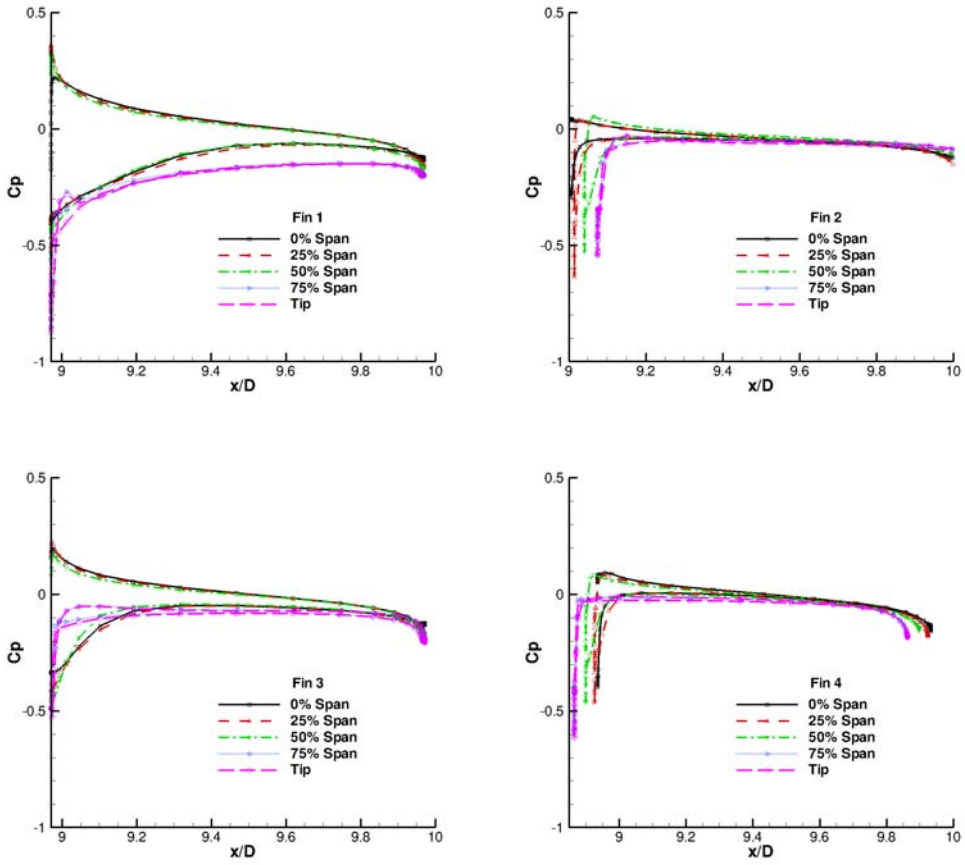

Figure 5.17: Computed pressure coefficient for AoA=4°

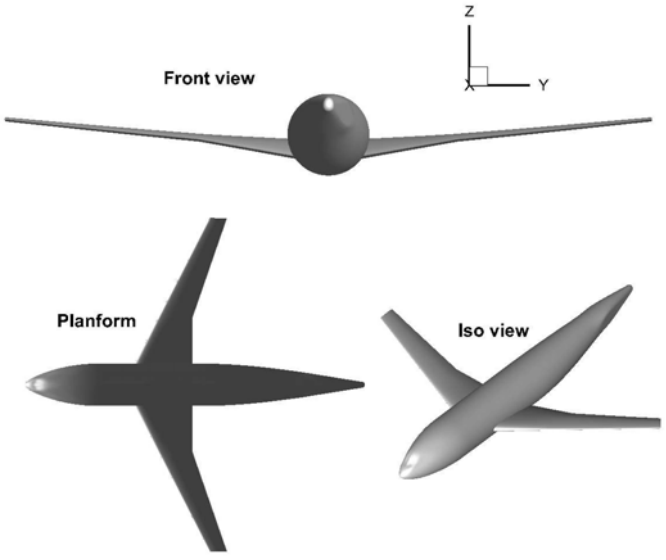

Figure 5.18: Geometry of wing-body configuration

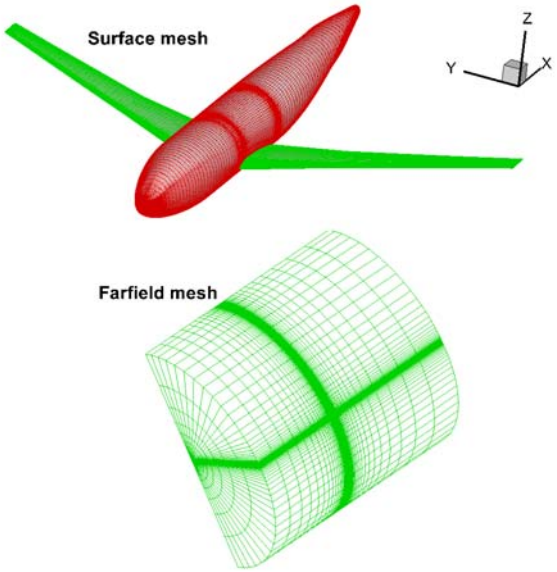

Figure 5.19: Meshes on wall and far field

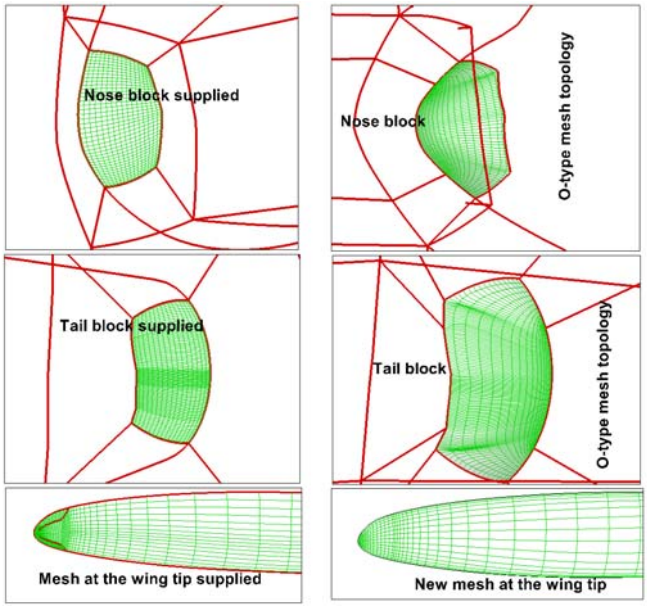

Figure 5.20: Mesh topology comparison

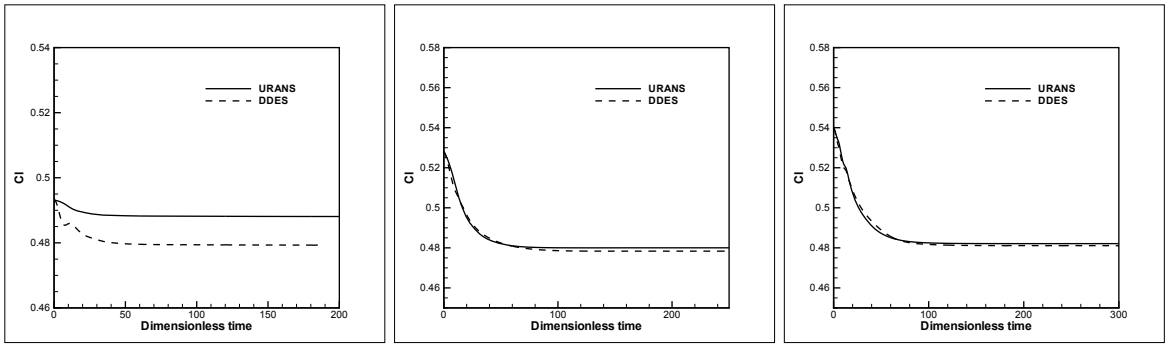

Figure 5.21: Time history of lift coefficient. Left: Coarse mesh; Middle: Medium mesh; Right: Fine mesh

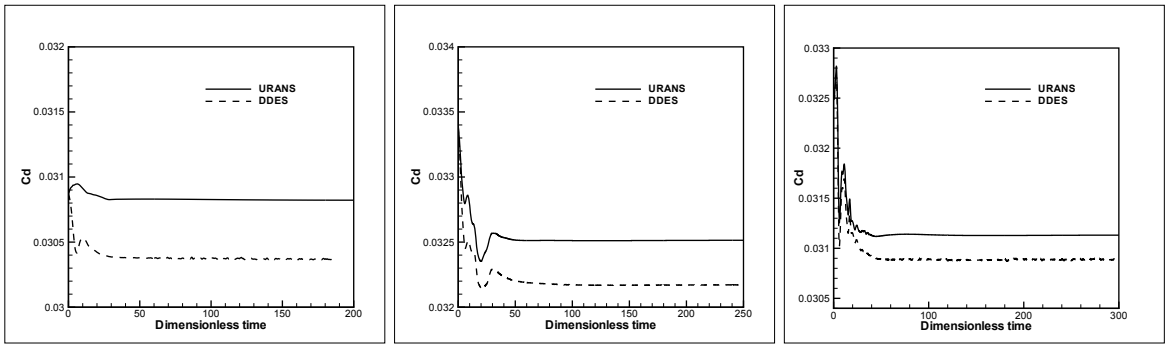

Figure 5.22: Time history of drag coefficient. Left: Coarse mesh; Middle: Medium mesh; Right: Fine mesh

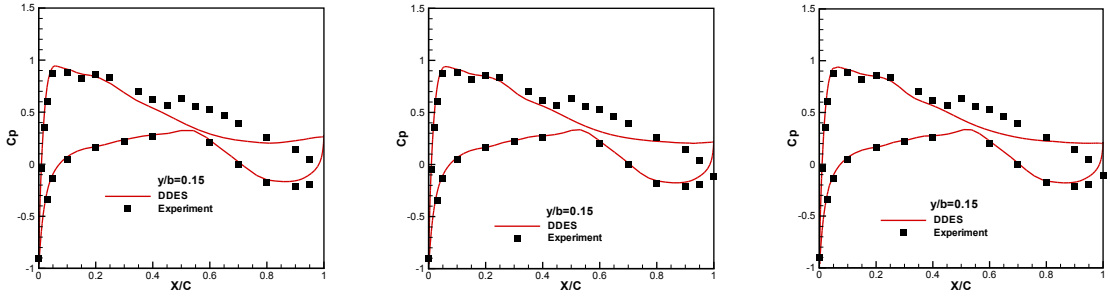

Figure 5.23: Wing pressure coefficient comparison using DDES at 0.15 semispan. Left: Coarse mesh; Middle: Medium mesh; Right: Fine mesh

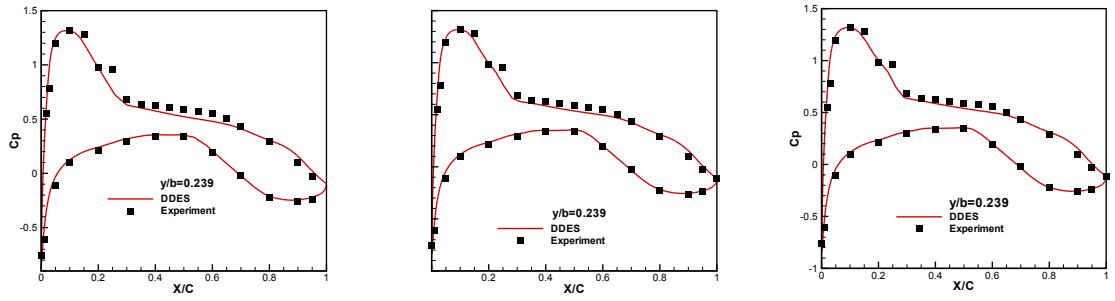

Figure 5.24: Wing pressure coefficient comparison using DDES at 0.239 semispan. Left: Coarse mesh; Middle: Medium mesh; Right: Fine mesh

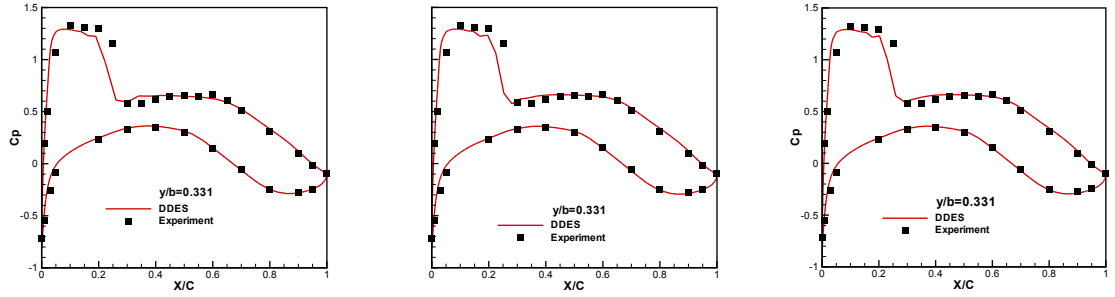

Figure 5.25: Wing pressure coefficient comparison using DDES at 0.331 semispan. Left: Coarse mesh; Middle: Medium mesh; Right: Fine mesh

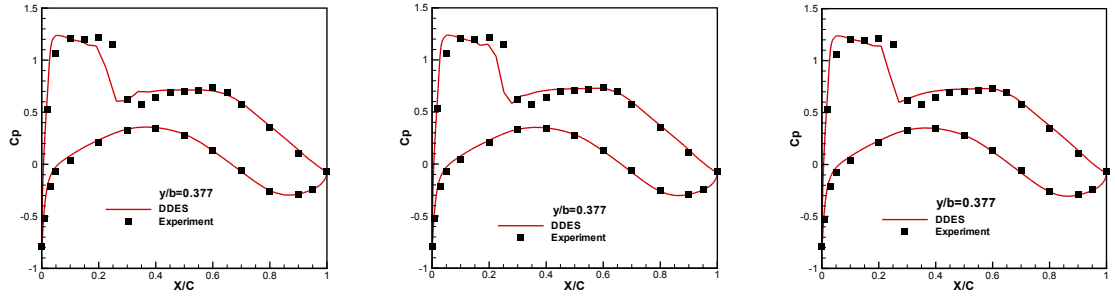

Figure 5.26: Wing pressure coefficient comparison using DDES at 0.377 semispan. Left: Coarse mesh; Middle: Medium mesh; Right: Fine mesh

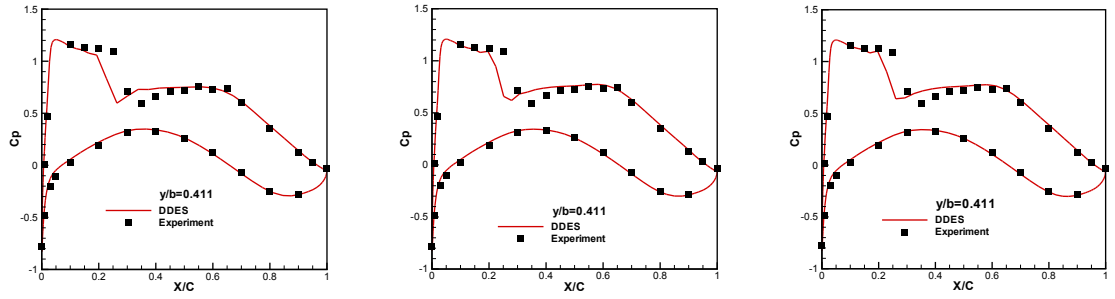

Figure 5.27: Wing pressure coefficient comparison using DDES at 0.411 semispan. Left: Coarse mesh; Middle: Medium mesh; Right: Fine mesh

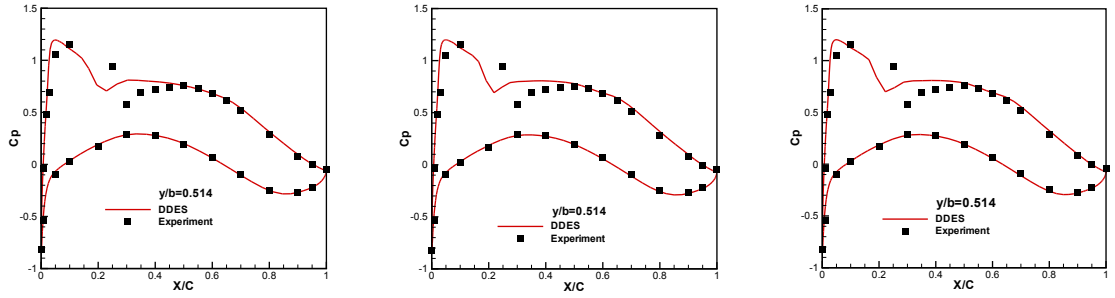

Figure 5.28: Wing pressure coefficient comparison using DDES at 0.514 semispan. Left: Coarse mesh; Middle: Medium mesh; Right: Fine mesh

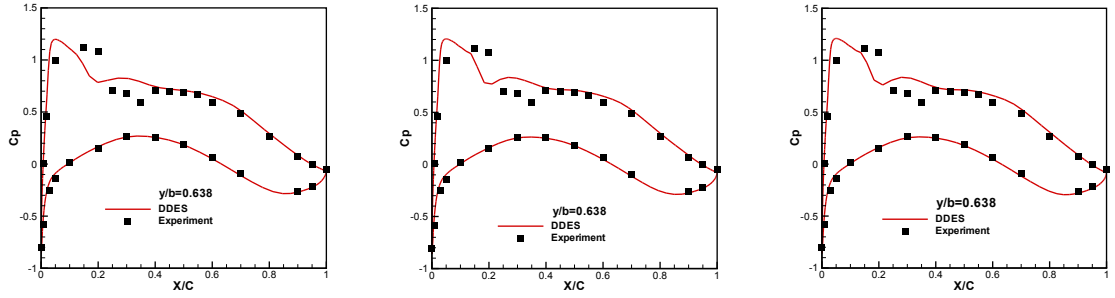

Figure 5.29: Wing pressure coefficient comparison using DDES at 0.638 semispan. Left: Coarse mesh; Middle: Medium mesh; Right: Fine mesh

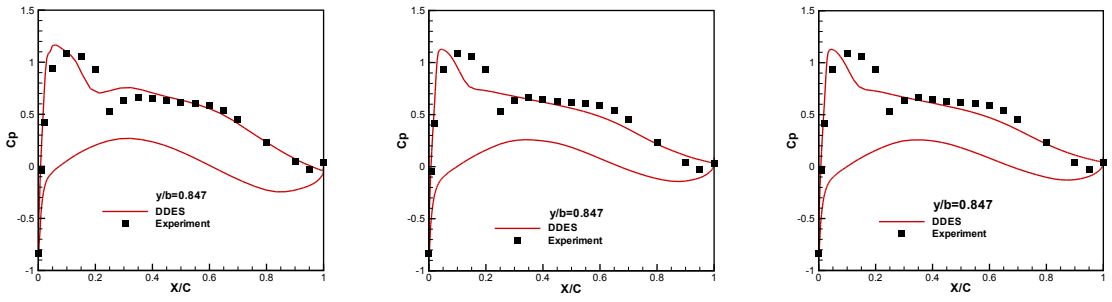

Figure 5.30: Wing pressure coefficient comparison using DDES at 0.847 semispan. Left: Coarse mesh; Middle: Medium mesh; Right: Fine mesh

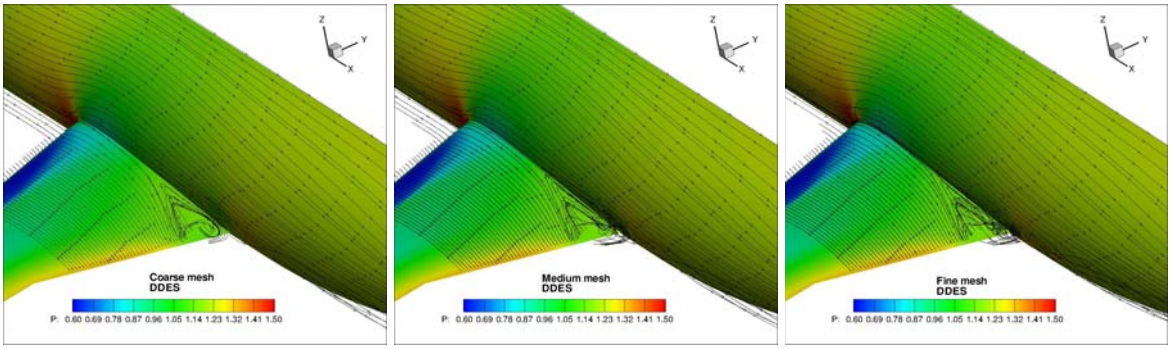

Figure 5.31: Surface pressure and streamline comparisons of different mesh sizes

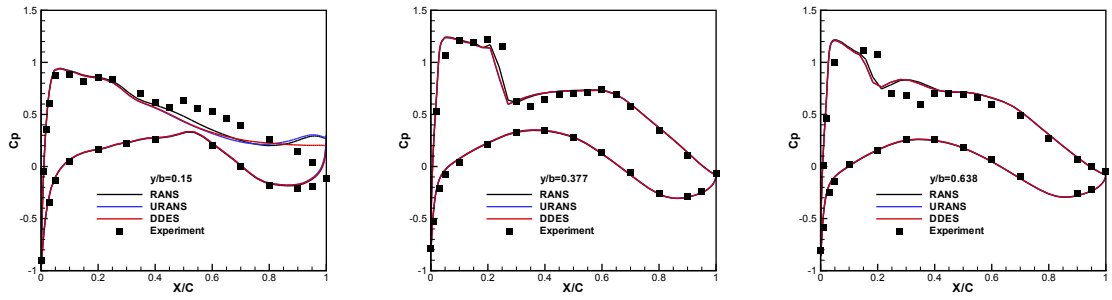

Figure 5.32: Pressure coefficient comparison at different wing span for AoA=0.49°, showing the effect of turbulence modeling

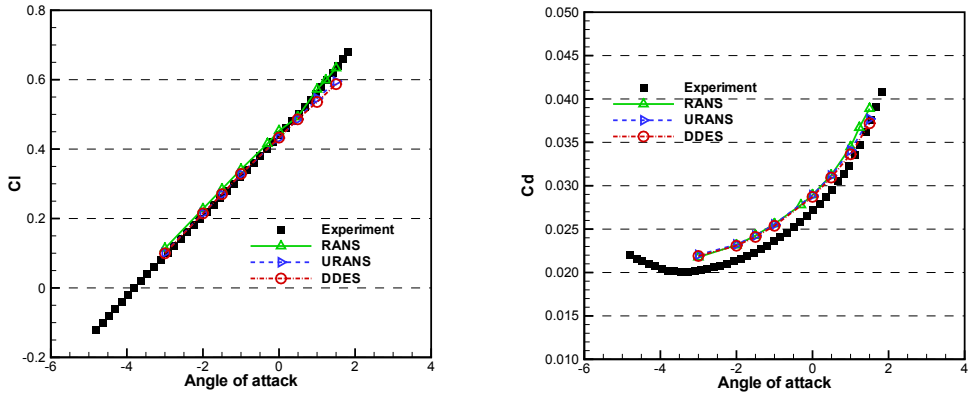

Figure 5.33: Lift curve (Left) and Drag curve (Right) of DLR-F6, showing the effect of turbulence modeling

Chapter 6

Transonic Wing Flutter

The purpose of this chapter is to calculate the full AGARD wing flutter boundary to investigate the flutter mechanism using high order schemes and DDES with a fully coupled FSI. In particular, the focus is to understand the sonic dip phenomenon in the transonic regime. The work appears to be the first effort using DDES with high order shock capturing schemes to simulate transonic wing flutter. Benefiting from this high fidelity transonic flutter wing simulation, some new observations and explanation are given for the sonic dip mechanism, including the anticlimax of torsional mode and decrease of pitching moment at sonic dip due to shock oscillation.

6.1 Computational Model

6.1.1 Geometry of AGARD Wing 445.6

A limited number of AGARD standard wing configurations were tested [2] in order to promote the evaluation of existing and emerging unsteady aerodynamics codes and meth-

Table 6.1: AGARD Wing 44.5 Weakend model 3 [2]

Airfoil section	NACA 65A004
Measured panel mass($\bar{m}$) [kg]	1.8627
Panel span(H) [m]	0.762
Sweep angle at half chord [deg]	43.15
Root chord(b_s) [m]	0.559
Tip chord(b_t) [m]	0.3682
Aspect ratio	1.65

ods for flutter from subsonic to supersonic regime. In this study, the AGARD Wing 445.6 Weakend 3 is used for flutter simulation. This wing model has the symmetric NACA65A004 airfoil with a 4% thickness, and the wing structural details are listed in Table 6.1.

6.1.2 Mesh

The O-mesh topology is used as shown in Fig. 6.1. The outer span boundary away from the wing tip is about 10 span length of the wing. Total 18 partitioned blocks are used for parallel computation. The 1st grid spacing away from the the wing surface is set to yield y^+ less than unity. The inlet and outlet boundary is located 50 root chords away from the wing.

6.1.3 Mode Shape

The first five mass normalized mode shapes in the report [2] are used, which are displayed in Fig. 6.2. In the plot, the mode shapes are interpolated from structural nodes to CFD mesh nodes by using radial basis function method so that the grids in the interface between fluid and structure are one to one connected. Among the five modes, the 1st, 3rd and 5th mode

are bending mode, and 2nd and 4th mode are torsion mode. As the initial conditions to start the structure vibration, 1st mode initial velocity of the structure in the modal coordinates is prescribed with a very small value whereas other modal displacements are set to zero. The uniform modal damping ratio(ζ) of 0.0 is applied for all flutter computations to isolate the aerodynamic damping. The unsteady flutter computation is started using the initialized flow field obtained by the unsteady CFD simulation without FSI. The residual in each physical time step is reduced by three orders of magnitude, which is achieved usually within 30 iterations.

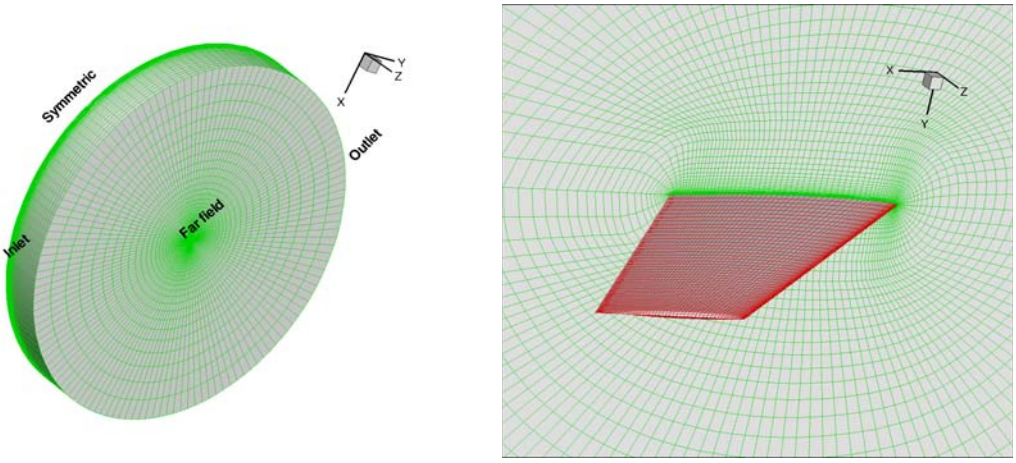

Figure 6.1: Computational mesh of 289×64×77 for AGARD Wing 445.6 Weakend 3

6.2 Results and Discussion

6.2.1 Computational Mesh Test

Mesh convergence test is done for Mach number of 1.072. Three mesh sizes were tested; mesh A=129 (around airfoil)×49(normal to the surface)×49(span), mesh B=137 × 90 × 60, mesh C=289 × 64 × 77. When the mesh is changed, the mode shapes corresponding to the surface mesh coordinates are interpolated by a radial basis function interpolation. Fig. 6.3

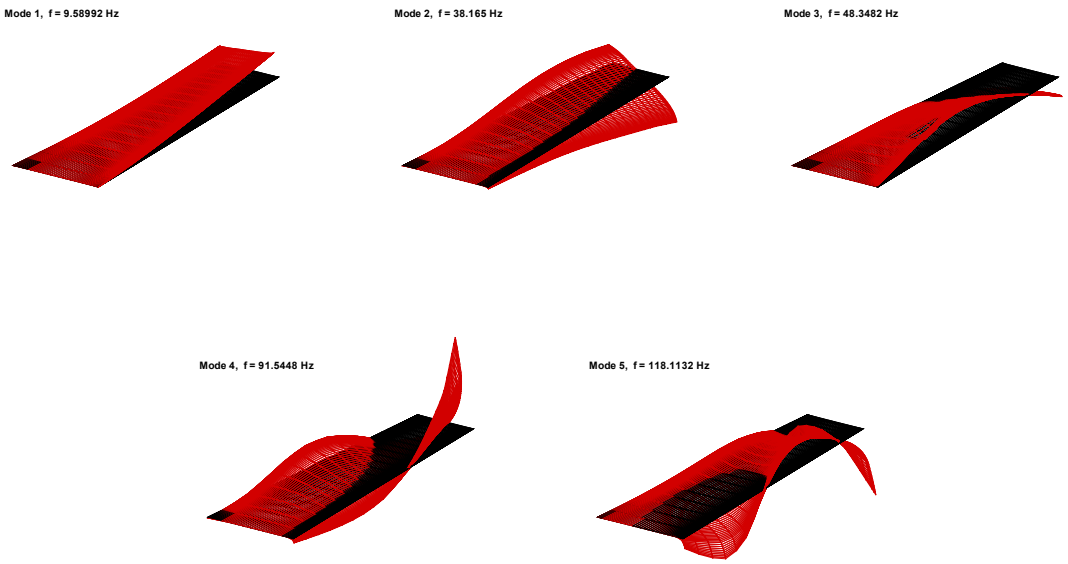

Figure 6.2: The first 5 mode shapes of AGARD Wing 445.6 Weakend 3 [2]

shows the modal displacements of mode 1 for different meshes. The flutter velocity index V_f used for mesh test is 0.30. The predicted responses for mode 1 using mesh B are well converged with mesh C. Therefore, mesh C is chosen for flutter simulations in this study.

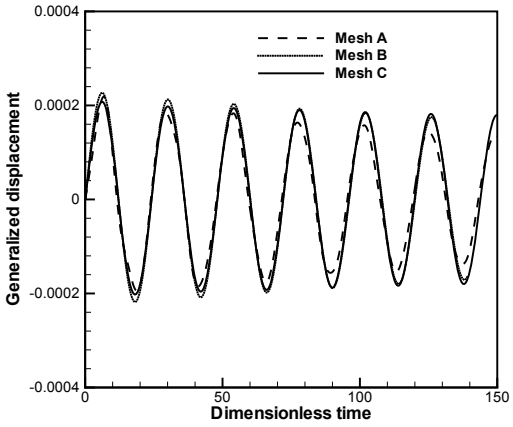

Figure 6.3: Mesh convergence test for $M = 1.072$, $V_f = 0.30$

6.2.2 Flutter Boundary

The computed flutter velocity index and frequency compared with experimental data at flutter boundary for six free-stream Mach numbers are shown in Fig. 6.4. Overall, the computed flutter boundary points are in good agreement with the experiment. In particular, the predicted flutter boundaries at the two supersonic conditions match the experiment accurately. The sonic dip near $M = 1.0$ in the flutter map is very well captured for both the speed index and frequency by the computation. In the frequency plot in Fig. 6.4, the frequency ratio is defined by the ratio of the first mode frequency over the first natural torsional frequency(second mode) during the neutral vibration. The simulation over-predicts the frequency ratio with maximum deviation about 3.0% for Mach number less than 1.141.

The predicted modal displacements for Mach number of 0.499, 0.901, 0.960 and 1.072 with different flutter velocity index(V_f) are displayed in Fig. 6.5, 6.6, 6.7 and 6.8 respectively. Three different responses, including damped, neutral, diverging are shown in each of the plots on the left, middle, and on the right. Take the transonic dip M=0.96 as an example at $V_f = 0.2961$, the response decays in time, whereas at $V_f = 0.3021$ the response is divergent. A neutrally stable point, the flutter boundary, is captured at $V_f = 0.2991$. The damped oscillation with $V_f = 0.2961$ is 1.0% below the measured flutter boundary. It indicates that the present FSI approach has very good accuracy and is sensitive to a small change of the flutter speed index.

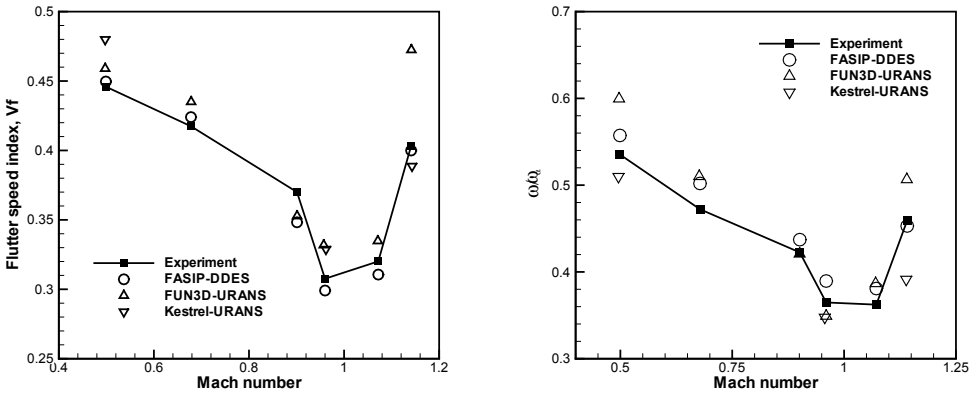

Figure 6.4: Flutter boundary predicted by fully coupled FSI methods and DDES for Wing 445.6

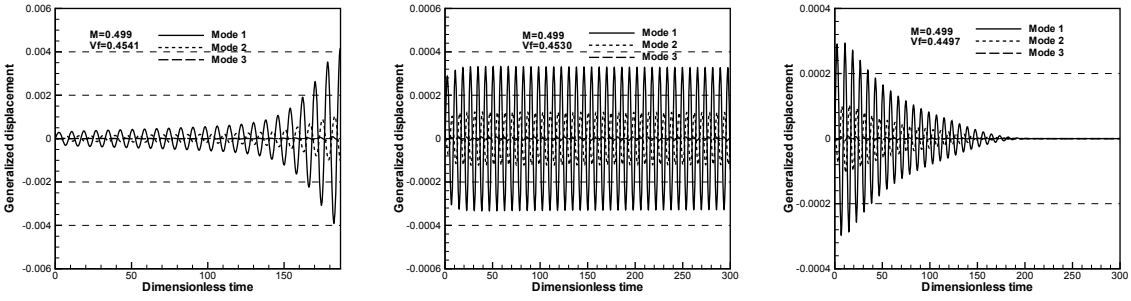

Figure 6.5: Modal displacements for $M = 0.499$

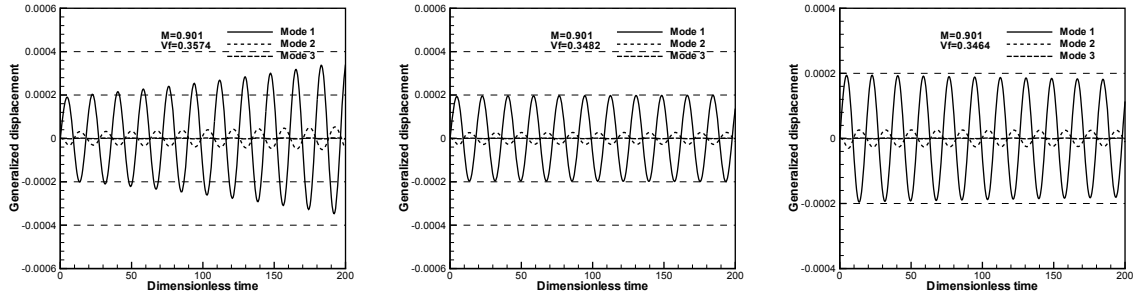

Figure 6.6: Modal displacements for $M = 0.901$

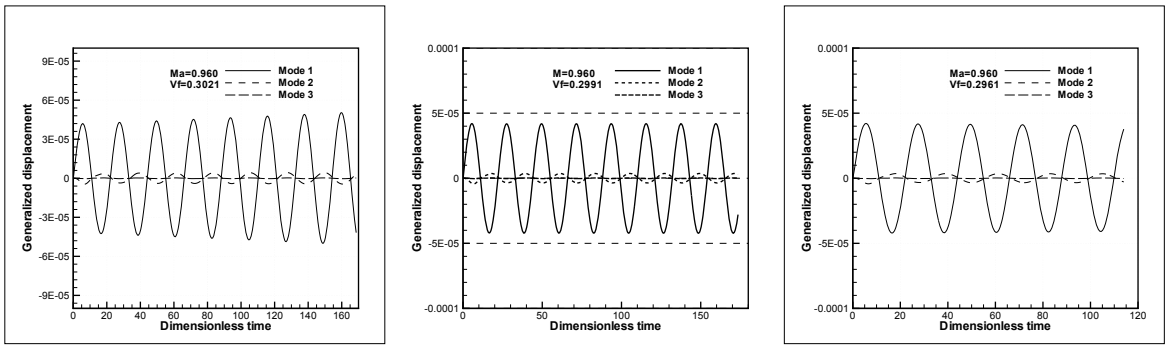

Figure 6.7: Modal displacements $M = 0.960$

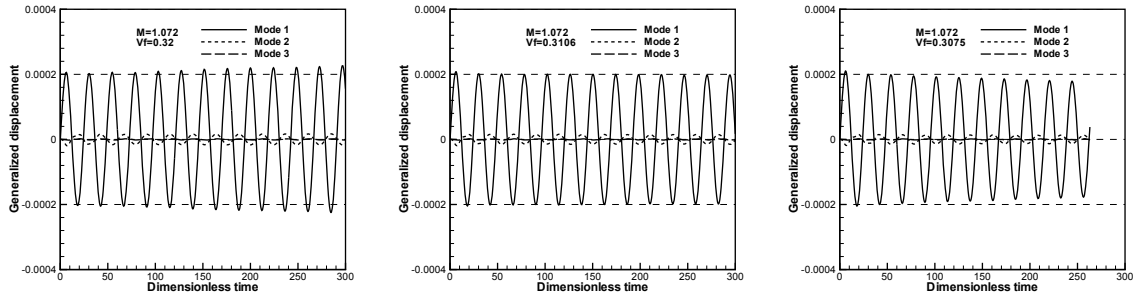

Figure 6.8: Modal displacements for $M = 1.072$

The predicted aerodynamic damping coefficients at $M = 1.072$ are plotted in Fig. 6.9. The aerodynamic damping can be derived from the logarithmic decrement: $\delta = \frac{1}{n} \ln \frac{x(t)}{x(t+nT)}$, where x(t) is the amplitude at time t and x(t+nT) is the amplitude of the peak n periods away, where n is any integer number of successive and positive peaks. Then the damping ratio

can be calculated by $\zeta = \frac{1}{\sqrt{1+(\frac{2\pi}{\delta})^2}}$. The structural damping has been set to zero, so the coefficients are the net aerodynamic damping. The flutter occurs with negative aerodynamic damping. The damping of the response is plotted as a function of the dynamic pressure, which corresponds to the flutter speed index. The flutter boundary can be determined by a set of test points. The predicted aerodynamic damping shows that the flutter boundary is at P3, the dynamic pressure at P3 is about 3100 Pa, which is close to the experimental value 3166 Pa.

As shown in Fig. 6.5, 6.6, 6.7 and 6.8 the generalized amplitude of the first mode at the neutral point does not vary much with the Mach number except at the sonic dip point with a large drop. However, it can be also seen from those plots that the amplitude of the second mode decreases with the increased Mach number.

The ratio of the maximum amplitude of the first mode(bending mode) to the second mode versus Mach numbers at neutral vibration is shown in Fig. 6.10, which almost has a shape of the reversed flutter boundary shown in Fig. 6.4. It is clear that the weight of the torsional mode(second mode) contributing to the flutter of the wing decreases sharply at transonic and supersonic regime. At the sonic dip Mach number of 0.96, even though the first mode amplitude has a large drop, the amplitude of the second mode drops even more. It gives the ratio a sonic rise. The contribution of the bending mode to structural flutter increases abruptly at transonic Mach number 0.96. It appears that the transonic dip is related to the anticlimax of the second mode in transonic regime.

The lift and drag coefficients neutral vibration across the sonic dip at M=0.901, M=0.96 and M=1.072 are shown in Fig. 6.11. At the flutter boundary, the C_l of all free stream flow shows limited cycle oscillation due to the periodic vibration of wing. The average of C_l

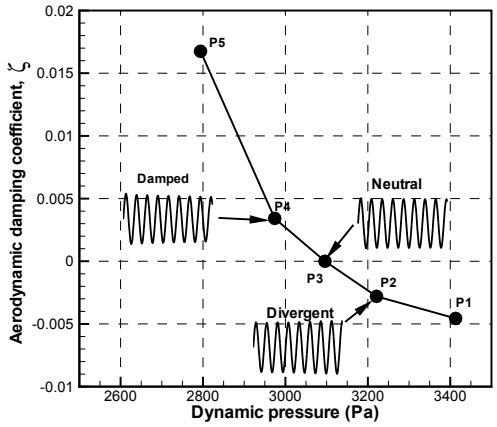

Figure 6.9: Aerodynamic damping as a function of the dynamic pressure for $M = 1.072$

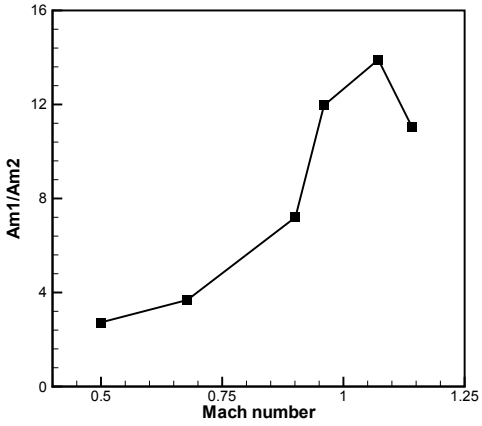

Figure 6.10: The amplitude ratio of the first mode to the second mode at neutral vibration flutter boundary

is about zero. Compared to the average amplitudes of C_l , the average amplitudes of C_d increase from subsonic to supersonic due to the wave drag. Particularly, there is an abrupt increase of the amplitude of Cd at transonic condition. The variation of C_d at $M = 0.901$ is LCO and the average amplitude is about 0.0104. The C_d at transonic and supersonic flow are increased to 0.0116 at $M = 0.96$ and 0.0145 at $M = 1.072$. The pitching moment coefficients(C_m) during the wing neutral vibration are shown in Fig.6.12. The moment is calculated around z axis, which is in the direction of the wing span. The left plot is the time

history of C_m and the right plot is the maximum amplitude of C_m versus of Mach numbers. There is also a dip for C_m at transonic condition as shown in Fig.6.12. Since the pitching moment is the primary cause of torsional vibration, the dip of C_m at sonic point is consistent with the anticlimax of the torsional mode.

Fig. 6.13 shows the modal force defined as $\frac{\tilde{\phi}_j^{*T}}{m_j^*} \cdot \mathbf{F}^* \cdot {V_f}^2 \cdot \frac{b_s^2 L}{V} \cdot \bar{m}$ and modal displacement for M=0.901, M=0.96 and M=1.072. For all the three Mach numbers, all the modal forces and displacements have reversed phase, which are also the case for the subsonic Mach numbers(not shown). This means that the reversed phase is not the cause for sonic dip. The phase of the first modal force is lag half period of that of the first modal displacement at all free stream conditions. And there are no phase lag between the second modal force and the second modal displacement.

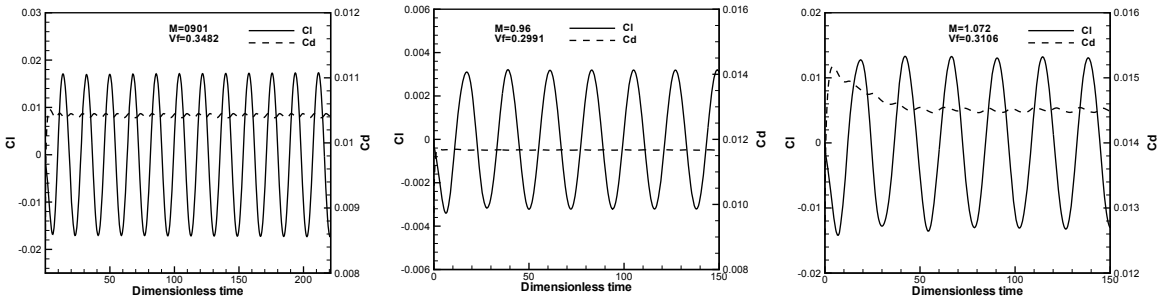

Figure 6.11: Comparison of predicted lift(C_l) and drag(C_d) coefficients during neutral vibration

Fig. 6.14 illustrates the wing tip physical displacement during half a period at the neutral vibration across the sonic dip at M=0.901, M=0.96 and M=1.072.The amplitude of the trailing edge is larger than that of the leading edge, which indicates that both the pitching(torsion) and plunging(bending) are associated with the wing flutter. The pitching makes the wing experience a variation of angle of attack(AOA) with time.

The instantaneous isentropic Mach number(M_{is}) contours on the pressure and suction

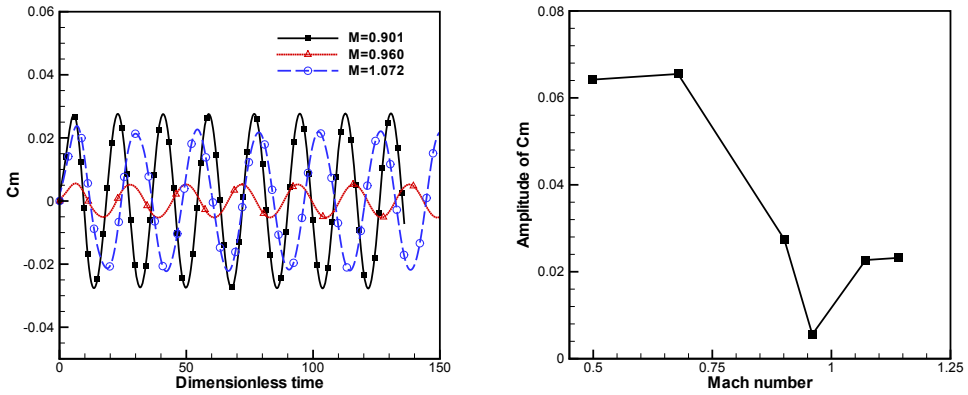

Figure 6.12: Comparison of predicted momentum coefficients(C_m)(left) and maximum amplitude(right) during neutral vibration

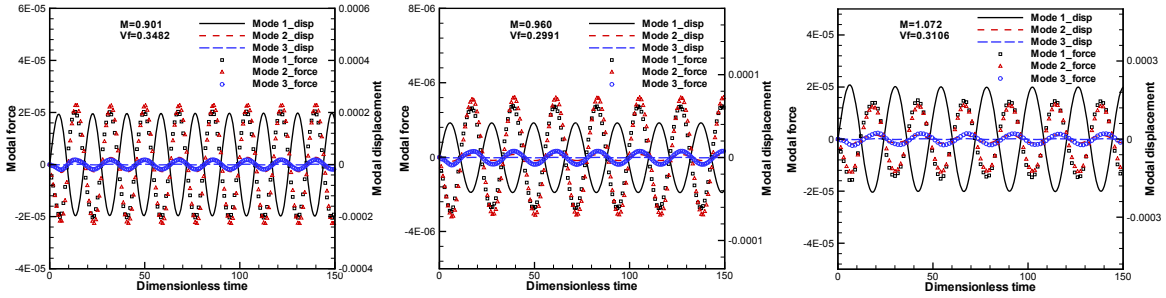

Figure 6.13: Comparison of modal force and modal displacement during neutral vibration at different Mach numbers

surface at 4 different freestream Mach numbers at three instants during half a period are shown in Fig. 6.15 and Fig. 6.16. M_{is} reflects both the local static pressure and the flow speed assuming it is an inviscid flow. At subsonic freestream Mach number of 0.499, the M_{is} does not have large variation on the wing surface. At M=0.96, M_{is} contours on the wing surface show a shock wave near the trailing edge. The shock strength is stronger near the wing tip and is mitigated toward the root. The peak isentropic Mach number is high in the inner span and outer span and is reduced in the span from 50% to 70%. The strength of shock wave on the wing surface varies during the vibration, but the shock patterns are not changed much. At supersonic conditions, M=1.072 and M=1.141, the shock strength

becomes stronger near the trailing edge, which may be responsible for the torsion mode amplitude depletion in the transonic and supersonic regime shown in Fig. 6.10.

Fig. 6.17, Fig. 6.18 and Fig. 6.19 are the surface isentropic Mach number distributions at near root, mid-span and near tip at three different free stream conditions. At the sonic dip Mach number 0.96, the smaller pitching oscillation than at Mach number 0.901 creates less lift shown as the Mach number deviation on the suction surface and pressure surface. Fig. 6.19 shows M_{is} profiles at different span locations and time instants during the supersonic flutter. The unsteady shock waves near the trailing edge of the wing is well resolved by present method. It can be seen that the maximum lift coefficient is generated in the mid-span and the lift coefficient is reduced toward the inner span and tip. The same phenomenon is observed for the other two Mach numbers. It appears that the structural deformations affects the location and strength of the part-chord shock to a significant degree, which in turn results in a shift in the aeroelastic stability of the wing. The shocks is thus capable of turning bending-torsion flutter instability into mostly bending flutter after the sonic dip.

Fig. 6.21, Fig. 6.21 and Fig. 6.21 show the Mach number contours during neutral vibration at three time instants and three different span locations three different free stream conditions. At M=0.901, the Mach number variation is stable during vibration and no shock waves are observed. At M=0.96, shock oscillation can be seen in this figure. The shock oscillation near tip span is more stronger than that near wing root. And the oscillation may become discontinuous. As the wing deforms, the Tijdeman type B shock oscillation is seen at the mid span. This kind of shock oscillation may suppress the energy flow from the fluid to structure [3]. At M=1.072, the shock wave patterns are quite different from that in transonic condition. And shock wave become more oblique and shock oscillation become

stronger. There are is small expansion wave at 75% span near the trailing edge. At the flutter boundary including at the sonic dip, no flow separation due to shock/boundary layer interaction is observed.

6.3 Conclusion

In this chapter, DDES of a 3D transonic wing flutter is conducted with free stream Mach number varied from subsonic to supersonic. Unsteady 3D compressible Navier-Stokes equations are solved with a system of 5 decoupled structure modal equations in a fully coupled manner. The low diffusion E-CUSP scheme with a 5th order WENO reconstruction for the inviscid flux and 2nd order central differencing for the viscous terms are used to accurately capture the shock wave/turbulent boundary layer interaction of the vibrating wing. The radial basis function is employed to interpolate the mode shapes from the coarse mesh to refined mesh.

The predicted flutter boundary at different free stream Mach number including the sonic dip achieves very good agreement with experiment. In particular, the predicted flutter boundaries at the two supersonic conditions match the experiment accurately.

The weight of the torsional mode that contributes to the flutter of the wing decreases at transonic and supersonic regime. The contribution of the bending mode to structural flutter increases abruptly at transonic Mach number 0.96 at which the sonic dip occurs. It appears that the transonic dip is related to the anticlimax of the second mode in transonic regime. The FSI simulation gives the following observations at the sonic dip condition. The shock strength is enhanced more near the trailing edge at near sonic Mach number. The shock

location and motion decrease the pitching moment of the wing, which drops sharply at the sonic dip Mach number, The decreased pitching moment induces lower torsional mode vibration. It creates an anticlimax of the amplitude ratio of the first mode to second mode at the sonic dip.

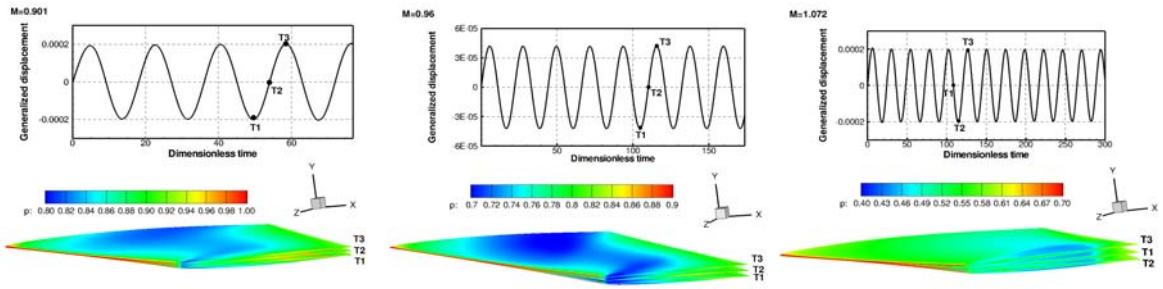

Figure 6.14: Wing fluttering at $M = 0.901$, $M = 0.960$ and $M = 1.072$ during neutral vibration

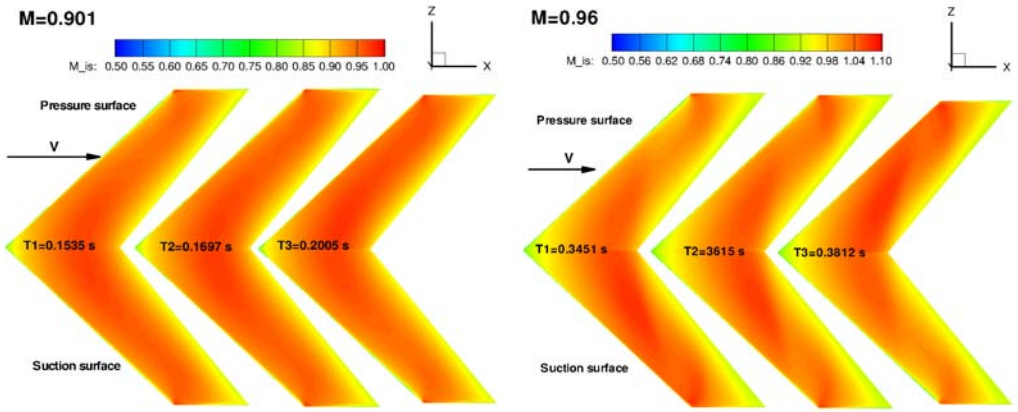

Figure 6.15: Instantaneous isentropic Mach number contours on suction surface. Left: $M = 0.901$; Right: $M = 0.96$

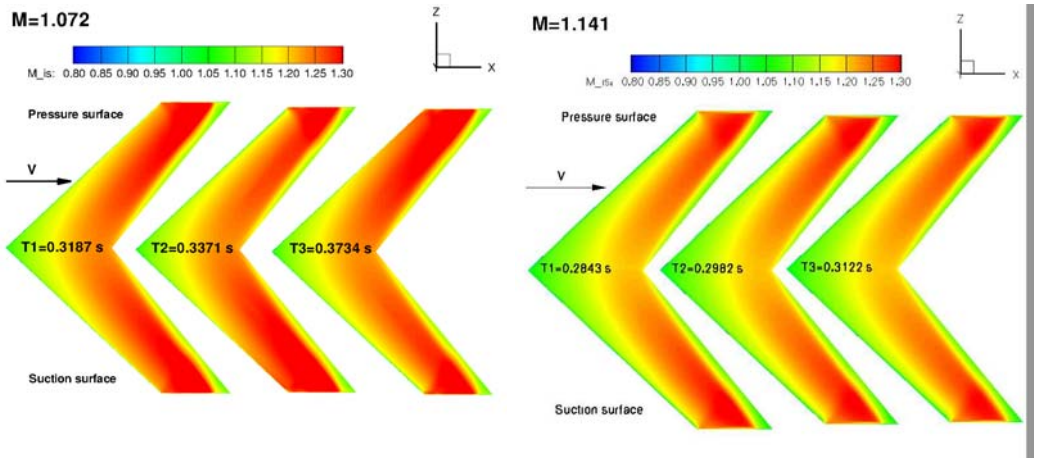

Figure 6.16: Instantaneous isentropic Mach number contours on suction surface. Left: $M = 1.072$; Right:$M = 1.141$

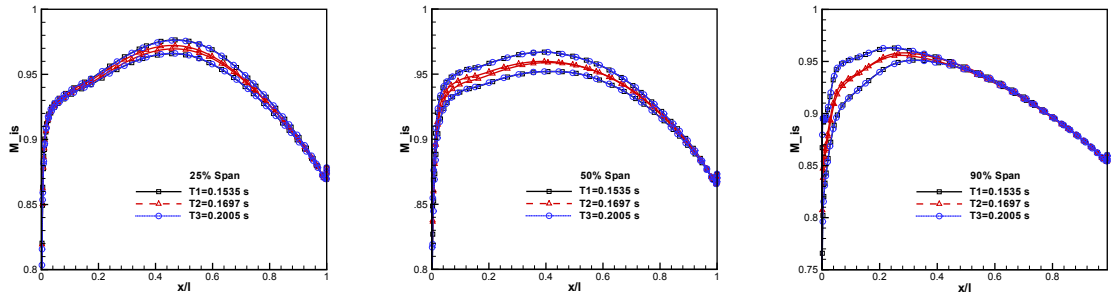

Figure 6.17: Isentropic Mach number profile for $M = 0.901$

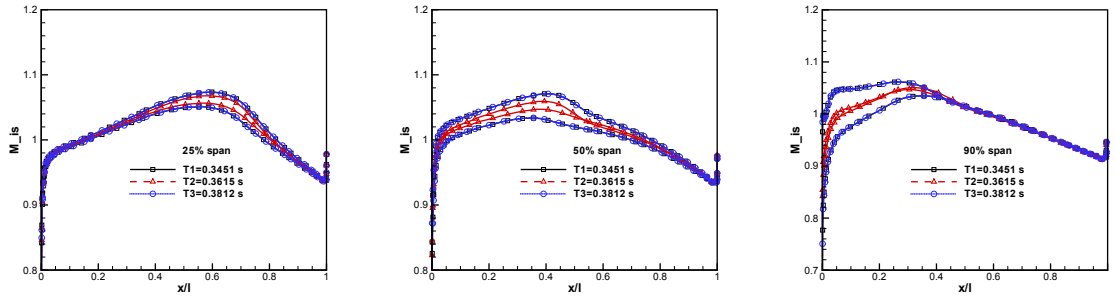

Figure 6.18: Isentropic Mach number profile for $M = 0.960$

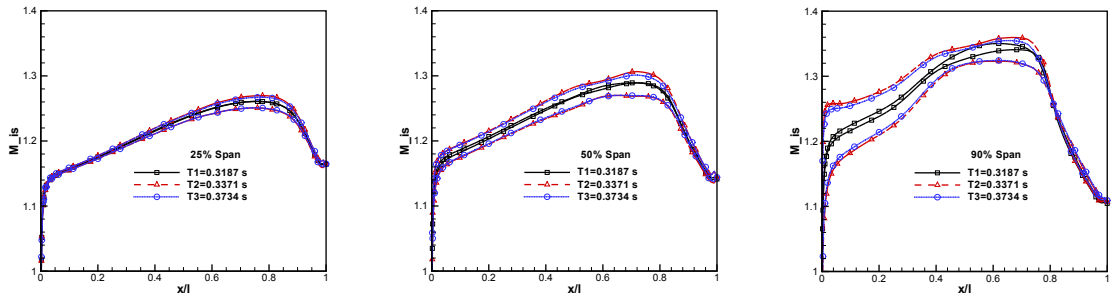

Figure 6.19: Isentropic Mach number profile for $M = 1.072$

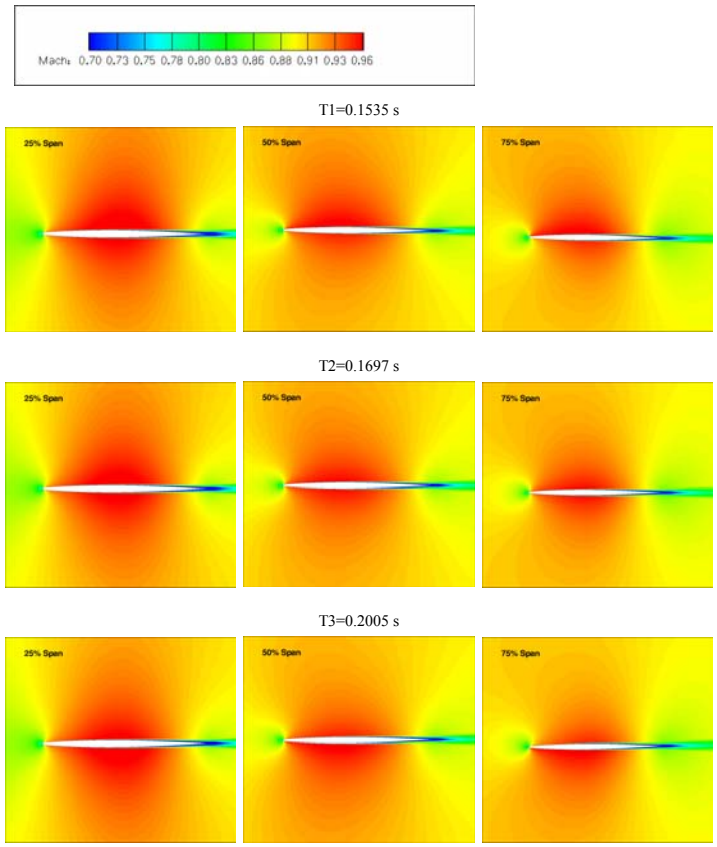

Figure 6.20: Mach number contours for $M = 0.901$

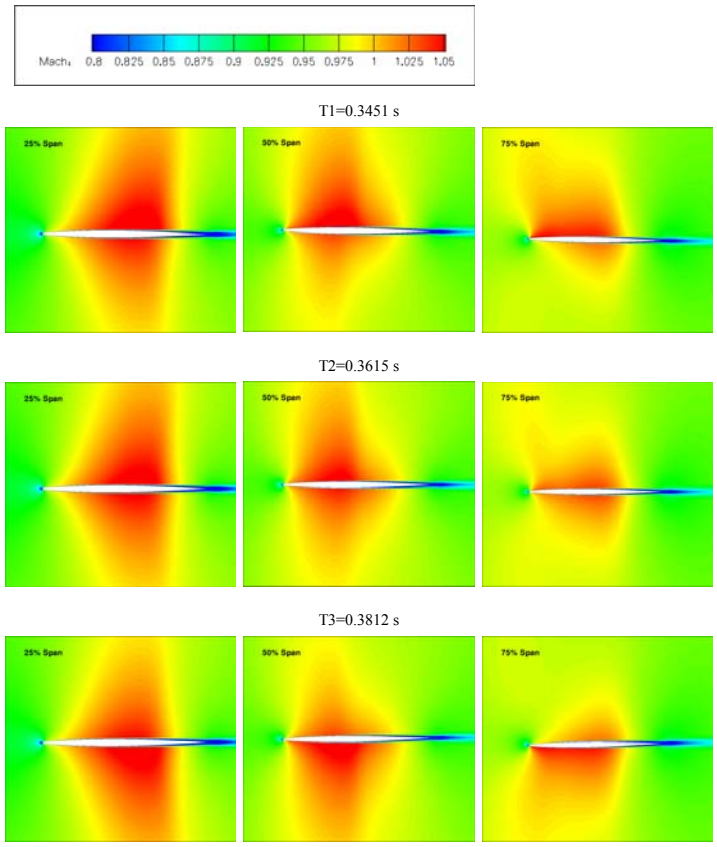

Figure 6.21: Mach number contours for $M = 0.96$

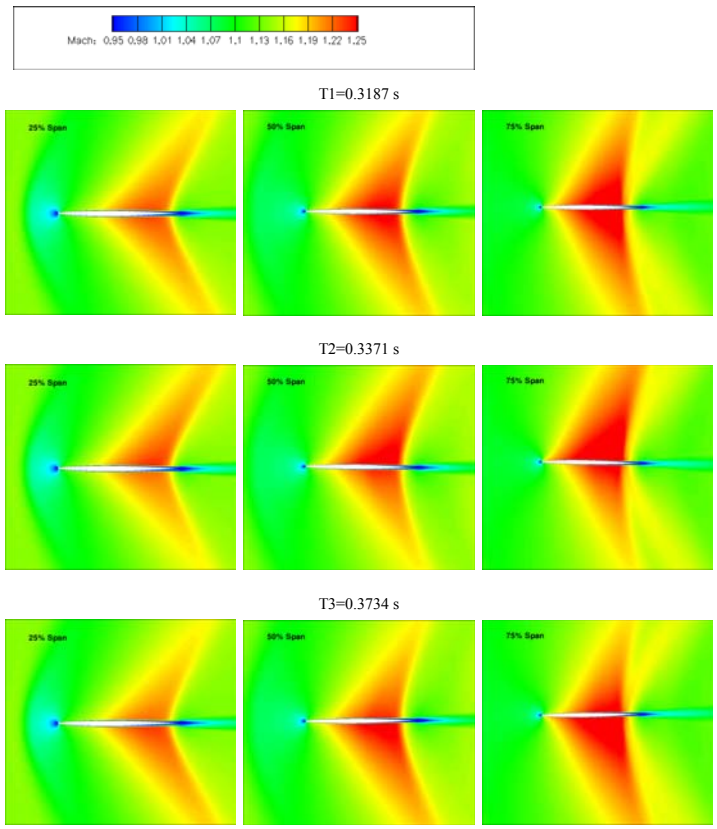

Figure 6.22: Mach number contours for $M = 1.072$

Chapter 7

Supersonic Panel Aeroelasticity

Supersonic panel flutter is a self-excited aeroelastic instability which typically has high amplitude and may cause fatigue damage. Study of supersonic panel flutter is very important for supersonic/hypersonic vehicle design. However, high fidelity numerical simulation of supersonic panel flutter is very challenging due to the complex shock-turbulent boundary layer interaction(STBLI). For the structure, the skin panel temperature could be sufficiently high to cause large nonlinear deflection.

The purpose of this chapter is to simulate supersonic fluid-structural interaction of a flat panel using Delayed Detached Eddy Simulation with high order shock capturing scheme. As the first step, the motion of the panel is treated using linear modal approach. The dynamic motion of the panel is decoupled with the first 5 modes and is solved with Navier-Stokes equations in a fully coupled manner

7.1 Computational Model

The configuration simulated is tested at AFRL Aerospace Systems Directorate large-scale RC-19 supersonic combustion research cell [114], as shown in Fig. 7.1. The position of shock generator is carefully controlled so that the oblique shock hits the vibrating panel on the top side of the test section. The detailed geometry parameters can be found in the chapter of Gogulapati et al [56]. The compliant panel has dimensions L = 254 mm, S= 127 mm, and h = 0.635 mm. The wedge angle of the shock generator is 8°. It should be noted that the cross section of the shock generator is not a isosceles triangle.

The computational mesh for the shock generator model is shown in Fig. 7.2. A mesh topology that aligns with shock angle is created to capture the oblique shock wave and its reflection on the panel. The incline angle of mesh is determined by shock angle based on the wedge angle and the incoming Mach number. For comparison, a mesh distributed in the streamwise direction normal to the axis is also shown in Fig. 7.2. The total number of grid points is 6939297 with 417 points in streamwise direction, 129 points in the transverse direction and 129 points in the spanwise direction. The mesh is clustered near the wall to resolve the turbulent boundary layer. Total 264 CPUs are used for the simulation with parallel computing.

The inlet boundary conditions [56] for the computational domain is total pressure $p_0 =$ 345kPa, total temperature $T_0 = 290$K, and M=2.0. All other variables are fixed based on these conditions for supersonic inlet flow, zero gradient BC for the outlet, no slip and isothermal BC for top and bottom wall. The slip BCs for side walls are used as shown in Fig. 7.3 to save CPU cost to avoid resolving side wall boundary layers, which are considered as having secondary effect on the panel aeroelasticity caused by STBLI. In the

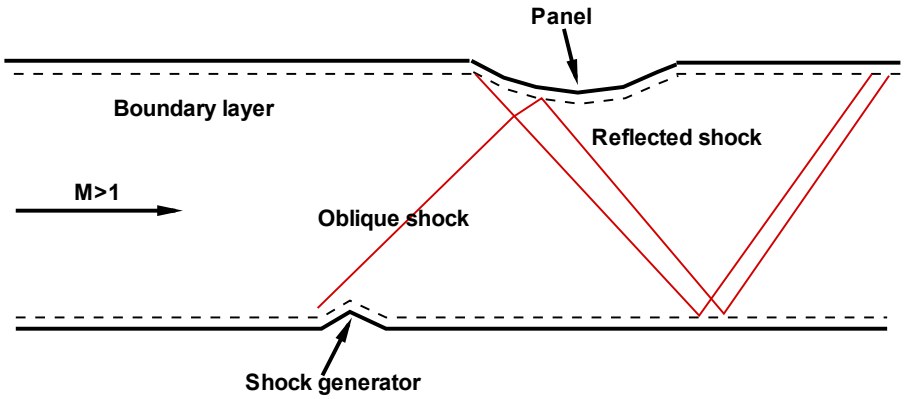

Figure 7.1: Computational configuration of shock wave turbulent boundary layer interaction

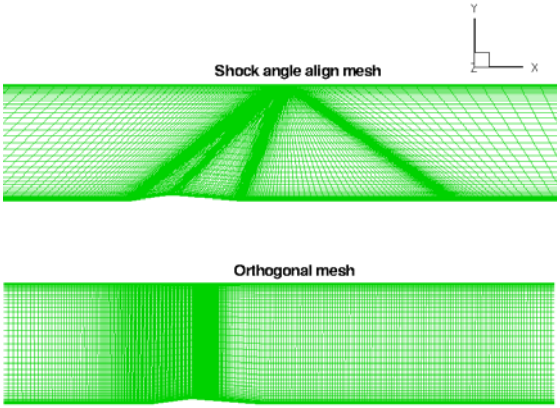

Figure 7.2: Different computational mesh

experiment, a pressure ports was added to the top section of the tunnel wall downstream of the panel in order to prevent panel failure during tunnel start-up. This study uses the static pressure right downstream of the panel to mimic the tunnel test during FSI simulation.

The non-dimensional physical time step used in the simulation is 0.05. The CFL number used for the pseudo time step is 1. Typically, it takes 30 iterations to reduce the residual by three orders of magnitude within each physical time step. It takes one week wall clock time to run 0.1s physical time with 264 CPUs using parallel computing. Since it is a fully

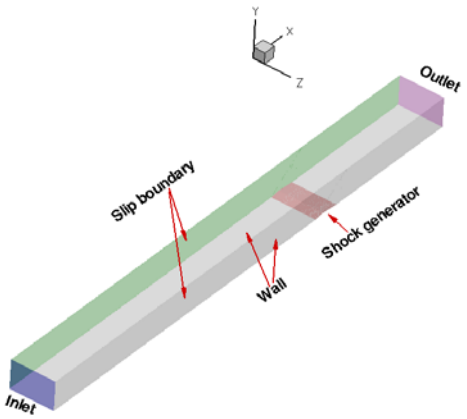

Figure 7.3: Boundary condition of the domain

coupled fluid-structural interaction simulation, the flow and structure response are captured by the solver itself with no parameter adjustment.

7.2 Results and Discussion

An initial investigation of the flow is undertaken aiming to identify the effect of length of inlet duct and the side walls and assess the capability of DDES computations for this flow case. A steady state RANS simulation was firstly conducted to examine if the shock waves positions are captured correctly. With a 8° wedge, shock angle is about 39° at free stream M=2.0. To achieve the correct boundary layer thickness that creates a shock angle of 39°, the inlet length is iterated until the shock impingement position matches the one measured in the experiment. Fig. 7.4 shows the Mach number contour from the final computational domain that generates satisfactory shock angle and impingement position.

The effect of the incline mesh topology is evaluated by comparing with a vertical mesh. Fig. 7.5 shows the Mach contours of the vertical mesh. The shock angle of the first oblique

shock agree very well with that captured by the inclined mesh as shown in Fig. 7.4. So is the shock reflection. However, the triple point phenomenon in vertical mesh is captured more clearly than that in the inclined mesh model. The inclined mesh shows overall higher resolution of the front shock and its reflection than that in the vertical mesh model. Because it is more convenient to implement the FSI simulation with a vertical mesh, the unsteady and FSI simulation employ the vertical mesh in this study. Mesh refinement study is conducted by using a total 63 million grid points in the refined mesh. Even though the shock wave and expansion wave of refined mesh are captured with higher resolution as show in the right plot of Fig. 7.5, the magnitude of the pressures are very similar between the coarse and refined mesh. Due to high CPU cost of the refined mesh, the panel FSI simulation uses the coarse mesh.

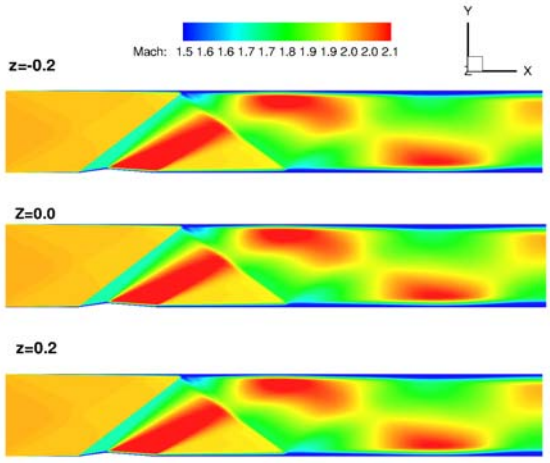

Figure 7.4: Mach number contours of the inclined mesh

The first five mode shapes of the panel are obtained by using ABAQUS software and are shown in Fig. 7.6. The natural frequencies of the first 5 modes are f1=236 Hz, f2=306 Hz, f3=433 Hz, f4=612 Hz, f5=618 Hz. The computed results are in excellent agreement with that from Gogulapati [56].

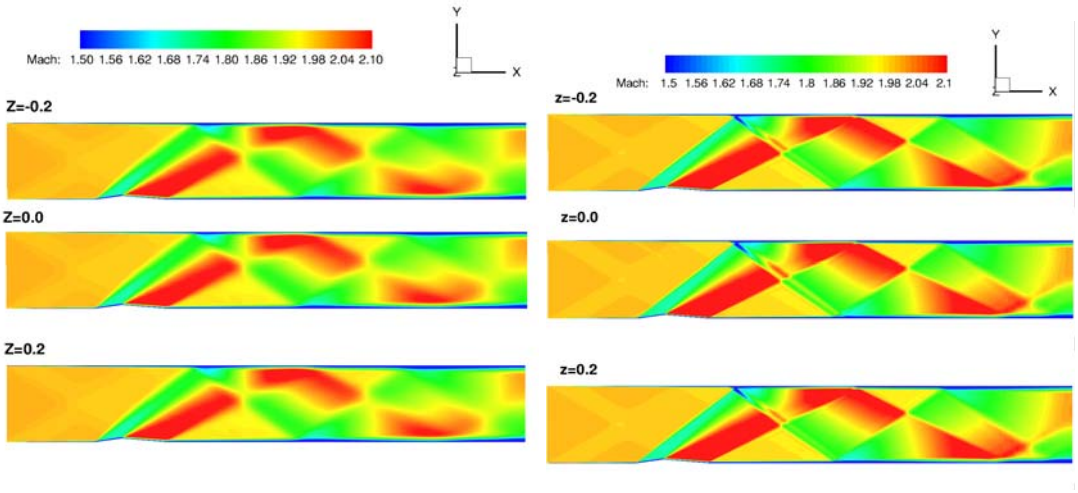

Figure 7.5: Mach number contours of the vertical mesh, coarse mesh(left), refined mesh(right)

Fig. 7.7 shows modal displacement of the first five modes of the panel. A dynamically stable vibration is achieved after the physical time of about 0.6s. The vibration is similar to a limited cycle oscillation as shown in Fig. 7.8. The first mode has the largest contribution to the physical displacement amplitude among the first five modes. The contributions of the second and the third modes are almost the same and are substantially smaller than that of the first mode as shown in Fig. 7.7. The contributions of the fourth and fifth mode are almost negligible compared to that of the first mode.

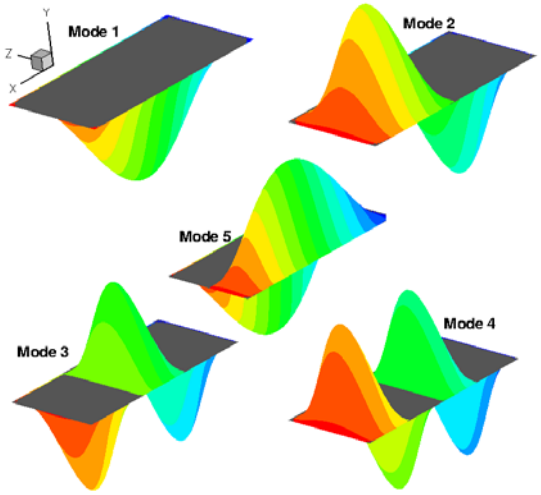

Figure 7.6: The first 5 mode shapes of the steel panel

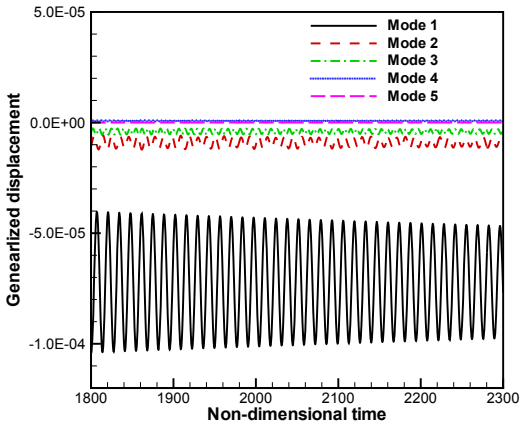

Figure 7.7: Time history of modal displacement.

Fig. 7.8 illustrates physical displacements in center-line of the panel. The largest displacement occurs near the center point of the panel instead of the shock impingement point. The corresponding spectrum analysis of physical displacement are shown in Fig. 7.9. The maximum predicted mean displacement during the vibration is about 0.19 mm. The predicted displacement is close to that measured in the experiment [114], which is 0.089 mm. In the simulation of Gogulapati, et al. [56], the computed mean displacements for the unheated cases is 0.886 mm, which is substantially more over predicted than the present results. The dominant frequency predicted by the present FSI simulation is the 236 Hz, which is very close to the measured frequency and is the same as the natural frequency of the first mode.

Fig. 7.10 is Mach contours at three spanwise locations. Since the slip boundary conditions are used on the side walls to reduce CPU cost, the Mach number contours are similar along the span. Fig. 7.11 displays pressure contours at three spanwise locations. Fig. 7.12 shows pressure contours at three horizontal surfaces, bottom wall, middle plane and upper wall. It is clearly seen that there are high pressure jumps at shock generator location,

mid-channel shock and its reflections impingement locations. The time history of pressure along the center line of the panel is shown in Fig. 7.13. It is seen that there is a large pressure fluctuation during the panel vibration.

7.3 Conclusions

In this chapter, delayed detached eddy simulation is performed to simulate a supersonic panel vibration at Mach 2.0. Unsteady 3D compressible Navier-Stokes equations are solved with a system of 5 decoupled structure modal equations in a fully coupled manner. The low diffusion E-CUSP scheme with a 5th order WENO reconstruction for the inviscid flux and a set of 2nd order central differencing for the viscous terms are used to accurately capture the shock wave/turbulent boundary layer interaction of the vibrating panel.

The shock waves and their reflection interacting with turbulent boundary layer in the tunnel are well captured by the DDES. The panel vibration induced by the shock boundary layer interaction is well resolved. The dominant panel response agrees with the experiment in terms of the mean panel displacement and frequency. Even though the linear model structure model performs very well in this simulation, the next step would be to incorporate nonlinear finite element model to further improve the accuracy. It takes one week wall clock time to run 0.1s physical time with 264 CPUs using parallel computing. Since it is a fully coupled fluid-structural interaction simulation, the flow and structure responses are captured by the solver itself with no parameter adjustment.

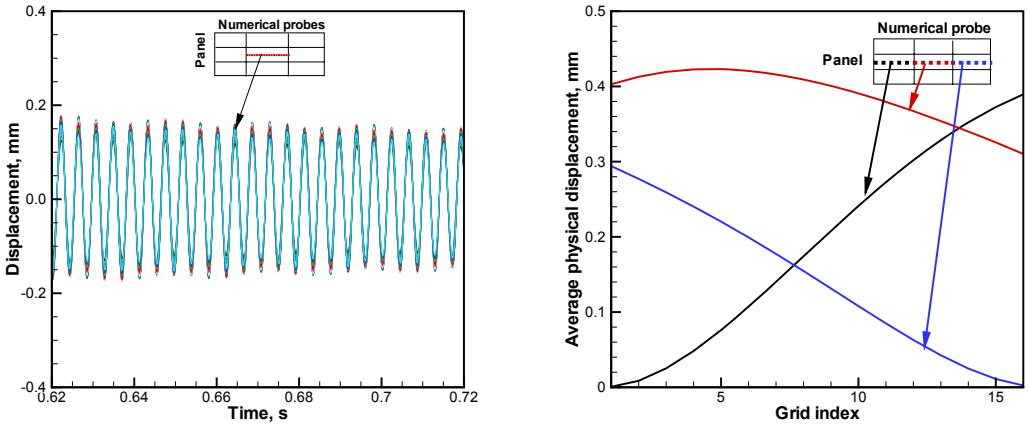

Figure 7.8: Time history(left) and time average(right) of physical displacement in the center of panel.

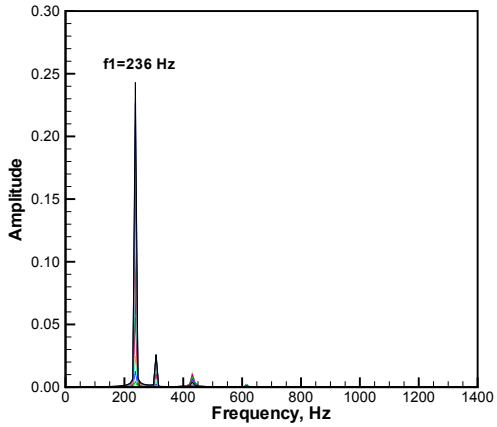

Figure 7.9: Spectrum of physical displacement in the center-line of panel.

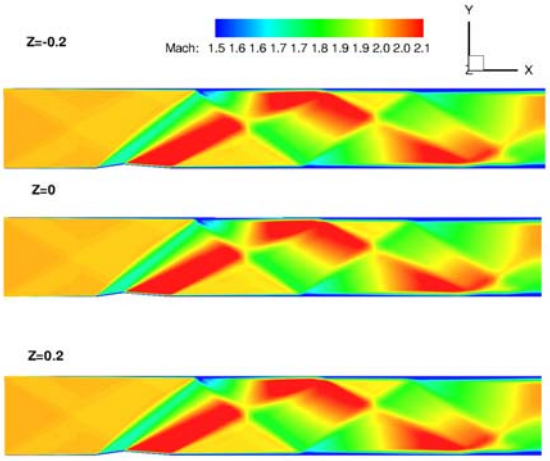

Figure 7.10: Mach contour showing the shock wave during panel vibration.

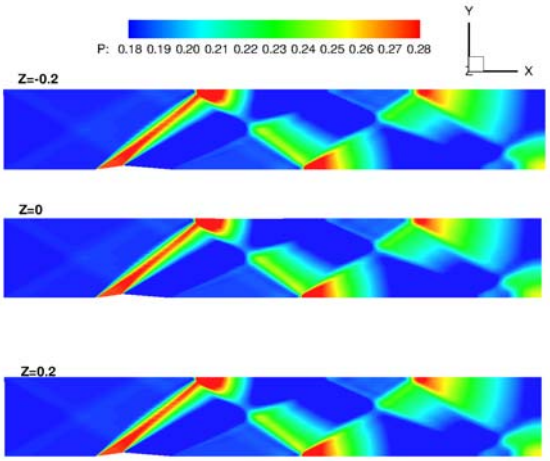

Figure 7.11: Pressure contour in spanwise sections.

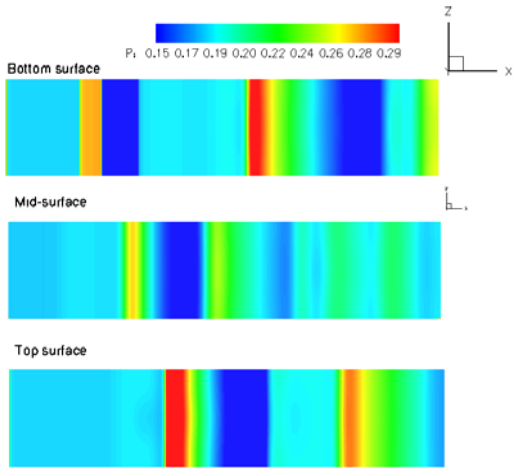

Figure 7.12: Pressure contour in horizontal sections.

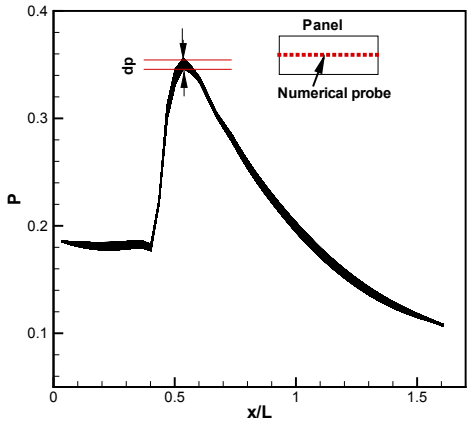

Figure 7.13: Time history of pressure along center line of the panel with the width of the line representing the range of pressure

Chapter 8

Stall Inception of a High Speed Compressor Stage

High fidelity prediction of turbulent flows is very important for accurate simulation of rotating stall characteristics with three-dimensional vortical flows, nonlinear shock wave-boundary layer interaction, and different time scale of disturbance cells in high speed axial compressor. These features play important roles in the formation of stall cells characterized by propagating speed and number of cells in the annulus. Accurate prediction of the number of cells and their speeds is important since their product will give the frequency of stall cells passing each blade. If such a frequency is near a natural frequency of the blade, resonance may occur and result in mechanical failures of the blade.

The objectives of this chapter are to use DDES of turbulence modeling method to simulate the stall inception of NASA Stage 35, and to reveal the rotating stall mechanism for the high speed axial compressor involving strong shocks with the low diffusion shock capturing scheme. For comparison, URANS turbulence modeling method was also adopted to simulate the rotating stall.

8.1 Mesh and Boundary Condition

8.1.1 Computational Grid

A transonic axial compressor, NASA stage 35 consisting of 36 rotor blades and 46 stator blades [115], is simulated to investigate the stall inception mechanism. The total pressure ratio of NASA stage 35 at design speed of 17189 rpm is 1.82. The full annulus of Stage 35 geometry and mesh are shown in Fig.8.1. The mesh size and distribution is outlined here for completeness. An O-mesh topology around blades with H-mesh for stage inlet/outlet duct region are used. For the rotor and stator, a grid size of $121 \times 69 \times 45$ in the direction around the blade, blade to blade, and span respectively is used. The rotor tip clearance is modeled using a fully gridded O-mesh with mesh size of $121 \times 15 \times 11$ as shown in bottom plot in Fig. 8.1. Within the tip clearance, 11 grid points are placed radially. This mesh is referred as the baseline mesh or main mesh with the total mesh points of about 200,000.

The tip gap is shown to have a significant effect on overall performance of axial compressors [116]. The fully gridded tip mesh generation technique adopted in this study is shown to better predict the tip clearance flow than the pinched tip or simplified tip model [117]. In the model of the fully gridded tip, about 4 to 10 points in the tip clearance are generally considered as adequate to predict the primary effects of the leakage flow in axial compressor [1, 86, 116–118]. A non-gridded tip model is used by Chen et al [85]to investigate the pre-stall behavior of NASA Stage 35. Their results indicated that the inception type of the rotating stall can be captured without fully gridded tip model. However, it is not possible to determine the precise impact of the tip clearance modeling on stall

inception due to the lack of detailed flow measurements in the tip clearance of NASA Stage 35 during rotating stall.

The effect of grid size on solution accuracy for Rotor 37 using H-O-H grids with O-grid tip clearance region by McNulty [117] shows remarkably similar predictions using three grid size approximately with 200,000, 350,000 and 400,000 points. Similar results are obtained for the mesh refinement study using the rotor-alone single passage in their study. Their mesh size is similar or coarser than what is used in the present study. Im et al. [1] uses a NASA Rotor 67 full annulus mesh with about 7 million grid points to capture the stall cell rotating at about 48% of rotational speed. The mesh size and distribution of a single blade used by Im et al. [1] is also similar to what are used in this thesis. The steady state mesh refinement study was conducted in [87]. The mesh is mainly refined around the blade, which has the dimension of $201 \times 77 \times 51$. The results indicate that the solution is converged based on the chosen mesh size. The excellent agreement between the predicted radial profiles of NASA Stage 35 compared with the experiment also evidences that the mesh is sufficiently fine to resolve the wakes [87]. The low diffusion E-CUSP scheme employed in the thesis also contributes to minimize the numerical diffusion and hence mesh size

Considering a disturbance with its wavelength on the order of the circumference, it is desirable to locate the inlet and outlet boundary of the computational domain far away from the rotor blade. In this study the inlet plane are located about 8 axial tip chord length upstream of the rotor and about 6 axial tip chord length downstream of the stator. Total mesh points of the full annulus are about 16 million with 482 blocks.

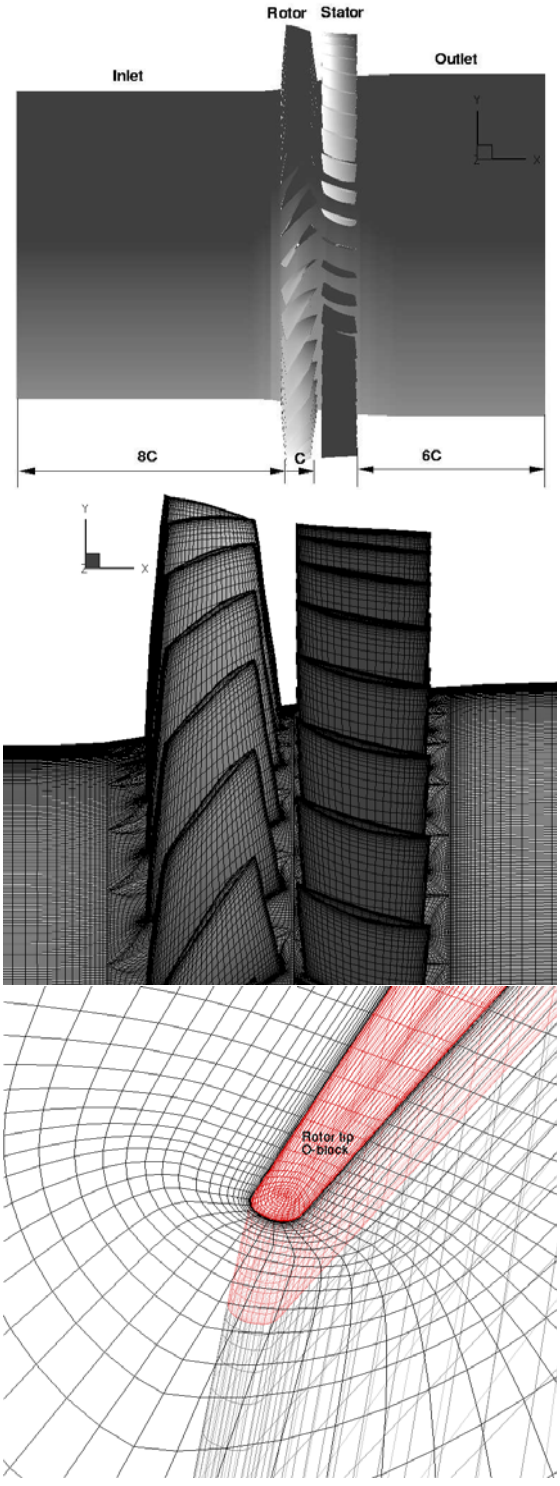

Figure 8.1: Full annulus mesh of NASA stage 35

Boundary Condition

For unsteady rotor-stator interaction simulation, the rotor mesh will rotate with the rotor blades and the stator mesh will be stationary. Solving the Navier-Stokes equations requires

transferring the fluxes between these two meshes. In [119], a conservative sliding BC is developed by making the meshes on both side of the sliding boundary one-to-one connected. Even though the conservative BC is mathematically more rigorous, it is not always convenient to make a multi-block mesh one-to-one connected. For engineering applications, independent mesh for rotor and stator is desirable for efficient setup of a simulation. This paper thus adopts an interpolation sliding BC [87] with high accuracy to remove the requirement that the rotor and stator mesh needs to be one-to-one connected.

At the inlet, the radial distributions of total pressure, total temperature, swirl angle and pitch angle are specified and the velocity is extrapolated from the computational domain in order to determine the rest of the variables. In this paper, no inlet perturbations are used to trigger the stall inception in order to keep the same operation condition as that in [80,85]. On the blade surface a non-slip boundary condition is applied, while an efficient wall function BC [1] is used on the hub/casing surface where y^+ is greater than 11 to avoid an excessive fine mesh in the end-wall boundary layer. At the stator outlet, a static pressure profile is specified in the spanwise direction. The velocity components are extrapolated from the computational domain and an isentropic relation is used to determine density. The hub/casing wall static pressure for the inviscid momentum equation is determined by solving the radial equilibrium equation, whereas the static pressure gradient across the wall boundary is set to zero for the blade wall surface. An adiabatic condition is used to impose zero heat flux through the wall.

8.1.2 Interpolation Rotor/Stator Sliding BC

For unsteady rotor-stator interaction simulation, the rotor mesh will rotate with the rotor blades and the stator mesh will be stationary. Solving the Navier-Stokes equations requires transferring the fluxes between these two meshes. In [119], a conservative sliding BC is developed by making the meshes on both side of the sliding boundary one-to-one connected. Even though the conservative BC is mathematically more rigorous, it is not convenient to make the mesh one-to-one connected. For engineering applications, independent mesh for rotor and stator is desirable for efficient setup of a simulation. This paper thus adopts an interpolation sliding BC with high accuracy to remove the requirement that the rotor and stator mesh needs to be one-to-one connected.

The working mechanism of present interpolation rotor/stator sliding BC is sketched in Fig. 8.2, where S1, S2, S3, S4 and R1, R2, R3 are the arbitrary computational mesh cells of the stator and rotor in the circumferential direction on the two sides of the sliding interface. The current interpolation sliding boundary condition is based on the same grid radial distribution of the mesh on both side of the sliding boundary.

To interpolate the conservative variable vector $\mathbf{Q}$, the circumferential mesh angle is first obtained at each mesh cell center, e.g. the angle of a stator cell s1, θ_{s1} can be defined as $tan^{-1}(z/y)_{s1}$. Then, two adjacent mesh angles in the opposite interface corresponding to current mesh cell are found for linear interpolation, e.g. $\mathbf{Q}$ at R3 is interpolated in terms of $(\theta_{R3} - \theta_{S2})$ and $(\theta_{S3} - \theta_{S2})$ as given in Eq. (8.1). Note that a rotation rule based on the geometric periodicity is used to interpolate $\mathbf{Q}$ in the non-overlap region, e.g. $\mathbf{Q_{S1}}$ is rotated

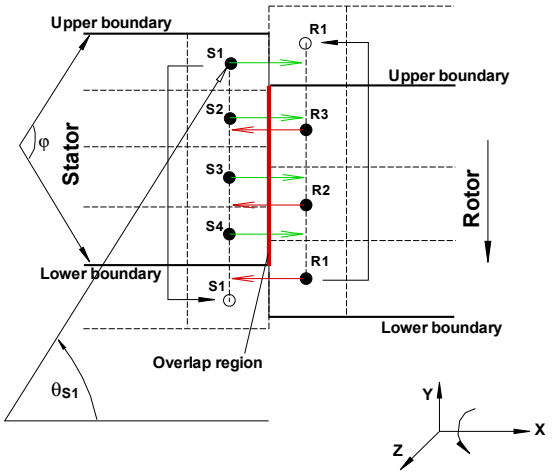

Figure 8.2: Working mechanism of interpolation rotor/stator sliding BC

by the periodic sector angle (φ) to interpolate $\mathbf{Q_{R1}}$ vice versa for $\mathbf{Q_{R1}}$.

$$\mathbf{Q}_{R3} = \frac{\theta_{R3} - \theta_{s2}}{\theta_{s3} - \theta_{s2}}(\mathbf{Q}_{s3} - \mathbf{Q}_{s2}) + \mathbf{Q}_{s2} \tag{8.1}$$

Since the frame of reference taken in this study is a fixed frame for the stationary blades and a moving relative frame for the rotor, the following exchange relations between the fixed and moving relative frame are used.

$$\begin{pmatrix} \rho \\ \rho u \\ \rho v_r \\ \rho(v_\theta + rR_o) \\ \rho(e + c_\theta rR_o) \end{pmatrix}_{Fixed} \rightleftharpoons \begin{pmatrix} \rho \\ \rho u \\ \rho v_r \\ \rho v_\theta \\ \rho e \end{pmatrix}_{Moving} \tag{8.2}$$

8.2 Results of Rotating Stall Simulation

8.2.1 Stage Performance Prediction and Validation

Fig.8.3 shows the predicted speedline for NASA Stage 35 using steady state single blade passage with mixing plane boundary condition on the rotor and stator interface. A refined mesh of total 550,750 grid points and a baseline mesh (main mesh) of 449,790 grid points per blade passage are used for the mesh refinement study using the mixing plane [119]. The speedline predicted by the two meshes shows good agreement. Therefore, the baseline mesh is used to construct the full annulus mesh in Fig.8.1. The simulation is conducted at 4004 test condition [115] since the measured radial profiles for CFD comparison are available. The mass flows at choke condition predicted by both unsteady rotor/stator interaction and steady mixing plane are about 20.82 kg/s, which is about 0.62% lower than the measured choke flow of 20.95 kg/s [115].

The circumferential mass averaged total pressure ratio, total temperature ratio, adiabatic efficiency and absolute flow angle at stage outlet are compared with the measurement at 4004 point [115] in Fig.8.4. Overall good agreement with the experiment is achieved by both approaches; the mixing plane and the interpolation rotor/stator sliding BC.

Fig.8.5 shows instantaneous entropy at mid span of the compressor. The wake propagates through the rotor/stator interface smoothly. Fig.8.6 compares the instantaneous normalized mass flux ρU (left) and static pressure P (right) immediately upstream and downstream of the sliding interface. It indicates excellent flux conservation through the rotor/stator interface. The simulation of stall inception in the following section employs full annulus.

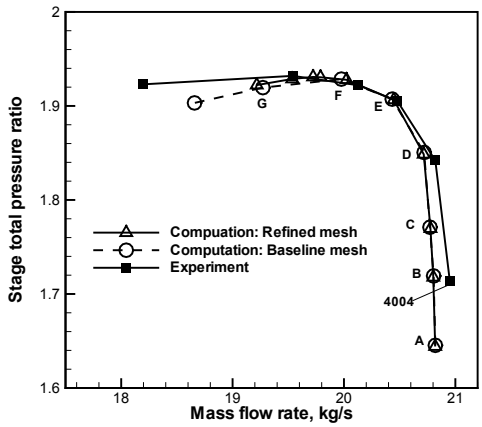

Figure 8.3: Predicted speedline of NASA stage 35

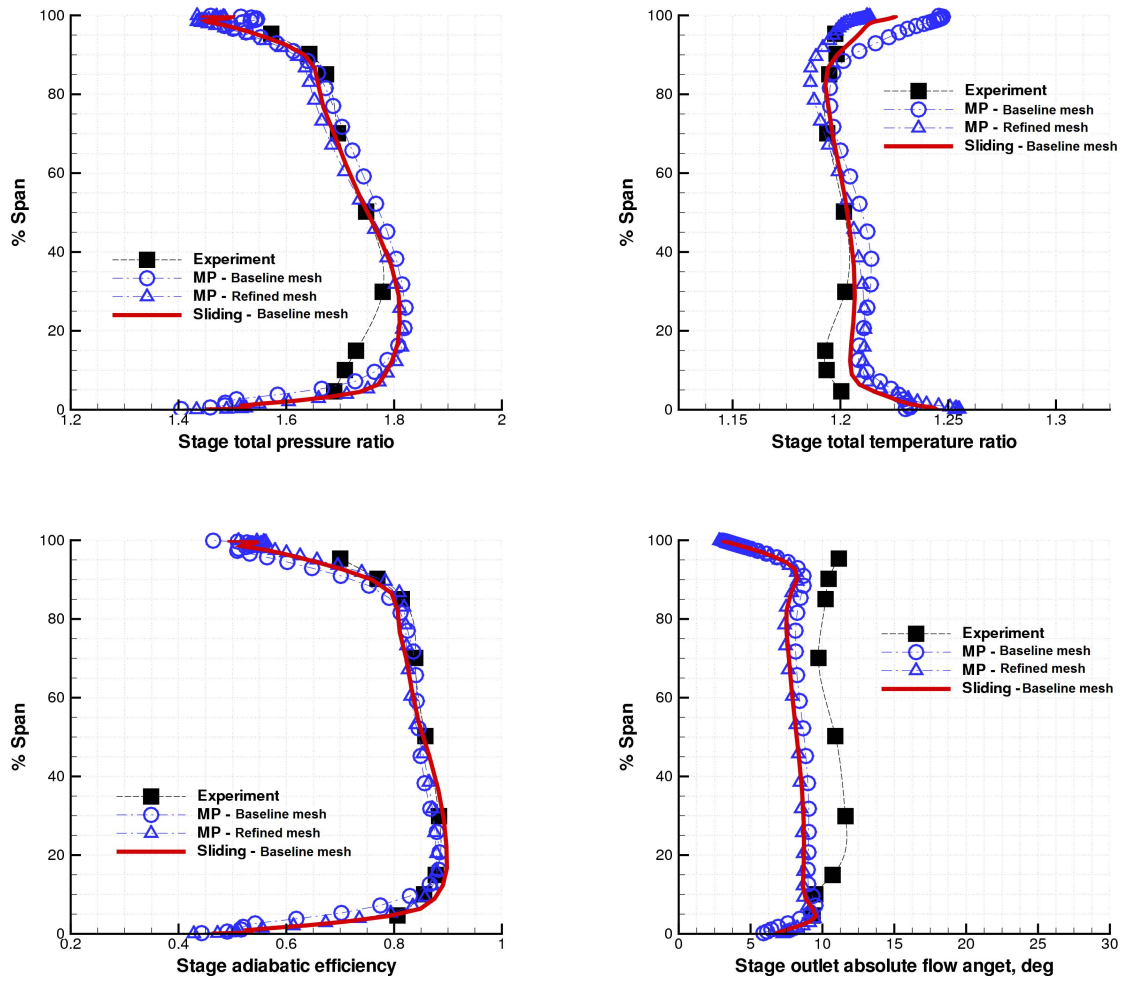

Figure 8.4: Predicted pitch averaged radial profiles at 4004 including stage total pressure ratio, total temperature ratio, adiabatic efficiency and outlet absolute flow angle

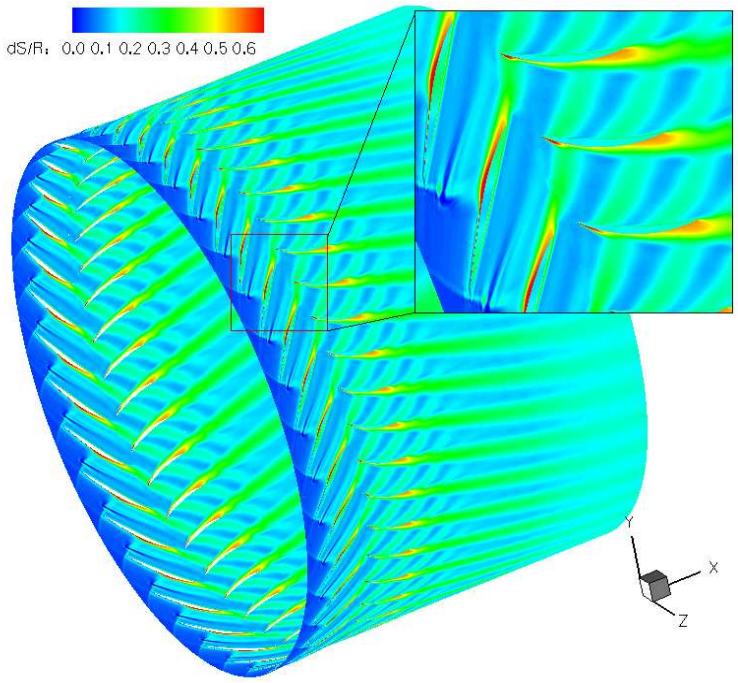

Figure 8.5: Instantaneous entropy contour at mid span of NASA stage 35

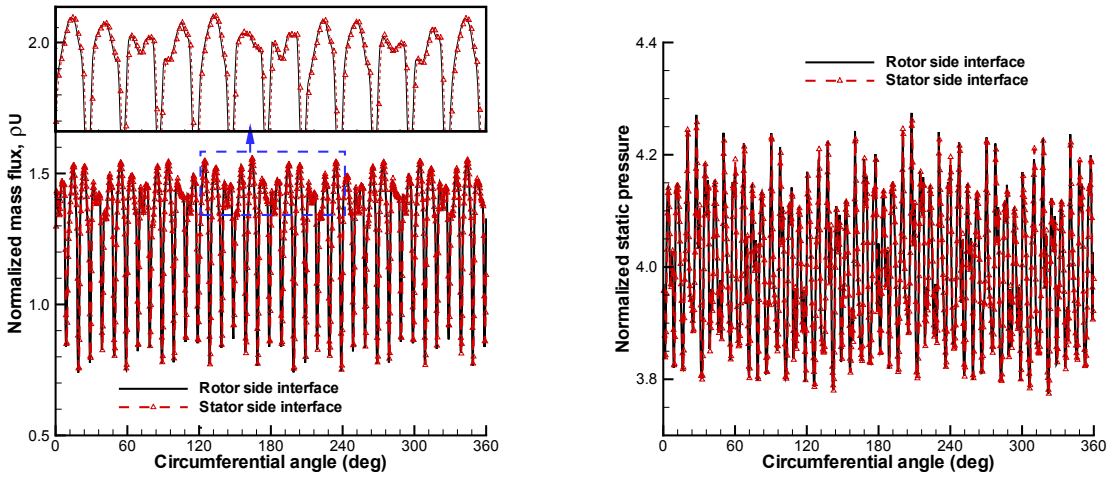

Figure 8.6: Instantaneous normalized mass flux ρU (left) and static pressure P (right) at mid span of the rotor/stator interface

8.2.2 Unsteady Calculation Convergence

The full annulus unsteady simulation begins with near stall points on the compressor characteristics map obtained by the RANS simulation [120]. This approach is employed by other researchers [83, 84, 121] for the rotating stall simulations in order to reduce computing efforts.

A physical time step of around 0.000009 sec. is used in this study. One rotor revolution will take 1440 steps. The study by Copenhaver et al. [122] shows a time step of 0.00025 sec. is necessary to capture shock instability in a transonic rotor. Hah et al. [78] used a time step of 0.0000125 sec. for predicting the stall inception of a similar high speed rotor originated by the interaction of the passage shocks and tip leakage vortices. As aforementioned, the rotating speed of the spike type stall cell in a high-speed compressor is roughly half of the rotor rotational frequency [79, 123], the time step size adopted in this study is significantly smaller than those used by all other researchers and is sufficient to resolve the primary flow features during the stall inception.

Fig. 8.7 shows the L2 norm residual and inlet mass flow rate converging history obtained by the RANS at choke and DDES during rotating stall. Due the strong shock occurred near the rotor leading edge, the RANS calculation began with a 1/3 of designed rotor speed. Once the computation has converged enough (for 10000 steps the calculation converged about 5 orders of magnitude) as shown in the left plot of Fig. 8.7, the results are used to start full speed unsteady simulation. The step changes in residual and mass flow rate around 10000 steps are due to the change of RPM. The unsteady simulation achieves 2 orders of magnitude residual reduced in each physical time step. The calculation becomes numerically unstable after 3.2 rotor revolutions. The maximum residual occurred at ro-

tor stator interface, which may be due to the high aspect ratio mesh used near the casing surface.

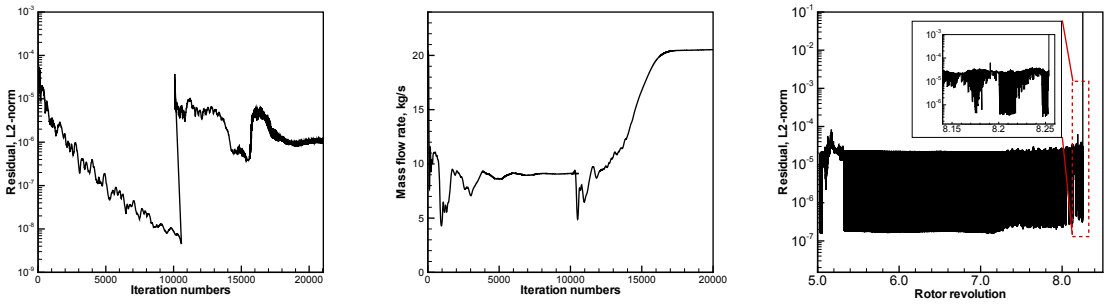

Figure 8.7: Convergence history: Residual of RANS(Left), Mass flow rate of RANS (Middle), Residual of DDES(Right)

8.2.3 Stall Pressure Rise Characteristics

The predicted unsteady stage speed line is illustrated in Fig. 8.8, which starts from the near stall point D. From point A to point D, the simulation is steady state and the results at point D are used as initial flow field of the unsteady calculation. The results of DDES are compared with that of URANS. It can be seen that the stall onset predicted by URANS starts at higher back pressure than that by DDES. In the speedline of DDES, the rotating stall inception simulation begins at point P1 with the back pressure fixed and letting the stall inception develops by itself. The stage total pressure ratio drop is slow from point P1 to point P2. The total pressure ratio decrease rapidly after point P2, which indicates the onset of rotating stall. Large pressure ratio oscillation is observed between point P4 and P5. The unsteady calculation diverged at point P6 due to numerical instability. In the results of URANS, rotating stall simulation starts from the near stall point M1. It can be see that

pressure drop after the near stall point is almost linear without oscillation. The URANS modeling appears to smear the oscillation.

Fig. 9.2 shows the variations of mass flow rate during rotating stall for both DDES and URANS. The mass flow drops linearly up to 2.0T (T is the rotating time in one rotor revolution) at Point P2 where the stall inception occurs for the DDES simulation and decrease oscillatory and rapidly after that. The deep rotating stall occurs at P4 with the stall region growing toward inner span. In URANS, the mass flow drops slowly at the first 3T and starts oscillating after that.

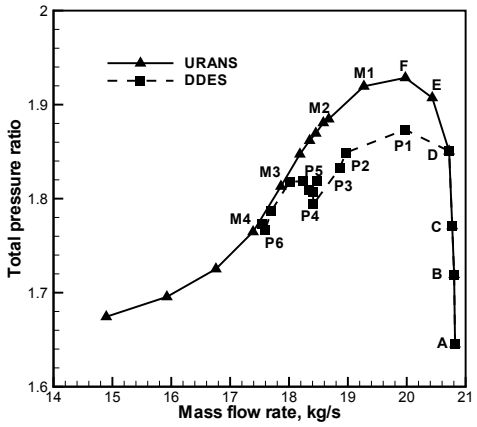

Figure 8.8: Predicted unsteady speed line with full annulus simulation

8.2.4 Rotating Stall Onset and Propagation

Rotating stall is usually initiated from rotor tip. This is also the case for the NASA Stage 35. To capture the rotating stall inception, the numerical probes are located about 50% tip chord length upstream and downstream at the rotor tip span. The term 'stall cell' used in the current study is to describe a continuous structure of disturbances.

Fig.8.10 shows the variations of instantaneous static pressure and axial velocity pre-

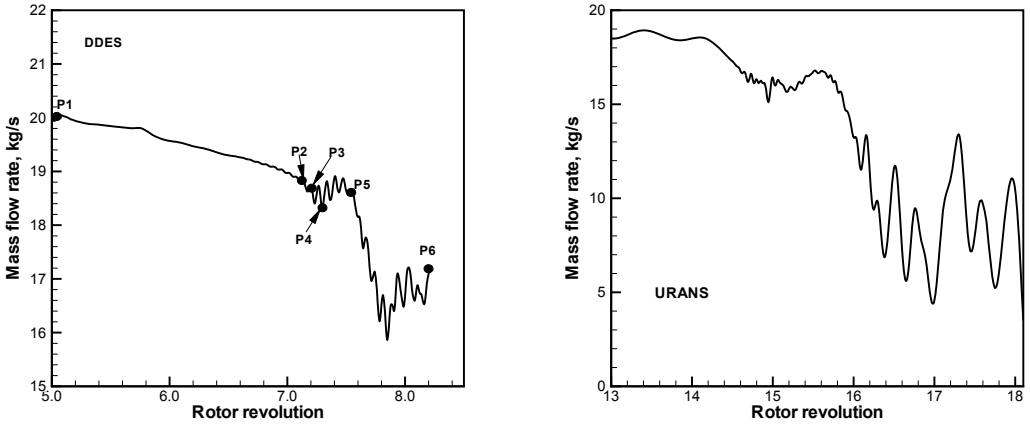

Figure 8.9: Inlet mass flow rate variation during rotating stall. Left: DDES. Right: URANS

dicted by both DDES and URANS at the rotor tip upstream. In the results of DDES, small amplitude of pressure fluctuations that is about 0.8% of the average pressure are observed near 7.0T, which covers about full annulus of the compressor and appear to be modal disturbance. Generally, the modal disturbance has a length scale of one rotor circumferential and propagates at about 20% to 50% of rotor speed. The modal disturbance observed in this study does not propagate, which is different from the classical modal wave. At about 7.3T, two spike disturbances with amplitude about 10.0% of the local pressure appear. The propagation arrows shown in plots are obtained by roughly connecting the peak of pressure in adjacent passage. The propagating speed of stall cell can be determined by the slope of the line. The two disturbances rotate at about 42% rotor speed. Large mass flow drop and fluctuations occur after the two stall inception cells are formed at about 7.5T as shown in Fig. 9.2.

At about 1T after the emergence of the two spike like inception stall cells(P2), the numerical simulation becomes unstable before the fully developed stall cells are captured. However, it does not affect the investigation of stall inception mechanism that is far before

the fully developed stall cells are formed. The trigger of stall inception is the flow instability instead of numerical instability, since the residual is less than 10^{-5} and 2 orders of magnitude residual reduction is achieved as shown in Fig. 8.7. The calculation is diverged quickly in a few pseudo time iteration within one physical time step.

For the results of URANS, the right plot in Fig. 8.10, a spike like disturbance traveling with full rotor speed is seen at about 14.5T. The spike disturbance continues to rotate and is transported to more blade passages with about 90% rotor speed. At about 1.5T after the stall inception occurs, the stall cells propagation slows down to 50% of the rotor speed in the opposite direction of the rotor rotation. The rotating stall is fully developed within 1.2 rotor revolutions. Both DDES and URANS captured spike like stall inception, which begin with modal like disturbance. However, DDES predicts the initial pressure disturbance with higher wave number than the URANS. In particular, the DDES captures two very distinct spike stall inception whereas the URANS tends to have the disturbance more smeared and organized. DDES captures two stall cells with lower propagating speed compared with URANS, which predicted one stall cell. The URANS can predicted a fully developed rotating stall cell that can not be obtained by using DDES due to numerical instabilities.

The time history of axial velocity(U_x) at half tip chord length upstream of the rotor are shown in Fig.8.11. The variation of U_x is similar to that of pressure, and the difference is that the lower of the axial velocity corresponding to the higher of pressure at the same time. The propagating speed of the stall cell is more clear and we can roughly calculate the propagating speed of the stall cell from this plot.

The time traces of pressure and axial velocity located at rotor stator interface are illustrated in Fig. 8.12 and Fig. 8.13 respectively. It can seen that the propagating behavior of

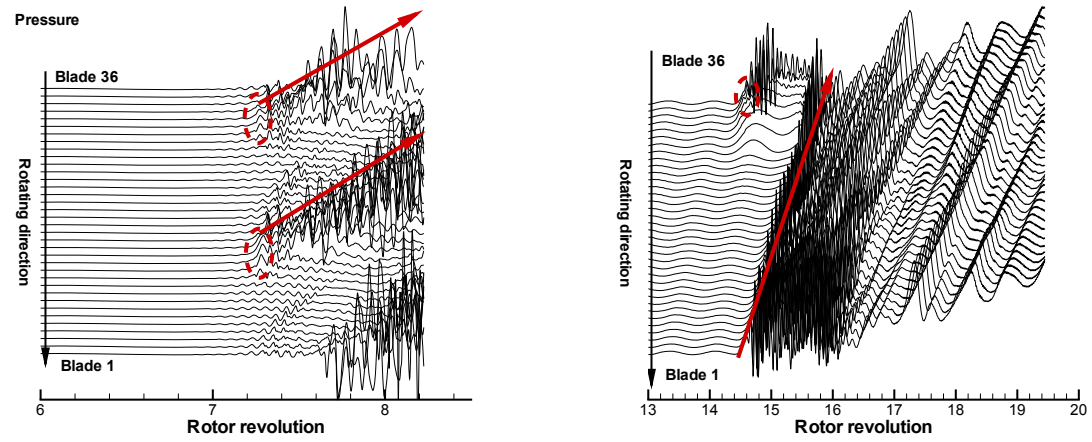

Figure 8.10: Time traces of pressure near half tip chord length upstream of the rotor leading edge at the tip span. Left: DDES. Right: URANS

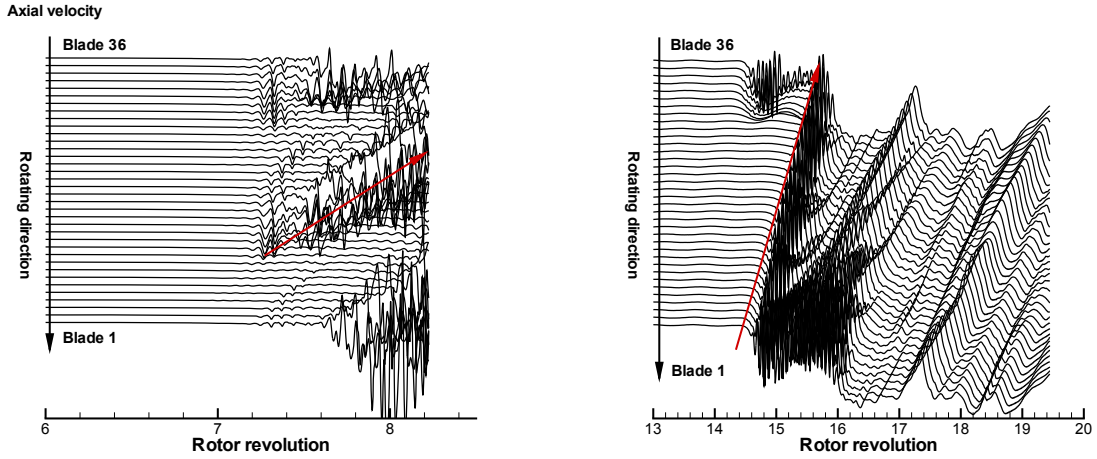

Figure 8.11: Time traces of axial velocity near half tip chord length upstream of the rotor leading edge at the tip span. Left: DDES. Right: URANS

the stall cell is also observed at rotor downstream. Two main rotating stall cells are also observed in the left plot (DDES) and one stall cell in the right plots (URANS). They indicate the axial range of the stall cell is at least from the leading edge of the rotor to the sliding interface between the rotor and the stator. Considering the results of DDES, the propagating speed of the two stall cells are almost the the same as that observed in the rotor upstream, but the propagating direction of the stall cells at downstream of rotor is opposite to that at

rotor upstream in the relative frame. Furthermore, the rotating stall at the downstream of the rotor starts about 0.1T earlier than that at the upstream, which may be due to the rotor stator interaction. The pressure and axial velocity predicted by the URANS at downstream of the rotor trailing edge also show one stall cell.

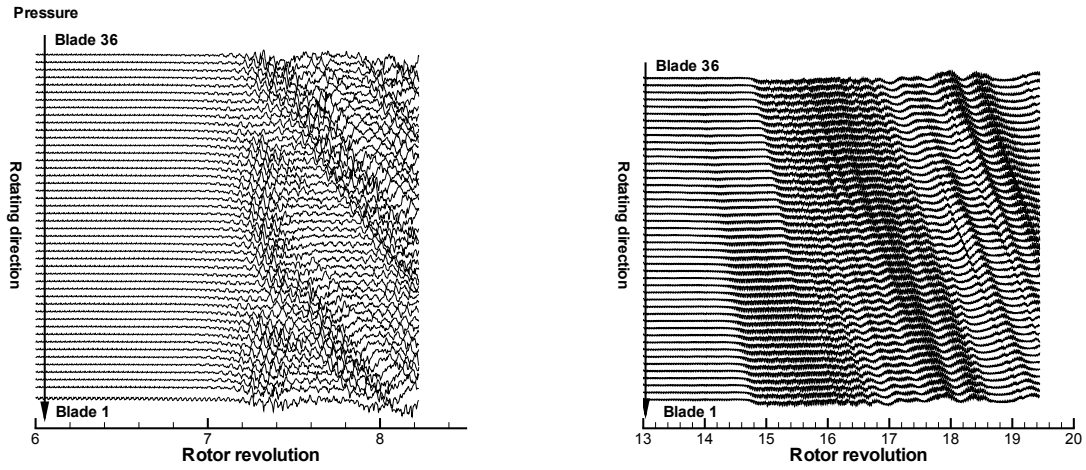

Figure 8.12: Time traces of pressure near half tip chord length downstream of the rotor trailing edge at the tip span. Left: DDES. Right: URANS

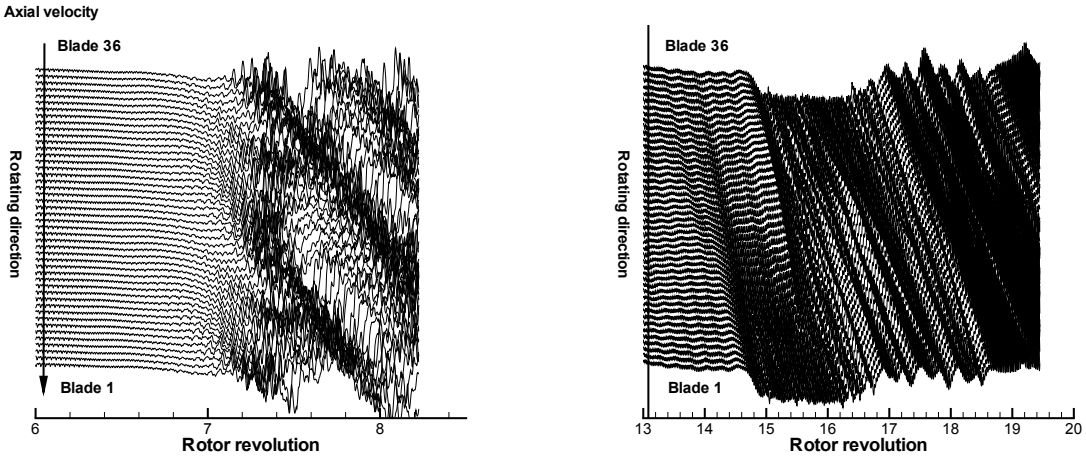

Figure 8.13: Time traces of axial velocity near half tip chord length downstream of the rotor trailing edge at the tip span. Left: DDES. Right: URANS

In the stall simulation of Stage 35 by Chen et al. [85], the modal disturbance is observed at the first 2 rotor revolutions and then it transforms into spike disturbance. The modal

disturbance in their study is also not a classical one, because the propagating speed is 100% of rotor speed. The forming process of the spike disturbance in this study has similar pattern, but occurs more rapidly. From the modal wave to spike, the present simulation has only 0.3 rev. However, the spike disturbances captured in this thesis are more compact, covering about 6 blade passages. The number and size of stall cells can not be observed in the similar plot of time trace of pressure in the results of Bright et al. [80] and Chen et al. [85], since there are only 8 numerical probes located near the rotor leading edge. Casing wall static pressure experimental measurements of Stage 35 by Bright et al. [80] shows the spike(pip) inception is a disturbance standing on the modal wave. This phenomenon is not clearly seen in the numerical results of Chen et al. [85] and Gan et al. [87].

The time history of circumferential flow variables can be also used to investigate the stall inception characteristics. Fig. 8.14 and Fig. 8.15 show the circumferential distributions of the normalized static pressure and velocity respectively, located at 50% tip chord upstream of rotor at different instant. For easy comparison, the results at different instant of the 50% span are plotted at the same figure at different radial location. Readers should not confuse them as the results at different span. For DDES, at t=7.0T(P1), the flow around the full annulus is periodic and no disturbances are observed. The variation of static pressure through full annuls appears to have sharp oscillations, which indicates that there exit strong shock waves near the leading edge of the rotor. At t=7.25 T(between point P3 and P4), the flow periodicity is lost at some parts of the annulus, and the annulus region containing large disturbance are from $90^\circ \sim 150^\circ$ for the first stall cell, and $280^\circ \sim 340^\circ$ for the second stall cell. It indicates that the sizes of the stall cell at this moment cover about 5 to 6 passages. The local non-uniform pressure indicates the onset of the spike type rotating stall. At about

1T after the stall inception point P2, the rotating stall reaches point P6 at 8.2T. Fig. 8.14 shows that the sharp edge shapes of pressure distribution disappear after t=7.25T in the stall cell region due to the shock waves moving to upstream. For the URANS result, one stall cell was captured, but the size of the stall cell is about the same as that of the DDES.

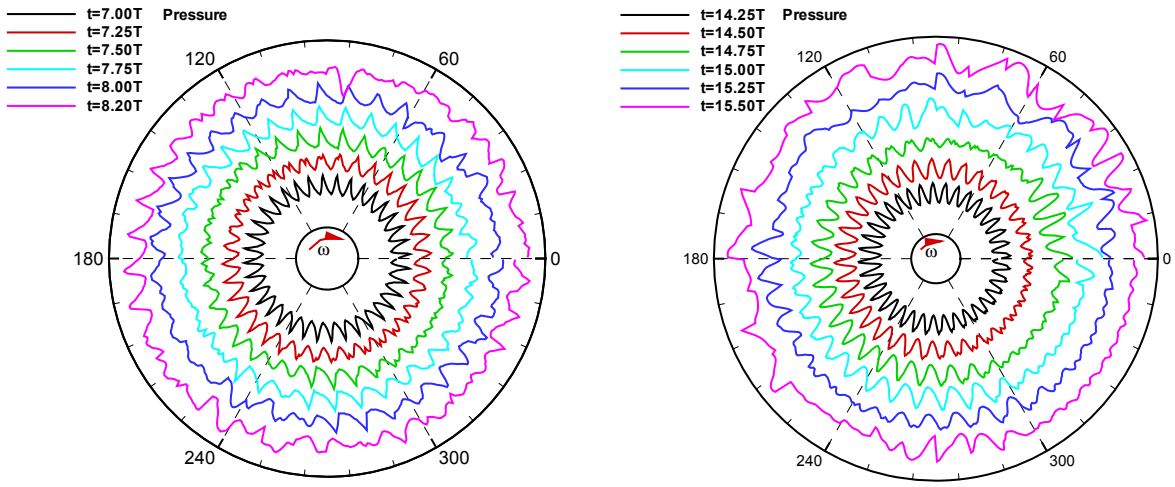

Figure 8.14: Circumferential variations of pressure at tip span. Left: DDES. Right: URANS

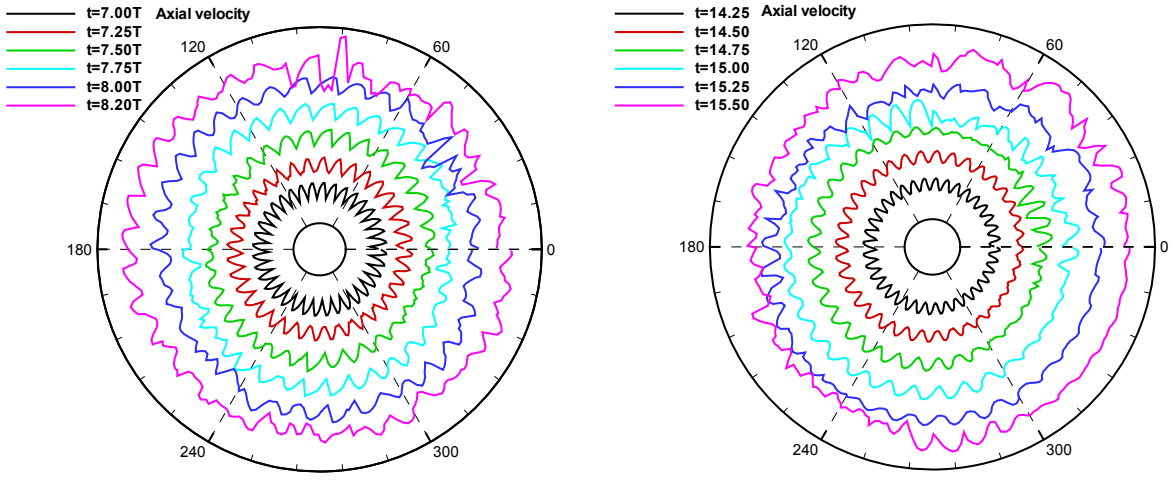

Figure 8.15: Circumferential variations of axial velocity at tip span. Left: DDES. Right: URANS

The previous results show that the predicted propagating speed of stall cell by using URANS method is about 90% of rotor speed, which is about two times of the DDES. The mass flux in circumferential direction at 7.33T, as shown in Fig. 8.16 may be used to understand the cause of the speed difference in the methods of URANS and DDES. It is seen that the amplitude of circumferential mass flux oscillation predicted by the URANS is about the same as the DDES at the mid span where there is no stall flow. However, the amplitude of the mass flux oscillation at stall region predicted by the URANS at tip span is about two times greater than that of the DDES. The large gradient of tangential mass flux between the stalled region and unstall region may cause the stall cell propagating with such high speed in the URANS. It appears that the propagating speed of rotating stall is determined by the circumferential mass flux oscillation in the relative rotating frame.

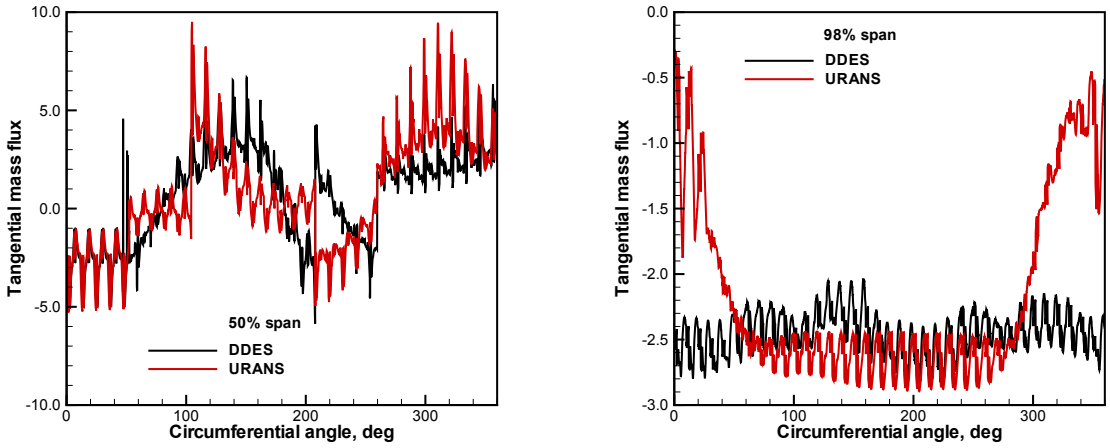

Figure 8.16: Relative circumferential flux at the mid span(Left) and tip span(Right) near rotor leading edge

Fig. 8.17 and Fig. 8.18 illustrate entropy contours in axial cross section near the rotor leading edge and trailing edge. Entropy stands for the degree of energy loss and high entropy reflects the stalled region of the annulus. For DDES, at 7.33T(right after stall onset),

two high entropy regions near casing appear as the indication of the stall stall inception covering about 6 blade passage. Fig. 8.17 shows that the stall cell starts from the rotor tip area, and grows along the circumference as well as inward. Compared with DDES, the stalled flow region predicted by URANS is more smooth and continuous. This is because that the RANS modeling using time average creates false isotropic structures that smears the large flow structures. The stall cell of the URANS developed faster than that of the DDES in both circumferential direction and inward span within the same time.

The entropy contours near the rotor trailing edge are shown in Fig. 8.18. It is observed that the flow at the rotor trailing edge has larger blockage and more energy loss than that at the rotor leading edge. The tip leakage vortices, flow separation on suction surface, and trailing edge wakes all contribute to the blockage and energy loss.

Fig. 8.19 shows the entropy contour lines within the tip clearance predicted by both DDES and URANS during the stall inception. It can be seen that the axial length scale of the initial stall cell is about one tip chord length in both DDES and URANS. As the stall cells develop, the flow blockages extend both upstream and downstream of the rotor.

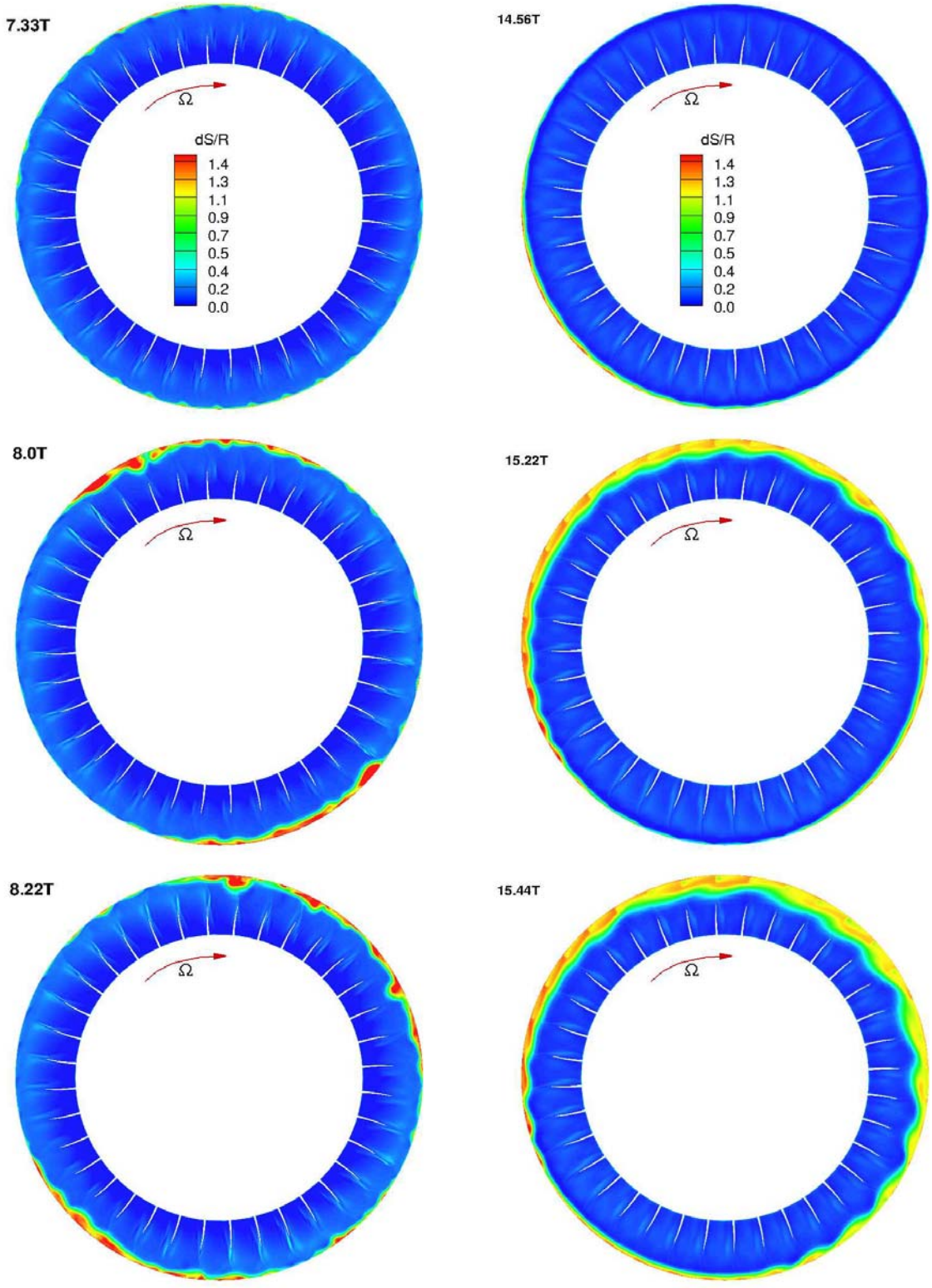

Figure 8.17: Entropy near rotor leading edge. Left: DDES. Right: URANS

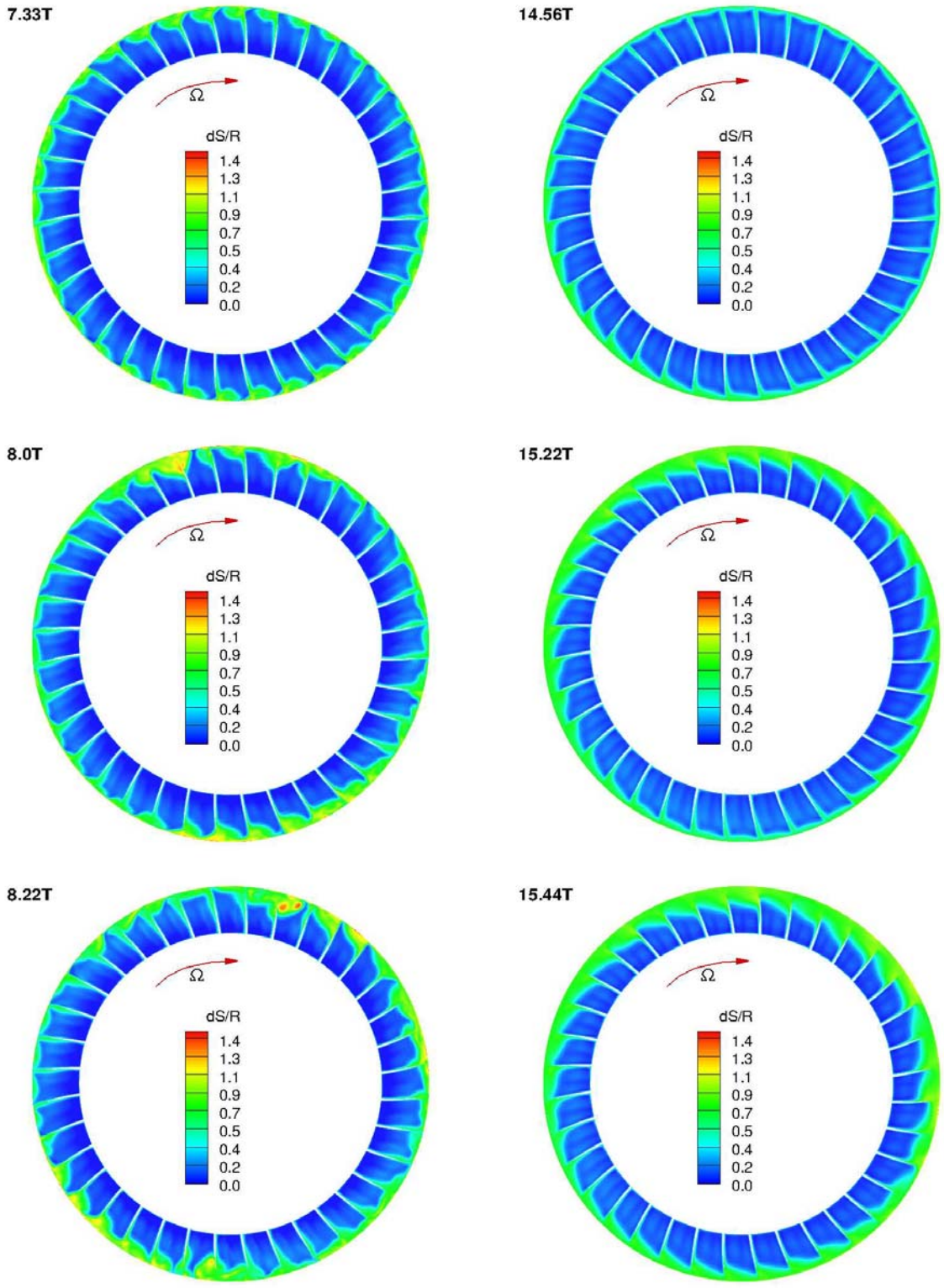

Figure 8.18: Entropy near trailing edge. Left: DDES. Right: URANS

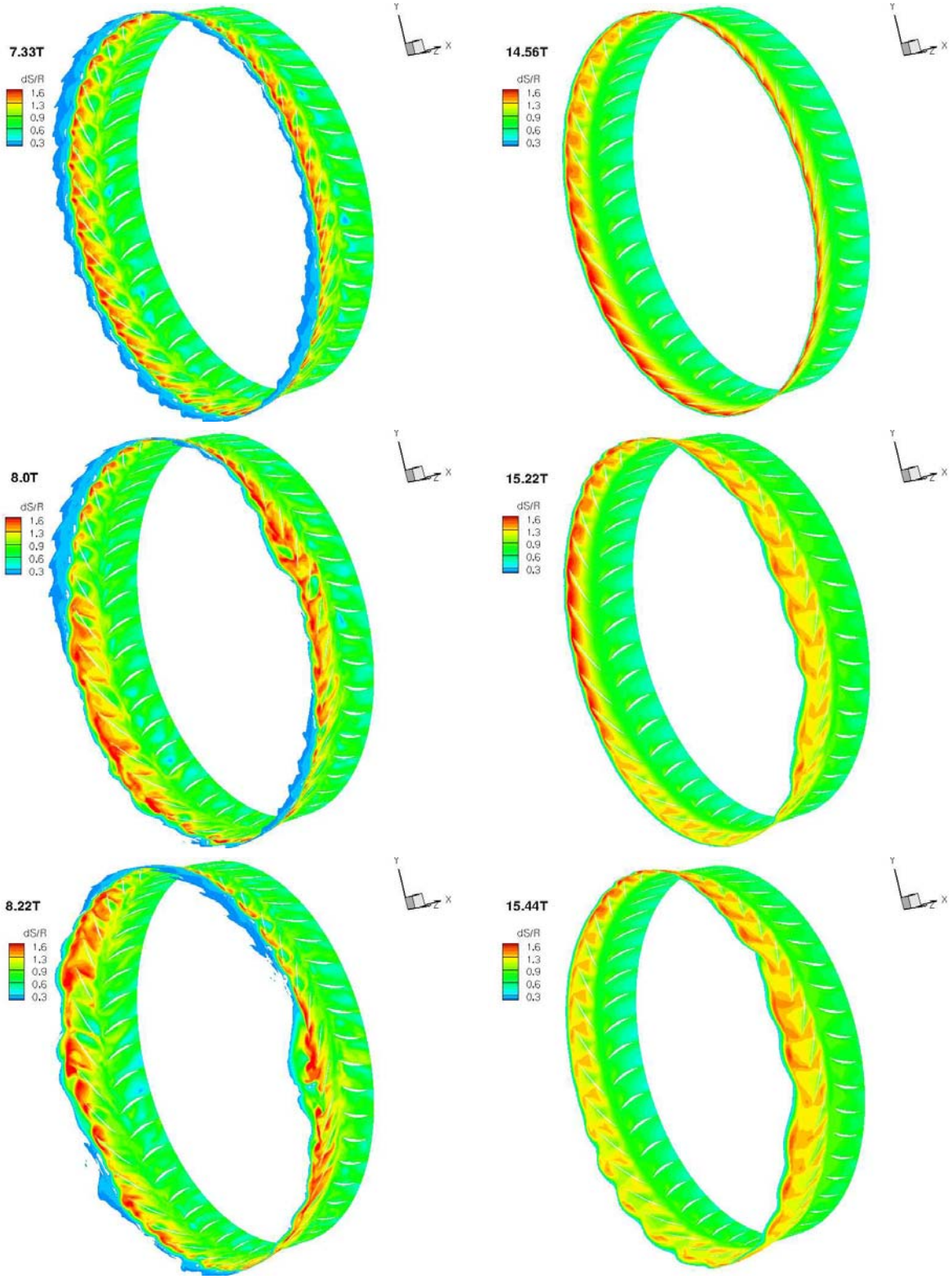

Figure 8.19: Entropy at the mid tip clearance span. Left: DDES. Right: URANS

Flow mechanism of rotating stall

Fig. 8.20 shows the relative velocity vector and Mach number contour indicating the sonic boundary at the tip span. The results of DDES are compared with that of URANS. The plots are used to track the stall cell in the annulus. Considering first the results of DDES, at 7.11T, before the onset of rotating stall, the sonic lines is attached and oblique to the rotor leading edge. And there are no back flow observed from the rotor trailing edge. At 7.33T, the stall onset point, a large distinct passage vortex is formed in each blade passage near the rotor tailing edge. The through flow is largely blocked by the vortex. The sonic boundary moves upstream of the leading edge due to the flow blockage. At 8.0T, the stall cells grows larger and the sonic line is pushed further upstream. The vortex moves upstream and interacts with tip leakage flow, which forms a large vortex located in the middle of the blade passage near the rotor leading edge.

The URANS method also predicts similar large blockage at 15.56T at stall onset as shown in the right plots of Fig. 8.20. However, the blockage is mostly formed by the reversed flow instead of distinct passage vortex as observed in DDES. The sonic boundary movement predicted by URANS is similar to that of DDES, but is smoother.

The instantaneous contours of static pressure predicted by both DDES and URANS at the tip span are shown in Fig. 8.21. It can be seen that the spike stall inception region has higher blockage that generates highly spiky and oscillatory pressure wave propagating upstream, which destroys the circumferential periodicity. Similar phenomenon can also be seen in the results of the URANS on the right of Fig. 8.21. However, the pressure wave is much smoother due to being smeared bye the RANS model. As the rotor rotating, the stall cell propagates in the opposite direction of rotor revolution in relative frame as shown

in Fig. 8.17 and grows rapidly. The flow blockage becomes larger with time at 8.0T, the non-periodic flow near the tip span covers most of the rotor passages. Furthermore, it is evident that the rotating stall is convected downstream of rotor and interacts with stator, which creates a significant blockage in the stator blades.

The vortex structures captured by DDES during rotating stall near the rotor tip span are shown in Fig. 8.22. At 7.11T before stall inception,the tip vortex from the blade leading edge has the streamwise trajectory going downstream in the vicinity of leading edge. The vortex then merges with the tip leakage flow from the upstream rotating blade passage. The vortex trajectory becomes tangential and reaches the leading edge of the downstream rotating blade. An obliques tip leading edge vortex forms again in the next blade and the pattern repeats in each blade. The vortex structure is circumferentially connected from one blade to the next in the stall regime.

At 7.33T when the stall inception occurs, the vortex emanating from the blade tip leading edge rolls up to end on the casing wall with the vortex axis mostly in the radial direction and normal to the casing wall. This radial vortex can be clearly seen in Fig. 8.20 and 8.22. The vortex structures during stall inception are similar to those observed in [124]. The radial vortex appears in each of the stall inception blades. With the rotating stall inception growing, the radial vortex shedding frequency is also increased that there are two clear strong radial vortices appearing in the same blade passage at 8.0T as shown in Fig. 8.22. It appears that the stall inception occurs with the tip vortex changing from streamwise to radial. Fig. 8.22 also shows that there is a weak vortex near the trailing edge that is formed by the back flow from the upstream blade.

Fig. 8.23 shows the radial distributions of total pressure ratio predicted by DDES during

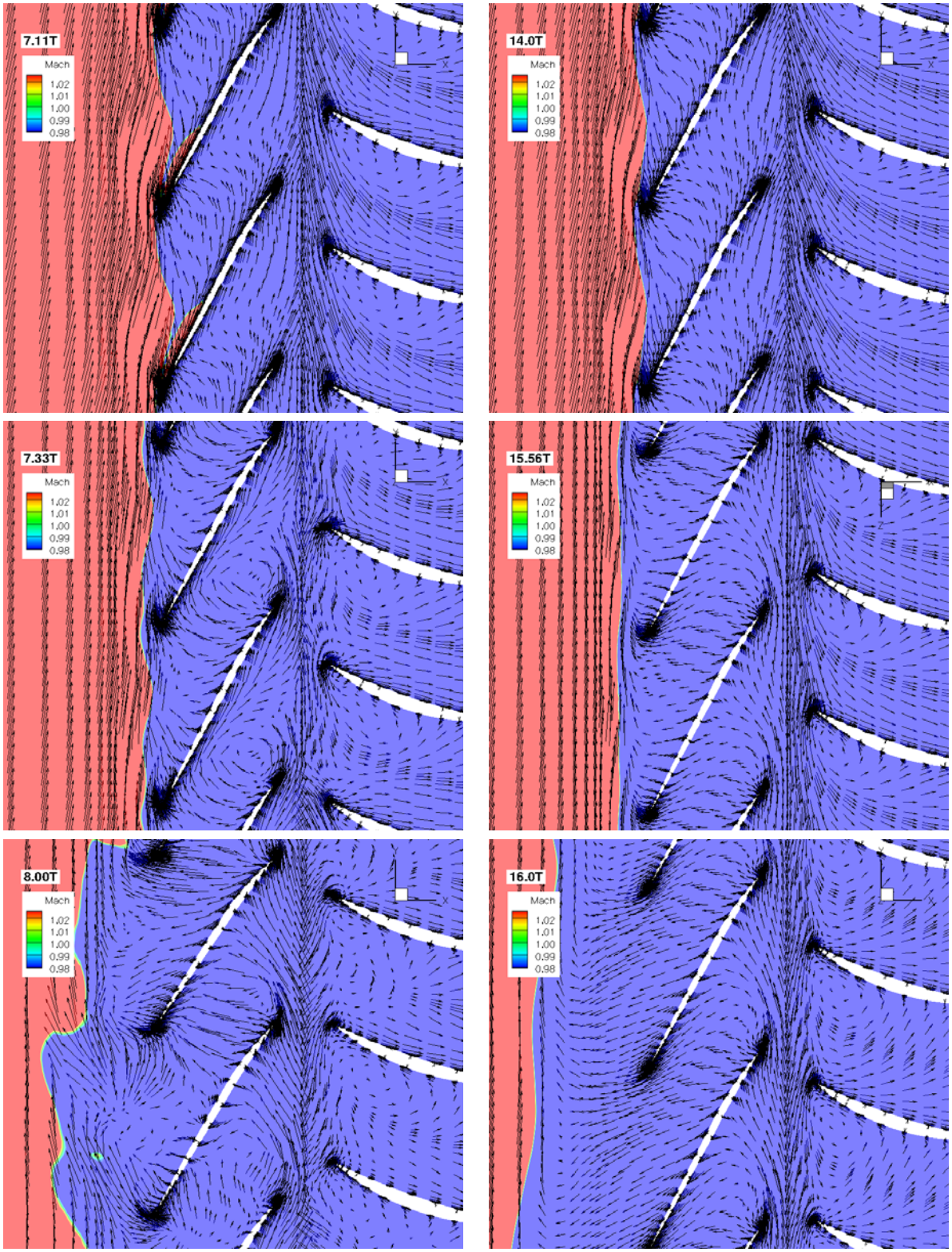

Figure 8.20: Velocity vector of rotor tip span with Mach number contour indicating sonic boundary. Left: DDES. Right: URANS

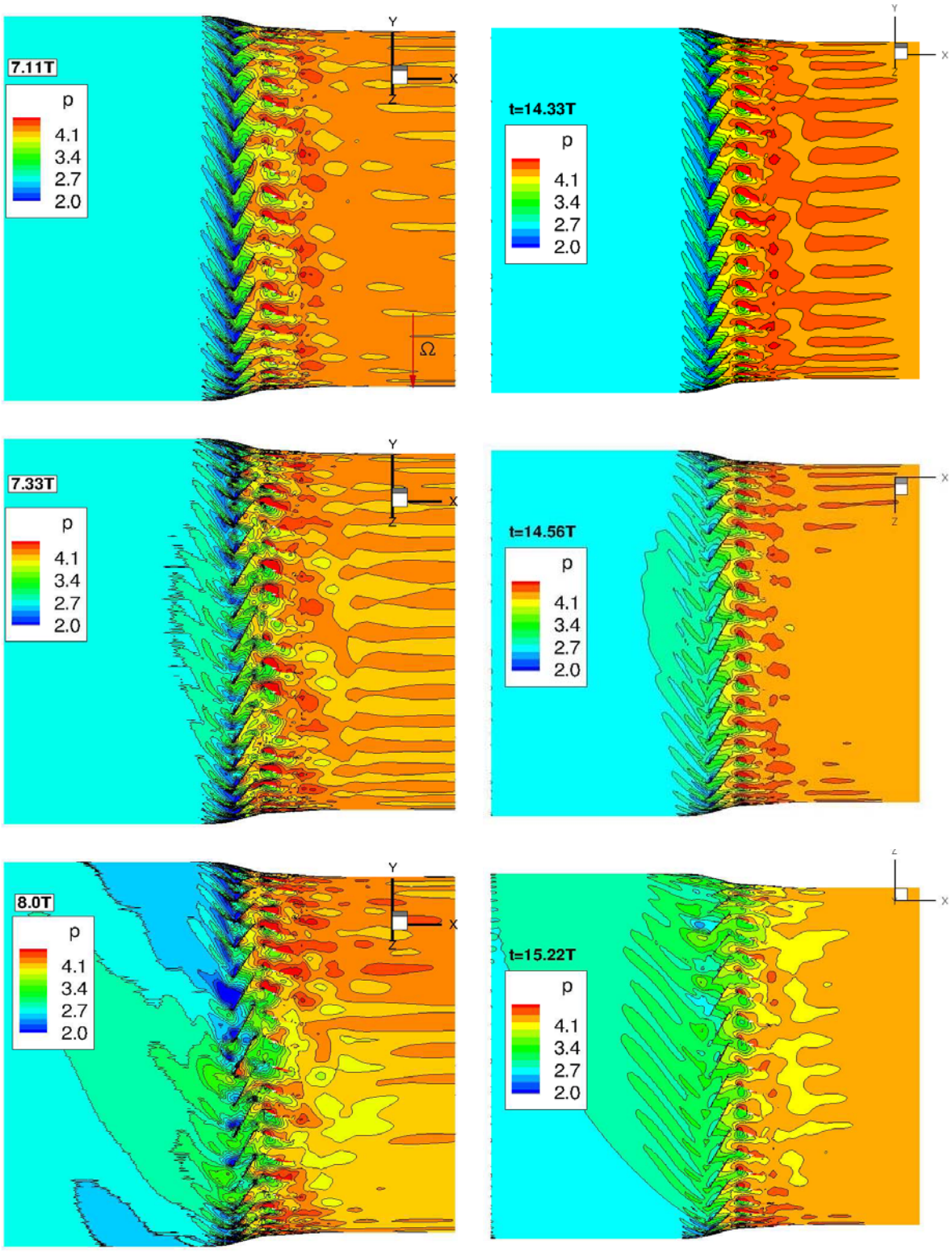

Figure 8.21: Static pressure at the tip span. Left: DDES. Right: URANS

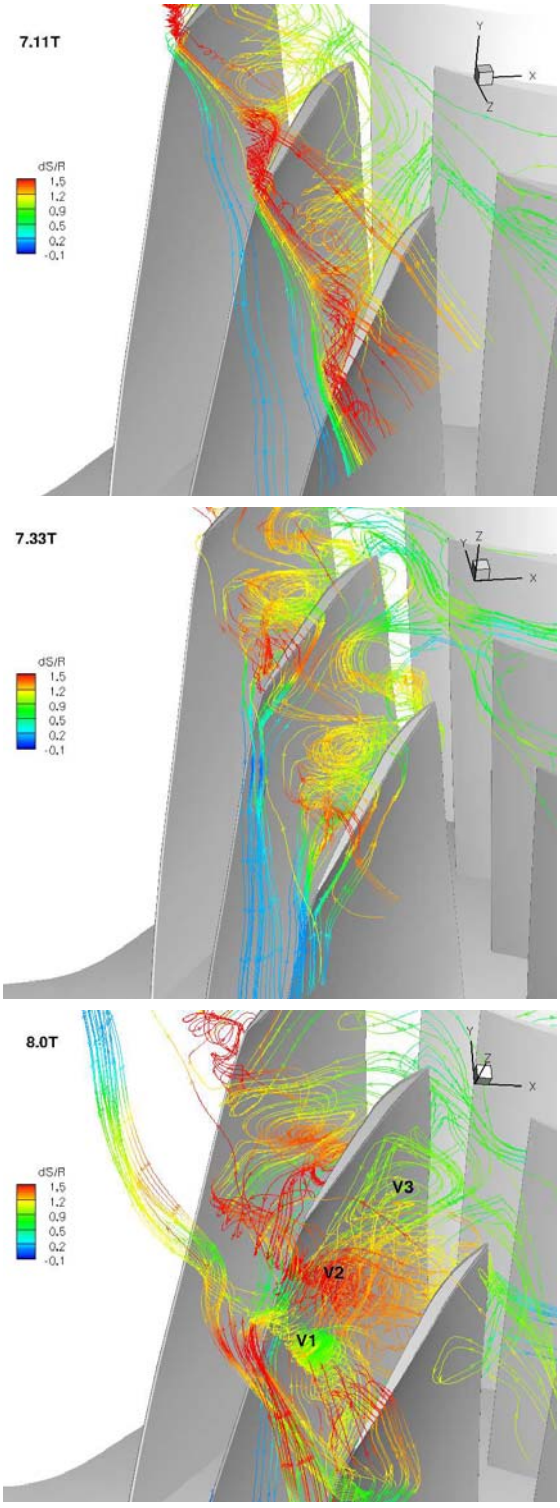

Figure 8.22: Flow structure colored with entropy near tip span

rotating stall. There is a sudden decrease of total pressure ratio near the rotor tip span at the onset of spike inception at 7.22T. Interestingly, the large total pressure drop in the tip

region of the rotor disappears with the stall inception growing. Instead, the total pressure drop is spread to the whole span. This appears to be because the blockage created by stall inception is quickly spread to the whole span. It relieves the tip blockage, but increases the overall blockage along the span.

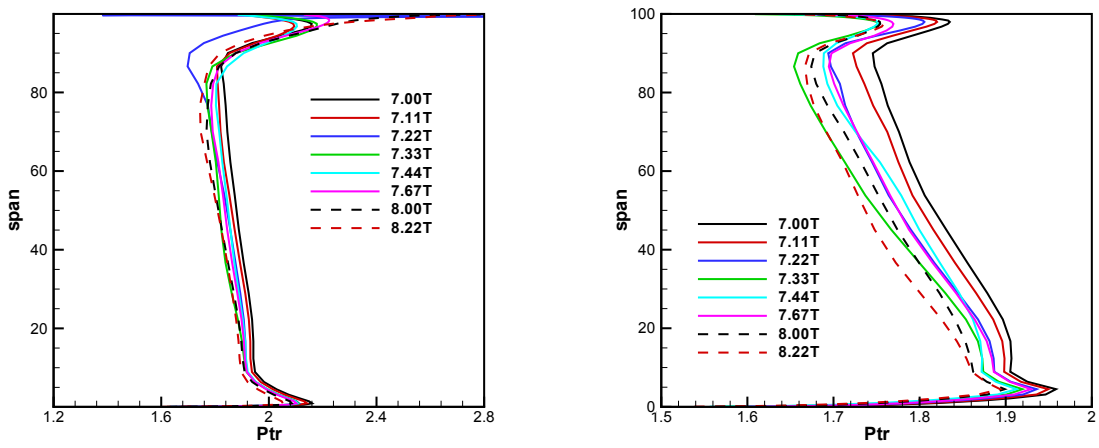

Figure 8.23: Spanwise distributions of pitchwise mass-averaged rotor (Right) and stage (Left) total pressure ratio during rotating stall

Conclusions

DDES is conducted for the first time to investigate a full compressor stage , NASA Stage 35, rotating stall inception mechanism with sliding interpolation BC between the rotor and the stator. The details of the flow breakdown that leads to fully developed rotating stall is well captured by the present numerical simulation. The simulation shows that the rotor stall onset begins with modal disturbance followed rapidly by two spike disturbances. The size of an onset stall cell covers about 5 to 6 rotor blade passages. The propagation speed of stall cell is about 42% of rotor rotating speed. This DDES of stall inception captures two stall cells whereas the URANS simulation only has one stall cell propagating at about 90% rotation speed. The different propagating speed of stall cells between the URANS and the DDES appears to be caused by the different circumferential mass flux and flow speed.

The vortex trajectory aligned in the blade pitching direction is an indicator that the stall inception is imminent. The spike stall inception appears to be characterized as the tip vortex rolling up and ending on the casing wall with the vortex axis mostly in the radial direction. Similar to the conclusions in Im et al. [1], the DDES captures many small scale structures of the stall inception, whereas the URANS tends to smear the flow structures due to the Reynolds time average.

Chapter 9

Stall Flutter of a High Speed Compressor Stage

Stall flutter is an aeromechanic instability that usually occurs at part-speed operation in turbomachinery. It occurs when the energy absorbed by the blades from surrounding fluid exceeds the dissipating energy of the material and mechanical damping. The blade will vibrate exponentially and cause possible structure failure. Transonic stall conditions in turbomachinery are highly unsteady, non-linear and three dimensional, which include flow induced vibration, flow separation, shock unsteadiness, shock wave/turbulent boundary interactions. The driving mechanism of the stall flutter in transonic turbomachinery may vary due to separation and shock wave oscillation.

The purpose of this chapter is to simulate a transonic stall flutter in a full stage with rotor-stator interaction and traveling waves. In this thesis, the URANS is used in most stall flutter calculations and the DDES is also utilized at near stall condition for comparison. The full annulus of NASA Stage 35 is selected to demonstrate this capability and to avoid introducing the error due to circumferential phase lag boundary conditions. This is an important step forward to improve the industrial aeromechanic design and analysis accuracy.

9.1 Mesh and Mode Shape

The same transonic axial compressor, NASA stage 35 used in the study of rotating stall in Chapter 8 is simulated to investigate the driving mechanism of stall flutter. The same mesh for the stall inception is also used in the calculation. The blade structure is modeled by its first 5 natural vibration mode shapes generated by using commercial solver ABAQUS. The design rotating speed is 17188.7 rpm. The blade is made of material Maraging200 with a density of 8200 kg/m3 approximately. Fig. 9.1 shows the 1st to 5th mode shapes. The blades are modeled as fixed at the rigid body rotor and the centrifugal force is considered in mode extrapolation. The mass ratio between the blade and air is about 7528. It is not clear if Stage 35 actually had flutter since the material appears to be very rigid with high density ratio to air. This rotor is selected because the geometry data is available in the public domain.

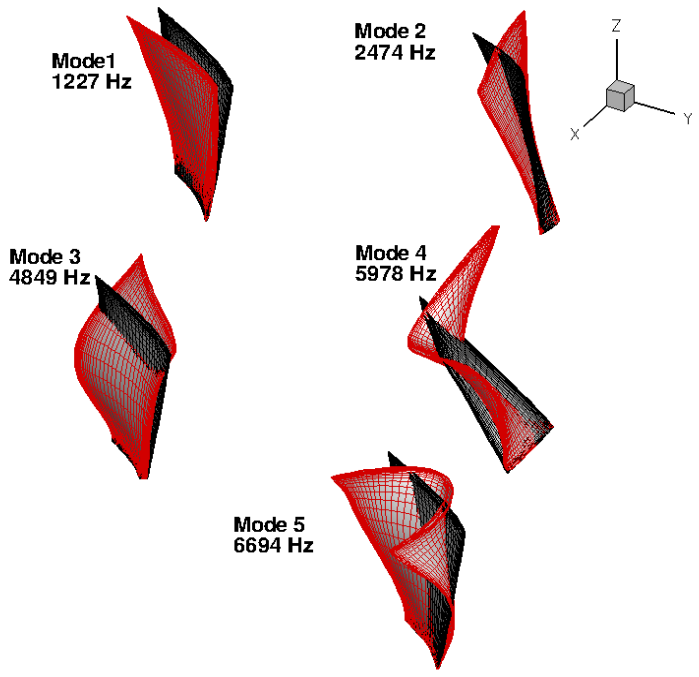

Figure 9.1: Mode shape of Rotor 35

9.2 Stall Flutter Simulation

The simulations start with the unsteady calculation of the flow field of the stationary rigid blades. The FSI simulations start when the unsteady flow field around the blades is fully developed. Because the stall flutter usually occurs at near stall point, the back pressures are adjusted along the speedline as shown in Fig. 8.3 for point B, C, D and E to capture the flutter. As a small imposed initial perturbation, all the five modes of the blade structural motion are given the same normalized initial velocity, which is 1.0e-6. Then the blades are allowed to deflect in response to the dynamic force load. Within each physical time step, the solution is usually converged with 20-30 iterations with the residual reduced by 2-3 order magnitude. Fig. 9.2 shows the variations of mass flow rate during rotating stall with FSI simulation. It can be seen that the mass flow drops slowly up to 1.0 revs and decreases quickly after point E. The mass flow rate is dynamically stable for FSI simulation from point A to E.

The time history of the first 5 modal displacements with a backward traveling wave of ND=1 at condition point C in the map (Fig. 8.3)is shown in Fig. 9.3. In this result, zero structural damping ratio is used in the calculation. The response of the first mode increases gradually, while the other modes decay with time. The first mode is dominant since the amplitude of the first mode is about 4 times higher than that of the second mode. The response of the first mode at working conditions of point B, C, D and E are compared in Fig. 9.4. It can be seen that the amplitudes of the first mode at all conditions diverged gradually, which indicates that the predicted response is flutter in the first mode without structural damping. As the working point shifting from near peak condition (point D) to near stall condition (point E), the vibration amplitude continue to increase. The largest

blade vibration occur at point E and the response become diverging due to the non-periodic rotating stall flow acting on the blade surfaces.

Turbomachinery blade flutter usually occurs with a traveling wave in which the blades vibrate at the same frequency but with a constant phase difference termed as inter blade phase angle. The numbers of nodal diameter are unknown before an engine is made and tested. One of the preliminary jobs of aeroelastic design of compressors is to find the least stable nodal diameter. The modal displacements with different inter blade phase angle in backward traveling mode is shown in Fig. 9.5. The results in the plot are used zero structural damping coefficient at point C. It is shown that the amplitude of the 1st mode decreases as the number of ND is increased. The phase angle of ND=1 is least stable condition. Fig. 9.6 shows the generalized displacement for all the blades. It can be seen that the traveling waves are clearly captured. For ND=1, one blade vibration cycle of the rotor full annulus is clearly captured where two cycles appear for ND=2.

The structural damping is one of the important parameters in the vibrating behavior of the rotor blades, which is difficult to obtain from experiment. The structural damping value of the blades in NASA Stage 35 is not available. All the structural damping coefficients used in the calculation are set with empirical values. The modal displacement of the 1st mode with different damping coefficient are shown in Fig. 9.7. It can seen that the vibration amplitude decreases as the structural damping is increased. Fig. 9.8 shows the response of the 1st mode with damping value of 0.003 at different working conditions. It is observed that the vibration damped quickly with this higher damping coefficient at all points except at point E. The response of point E damped in the first three rotor revolutions and diverged after that. The Stage 35 compressor rotating stall inception occurs at near point E. It appears

that the stall flutter in Stage 35 is due to the rotating stall.

The DDES method is more capable of predicting flow separation than URANS. Thus DDES is also used for FSI calculation at rotating stall point E. The predicted modal displacements of the 1st mode by using both URANS and DDES are shown in Fig. 9.9. It can be seen that both methods predicted damped responses in the first 2 rotor revolutions. The response predicted by URANS begin to diverge after 3.5 rotor revolutions. And the amplitude of the 1st mode predicted by DDES begin to diverged after 2.5 rotor revolutions. The amplitude of vibration predicted by DDES is higher than that of URANS. The DDES method predict more energetic flow structure than the URANS method. The onset of rotating stall in the DDES starts earlier than that of URANS.

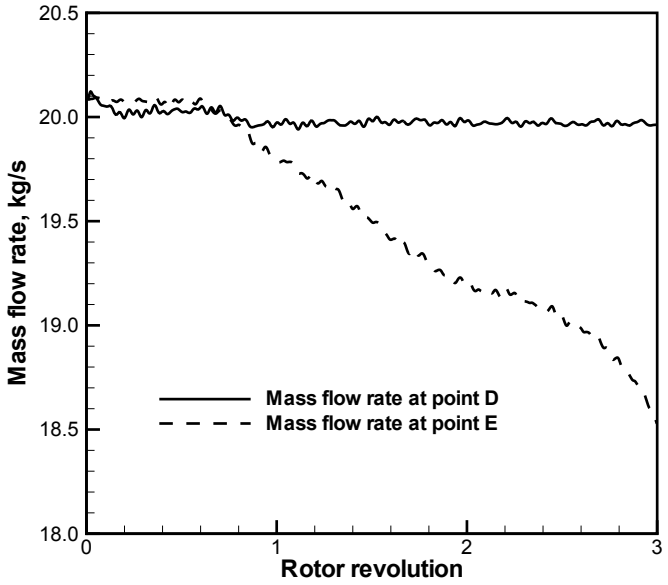

Figure 9.2: Mass variation during blade vibration

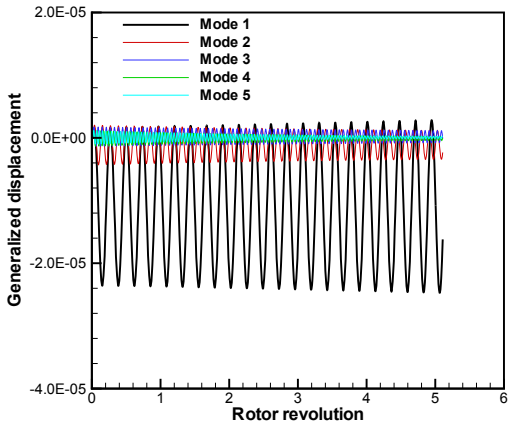

Figure 9.3: Modal displacements with ND=1 and zero structural damping at point C

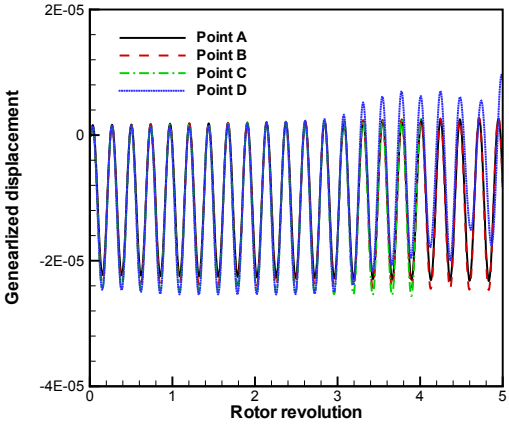

Figure 9.4: Modal displacements with ND=1 and zero structural damping at different working points

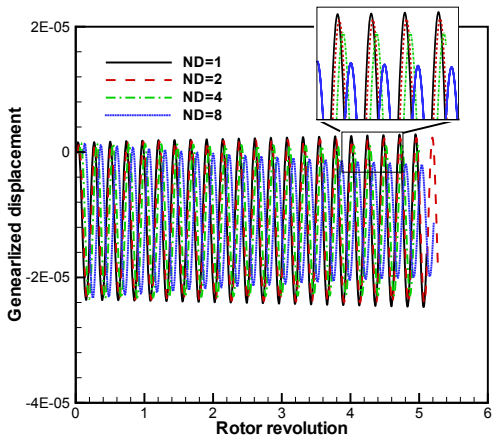

Figure 9.5: Blade 1st mode response with different nodal diameter at Point C

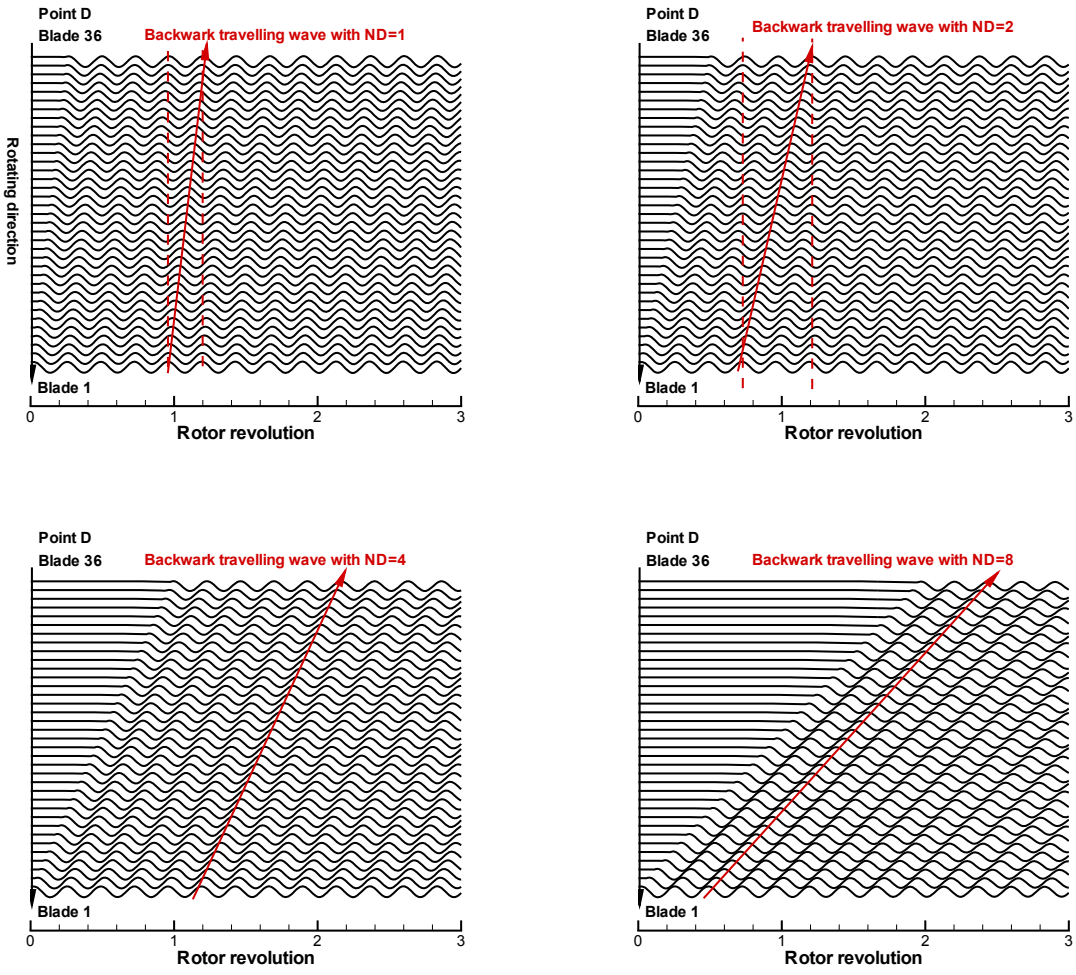

Figure 9.6: Predicted the backward traveling wave of 1st mode with a constant phase angle at point C

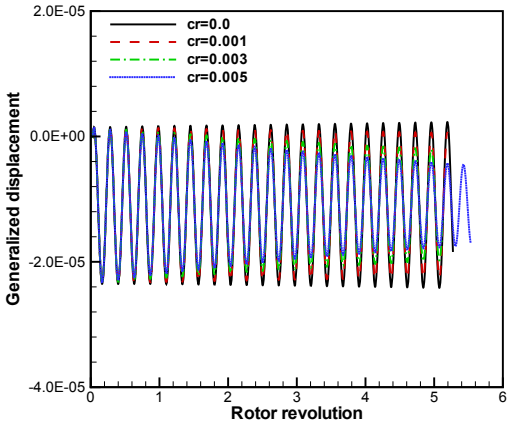

Figure 9.7: Blade 1st mode response with different structural damping and ND=1 at Point C

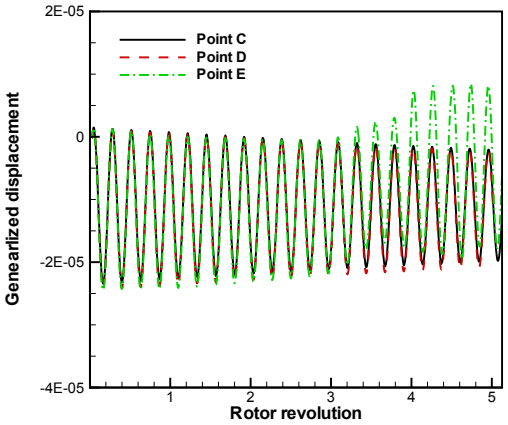

Figure 9.8: Blade 1st mode response with ND=2 at different working points

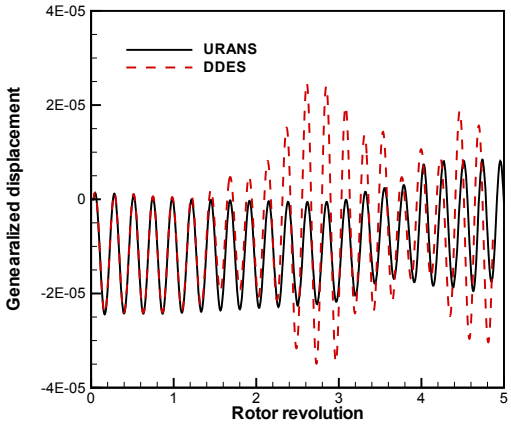

Figure 9.9: Predicted 1st mode displacements using DDES compared with URANS

9.3 Stall Flutter Mechanism

9.3.1 Without Damping

Simulations are conducted at stable condition point C with 2 nodal diameters and zero structural damping. Hence, all the damping in the structural response is from the aerodynamic damping. The blade vibration is unstable with these input parameters as shown in Fig. 9.5.

Fig. 9.10 shows the modal force and modal displacement during flutter. The modal force and modal displacement is about in phase, which indicates an unstable condition. Fig. 9.11 shows the time histories of angular displacement and pressure at leading edge near tip span during flutter. The unsteady pressure fluctuation is also about in phase with that of the angular displacement.

Fig. 9.12 shows the spectrum of angular displacement at the leading edge of rotor tip. The blade vibration is mainly at the first mode. The higher modes have the amplitudes at least three times smaller than that of the first mode. This is consistent with the modal displacement shown in Fig. 9.3. Fig. 9.13 shows the spectrum of static pressure at the leading edge of rotor tip. The dominant frequency is near the first natural frequency. Fig. 9.14 illustrates the pressure contours at point C during fluid structure interaction. The flow near rotor tip is periodic and dynamically stable. Shock waves are the dominant flow structure in the blade passages.

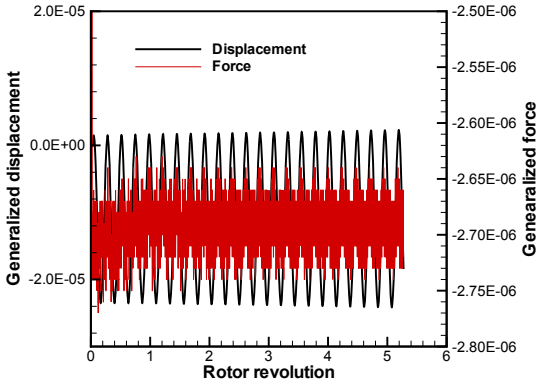

Figure 9.10: Modal displacement and force of 1st mode at point C with ND=2 and zero damping

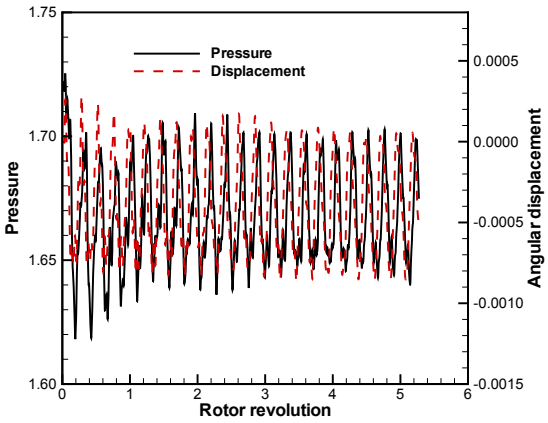

Figure 9.11: Time history of pressure and angular displacement at point C with ND=2 and aero damping

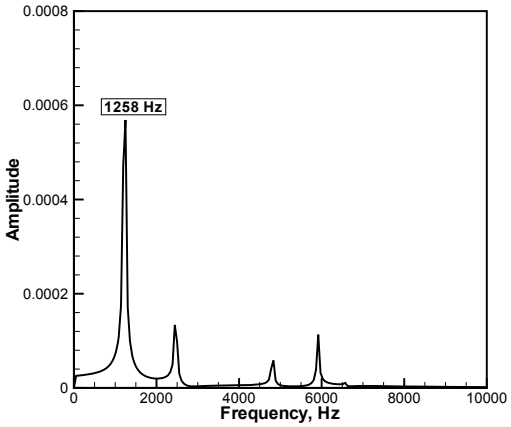

Figure 9.12: Spectrum of angular displacement near the leading edge at the rotor tip

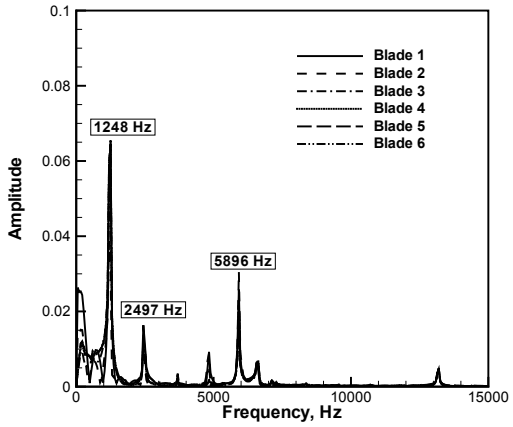

Figure 9.13: Spectrum of pressure near the leading edge at the rotor tip

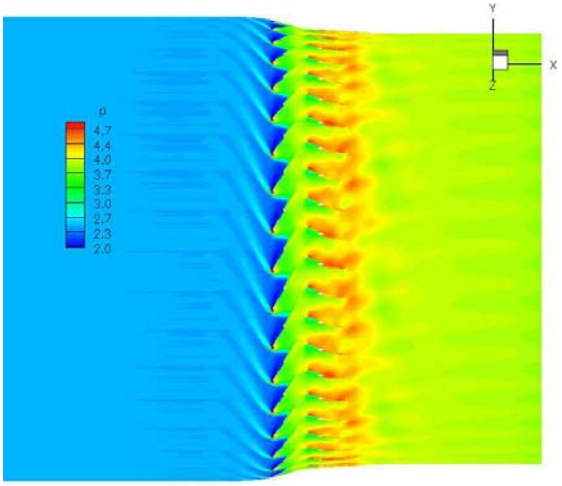

Figure 9.14: Pressure contour near tip span at time of 4 rotor revolution

9.3.2 With Damping

The blade vibration is damped with the structural damping coefficient of 0.003 at all points on the compressor characteristics map, except at the near stall point E. Fig. 9.15 shows the time history of mass flow rate at point E by using URANS and DDES. It can be seen that the predicted mass flow rate drops sharply after about 2 or 3 rotor revolutions with both URANS and DDES, which indicates the onset of rotating stall. The stall inception predicted by DDES starts about 2 rotor revolution earlier than that of URANS. The mass flow fluctuation amplitude of the DDES appears to be higher than that predicted by URANS. This maybe the reason that the predicted amplitude of blade vibration by DDES is higher than that of URANS as shown in Fig. 9.9.

Rotating stall in Stage 35 starts from rotor tip as described in Chapter. 8, the onset of rotating stall may be sensitive to the flow perturbation in the near tip region. The interaction of tip leakage flow with rotor tip shift the onset of stall with lower back pressure. Fig. 9.16 shows the variations of instantaneous static pressure at half rotor tip chord length upstream of the rotor at point E by using URANS and DDES. With the blade vibration, rotating stall inception appears to be triggered at about the same time for the both URANS and DDES. The stall inception of Stage 35 simulated using rigid blades in Chapter. 8 shows that the URANS predicts the stall inception with substantially more rotor revolutions than the DDES. The results of Fig. 9.16 showing that both the DDES and URANS predict the stall inception at about the same time indicates that the blade vibration does enhance the stall inception.

Fig. 9.17 illustrates the modal force and modal displacement of the first mode predicted by URANS and DDES during stall flutter. It is shown in the figure that modal force and

modal displacement decay before the stall inception occurs at rotor revolutions of 3.2 for the DDES and 1.8 for the URANS as shown in Fig. 9.16. The modal force and displacement predicted both by DDES and URANS diverge when the rotating stall occurs. Their oscillations are in phase and enhance the flutter.

Fig. 9.18 shows the time histories of angular displacement and pressure near the leading edge of rotor tip during stall flutter. The pressure oscillation sharply increase while the displacement is amplified when the stall occurs. The variation of both parameters is similar to the modal force and displacement shown in Fig. 9.18 since the 1st mode is the dominant mode of the rotor blades flutter.

Fig. 9.19 shows the spectrum of static pressure at the leading edge of rotor tip, in which the temporal samples are recorded from point E. It can be seen that both URANS and DDES capture similar unsteady flow behavior. For example, the peak amplitudes are at low frequency of around 200 Hz, and considerable fluctuation near the 1st natural frequency of 1227 Hz are captured. However, DDES predicts two dominant frequencies near 1st natural frequency, and URANS only predicts one. Fig. 9.20 shows the spectrum of angular displacement at the leading edge of rotor tip at point E. Both the URANS and DDES predict one dominant frequency near the 1st natural frequency.

Fig. 9.21 illustrates the pressure contours after 1 rotor revolution at the middle of tip clearance span. The flow predicted by URANS is stable as shown in Fig. 9.15, but the DDES results already loss the periodicity as indicated by Fig. 9.15 that the DDES mass flow already has a significant drop at 1 rev. At 4 rotor revs, both the URANS and DDES predict the flows with deep stall as shown in Fig. 9.22. The flow blockage predicted by DDES is larger than the URANS in both circumferential and streawise directions as shown

by Fig. 9.23 of the entropy contours at cross section near rotor leading edge at 4 revs. The interaction between rotating stall cells and blades predicted by DDES is stronger than that in URANS, which lead to higher amplitude of vibration as shown in Fig. 9.20. The large flow oscillation due to the flow blockage predicted both DDES and URANS makes the blades absorb more energy from the flow. It enhances the rotor blades flutter.

Conclusions

The fully coupled FSI simulation is conducted using DDES and URANS with full annulus and a full compressor stage, NASA Stage 35. For all the operating points, if no mechanical damping is used, the amplitudes of the blade vibration increase gradually and flutter occurs. With 0.001 structural damping, the blades are damped before the stalling point E. However, the blade vibration response diverges at stalling point E due to the rotating stall.

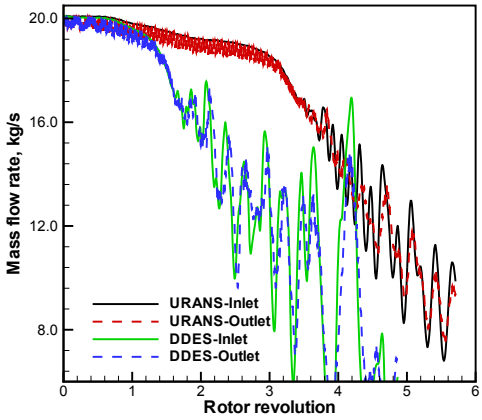

Figure 9.15: Time history of mass flow rate during stall flutter

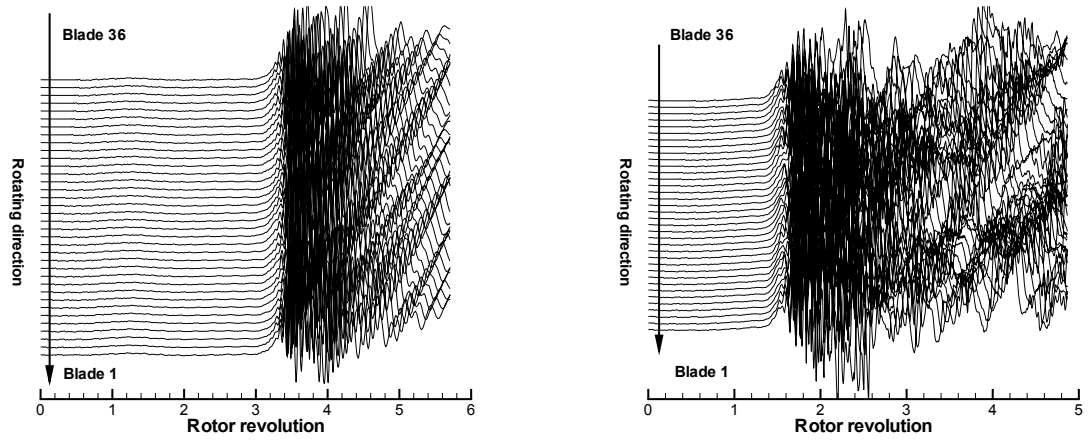

Figure 9.16: Time traces of pressure near half tip chord length upstream of the rotor leading edge at the tip span

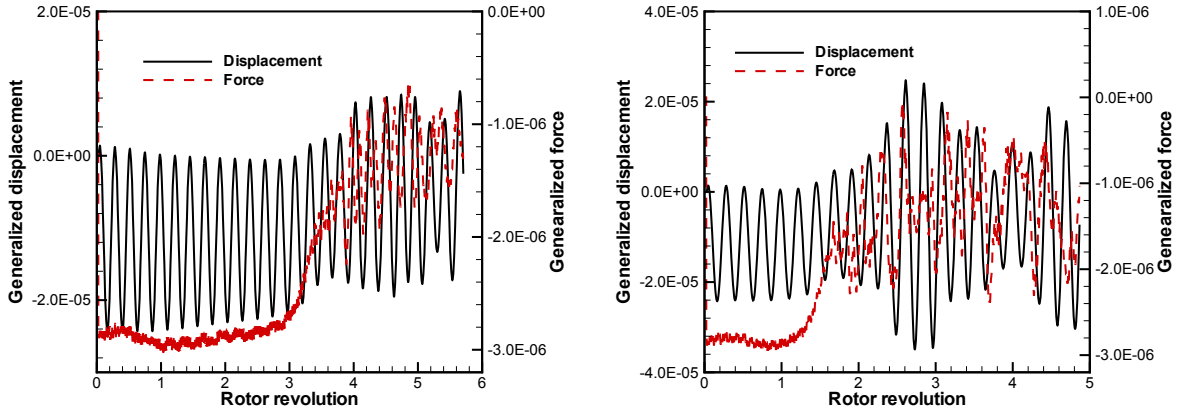

Figure 9.17: Modal displacement and force of 1st mode at point C with ND=2 and zero damping

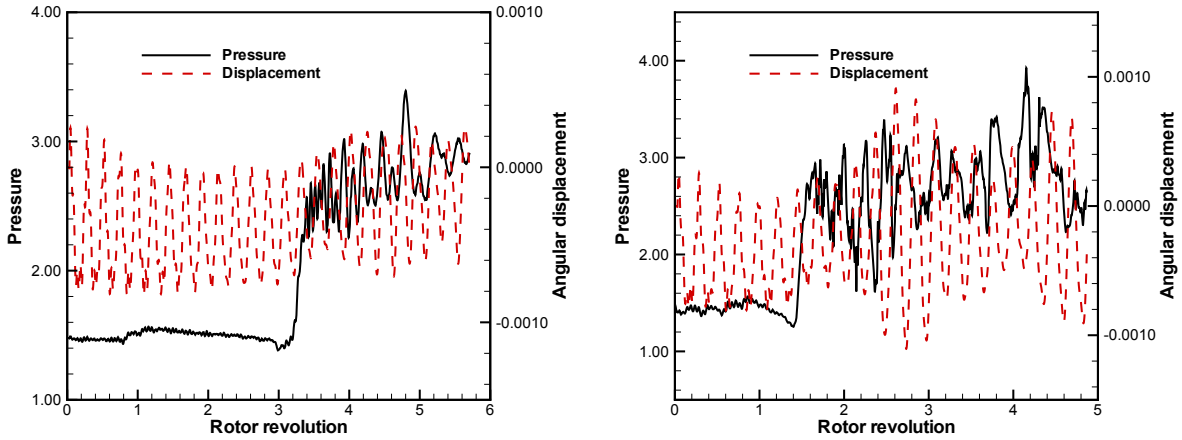

Figure 9.18: Time history of pressure and angular displacement at point C with ND=2 and aero damping

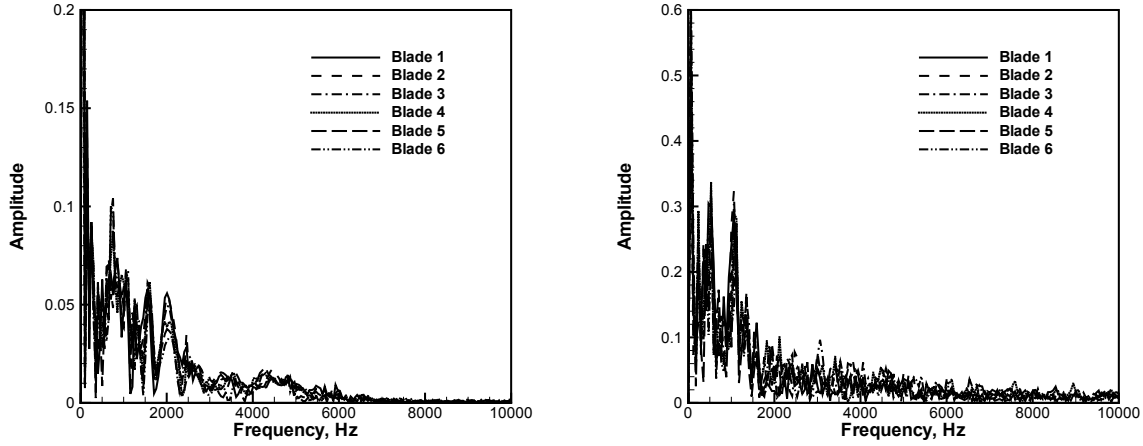

Figure 9.19: Spectrum of pressure near the leading edge at the rotor tip

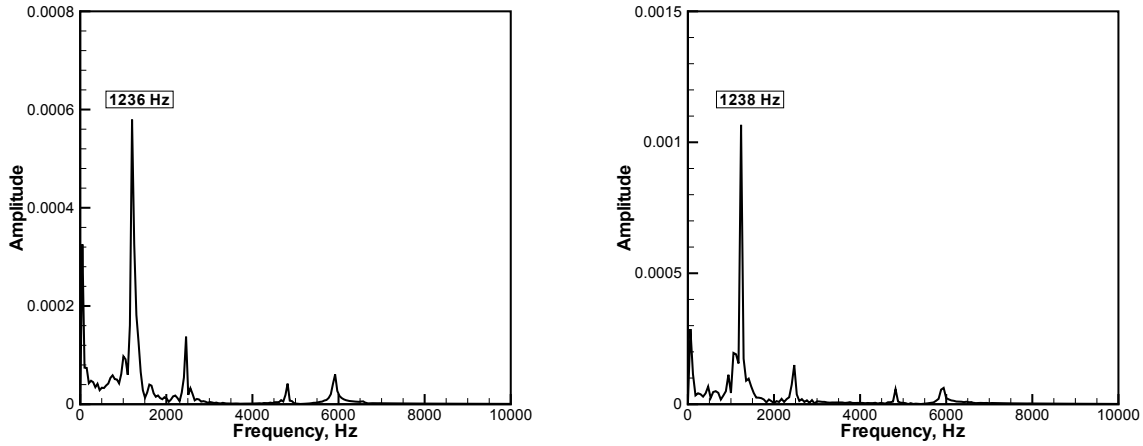

Figure 9.20: Spectrum of angular displacement near the leading edge at the rotor tip

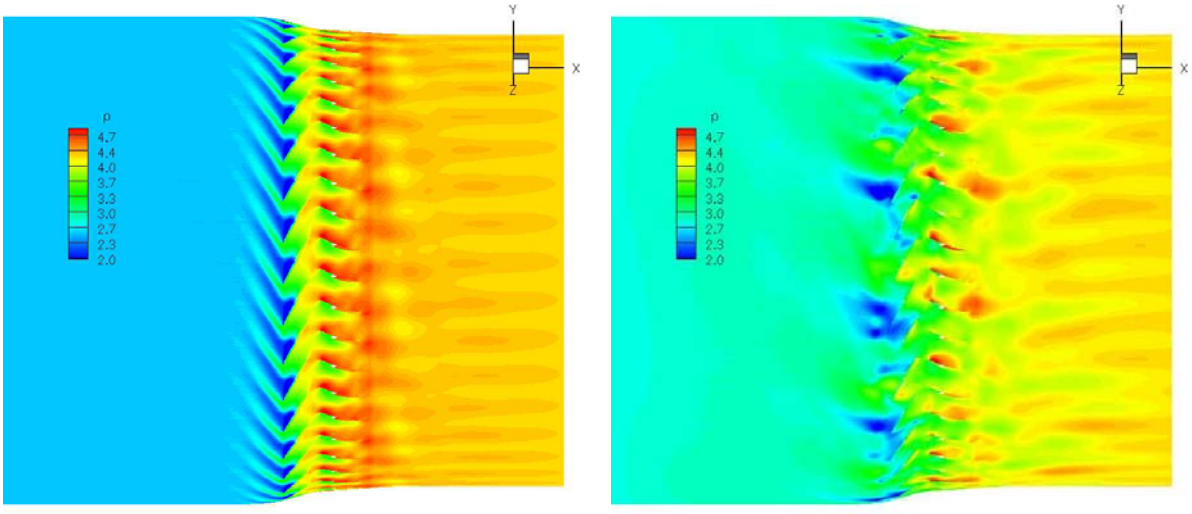

Figure 9.21: Pressure contours at the tip span before rotating stall

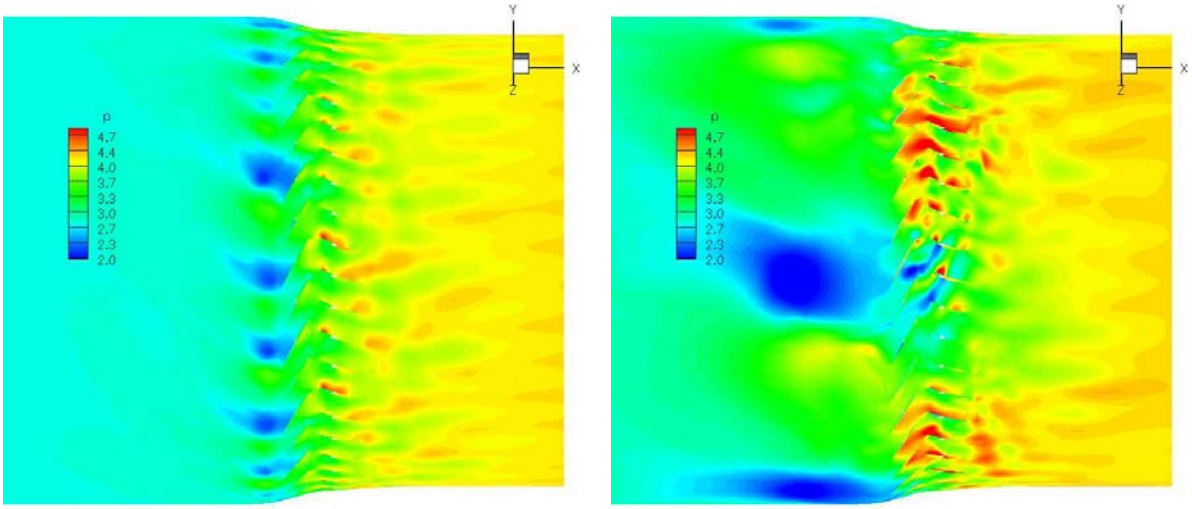

Figure 9.22: Pressure contours at the tip span rotating rotating stall

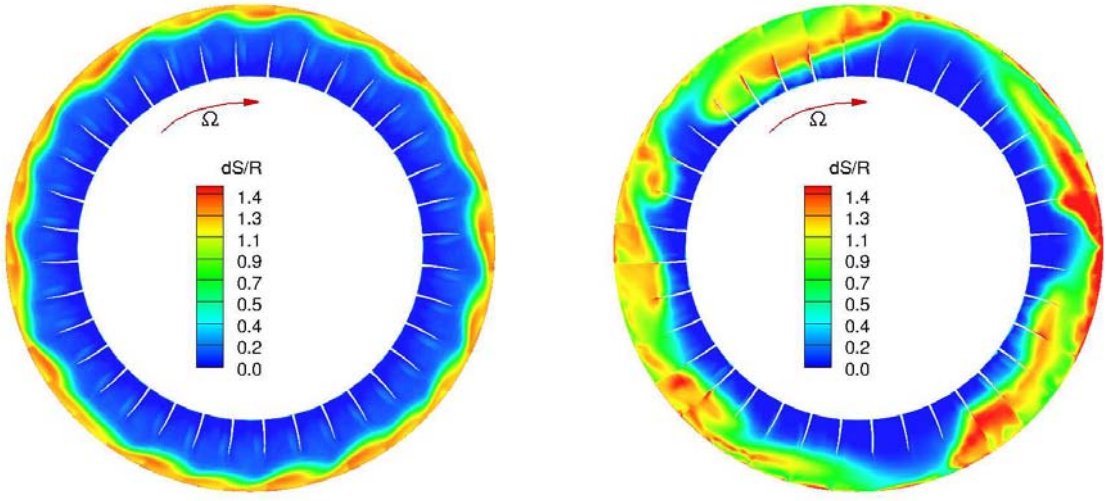

Figure 9.23: Entropy contours during rotating stall

Chapter 10

Investigation of The Mechanism of Non-Synchronous Vibration

The non-synchronous vibration (NSV) is a new phenomenon discovered recently and is a type of rotor blade vibration asynchronous to the rotor rotating speed. It is observed that the NSV occurs mostly in the compressor/fan rotor tip region when the tip clearance is large. NSV may generate high cycle fatigue for the rotor blades and is also known to generate a whistling tone noise. Understanding the NSV mechanism is crucial to guide the design to mitigate or avoid the HCF and noise caused by NSV.

However, the driving mechanism of NSV is not fully understood yet. Currently, there are two hypotheses explaining NSV: one attributes NSV to vortex shedding and rotating instability, the other attributes it to the resonance of the tip clearance back flow and the acoustic wave feedback. The aim for the present work is to study the mechanism of compressor/fan Non-Synchronous Vibration (NSV) using high fidelity simulation with a fully coupled fluid-structural interaction model.

10.1 Numerical Methods

The numerical simulation of NSV is conducted by using a fully coupled fluid/structure interaction. Time accurate compressible 3D Navier-Stokes equations with Spalart-Allmaras turbulence model are solved with a system of 5 decoupled structural modal equations in a fully coupled manner. The 3rd order WENO scheme for the inviscid flux and 2nd order central difference for the viscous terms are used to accurately capture the interactions of the fluid and structure.

10.1.1 The NSV Compressor

The high speed axial compressor used in this research is the same as the one studied in [17, 22], which exhibits a NSV at the first stage rotor blades. The first 1-1/2 stage has 56 IGVs, 35 rotor blades and 70 stator blades, which provides a geometry periodicity in every 5 rotor blades. Hence, 1/7 sector of the compressor is simulated to save the computational cost. The tested rotor tip clearance in the compressor rig is 1.1% of tip chord. In this research, two different tip clearance models including tip1 model with clearance size of 2.4% tip chord, tip2 model with clearance size of 1.1% have been studied. Tip1 model is used to validate the recent developed the sliding interpolation BC [87]. Tip2 model is used to examine the lock-in phenomenon during NSV and to be consistent with the work of Im and Zha [21]. The measured blade NSV has a response close to 1st torsional blade natural frequency. The experiment shows a NSV frequency of 2600 Hz at around 12880 RPM and 2661 Hz as the rotor speed slightly decreases to about 12700 RPM as shown in Fig. 10.1. Unfortunately, the unsteady blade response signal from the strain gage on the

blade surfaces are not available.

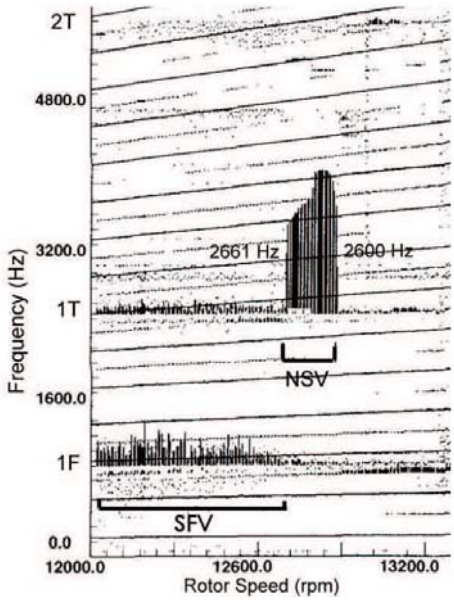

Figure 10.1: Strain gage response of the first-stage rotor blades of the high-speed compressor showing NSV(non-synchronous vibration) frequencies

10.1.2 Computational Mesh

It is very important to create high quality orthogonal mesh for a flow solver based on structural mesh in order to achieve high fidelity solutions. The 1/7th sector mesh for tip1 model used in the simulation is shown in Fig. 10.2. The H-mesh layer used in [119] is removed and was replaced with O-mesh at the rotor/stator interface. The sliding interpolation BC is implemented for the flux exchange across the rotor/stator interface, which removes the requirement of one-to-one matched grid point at the sliding BC interface between a rotor and stator. The O-mesh topology is used around blade to achieve high orthogonal mesh near the blade surface. For the IGV and stator, the mesh size is 121(around blade)$\times$77(blade-to-blade)$\times$46(blade span). For the rotor, the mesh size is 201(around blade)$\times$77(blade-to-blade)$\times$46(blade span). The rotor tip clearance is modeled with 11 grid points using an

O-mesh block. The tip gap is shown to have a significant effect on overall performance of axial compressors [21, 116]. For fully gridded tip clearance, about 4 to 10 points in the tip clearance are generally considered as adequate to predict the primary effects of the leakage flow in axial compressor [86, 116–118]. The total mesh size for this 1/7 sector of 1-1/2 compressor is 12,332,628. The mesh of IGV/rotor/stator is partitioned to total 168 blocks for parallel computation. The grid used in the simulation of lock-in phenomenon is the same as that in [21], in which H-mesh layer and conservative sliding BC are used at rotor/stator interface.

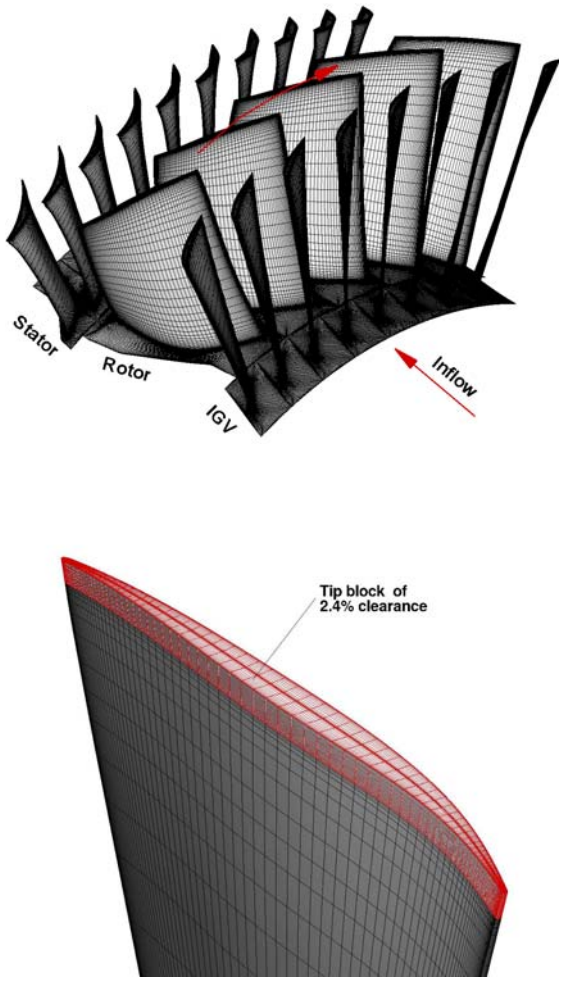

Figure 10.2: 1/7th Annulus mesh for NSV simulation

10.1.3 Mode Shape of the 1st Stage Rotor Blade

For FSI simulation, the finite element analysis is performed firstly o extract the mode shapes and frequencies of the blades. Since the first a few modes are usually dominant to describe turbomachinery blade vibration characteristics [10, 88], the first five mode shapes are used in this study and are normalized by the generalized mass($\sqrt{\phi^T m \phi}$) provided by manufacturer. The natural frequencies are 1065.5 Hz, 2621.0 Hz, 3591.0 Hz, 5275.4 Hz and 6226.4 Hz. The deflections of the first five modes are displayed in Fig. 10.3. The blades are modeled as fixed at the rotor disk. Note that the NSV of the compressor in this study is observed in the rig test close to the first torsional mode, which is the mode 2 in Fig. 10.3.

10.1.4 Boundary Conditions

The fully conservative sliding boundary condition (BC) [119] at the blade row interface is used in order to rigorously resolve wake propagation, shocks interaction and rotating instabilities. In addition, an efficient time-shifted phase-lagged BC [21] with nodal diameter of 7 is applied at the lower/upper circumferential periodic boundaries to facilitate 1/7th annulus simulations.

At the IGV inlet, the given radial distributions of total pressure, total temperature, swirl angle and pitch angle are applied and velocity is extrapolated from the computational domain in order to determine the rest of variables. On the blade surface and casing wall a non-slip boundary condition is applied, while on the hub surface the law of the wall is used to avoid an excessive fine mesh in the boundary layer [1]. At the stator outlet, the static pressure is specified in the spanwise direction. The velocity components are extrapolated from the computational domain and an isentropic relation is used to determine the density.

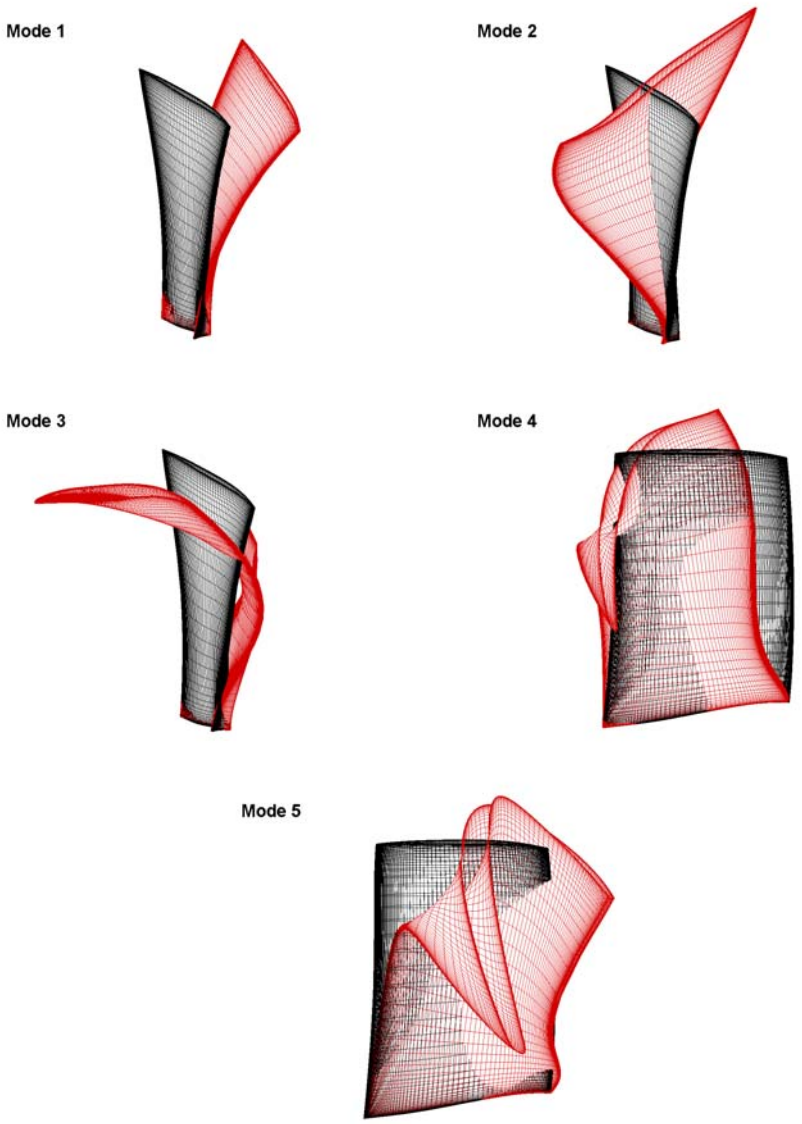

Figure 10.3: Rotor blade modal deflections

If the wall surface is rotating, the wall static pressure for the inviscid momentum equation is determined by solving the radial equilibrium equation. If the wall surface is stationary, the static pressure gradient across the wall boundary layer is set to zero. In addition, the adiabatic condition is used to impose zero heat flux through the wall.

The pressure on the rotor blade surface is a very important parameter to understand the aerodynamic excitation in the passage. A series of numerical probes are put on the blade

surface in order to capture the main flow excitation on the blades. The distribution of those numerical probes is the same as that in [22].

10.2 Results of Rigid Blade Simulation

10.2.1 The Speedline and NSV Location

Since NSV of axial compressors is typically observed in stable operation [16–19], unsteady flow simulations are first conducted with rigid blades at different back pressure conditions to find the region with dominant NSV flow excitation in the speedline. The tip clearance of 1.1% tip chord is used in this study.

Fig. 10.4 shows the predicted speedline of the 1-1/2 stage axial compressor. Note that the time averaged speedline data are obtained with rigid blades by averaging final 2 rotor revolutions. The back pressure is gradually increased from the point A to the near stall point D. The point A is about maximum mass flow condition. The NSV excitation is captured close to the near stall point D. No NSV excitations are observed at point A, B and C.

Fig. 10.5 shows time history of the rotor outlet mass flow rate . In this study the unsteady solutions between 4.0 and 12 rotor revolutions are used for the NSV frequency analysis since the predicted mass flow shows periodic oscillations after 4.0 revolution. The compressor at the NSV point operates without a mass flow breakdown as observed the experimental studies [16–19].

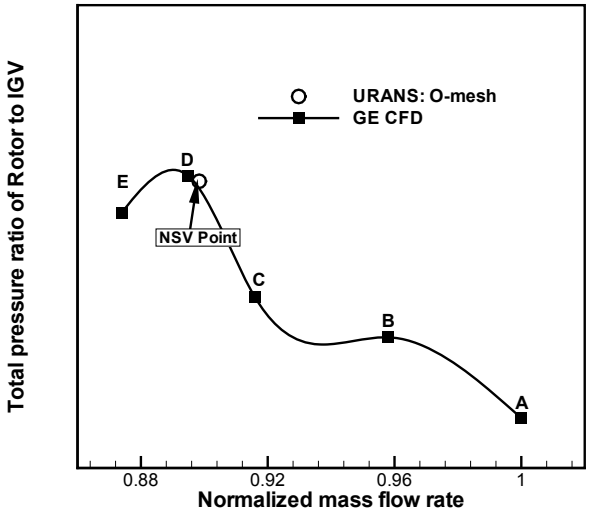

Figure 10.4: The 1-1/2 stage compressor speedline from rigid blade simulation

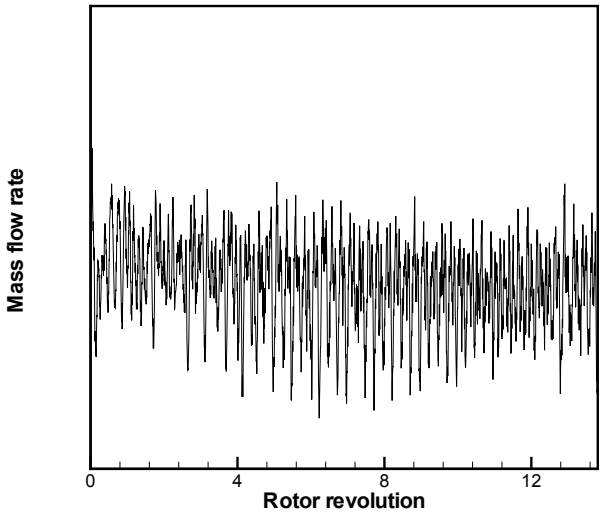

Figure 10.5: Instantaneous mass flow variation during NSV excitation

10.2.2 Driving mechanism of NSV

Fig. 10.6 shows instantaneous entropy ($\frac{\Delta S}{R} = \frac{\gamma}{\gamma-1} ln \frac{To}{To_\infty} - ln \frac{Po}{Po_\infty}$) near the rotor LE axial plane. The flow above 80% blade span is largely disturbed due to a circumferentially traveling vortex that triggers the non-engine order vibration of the compressor [69]. The NSV

with large blade vibration amplitude is attributed to the vortex traveling in the circumferential direction between 65% to 91% of the blade span.

The LE circumferentially traveling vortex captured for this compressor roughly above 80% rotor span is illustrated in Fig. 10.7. V1, V2, V3, V4, V5 show the vortices with the axis about normal to the blade suction surface. As indicated in [22], the tip vortex travels from a blade LE to trailing edge and then to the LE of the next blade in a repeated fashion. Such a vortex motion generates a pair of aerodynamic excitation for blade torsional vibration because of two low pressure regions followed by the vortex core positions, one near the LE and one near the trailing edge.

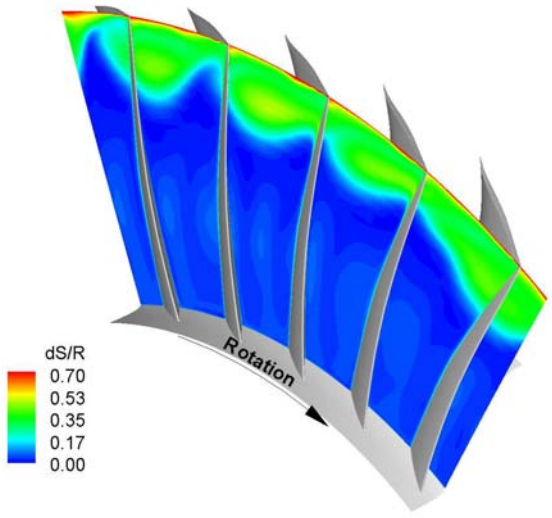

Figure 10.6: Entropy contour near the rotor LE axial plane

Fig. 10.8 indicates the reversal flow near the rotor tip region due to the vortices traveling. A locally stalled flow appears near the rotor tip, but no rotating stall happens during the compressor NSV. The vortex is examined at time T1, T1+Δt and T1+2Δt, where Δt is about 0.045 Rev (rotor revolutions). Fig. 10.9 shows instantaneous movement of the vortex V2 at t=T1, T1+Δt, T1+2Δt. It is obvious that the vortex travels in the opposite direction to the rotor rotation near the rotor LE, e.g. the vortex V2 near LE suction surface of blade

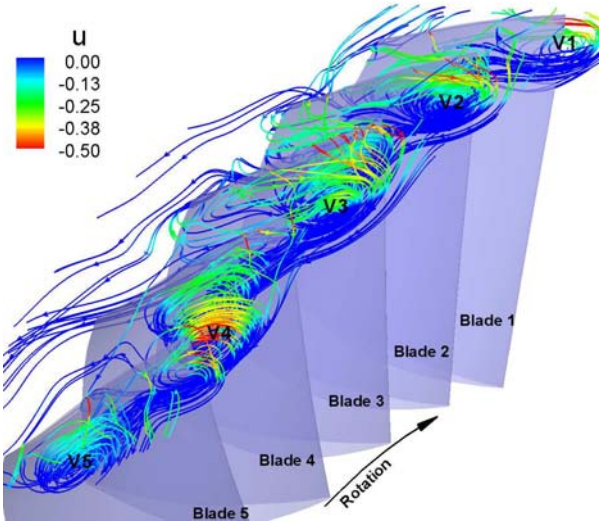

Figure 10.7: Structure of the LE vortex causing NSV above 80% rotor span colored by negative axial velocity

2 at t=T1 moves to blade 3 LE at T=T1+2Δt.

As another evidence of the circumferential vortices traveling, the normalized static pressure distributions on the rotor blade surface near 90% span are plotted in Fig. 10.10 and Fig. 10.11. The low pressure regions represent the core of circumferentially traveling vortices. For example, V1 core near 10% axial chord at t=T1 moves to about 20% axial chord at t=T1+Δt. At t=T1, two vortex cores simultaneously appear on the blade passage 5 due to the vortex leaving and coming, e.g. V4 and V5 in Fig. 10.7.

10.2.3 Propagating Frequency of the LE Vortex

The static pressure signals are acquired for the frequency analysis from total 60 numerical probes mounted on a blade surface including tip clearance. The peak fluctuations among those acquired pressure signals are observed around 80% span near the rotor LE due to the travelling vortices as plotted in Fig. 10.12. Such a pressure oscillation due to the traveling vortex generates a severe aerodynamic excitation, which results in the NSV of

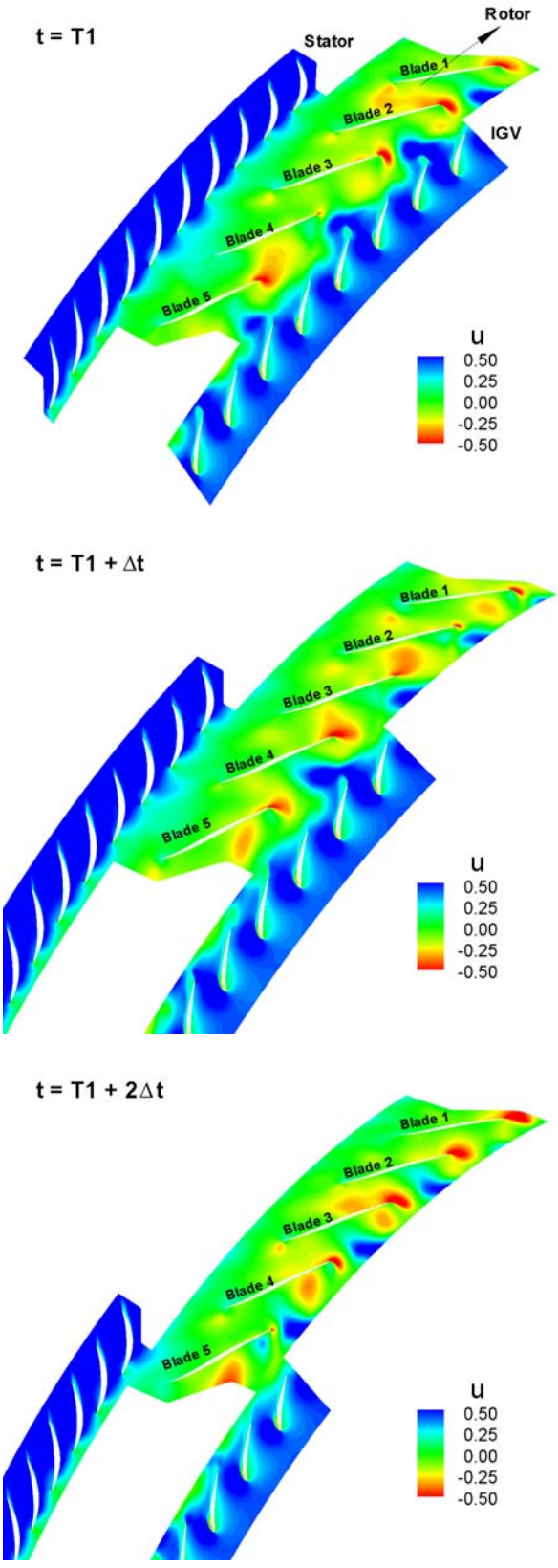

Figure 10.8: Axial velocity (u) contour near the blade tip section

the compressor as identified from the frequency analysis in Fig. 10.13. The total sampling time is about 7 rotor revolutions with more than 2048 samples. The frequency resolution is about 30 Hz. The predicted dominant NSV excitation frequency is 2603 Hz, which agrees excellently with the measured NSV frequency of 2600 Hz in the rig testing given in Fig. 10.1.

10.3 Results of Vibrating Blade Simulation

To be consistent with the work of [21], the computational mesh used for FSI simulation has H-mesh layer at the rotor/IGV/stator interface, in which the conservative sliding BC is used to handle the one-to-one matched grid. The model with a tip clearance of 2.4% tip chord is used in this study.

10.3.1 The Baseline NSV Point

Because the structural damping of the blades is not available and generally smaller than that of the aerodynamic damping, a uniform damping ratio of 0.001 is applied to all the first five modes of the blades. Fig. 10.14 shows the modal displacements and spectrum of physical displacement and unsteady pressure at about 80% span near the rotor leading edge. It can been seen that the first mode (1F) is not damped by using the using damping ratio and it is the dominant mode. Three dominant vibrations are observed in the spectrum plot of circumferential displacement. The first one has a frequency of 1064 Hz, which is the natural frequency of the 1F. The second one has a frequency of 1264 Hz, which is close to the 6 engine order(EO) excitation frequency. The third one is close to the second natural

mode (1T) and is considered as the NSV in this study. The 1F has highest amplitude and the magnitude of the EO vibration is similar to that of the 1T.

The aerodynamic excitation frequency is 2476 Hz, as shown on the right plot of Fig. 10.14, which is close to the measured NSV frequency. The simulation with rigid blades is also performed for comparison. It is observed that the same NSV excitation frequency was captured by the rigid blade simulation. The results of rigid blade simulation indicate that the NSV is caused by the flow excitation instead of the lock-in phenomenon that flow frequency is synchronized with the structure frequency. This result is consistent with the finding in [76] and the same aerodynamic excitation with the NSV frequency exists even when the blades are not vibrating. It appears that the blade vibration is excited by the aerodynamic forcing. However, it is too premature to draw the conclusion based on only one point simulation. To have a more certain conclusion, The rotor speed is varied within a small RPM range that the rig test detected the NSV to see if the structure response and flow excitation have the same relationship. The results will be presented in the following section.

10.3.2 Effects of Damping Ratio on NSV

Before studying if the NSV is a flow excitation phenomenon or lock-in phenomenon, efforts were made to decide what the damping ratio should be used to better capture the NSV with FSI simulation. In previous fluid structure interaction simulation [21, 76], there are two dominant frequencies in every predicted spectrum of circumferential displacement. One is near the first bending natural frequency and the other is close to the second natural frequency. There exits only one dominant frequency that is close to 1T in the spectrum of

strain gage measurement on the blade [17]. The other broad band frequencies near the 1F are due to separated flow vibration. One reason that the numerical simulation capture two dominant frequency may be that cantilever blade structure model is used to generate the mode shape without considering the disk. In reality, the mode shapes of the blades would be affected by the disk and shaft system. All these factors could affect the accuracy of mode shape and frequency using finite element method. As the attempt to make the single NSV frequency outstanding as in the rig test by using the numerical simulation, different damping ratio combinations are tested as an ad hoc approach.

Table. 10.1 lists different damping ratios tested in the calculations. Total 8 damping ratio combinations are tested to see if the torsional mode can be made dominant. The case D0 is the same as that used in the previous section 10.3.1

The results of D1 to D7 are shown in Fig. 10.16 to Fig. 10.22 respectively. In the combination of D1 to D6, The damping coefficient of the mode 1 is substantially increased with the hope to damp the 1T mode. However, the first mode is not damped much. The aerodynamic excitation near 1T may disappear when the amplitude of the 1F is much lower than the 1T as shown in the case D4 and D6. It is definitely not a simple relationship between the vibration of 1F and the aerodynamic excitation near 1T for the present compressor and the structural model. The damping ratio in case D7 is set to investigate the effect the vibration of the 1F on the NSV excitation. It can be seen that the NSV excitation is captured even the second mode is damped and the amplitude of 1F is higher. The NSV aerodynamic excitation is independent on the structure 1F and 1T modes.

Case D5 does capture a dominant 1T and the NSV excitation by this ad hoc method, as shown in Fig. 10.20. In case D5, ζ_1=0.05 is used and the damping coefficient of 0.001 is

used for all the higher order modes. Both 1F and 1T can be observed in modal displacement plot. The 1T has higher amplitude than the 1F. The spectrum of circumferential displacement is similar to the case D0. However, the frequency of the most dominant vibration is 2607 Hz, which is 1T. The 1F becomes the third dominant vibration. And the magnitude of the EO vibration is similar to the 1T.

Table 10.1: Damping ratio test cases

Case	ζ_1	ζ_2	ζ_3	ζ_4	ζ_5
D0	0.001	0.001	0.001	0.001	0.001
D1	0.005	0.001	0.0001	0.00007	0.00004
D2	0.010	0.001	0.0001	0.00007	0.00004
D3	0.010	0.001	0.001	0.001	0.001
D4	0.020	0.001	0.001	0.001	0.001
D5	0.030	0.001	0.001	0.001	0.001
D6	0.050	0.001	0.001	0.001	0.001
D7	0.000	0.050	0.000	0.000	0.000

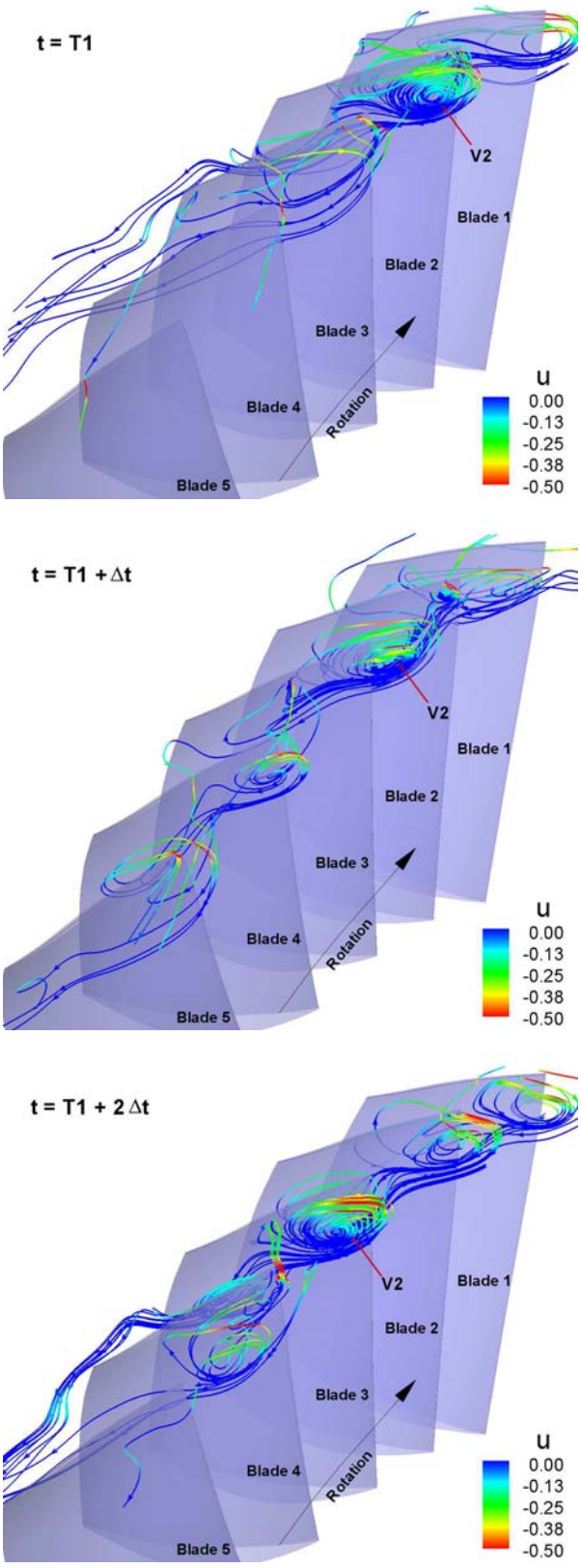

Figure 10.9: Movement of the traveling vortex V2 in the opposite rotor rotation direction at t=T1, T1+Δ*t*, T1+2Δ*t* during the NSV

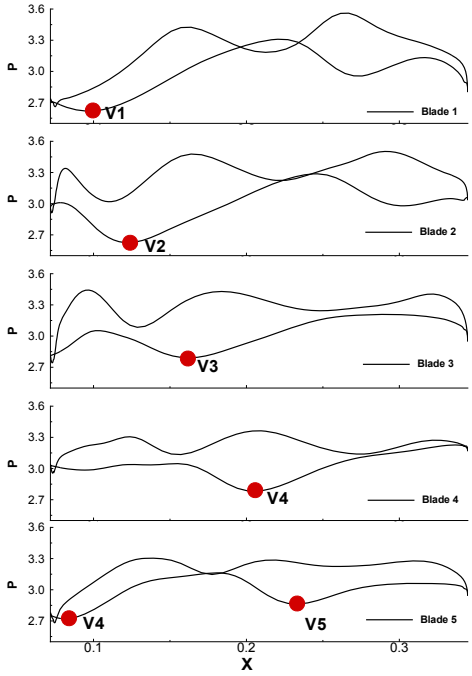

Figure 10.10: Normalized static pressure around the blade surface near 90% rotor span at T1

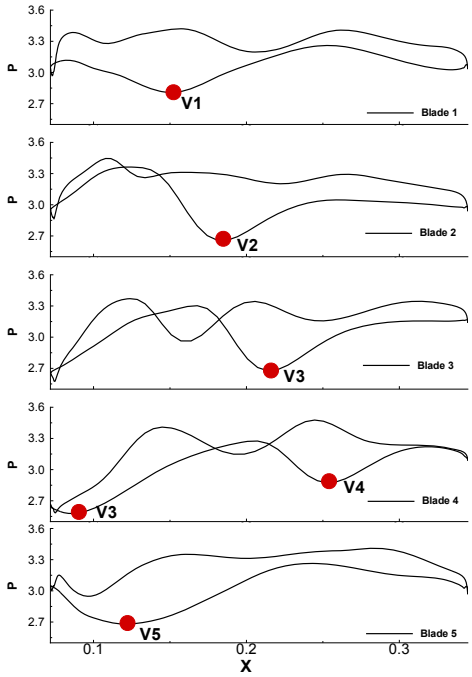

Figure 10.11: Normalized static pressure around the blade surface near 90% rotor span at T1+Δt, where Δt is about 0.045 Rev

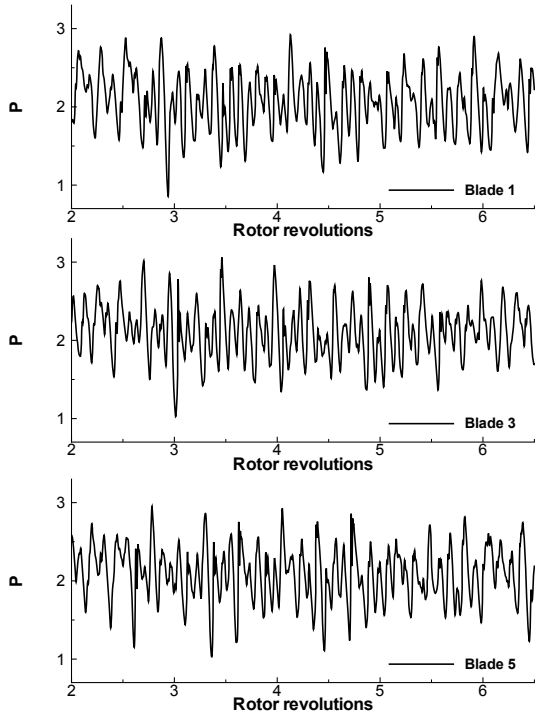

Figure 10.12: Normalized static pressure signal acquired near 80% span rotor LE

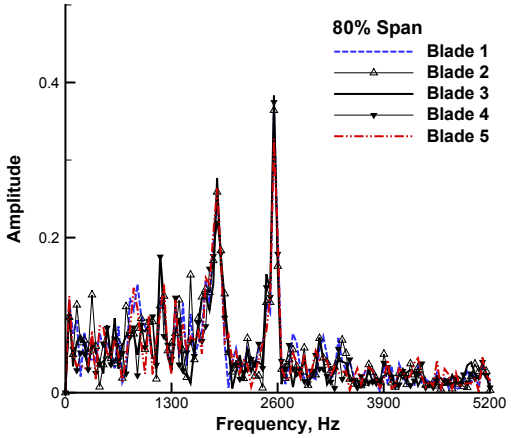

Figure 10.13: Predicted frequencies using the normalized static pressure signal near 80% span rotor LE

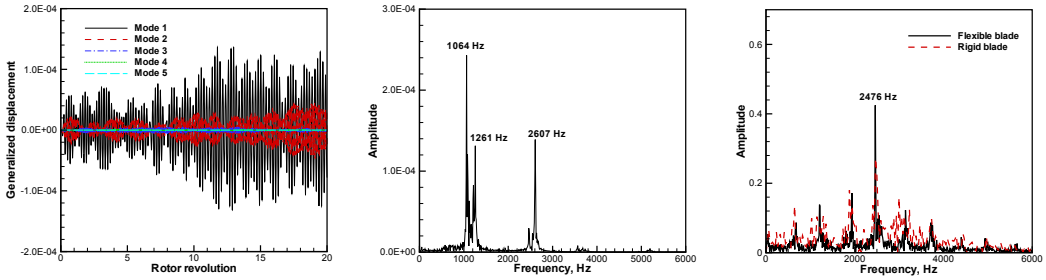

Figure 10.14: Case D0: Modal displacement(Left), FFT of physical displacement(Middle) and pressure(Right)

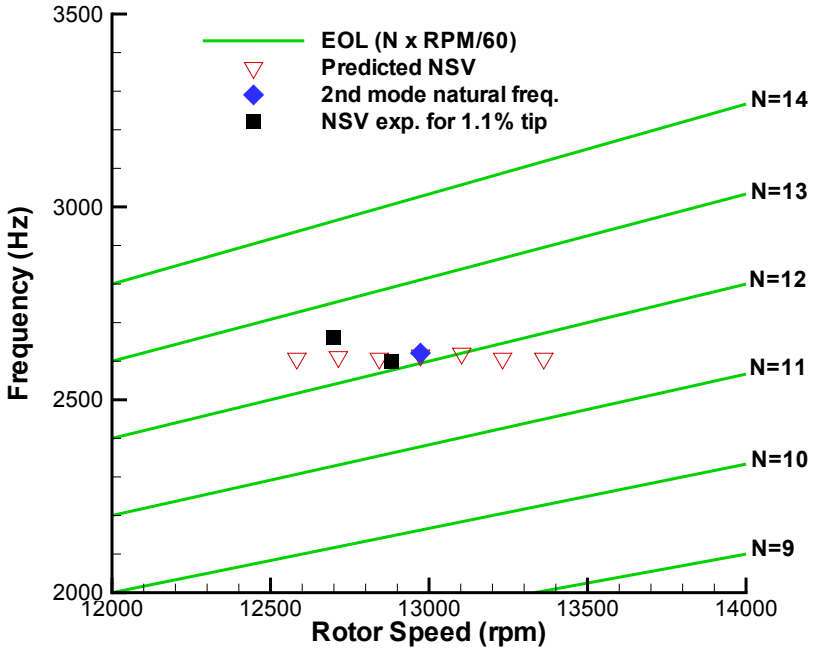

Figure 10.15: Campbell diagram of the compressor, showing the NSV excitation near 1T

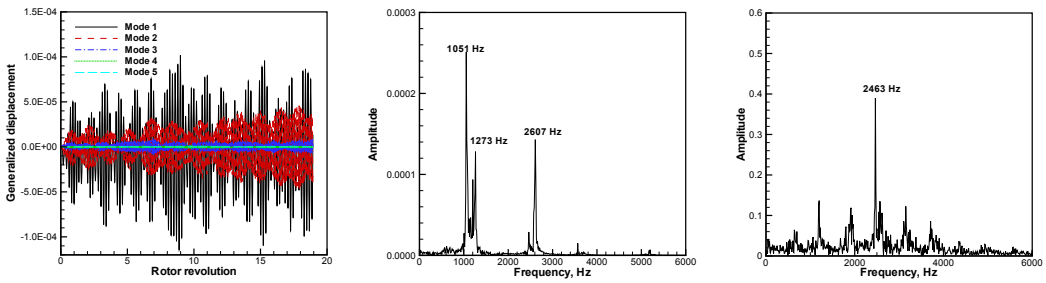

Figure 10.16: Case D1: Modal displacementleft, FFT of physical displacement(middle) and pressure(right)

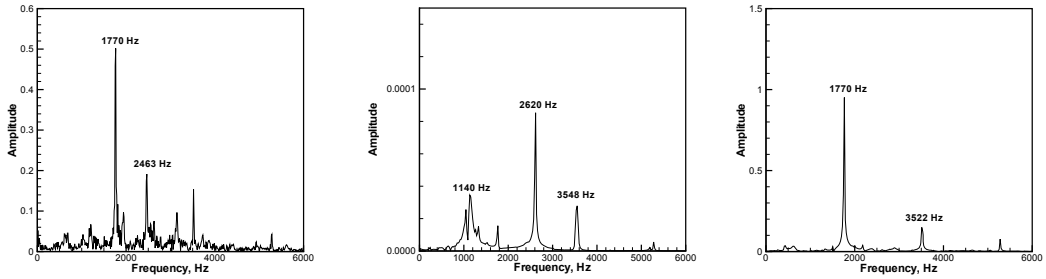

Figure 10.17: Case D2: Modal displacement(Left), FFT of physical displacement(Middle) and pressure(Right)

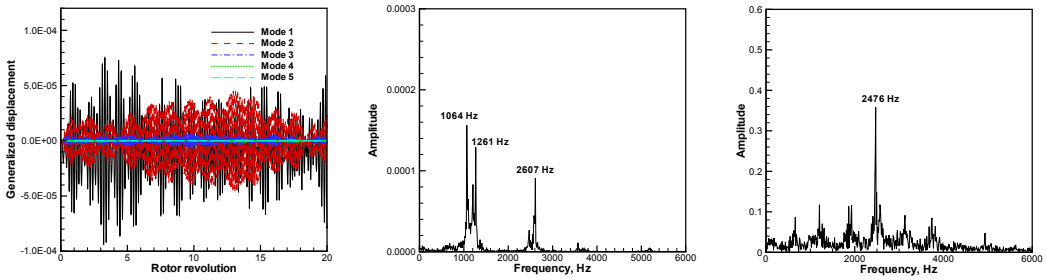

Figure 10.18: Case D3: Modal displacement(Left), FFT of physical displacement(Middle) and pressure(Right)

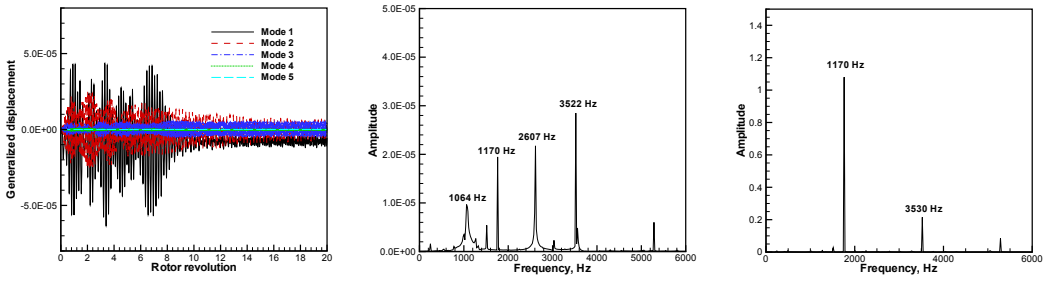

Figure 10.19: Case D4: Modal displacement(Left), FFT of physical displacement(Middle) and pressure(Right)

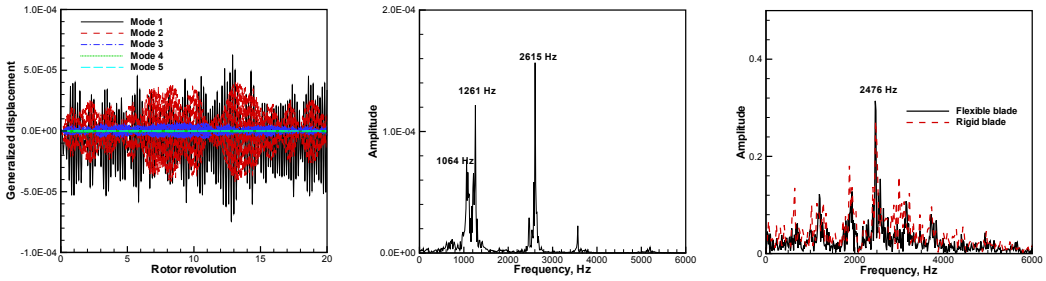

Figure 10.20: Case D5: Modal displacement(Left), FFT of physical displacement(Middle) and pressure(Right)

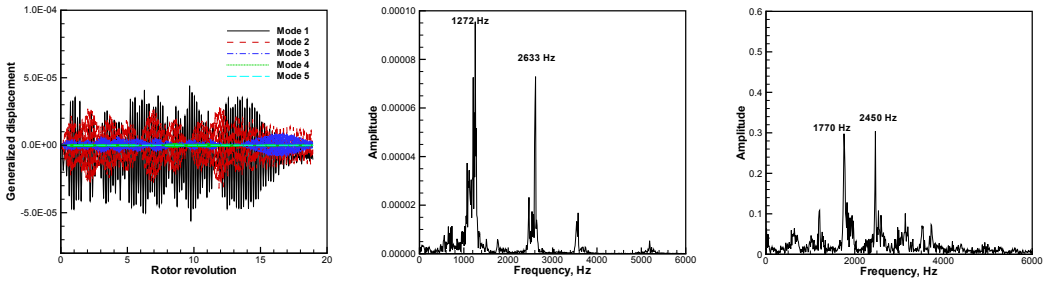

Figure 10.21: Case D6: Modal displacement(Left), FFT of physical displacement(Middle) and pressure(Right)

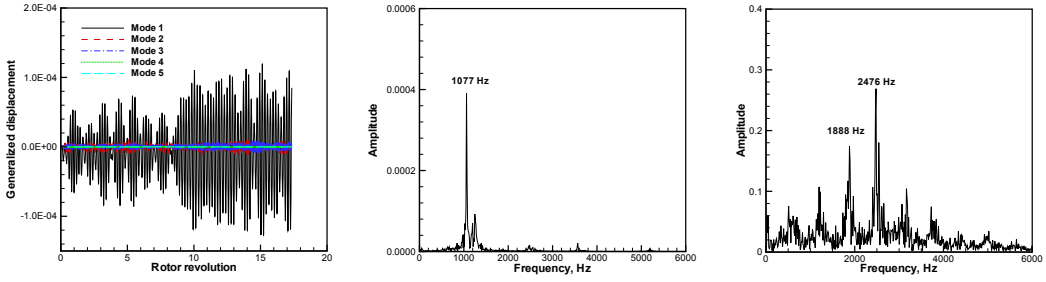

Figure 10.22: Case D7: Modal displacement(Left), FFT of physical displacement(Middle) and pressure(Right)

10.3.3 Examination of the Locked-in Phenomenon

In the rig test as shown in Fig. 10.1 [17], the NSV frequency varies from 2661 Hz to 2600 Hz when the wheel speed is increased from 12700 to 12880 RPM The shaft speed used in previous simulations is 12973 RPM, about 0.7% away from 12880 RPM. The previous simulation shows that the blade NSV frequency is the same as the aerodynamic excitation frequency when the rigid blades are used. It means that the NSV in this compressor is not a lock-in phenomenon. it is not conclusive if the simulation is conducted at only one point since the blade vibration frequency may happen to be the same as the aerodynamic excitation frequency.

To have a more conclusive understanding whether NSV is caused by flow excitation or a lock-in phenomenon, more points at different rotor speeds need to be studied. FFT analysis will be performed with the time history of pressure and displacement near the rotor leading edge in order to check if the aerodynamic frequency is lock in to the blade natural frequency. If the aerodynamic frequency follows the blade natural frequency at different RPM, the lock-in occurs. Otherwise, it is not. The spectrum analysis in this study are conducted mainly by using the data near the rotor leading edge at about 80% span since high amplitude of aerodynamic excitation is found in this region. Fig. 10.23 shows the spectrum of pressure from all the numerical probes on the blade surface. The highest pressure amplitude occurs near the the rotor leading edge at about 80% span.

Fig. 10.24 shows the operating line with varied rotor speeds calculated by the unsteady simulations with and without FSI. On the operating line, the total pressure and mass flow rate at the IGV inlet and rotor exit are averaged. It can be seen that the total pressure ratio increases linearly as the wheel speed increases. All the flows are dynamically stable.

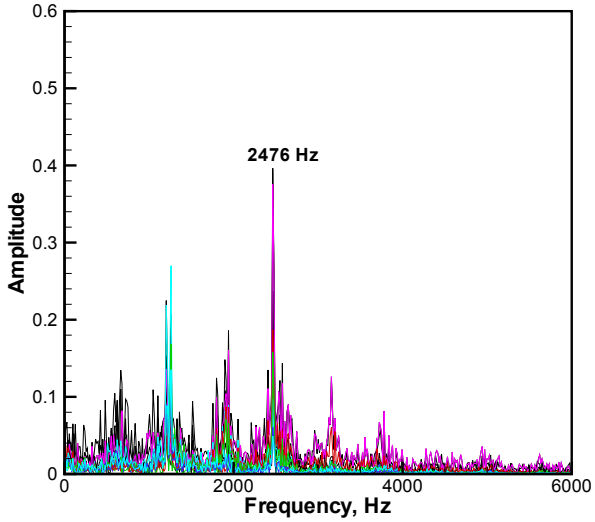

Figure 10.23: Spectrum of pressure on blade 3

The modal displacements and spectrum of physical displacement and unsteady aerodynamic pressure of different cases are shown in Fig. 10.26 through Fig. 10.33. The spectrum of rigid blade simulations are also plot for comparison.

Table. 10.2 summarizes all the results of different shaft speeds in the simulations. Case R5 is the same as the previous case as shown in Fig. 10.20, which used 12973 RPM as the wheel speed. The shaft speed of R1 is about 0.9% lower than the left boundary(12700 RPM), and R9 is about to 3.7% higher than the right boundary(12880 RPM) in the RPM range that shows near 1T NSV in the rig test, as shown in Fig. 10.1. In the table, the third row is the dominant frequency of the aerodynamic excitation from rigid blade simulation. The 4th row is the dominant frequency of the aerodynamic excitation from flexible blade simulation. The 5th row is the structure vibration frequency near 1T, which is taken as NSV in this research.

Fig. 10.25 is the Campbell diagram of the predicted blade vibration frequency near the 2nd mode compared with the experiment. It can be seen that most of the predicted

responses are not engine order vibration. The near engine order vibrations occur in case R6 and R7, in which the wheel speeds are 13037 RPM and 13103 RPM respectively. It is noted that not all those structure responses near the 1T mode are dominant because the 1st mode may be more dominant. The criteria to determine if NSV occurs are two folds determined from the FSI simulation: 1) The blade vibration frequency must be near 1T as observed in the rig test; 2) The blade vibration amplitude under that frequency must be the dominant one. The dominant blade vibration frequency near the 1T mode captured are case R1, R2, R5, R6 and R9. Since the frequency in R6 is on engine order that disqualifies R6 as a NSV case. The dominant NSV near 1T mode in this rotor speed variation study are case R1, R2, R5 and R9.

After examining the results from Fig. 10.26 to 10.33 and Table. 10.2, NSV cases of R1, R2, R5, and R9, the aerodynamic excitation frequencies of the rigid blades are the same as those with vibrating blades in the rotor speed variation study. This observation confirms the previous speculation from the single rotor speed simulation that the NSV is excited by the aerodynamic forcing instead of a lock-in phenomenon. For the NSV case R9 as shown in Table. 10.2, the rigid blade aerodynamic excitation frequency does not match the NSV blade vibration frequency. When the blades vibrate as NSV, the pressure oscillation frequency remains the same and is not changed to "lock-in" with the blade 1T vibration frequency. Hence, it can be concluded that the NSV occurred in this compressor is not a lock-in phenomenon, but is excited by aerodynamic force.

Fig. 10.34 compares the blade vibration amplitude of the near 1T vibration mode in the FSI simulation with rotor speed variation. The trend does agree well with the NSV amplitude measurement as shown in Fig. 10.1. The wheel speeds with the highest amplitude

are found in case R5 and R6. Since case R6 is disqualified as an NSV point due to the frequency being very close to the engine order, the case R5 has the largest NSV amplitude.

Table 10.2: Shaft speed test cases with and without FSI

Case	R1(NSV)	R2(NSV)	R3	R4	R5(NSV)	R6	R7	R8	R9(NSV)
RPM	12584	12714	12843	12908	12973	13037	13103	13232	13362
Rigid blade (Dominant pressure frequency,Hz)	2453	2489	2453	2470	2476	2489	1783	1796	1860
FSI, (Dominant pressure frequency, Hz)	2453	1731	2453	2470	2476	1845	2489	1796	1845
FSI, Response near 1T (θ, Hz)	2607	2611	2607	2620	2615	2607	2620	2607	2607

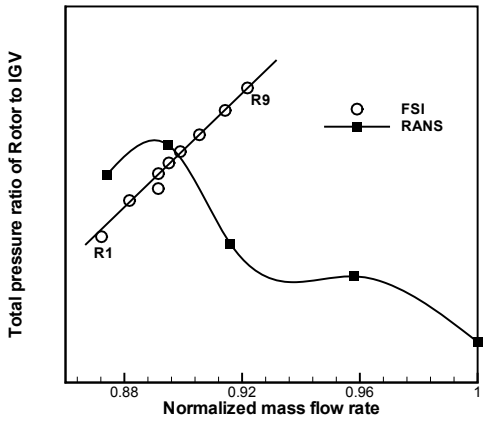

Figure 10.24: Speedline with FSI and without FSI

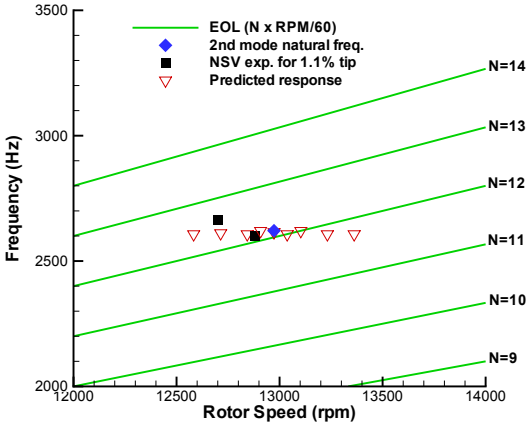

Figure 10.25: Campbell diagram of the compressor. The frequency used in the plot is the blade vibration frequency near the 1T mode

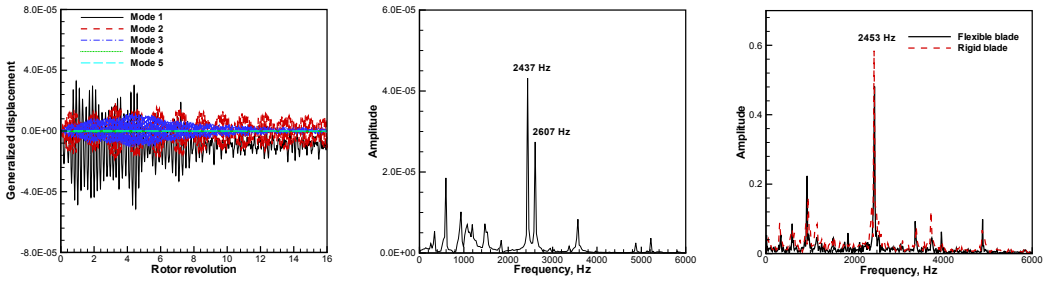

Figure 10.26: Case R1: Modal displacementleft, FFT of physical displacement(middle) and pressure(right).

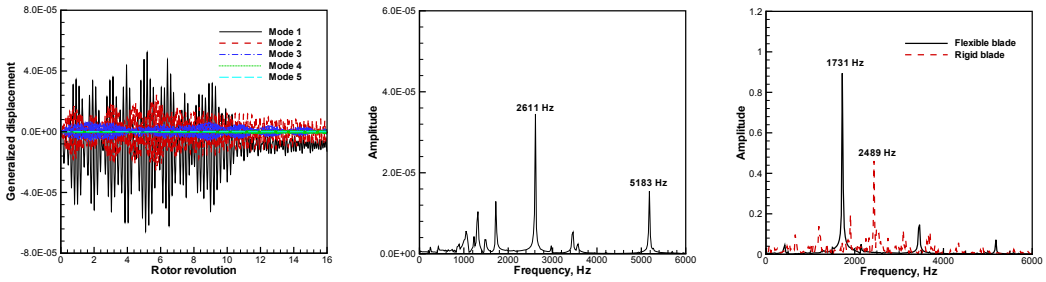

Figure 10.27: Case R2: Modal displacementleft, FFT of physical displacement(middle) and pressure(right).

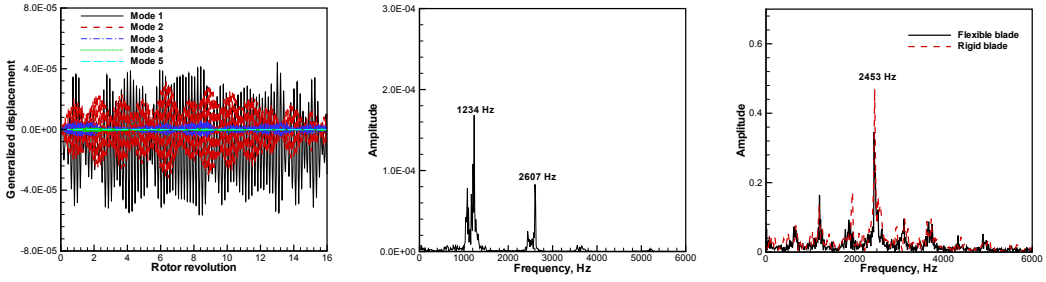

Figure 10.28: Case R3: Modal displacementleft, FFT of physical displacement(middle) and pressure(right)

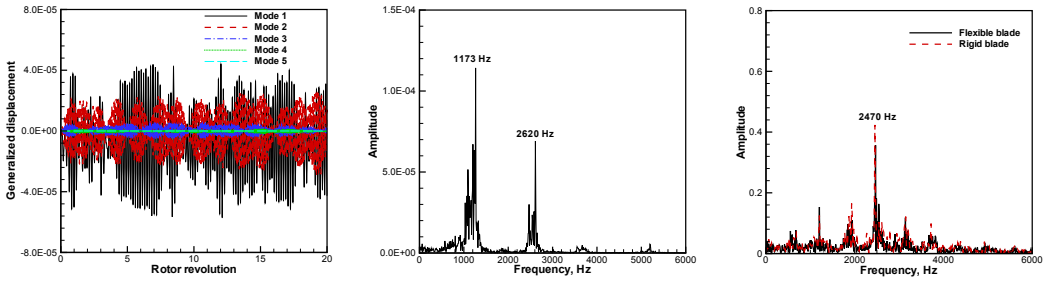

Figure 10.29: Case R4: Modal displacementleft, FFT of physical displacement(middle) and pressure(right).

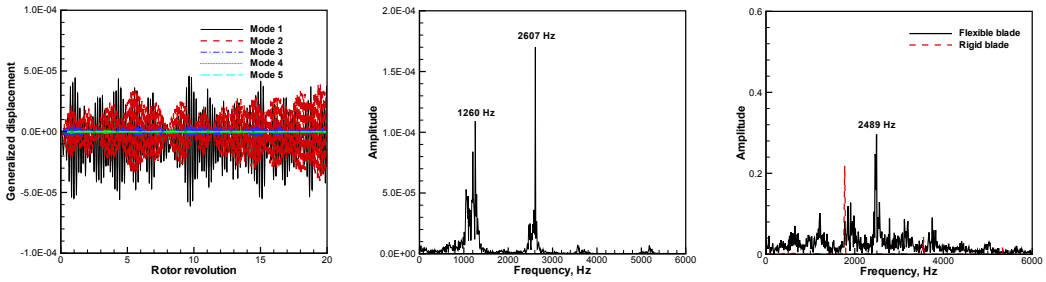

Figure 10.30: Case R6: Modal displacementleft, FFT of physical displacement(middle) and pressure(right).

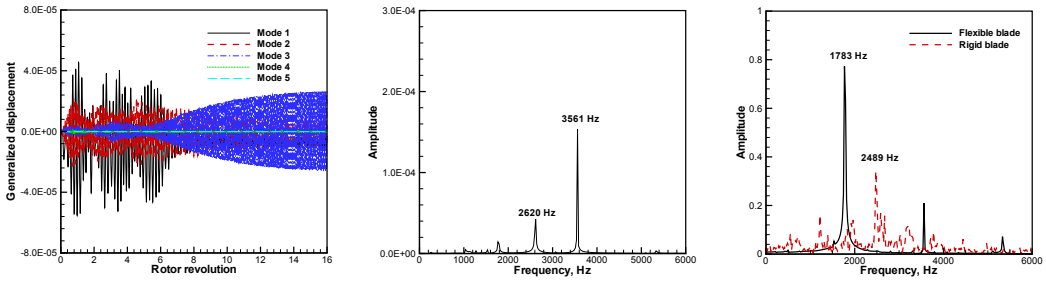

Figure 10.31: Case R7: Modal displacementleft, FFT of physical displacement(middle) and pressure(right).

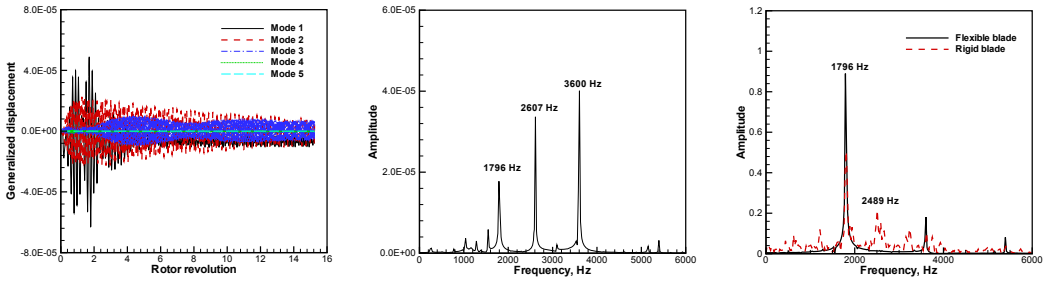

Figure 10.32: Case R8: Modal displacementleft, FFT of physical displacement(middle) and pressure(right).

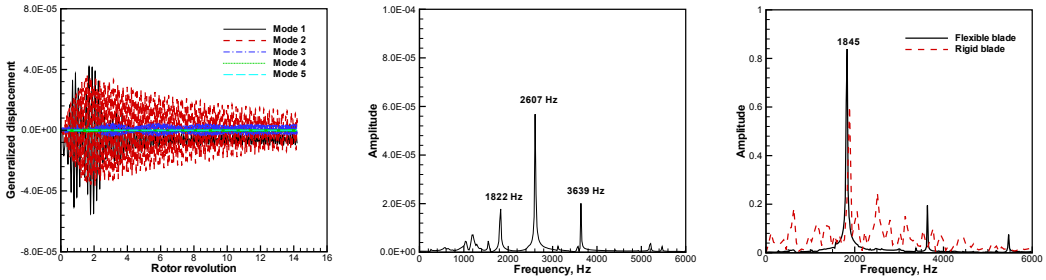

Figure 10.33: Case R9: Modal displacementleft, FFT of physical displacement(middle) and pressure(right).

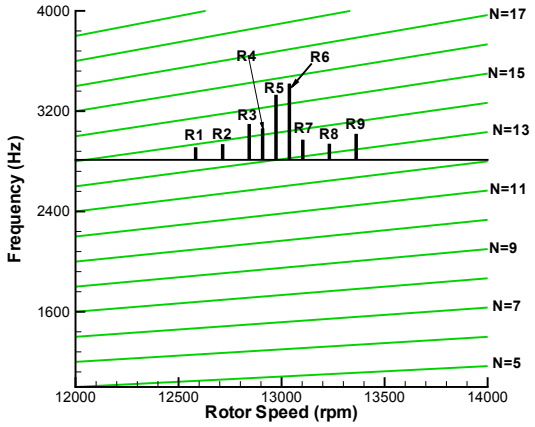

Figure 10.34: Campbell diagram of the compressor, showing the amplitude of the NSV excitation near 1T

10.3.4 Single Mode FSI Simulation

Flutter in a single natural mode is usually observed in turbomachinery blade rows vibration [4]. Hence, engineers often conduct a single mode blade aeroelastic analysis to save computational cost [8]. The NSV frequency observed in the present compressor stage is near the 1st torsional mode. One more efficient way of numerical simulating the NSV behavior may be to ignore all the other four modes and consider only the 2nd mode in the structural equation. The FSI simulation with one mode only is conducted in this section with the damping coefficient of 0.001 for the 2nd mode. The purpose of conducting the one mode FSI simulation is to compare its performance with the multiple modes simulation presented in the previous subsections.

Fig. 10.35 shows the modal displacements and spectrum of physical displacement and unsteady pressure with the R5 wheel speed at about 80% span near the rotor leading edge. The NSV excitation and vibration are well captured with the 2nd mode only simulation. Both the predicted structural vibration frequency and aerodynamic excitation frequency match well with the case considering all modes.

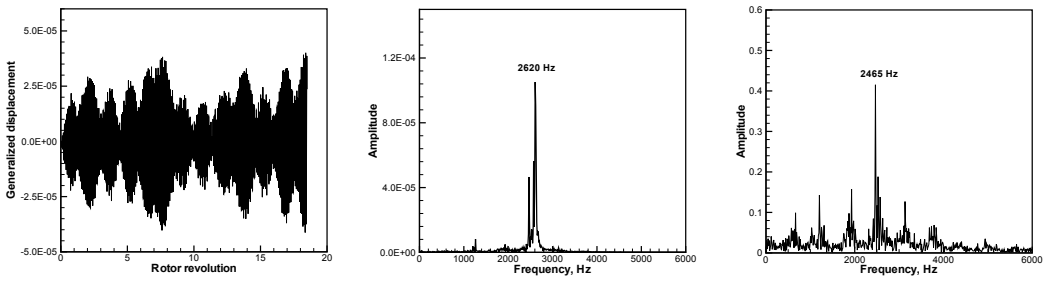

Figure 10.35: Modal displacement(Left), FFT of physical displacement(Middle) and pressure(Right) of case R5

10.4 Conclusion

In this chapter a high speed axial compressor is simulated with and without blade vibration to investigate the lock-in phenomenon during NSV mechanism. Time accurate 3D compressible Navier-Stokes equations are solved with a system of 5 decoupled modal equations in a fully coupled manner. A 1/7th annulus sector of IGV-rotor-stator is used with a time-shifted phase lag BC at circumferential boundaries to reduce computational efforts.

The URANS simulation with tip model 1 predicting a dominant frequency of 2476 Hz caused by an aerodynamic excitation from circumferentially traveling vortices agrees the NSV frequency measured from the rig testing. The results from the fully coupled fluid structure simulation captures the blade NSV frequency that also agrees with the measurement. The predicted aerodynamic excitation frequency at one rotor speed matching the predicted blade NSV frequency indicates that the NSV is caused by the flow excitation instead of a lock-in phenomenon. Lock-in will have the flow frequency altered from its inherent frequency and synchronized with the structure frequency. To confirm this observation, multiple rotor speeds varied around the resolved NSV condition are simulated with rigid and vibrating blades. The same conclusions are drawn. With the rotor speed variation, the blade NSV amplitude step variation trend similar to that measured in the rig test is obtained.

The FSI simulation capturing the 1T NSV frequency is usually accompanied with a dominant amplitude of the 1F mode. In the rig test, only the dominant 1T mode was observed. Such inconsistency with the rig testing is attributed to the inaccurate damping coefficients prescribed. Since the mechanical damping coefficients are in general not known, but are considered as very small, an ad hoc approach by assigning values guessed based

on physical estimation is used. The 1T dominant NSV excitation is achieved by using a damping ratio of 0.03 for the first mode and 0.001 for the other modes. The FSI simulation with one dominate structure mode only gives similar results as using multiple modes.

Chapter 11

Conclusions

In this thesis a high fidelity FSI methodology is developed and adopted for aircraft wing and turbomachinery aeromechanics simulation by the following numerical techniques, including the low diffusion E-CUSP shock-capturing Riemann solver with high order WENO schemes, the delayed detached eddy simulation of turbulence, the fully coupled fluid-structure interaction, the sliding interpolation BC for rotor/stator interaction, and the phase lag boundary conditions. Thorough validation is conducted to demonstrate high accuracy and robustness of the high fidelity FSI simulation methodology. The mechanisms of sonic dip of transonic wing, stall inception and stall flutter of transonic compressor stage and non-synchronous vibration of high speed compressor stage are investigated with the high fidelity FSI methodology.

11.1 Main Conclusions

11.1.1 Projectile Flows

In the validation of projectile flows, the DDES demonstrates its excellent ability to accurately simulate the vortical base flow. The predicted drag coefficient for the projectile by the DDES shows a good agreement with the experiment. For an ARDEC Projectile at M=0.752, AoA=0° and 4°, the DDES significantly reduces the axial force prediction error to about 4%, whereas the URANS has an error of 12%, and the RANS has an error of 16% to 23%. The primary difference of the drag prediction between the DDES and URANS is the pressure drag prediction in the base region. The DDES is demonstrated to be superior to the URANS for the projectile flow prediction due to more accurate base large vortex structures and pressure simulation.

11.1.2 Wing-Body Flows

For the wing body configuration simulation, the predicted C_L results of both RANS and URANS show good agreement with experiment. The maximum errors are less than 3% in all test cases. The coarse mesh provides better results than medium and fine mesh. The drag counts deviation from the experiment predicted by the DDES are less than those of RANS and URANS. This indicates the advantage of DDES in turbulence modeling. The predicted friction drag counts difference between the URANS and DDES is less than one count for the case at AoA=0.49°. The reason may be that DDES method employ the same turbulence model as URANS within the wall boundary layer. For the predicted pressure drag, DDES provides about 2 drag counts more accurate than RANS and URANS. The

prediction by using the 5th WENO scheme provides lower C_L and drag counts than the 3rd order schemes.

11.1.3 Transonic Wing Flutter

The high fidelity FSI methodology is validated by predicting the transonic AGARD wing flutter boundary with free stream Mach number varied from subsonic to supersonic. The predicted flutter boundary at different free stream Mach number including the sonic dip achieves very good agreement with experiment. In particular, the predicted flutter boundaries at the two supersonic conditions match the experiment accurately.

The weight of the torsional mode that contributes to the flutter of the wing decreases at transonic and supersonic regime. The contribution of the bending mode to structural flutter increases abruptly at transonic Mach number 0.96 at which the sonic dip occurs. It appears that the transonic dip is related to the anticlimax of the second mode in transonic regime. The FSI simulation gives the following observations at the sonic dip condition. The shock strength is enhanced more near the trailing edge at near sonic Mach number. The shock location and motion decrease the pitching moment of the wing, which drops sharply at the sonic dip Mach number, The decreased pitching moment induces lower torsional mode vibration. It creates an anticlimax of the amplitude ratio of the first mode to second mode at the sonic dip.

11.1.4 Supersonic Panel Flutter Simulation

In the panel aeroelasticity investigation, delayed detached eddy simulation is performed to simulate a supersonic panel vibration at Mach 2.0. The shock waves and their reflection

interacting with turbulent boundary layer in the tunnel are well captured by the DDES. The panel vibration induced by the shock boundary layer interaction is well resolved. The dominant panel response agrees with the experiment in terms of the mean panel displacement and frequency. Even though the linear model structure model performs very well in this simulation, the next step would be to incorporate nonlinear finite element model to further improve the accuracy. It takes one week wall clock time to run 0.1s physical time with 264 CPUs using parallel computing. Since it is a fully coupled fluid-structural interaction simulation, the flow and structure responses are captured by the solver itself with no parameter adjustment.

11.1.5 Compressor Stage Stall Inception

The full annulus DDES is conducted for the first time to investigate rotating stall inception mechanism of the transonic NASA Stage 35 with sliding interpolation BC. The details of the flow breakdown that leads to fully developed rotating stall is well captured by the present numerical simulation. The simulation shows that the rotor stall onset begins with modal disturbance followed rapidly by two spike disturbance. The size of the onset stall cell cover about 5 to 6 rotor blade passages. The propagation speed of stall cell is about 42% of rotor rotating speed. This DDES of stall inception captures two stall cells whereas the previous URANS simulation only has one stall cell propagating at about 90% rotation speed. The different propagating speed of stall cells between the URANS and the DDES may be due to the different circumferential mass flux in relative frame.

The vortex trajectory aligned in the blade pitching direction is an indicator that the stall inception is imminent. The spike stall inception appears to be characterized as the tip vortex

rolling up and ending on the casing wall with the vortex axis mostly in the radial direction. Similar to the conclusions in Im et al. [1], the DDES captures many small scale structures of the stall inception, whereas the URANS tends to smear the flow structures due to the Reynolds time average.

11.1.6 Compressor Stall Flutter

A high fidelity methodology of 3-D fluid-structural interaction is conducted for predicting blade flutter in a transonic compressor stage with rotor-stator interaction at near stall conditions. The full 3D unsteady Navier-Stokes equations are solved with Spalart Allmaras turbulence model. The DDES of stall flutter is conducted near stall condition for comparison. The flow solver and the structural solver are fully coupled via pseudo time step within each physical time step. An efficient and accurate modal approach solver is used for simulating the structural responses with the first five major mode shapes of the blade. The NASA Stage 35 is selected to demonstrate the methodology and simulation capability.

The fully coupled FSI simulation is conducted along the speedline. For all the operating points, the amplitude of the blade vibration increase gradually and the blade appear to flutter without adding structural damping to the vibration system. And with 0.001 structural damping, the blade are damped since the flows are fairly steady before the stalling point E. However, the blade vibration response diverges at stalling point E. It appear that the NASA Stage 35 flutter due to the rotating stall.

11.1.7 Compressor NSV Lock-in Investigation

The high fidelity method was also used to investigate the locked-in phenomenon of a high speed axial compressor stage. Time accurate 3D compressible Navier-Stokes equations are solved with a system of 5 decoupled modal equations in a fully coupled manner. A 1/7th annulus sector of IGV-rotor-stator is used with a time-shifted phase lag BC at circumferential boundaries to reduce computational efforts.

The URANS simulation for rigid blades predicts a dominant frequency of the traveling vortices at a non-engine order at 2476 Hz at physical speed recommended by manufacturer, which agree with the NSV frequency obtained from the rig testing. The results from the fully coupled fluid structure simulation captures the blade NSV that agrees with the measurement at the same predicted aerodynamic excitation frequency with rigid blades.

The 1T dominant NSV excitation is achieved by using a damping ratio of 0.03 for the first mode and 0.001 for the other modes. A similar step change of frequency versus rotor rotating speed as that in the measurement is obtained by the high fidelity fully coupled FSI. The mismatches of the forcing frequency and the blade response frequency at different shaft speeds indicate that the NSV of this compressor is excited by aerodynamic forcing instead of being caused by flow frequency/phase locking to structural frequency. The comparisons of the flexible blade simulations and rigid blade simulations demonstrate the NSV excitation is independent of the blade vibration.

11.2 Contributions

The main contributions in this research are the following:

- Sliding interpolation BC for rotor/stator interaction
- Investigation of sonic dip mechanism
- Develop fully coupled fluid-structure interaction for panel flutter simulation
- Delayed detached simulation of the stall inception in NASA Stage 35
- Delayed detached simulation of stall flutter in NASA Stage 35
- Examination of lock-in phenomenon for compressor non-synchronous vibration

11.3 Future Work

Further Investigation of the Mechanism of Sonic Dip Phenomenon

The physical mechanism of the sonic dip phenomenon is related to the anticlimax of the second mode and pitching moment. The complex shock oscillation near sonic dip is the cause of anticlimax of the second mode and pitching moment. However, a quantitative relation between the shock oscillation and the amplitude of the second mode is not available yet. Efforts to study the shock oscillation and aerodynamic damping at different Mach number should be made to further understand the mechanism of sonic dip.

DDES of NSV

In Chapter 10, the URANS under-predicts the NSV frequency because the URANS tends to smear the small scale vortices. The DDES has shown it's advantage in large vortex flow

simulation compared with that of URANS in Chapter 8. The use of DDES in NSV may improve the accuracy in the prediction of NSV frequency.

Appendix A

Publication List

- Gan, J.-Y., Im, H.-S., and Zha, G.-C. Numerical Examination of Lock-in Hypothesis of Non-synchronous Vibration in an Axial Compressor, Submitted to ASME IGTI-2017
- Gan, J.-Y., Im, H.-S., and Zha, G.-C. Stall Flutter Simulation of a Transonic Axial Compressor Stage Using a Fully Coupled Fluid-Structure Interaction, Accepted by AIAA SciTech 2017
- Gan, J.-Y., and Zha, G.-C. Large Eddy Simulation of Lock-in Phenomenon with High Order Schemes, Accepted by AIAA SciTech 2017
- Gan, J.-Y., Li, L.-X., and Zha, G.-C. Truck Rear View Mirror Drag Reduction Using Passive Jet Boat Tail Flow Control, Accepted by WCX17: SAE World Congress Experience 2017
- Gan, J.-Y., Im, H.-S., and Zha, G.-C. Delayed Detached Eddy Simulation of Rotating Stall For a Full Annulus Transonic Axial Compressor Stage, ASME paper GT2016-57985, ASME Turbo Expo 2016, June 13-17, 2016, Seoul, Korea
- Gan, J.-Y., Im, H.-S., and Zha, G.-C. Simulation of Stall Inception of a High Speed Axial Compressor with Rotor-Stator Interaction, 51st AIAA/SAE/ASEE Joint Propulsion Conference, 2015, 10.2514/6.2015-3932
- Gan, J.-Y., Im, H.-S., Espinal, D., Lefebvre, A., and Zha, G.-C., Investigation Of A Compressor Rotor Non-Synchronous Vibration With And Without Fluid-Structure Interaction, ASME Paper GT2014-26478, ASME Turbo Expo 2014: Turbine Technical Conference and Exposition, GT2014, June 16-20, 2014, Dusseldorf, Germany
- Gan, J.-Y., and Zha, G.-C. Delayed Detached Eddy Simulation of Supersonic Panel Aeroelasticity Using Fully Coupled Fluid Structure Interaction with High Order Schemes, 34th AIAA Applied Aerodynamics Conference, Washington, D.C., 13-17 June 2016

- Gan, J.-Y., and Zha, G.-C. Comparison of Drag Prediction Using RANS Models and DDES for the DLR-F6 Configuration Using High Order Schemes, AIAA-2016-0553, SciTech2015, 4-8 January 2016 Manchester Grand Hyatt, San Diego, California
- Gan, J.-Y., and Zha, G.-C. Delayed Detached Eddy Simulation of Projectile Flows, 33rd AIAA Applied Aerodynamics Conference, 2015, 10.2514/6.2015-2589
- Gan, J.-Y., Im, H.-S., Chen, X.-C., Zha, G.-C., and Pasiliao, C. L. Prediction of Wing Flutter Boundary Using High Fidelity Delayed Detached Eddy Simulation, AIAA Paper 2015-0442, SciTech2015, 53rd AIAA Aerospace Sciences Meeting, 5-9 January, 2015, Kissimmee, FL
- Gan, J.-Y. and Zha, G.-C. Near Field Sonic Boom Calculation of Benchmark Cases , AIAA Paper 2015-1252, SciTech2015, 53rd AIAA Aerospace Sciences Meeting, 5-9 January, 2015, Kissimmee, FL
- Gan, J.-Y. and Zha, G.-C., Analysis of a Low Boom Supersonic Flying Wing Preliminary Design , AIAA Paper 2015-1249, SciTech2015, 53rd AIAA Aerospace Sciences Meeting, 5-9 January, 2015, Kissimmee, FL
- Gan, J.-Y., Lefebvre, A., Espinal, D. and Zha, G.-C., Parametric Trade Study for Supersonic Bi-Directional Flying Wing , AIAA Paper 2014-2106, AIAA Aviation, 32nd AIAA Applied Aerodynamics Conference, 16-20 June 2014, Atlanta, GA

References

[1] H.S. Im, X.Y. Chen, and G.C. Zha, "Detached Eddy Simulation of Stall Inception for a Full Annulus Transonic Rotor." Journal of Propulsion and Power, to appear.

[2] E.C. Yates Jr., "AGARD Standard Aeroelastic Configurations for Dynamic Response. Candidate Configuration I.-Wing 445.6." NASA-TM-1000492, 1987.

[3] Bendiksen, O.O., "Influence of Shocks on Transonic Flutter of Flexible Wings." 50th AIAA/ASME/ASCE/AHS/ASC Structures, Structural Dynamics, and Materials Conference 4-7 May 2009, Palm Springs, California, 2009.

[4] R. Srivastava, M. A. Bakhle, T. G. Keith, Jr. and G. L. Stefko , "Flutter Analysis of a Transonic Fan." ASME Turbo Expo 2002, 2002.

[5] Miyakozawa, M., "Flutter and Forced Response of Turbomachinery with Frequency Mistuning and Aerodynamic Asymmetry." PhD thesis, Duke University, 2008.

[6] He, L.; Wang, D.X., "Concurrent Blade Aerodynamic-Aero-elastic Design Optimization Using Adjoint Method," *ASME J. of Turbomach.*, vol. 133, 2011.

[7] Castanier, M.P., and Pierre, C, "Modeling Analysis of Mistuned Bladed Disk Vibration: Status and Emerging Directions," *Journal of Propulsion and Power*, vol. 22, pp. 284–396, 2006.

[8] M. Vahdati, G. Simpson, and M. Imregun, "Mechanisms for Wide-Chord Fan Blade Flutter," *Journal of Turbomachinery*, vol. 133, pp. 041029–1–041029–7, 2011.

[9] A.J. Sanders, K.K. Hassan, and D.C. Rabe, "Experimental and Numerical Study of Stall Flutter in a Transonic Low-Aspect Ratio Fan Blisk," *Journal of Turbomachinery*, vol. 126, pp. 166–174, 2004.

[10] H.-S. Im, X.-Y. Chen, and G.-C. Zha, " Detached Eddy Simulation of Transonic Rotor Stall Flutter Using a Fully Coupled Fluid-Structure Interaction." ASME GT2011-45437, ASME Turbo Expo 2011, Vancouver, Canada, June 2011, 2011.

[11] R. Srivastava, and T.G. Keith Jr., "Influence of Shock Wave on Turbomachinery Blade Row Flutter," *Journal of Propulsion and Power*, vol. 21, pp. 167–174, 2011.

[12] R. Srivastava, J. Panovsky, R. Kielb, L. Virgin, and K. Ekici, "Nonlinear Flutter in Fan Stator Vanes With Time Dependent Fixity," *Journal of Turbomachinery*, vol. 134, pp. 021009–1–021009–8, 2012.

[13] M. Vahdati, A.I. Sayma, C. Bread, and M. Imregun, "Computational Study of Intake Duct Effects on Fan Flutter Stability," *AIAA Journal*, vol. 40, pp. 408–418, 2002.

[14] J.W. Chew, R.J. Hamby, J.G. Marshall, and M. Vahdati, " Part Speed Flutter of Transonic Fan." RTO AVT Symposium on Design Principles and Methods for Aircraft Gas Turbine Engines, Toulouse, France, May 1998, 1998.

[15] A.V. Srinivasan, "Flutter and Resonant Vibration Characteristics of Engine Blades." ASME 97-GT-533, October 1997.

[16] M. Baumgartner, F. Kameier, and J. Hourmouziadis, "Non-Engine Order Blade Vibration in a High Pressure Compressor." ISABE, Twelfth International Symposium on Airbreathing Engines, Melbourne, Australia, 10-15, 1995.

[17] R. Kielb, J. Thomas, P. barter, and K. Hall, "Blade Excitation by Aerodynamic Instabilites - A Compressor Blade Study." ASME Paper No. GT-2003-38634, 2003.

[18] J. Marz, C. Hah, and W. Neise, "An Experimental and Numerical Investigation Into the Mechanisms of Rotating Instability," *Journal of Turbomachinery*, vol. 124, pp. 367–375, 2002.

[19] R. Mailach, I. Lehmann, and K. Vogeler, "Rotating Instabilites in an Axial Compressor Originating From the Fluctuating Blade Tip Vortex." ASME Paper No. GT-2003-38634, 2003.

[20] J. Thomassin, H. Vo, and N. Mureithi, "The Tip Clearance Flow Resonance Behind Axial Compressor Nonsynchronous Vibration," *Journal of Turbomachinery*, vol. 133, pp. 041030–1–041030–10, 2011, doi:10.1115/1.4001368.

[21] H.S. Im, and G.C. Zha, "Simulation of Non-Synchronous Blade Vibration of an Axial Compressor Using a Fully Coupled Fluid/Strcuture Interaction." ASME GT2012-68150, 2012.

[22] H.S. Im, and G.C. Zha, "Effects of Rotor Tip Clearance on Non-Synchronous Blade Vibration for an Axial Compressor." ASME GT2012-68148, 2012.

[23] R. Kamakoti, and W. Shyy, "Fluid-Structure Interaction for Aeroelastic Applications," *Progress in Aerospace Sciences*, vol. 40, pp. 535–558, 2004.

[24] H. Doi, and J.J. Alonso, "Fluid/Structure Coupled Aeroelastic Computations for Transonic Flows in Turbomachinery." GT2002-30313,Proceedings of ASME Turbo Expo 2002, 2002.

[25] V. Gnesin, and R. Rzadkowski, "A Coupled Fluid-Structure Analysis for 3-D Inviscid Flutter of IV Standard Configuration," *Journal of Sound and Vibration*, vol. 251, pp. 315–327, 2002.

[26] V. Carstens, R. Kemme, and S. Schmitt, "Coupled Simulation of Flow-Structrue Interaction in Turbomachinery," *Aerospace Science and Technology*, vol. 7, pp. 298–306, June 2003.

[27] A.I. Sayma, M.V. Vahdati, and M. Imregun, "Turbine Forced Response Prediction Using an Integrated Non-Linear Analysis," *Proceedings of the Institution of Mechanical Engineers, Part K: Journal of Multi-body Dynamics*, vol. 214, pp. 45–60, 2000.

[28] X.Y. Chen, G.-C. Zha, M.-T. Yang, "Numerical Simulation of 3-D Wing Flutter with Fully Coupled Fluid-Structural Interaction," *Journal of Computers & Fluids*, vol. 36, pp. 856–867, 2007, doi:10.1016/j.compfluid.2006.08.005.

[29] B.Y. Wang, and G.C. Zha, "Detached Eddy Simulation of Transonic Limit Cycle Oscillations Using High Order Schemes," *To appear in Journal of Computer & Fluids*, 2011.

[30] B.Y. Wang, and G.C. Zha, "Numerical simulation of transonic limit cycle oscillations using high-order low-diffusion schemes," *Journal of Fluids and Structures*, vol. doi:10.1016/j.jfluidstructs.2010.02.003, 2010.

[31] H. Im, X. Chen, and G. Zha, "Prediction of a Supersonic Flutter Boundary Using a High Fidelity Delayed Detached Eddy Simulation." 50th AIAA Aerospace Sciences Meeting, Nashville, Tennessee, Jan. 2012, 2012.

[32] P.R. Spalart, W.H. Jou, M. Strelets, and S.R. Allmaras, "Comments on the Feasibility of LES for Wings, and on a Hybrid RANS/LES Approach." Advances in DNS/LES, 1st AFOSR Int. Conf. on DNS/LES, Greyden Press, Columbus, H., Aug. 4-8, 1997.

[33] P.R. Spalart, S. Deck, M. Shur, and K.D. Squires, "A New Version of Detached Eddy Simulation, Resistant to Ambiguous Grid Densities," *Theoritical and Computational Fluid Dynamics*, vol. 20, pp. 181–195, 2006.

[34] F.R. Menter, and M. Kuntz, "Adaptation of Eddy-Viscosity Turbulence Models to Unsteady Separated Flow Behind Vehilces, *The Aerodynamics of Heavy Vehicles: Trucks, Buses and Trains, Edited by McCallen, R. Browand, F. and Ross, J.* ," *Springer, Berlin Heidelberg New York, 2004*, 2-6 Dec. 2002.

[35] E. H. Dowell, and K. C. Hall, "MODELING OF FLUID-STRUCTURE INTERACTION," *Annual Review of Fluid Mechanics*, vol. 33, pp. 445–490, 2001.

[36] O. Bendiksen and K. Kousen, "Transonic Flutter Analysis Using the Euler Equations." AIAA Paper 87-0911, 1987.

[37] J. Rausch, R.D. Batina and T. Yang, "Three-dimensional time-marching aeroelastic analyses using an unstructured-grid euler method," *AIAA Journal*, vol. 33, pp. 1626–1633, 1993.

[38] B. B. Prananta, H. M. H. L., and Z. R. J., "Two-Dimensional Transonic Aeroelastic Analysis Using Thin-Layer Navier-Stokes Method," *Journal of Fluid and Structures*, vol. 12, pp. 655–676, 1998.

[39] E. Lee-Rausch and J. Batina, "Calculation of AGARD Wing 445.6 Flutter Using Navier-Stokes Aerodynamics." AIAA Paper 93-3476, 1993.

[40] K. Isogai, "Transonic Dip Mechanism of Flutter of a Sweptback Wing: Part II," *AIAA Journal*, vol. 19, pp. 1240–1242, September 1981.

[41] Tijdeman, H., "Investigations of the Transonic Flow Around Oscillating Airfoils." Doctoral Dissertation, Technical Universityof Delft, The Netherlands, 1977.

[42] Knight, D., Yan, H., Panaras, A. G., Zheltovodov, A., "Advances in CFD Prediction of Shock Wave Turbulent Boundary Layer Interactions," *Progress in Aerospace Sciences*, vol. 39, pp. 121–184, 2003.

[43] Sinha, K., Mahesh, K., Candler, G., "Modeling the Effect of Shock Unsteadiness in Shock/Turbulent Boundary-Layer Interactions," *AIAA Journal*, vol. 43, pp. 586–594, 2005.

[44] Morgan, B., Kawai, S., Lele, S. K., "Large-Eddy Simulation of an Oblique Shock Impinging on a Turbulent Boundary Layer." AIAA Paper 2010-4467, 40th Fluid Dynamics Conference and Exhibit, June 28 - July 1, Chicago, Illinois, 2010.

[45] S. Priebe, M. Martin, "Direct Numerical Simulation of Shockwave and Turbulent Boundary Layer Interactions." AIAA-2009-0589, 47th AIAA Aerospace Sciences Meeting, January 5-8, Orlando, FL, USA, 2009.

[46] Y.Q. Shen, G.C. Zha, and X. Chen, "High Order Conservative Differencing for Viscous Terms and the Application to Vortex-Induced Vibration Flows," *Journal of Computational Physics*, vol. 228(2), pp. 8283–8300, doi:10.1016/j.jcp.2009.08.004, 2009.

[47] Im, H-S., Chen, X-Y and Zha, G-C., " Detached Eddy Simulation of Rotating Stall Inception for a Full Annulus Transonic Rotor ," *AIAA Journal of Propulsion and Power*, vol. 28, No. 4, pp. 782–798, 2012.

[48] X.Y. Chen, B.Y. Wang, and G.C. Zha, "Delayed Detached Eddy Simulation of 3-D Wing Flutter with Fully Coupled Fluid-Structural Interaction." AIAA Paper 2010-0053, 48th AIAA Aerospace Sciences Meeting Including the New Horizons Forum and Aerospace Exposition, Jan. 4-7, 2010.

[49] X.Y. Chen, and G.-C. Zha, "Fully Coupled Fluid-Structural Interactions Using an Efficient High Solution Upwind Scheme," *Journal of Fluid and Structure*, vol. 20, pp. 1105–1125, 2005.

[50] X.-Y. Chen, G.-C. Zha, and M.-T. Yang, "Numerical Simulation of 3-D Wing Flutter with Fully Coupled Fluid-Structural Interaction," *Journal of Computers and Fluids*, vol. 35, pp. 856–867, 2007.

[51] Im, H.-S. and Zha, G.-C., "Prediction of a Supersonic Wing Flutter Boundary Using a High Fidelity Detached Eddy Simulation." AIAA Paper 2012-0039, 50th AIAA Aerospace Sciences Meeting, Jan. 9-12., Nashville, TN, USA, 2012.

[52] Dowell, E.H., "Panel Flutter: A Review of The Aeroelastic Stability of Plate and Shells.," *AIAA Journal*, vol. 8, pp. 385–399, 1970.

[53] Mei C, Abdel-Motagaly K, Chen R., "Review of Nonlinear Panel Flutter at Supersonic and Hypersonic Speeds," *Applied Mechanics Reviews*, vol. 52, pp. 321–332, 1999.

[54] Crowell, A. R., Miller, B. A., and McNamara, J. J., "Computational Modeling for Conjugate Heat Transfer of Shock-SurfaceInteractions on Compliant Skin Panels." 13th AIAA Dynamics Specialists Conference, Denver, CO, April 4-7 2011, pp.1-18, AIAA Paper 2011-2017., 2011.

[55] Dechaumphai, P., Wieting, A., Thornton, E., "Flow-Thermal-Structural Study of Aerodynamically Heated Leading Edges," *Journal of Spacecraft and Rockets*, vol. 26, pp. 201–209, 1989.

[56] A. Gogulapati , R. Deshmukh y, A. R. Crowell y, and J. J. McNamara, "Response of a Panel to Shock Impingement: Modeling and Comparison with Experiments." AIAA 2014-0148, 55th AIAA/ASMe/ASCE/AHS/SC Structures, Structural Dynamics, and Materials Conference, 13-17 January 2014, National Harbor, Maryland, 2014.

[57] Platzer, M.F., Carta, F.O., "AGARD Manual on Aeroelasticity in Axial-Flow Turbomachines. Volume 1. Unsteady Turbomachinery Aerodynamics,"

[58] Fransson, T.H.

[59] Hall, C.H., Kielb, R.E., Thomas, J.P., "Unsteady Aerodynamics, Aeroacoustics and Aeroelasticity of Turbomachines,"

[60] Whitehead, D.S, "Classical Two-Dimensional Methods," 1987.

[61] J. Lepicovsky, R. V. Chima, T. A. Jett, T. J. Bencic, and K. E. Weiland, "Investigation of flow separation in a transonic-fan linear cascade using visualization methods," *NASA/TM-2000-210521*, Dec 2000.

[62] Shaw, L.M., Boldman, D.R, and Buggele, A.E, "Unsteady Pressure Measurements on a Biconvex Airfoil in a Transonic Oscillating Cascade." NASA TM-86914, 1985.

[63] K. Isomura, and M.B. Giles, "A Numerical Study of Flutter in a Transonic Fan," *Journal of Turbomachinery*, vol. 120, pp. 500–507, 1998.

[64] P. Vasanthakumar, "Computation of Aerodynamic Damping for Flutter Analysis of a Transonic Fan." GT2011-46597, 2011.

[65] H.-S. Im, and G.-C. Zha, "Flutter Prediction of a Transonic Fan with Traveling Wave Using Fully Coupled Fluid/Structure Interaction." ASME Paper GT2013-94341, Proceedings of ASME Turbo Expo, San Antonio, Texas, USA, 2013.

[66] J. Thomassin, H. Vo, and N. Mureithi, "Blade Tip Clearance Flow and Compressor Nonsynchronous Vibrations: The Jet Core Feedback Theory as the Coupling Mechanism," *Journal of Turbomachinery*, vol. 131, pp. 11013–1–11013–9, 2009.

[67] A. Sanders, "Nonsynchronous Vibration(NSV) due to a Flow-Induced Aerodynamic Instability in a Composite Fan Stator," *Journal of Turbomachinery*, vol. 127, pp. 412–421, 2005.

[68] Vo, H.D., "Role of Tip Clearance Flow in Rotating Instabilities and Nonsynchronous Vibrations," *Journal of Propulsion and Power*, vol. 26, pp. 556–561, doi: 10.2514/1.26709, 2010.

[69] Im, H.-S. and Zha, G.-C., "Investigation of Flow Instability Mechanism Causing Compressor Rotor Blade Non-Synchronous Vibration," 2014.

[70] T.R. Camp, "A Study of Acoustic Resonance in in a Low Speed Multistage Compressor," *AMSE J. of Turbomach.*, vol. 121, pp. 36–43, 1999.

[71] Spiker, M.A.; Kielb, R.E.; Thomas, J.P.; Hall, K.C., "Application of Enforced Motion to Study 2-D Cascade Lock-in Effect." AIAA Paper 2009-892, 47th AIAA Aerospace Sciences Meeting, Jan. 2009.

[72] S. Clark, R. Kielb, and K. Hall, "Developing a Reduced-Order Model to Understand Nonsynchronous Vibration (NSV) in Turbomachinery." ASME GT2012-68145, 2012.

[73] S. Clark, R. Kielb, and K. Hall, "A van der Pol Based Reduced-Order Model for Non-Synchronous Vibration (NSV) in Turbomachinery." ASME GT2013-95741, 2013.

[74] Bourguet, M., Karniadakis, G., and Triantafyllou, M., "Lock-in of the vortex-induced vibrations of a long tensioned beam in shear flow," *Journal of Fluids and Structures*, vol. 27, pp. 838–847, 2011.

[75] Besem, F.M., Kamrass, J.D., Thomas, J.P., Tang, D. and Kielb, R.E., "Vortex-Induced Vibration and Frequency Lock-In of an Airfoil at High Angles of Attack," *Journal of Fluids Engineering*, vol. 138, p. DOI: 10.1115/1.4031134, 2016.

[76] Gan, J.-Y., Im, H.-S., Espinal, D., Lefebvre, A., and Zha, G.-C, "Investigation of a Compressor Rotor Non-Synchronous Vibration With and Without Fluid-Structure Interaction." GT2014-26478, ASME Turbo Expo 2014, 2014.

[77] K. Yamada, M. Furukawa, and K. Funazaki, "Numerical Analysis of Tip Leakage Flow Field in a Transonic Axial Compressor Rotor." IGTC2003 Tokyo TS-030, Proceedings of the International Gas Turbine Congress 2003, 2003.

[78] C. Hah, D.C. Rabe, and A.R. Wadia, "Role of Tip-Leakage Vortices and Passage Shock in Stall Inception in a Swept Transonic Compressor Rotor." GT2004-53867, Proceedings of ASME Turbo Expo 2004, 2004.

[79] N. Reuss, and C. Mundt, "Experimental Investigations of Pressure Distortions on the High-Pressure Compressor Operating Behavior," *Journal of Propulsion and Power*, vol. 25, pp. 653–667, doi: 10.2514/1.37412, 2009.

[80] Bright, M.M.; Qammar, H.K.; and Wang, L.Z., "Investigation of Pre-Stall Mode and Pip Inception in High-Speed Compressors Through Through the Use of Correlation Integral," *Journal of Turbomachinery*, vol. 121, pp. 743–750, 1999.

[81] M. Zake, L. Sankar, and S. Menon, "Hybrid Reynolds-Averaged Navier-Stokes/Kinetic-Eddy Simulation of Stall Inception in Axial Compressors," *Journal of Propulsion and Power*, vol. 26, pp. 1276–1282, doi: 10.2514/1.50195, 2010.

[82] R. Davis, and J. Yao, "Computational Approach for Predicting Stall Inception in Multistage Axial Compressor," *Journal of Propulsion and Power*, vol. 23, pp. 257–265, doi: 10.2514/1.50195, 2007, doi: 10.2514/1.18442.

[83] D.A. Hoying, C.S. Tan, H.D. Vo, and E.M. Greitzer, "Role of Blade Passage Flow Structures in Axial Compressor Rotating Stall Inception," *AMSE J. of Turbomach.*, vol. 121, pp. 735–742, doi:10.1115/1.2836727, 1999.

[84] H.D. Vo, C.S. Tan, and E.M. Greitzer, "Criteria for Spike Initiated Rotating Stall," *AMSE J. of Turbomach.*, vol. 130, pp. 1–8, doi:10.1115/1.2750674, 2008.

[85] J. Chen, B. Johnson, M. Hathaway, and R. Webster, "Flow Characteristics of Tip Injection on Compressor Rotating Spike via Time-Accurate Simulation," *Journal of Propulsion and Power*, vol. 25, pp. 678–687, doi: 10.2514/1.41428, 2009.

[86] J. Chen, M. Hathaway, and G. Herrick, "Prestall Behavior of a Transonic Axial Compressor Stage via Time-Accurate Numerical Simulation," *AMSE J. of Turbomach.*, vol. 130, pp. 1–12, doi:10.1115/1.2812968, 2008.

[87] Gan, J.Y., Im, H.S., Zha, G.C., "Simulation of Stall Inception of a High Speed Axial Compressor with Rotor-Stator Interaction." AIAA Paper 2015-3932, 51st AIAA/SAE/ASEE Joint Propulsion Conference, Orlando, FL.

[88] R. Srivastava, and T. S. R. Reddy, "Comparative Study of Coupled-Mode Flutter-Analysis Methods for Fan Configurations," *Journal of Propulsion and Power*, vol. 15, pp. 447–453, May-June 1999.

[89] Gan, J.Y., Im, H.S., Chen, X.Y., Pasiliao, C.L. and Zha, G.C., "Prediction of Wing Flutter Boundary Using High Fidelity Delayed Detached Eddy Simulation." AIAA Paper 2015, Kissimmee, Florida, Jan. 2015.

[90] I.H. Shames, "Engineering Mechanics : Dynamics." Prentice-Hall, Englewood Cliffs, New Jersey, 1980.

[91] S.A. Orszag, "Analytical Theories of Turbulence," *Journal of Fluid Mechanics*, vol. 41, pp. 363–386, 1970.

[92] G. Erlebacher, M. Y. Hussaini, C. G. Speziale, and T. A. Zang, "Toward the Large Eddy Simulation of Compressible Turbulent Flows," *Journal of Fluid Mechanics*, vol. 238, pp. 155–185, 1992, DOI:10.1017/S0022112092001678.

[93] P.R. Spalart, and S.R. Allmaras, “A One-equation Turbulence Model for Aerodynamic Flows.” AIAA-92-0439, 1992.

[94] M. Shur, P.R. Spalart, M. Strelets, and A. Travin, “Detached Eddy Simulation of an Airfoil at High Angle of Attack", 4th Int. Symp. Eng. Turb. Modeling and Measurements, Corsica.” May 24-26, 1999.

[95] Y.Q. Shen, B.Y. Wang, and G.C. Zha, “Implicit WENO Scheme and High Order Viscous Formulas for Compressible Flows .” AIAA Paper 2007-4431, 2007.

[96] R.V. Goggett, R.V. Rainey, and H.G. Morgan, “An experimental Investigsation of Aerodynamic Effects of Airfoil Thickness on Transonic Flutter Characteristics.” NASA TMX-79, 1959.

[97] F. Liu, J. Cai, and Y. Zhu, “Calculation of Wing Flutter by a Coupled CFD-CSD method.” AIAA-2000-0907, 2000.

[98] M.A. Bakhle, T.S.R. Reddy, and T.G. Keith Jr., “Time Domain Flutter Analysis of Cascades Using a Full-Potnetial Solver,” *AIAA Journal*, vol. 30, pp. 163–169, 1992.

[99] G.C. Zha, Y.Q. Shen, and B.Y. Wang, “An Improved Low Diffusion E-CUSP Upwind Scheme ,” *Journal of Computer and Fluids*, vol. 48, pp. 214–220, 2011, doi:10.1016/j.compfluid.2011.03.012.

[100] Y.Q. Shen, and G.C. Zha, “Improvement of the WENO Scheme Smoothness Estimator,” *International Journal for Numerical Methods in Fluids*, vol. 64,, pp. 653–675, DOI:10.1002/fld.2186, 2009.

[101] Y.Q. Shen, G.C. Zha, and B.Y. Wang, “Improvement of Stability and Accuracy of Implicit WENO Scheme,” *AIAA Journal*, vol. 47, pp. 331–334, DOI:10.2514/1.37697, 2009.

[102] Y.Q. Shen, and G.C. Zha, “Large Eddy Simulation Using a New Set of Sixth Order Schemes for Compressible Viscous Terms,” *Journal of Computational Physics*, vol. 229, pp. 8296–8312, doi:10.1016/j.jcp.2010.07.017, 2010.

[103] G.-C. Zha, and E. Bilgen, “Numerical Study of Three-Dimensional Transonic Flows Using Unfactored Upwind-Relaxation Sweeping Algorithm,” *Journal of Computational Physics*, vol. 125, pp. 425–433, May 1996.

[104] Y.Q. Shen, B. Wang, and G.C. Zha, “Comparison Study of Implicit Gauss-Seidel Line Iteration Method for Transonic Flows.” AIAA Paper 2007-4332, 2007.

[105] B. Van Leer, “Flux Vector Splitting for the Euler Equations,” *Eighth International Conference on Numerical Methods in Fluid Dynamics: Lecture Notes in Physics*, vol. 170, pp. 507–512, 1982.

[106] J. L Steger, and R.F Warming, “Flux Vector Splitting of the Inviscid Gasdynamic Equations With Application to Finite Difference Methods,” *Journal of Computational Physics*, vol. 40, pp. 263–293, 1981.

[107] J.R. Edwards, “A Low-Diffusion Flux-Splitting Scheme for Navier-Stokes Calculations,” *Computer & Fluids*, vol. 6, pp. 635–659, doi:10.1016/S0045–7930(97)00014–5, 1997.

[108] Zha, G.C., Shen, Y.Q., and Wang, B.Y., “Calculation of Transonic Flows Using WENO Method with a Low Diffusion E-CUSP Upwind Scheme.” AIAA Paper 2008-0745, 46th AIAA Aerospace Sciences Meeting, Reno, NV, Jan. 2008.

[109] P. Roe, “Approximate Riemann Solvers, Parameter Vectors, and Difference Schemes,” *Journal of Computational Physics*, vol. 43, pp. 357–372, doi:10.1016/0021–9991(81)90128–5, 1981.

[110] S. De Rango, and D. W. Zingg, “Aerodynamic Computations Using a Higher Order Algorithm.” AIAA 99-0167, 1999.

[111] D. W. Zingg, S. De Rango, M. Nemec, T. H. Pulliam, “Comparison of Several Spatial Discretizations for the Navier-Stokes Equations,” *Journal of Computational Physics*, vol. 160, pp. 683–704, 2000.

[112] A. Jameson, “Time Dependent Calculations Using Multigrid with Applications to Unsteady Flows Past Airfoils and Wings.” AIAA Paper 91-1596, 1991.

[113] J. Alonso, L. Martinelli, and A. Jameson, “Multigrid Unsteady Navier-Stokes Calculations with Aeroelastic Applications.” AIAA Paper 95-0048, 1995.

[114] Spottswood, S. M., Beberniss, T., and Eason, T., “Full-Field Dynamic Pressure and Displacement Measurements of a Panel Excited by Shock Boundary-Layer Interaction.” AIAA Paper 2013-2016, May, 2013.

[115] L. Reid, and R.D. Moore, “Design and Overall Performance of Four Highly-Loaded, High Speed Inlet Stages for an Advanced, High Pressure Ratio Core Compressor.” NASA TP.1337, 1978.

[116] J.D. Denton, “Lessons from Rotor 37,” *Journal of Thermal Science*, vol. 6, pp. 1–13, doi: 10.1007/s11630–997–0010–9, 1996.

[117] J. Dunham, “CFD Validation for Propulsion System Components.” AGARD-AR-355, 1998.

[118] R. V. Chima, “Calculation of Tip Clearance Effects in a Transonic Compressor,” *AMSE J. of Turbomach.*, vol. 120, pp. 131–140, 1998.

[119] H.S. Im, X.Y. Chen, and G.C. Zha, “Simulation of 3D Multistage Axial Compressor Using a Fully Conservative Sliding Boundary Condition.” ASME IMECE2011-62049, International Mechanical Engineering Congress & Exposition, Denver, November 2011, 2011.

[120] I.J. Day, and C. Freeman, “The Unstable Behavior of Low and High-Speed Compressors,” *AMSE J. of Turbomach.*, vol. 116, pp. 194–201, doi:10.1115/1.2928353, 1994.

[121] H. Khaleghi, M. Boroomand, A.M. Tousi, and J.A. Teixeira, "Stall Inception in a Transonic Axial Fan," *Journal of Power and Energy*, vol. 222, pp. 199–208, doi:10.1243/09576509JPE407, 2008.

[122] W.W Copenhaver, S.L. Puterbaugh, and C. Hah, "Unsteady Flow and Shock Motion in a Transonic Compressor Rotor," *Journal of Propulsion and Power*, vol. 13, pp. 17–23, 1997.

[123] C. Hah, J. Bergner, and H. Schifer, "Short Length Scale Rotating Stall Inception in a Transonic Axial Compressors : Criteria and Mechanisms." GT2006-90045, ASME Turbo Expo, 2006, doi:10.1115/GT2006-90045.

[124] M. Inoue, M. Kuroumaru, T. Tanino,and M. Furukawa, "Propagation of Multiple Short-Length-Scale Stall Cells in an Axial Compressor Rotor," *AMSE J. of Turbomach.*, vol. 122, pp. 45–54, 2000.